

Effects of disorder in Fractional Quantum Hall Systems

Christian Müller aus Wolgast

March 20, 2024

Abstract

The thesis deals with the influence of impurities on a two dimensional electron gas in the regime of the Fractional Quantum Hall effect [17]

Contents

1	Introduction	5
1.1	State of the art	5
2	Previous Results and theoretical foundations	6
2.1	Phenomena of electrons subjected to a magnetic field - the Hall effects	6
2.2	Some reminders of the quantum mechanical description of electrons in strong magnetic fields	10
2.2.1	The Aharonov Bohm Effect	10
2.2.2	Symmetries of the system - Translation operators	12
2.2.3	Eigenfunctions and spectrum of noninteracting electrons in a magnetic field - Landau levels	13
2.2.4	Localization	14
2.3	The Integer Quantum Hall effect	15
2.3.1	The Quantum Hall State as an example for a topological insulator	19
2.4	Interacting electrons in 2D - The Fractional Quantum Hall Effect	20
2.4.1	A closer look - The Hamiltonian with interaction term	21
2.4.2	Additional symmetries and new translation operators	22
2.4.3	Properties of the ground state	24
2.4.4	The Laughlin wave function	26
2.4.5	Topological conductance	32
2.4.6	Excitations to the Laughlin ground state	32
2.4.7	Liquid state vs. insulator	35
2.4.8	The Composite Fermion	36
2.5	Exact Diagonalization	39
2.5.1	The geometry - Disk world vs. Torus	39
2.5.2	Computational details	40
2.6	Alternative approaches	41
3	The homogenous FQH system	42
3.1	Preliminaries	42
3.1.1	Organization of this chapter	42
3.2	The spectrum of the homogenous system and derived values	43
3.2.1	The spectrum of the homogenous system	43
3.2.2	The ground state energy.	44
3.2.3	The Correlation Gap	47
3.2.4	Results for the $k = 0$ gap obtained in this work	49

3.2.5	The degeneracy of the ground state - band width E_b	55
3.3	The electronic density	56
3.4	Electron-Electron correlation in the homogenous ground state	60
3.4.1	Results	61
3.5	A short first summary	62
4	Investigating the inner structure of the electron-vortex complex	66
4.1	Background and some details of the calculations - How to find vortices in a many-particle wave function	67
4.1.1	Previous results from the literature	69
4.2	The vortex distributions in a homogeneous state	70
4.3	Eliminating the impact of the sample electron configuration - Electron vortex correlations $g_{ev/vv}$	71
4.3.1	Methodical considerations	72
4.3.2	Analysis of the distributions principal properties	73
4.3.3	Aspects of computer based evaluation of g_{ev} and g_{vv}	76
4.4	Electron-vortex correlations in homogeneous system	77
4.5	A short summary	78
5	Introducing disorder - The system with a single Gaussian impurity	79
5.1	Preliminaries and results from the literature	79
5.1.1	Organization of this chapter	80
5.1.2	How to model disorder - Introducing the model system	81
5.2	Global properties - Spectra, energetics and overlaps	82
5.2.1	Weak impurities	82
5.2.2	Strong impurities	94
5.2.3	Shape of the impurity	97
5.3	Electronic Density	99
5.3.1	Expectations based on literature: Response to an impurity	99
5.3.2	The density response of the 2 DEG in the presence of a magnetic field - Results	101
5.3.3	Electron-electron correlations	107
5.4	Discrete charging of a single impurity potential	108
5.5	The inner structure of the electron-vortex complex	112
5.5.1	Vortex distribution: The disturbed system	112
5.5.2	Quantized charging revisited	116
5.5.3	Conclusion	116
5.6	Correlations and many body properties of the disturbed state	117
5.6.1	Analysis of general features and properties of g_{ev} and g_{vv}	117
5.6.2	Quantitative exploration of the Electron-Vortex complex in inhomogeneous systems	123
5.6.3	Bridge the gap between global and local properties by virtue of the electron-vortex correlations	127
5.7	First Summary and Conclusions	130

6 Multiple impurities - localization and scaling in the FQH regime	133
6.1 Introduction and organization of this chapter	133
6.2 Creation and characteristics of the random potential	133
6.2.1 The generation method	134
6.2.2 The random electrostatic potential and its statistic properties	134
6.2.3 Numerical results for the variance and the correlation length of the random background potential	136
6.3 The electronic properties under the influence of a random background potential	139
6.3.1 Fluctuation of gap and bandwidth due to the randomness of the potential	143
6.3.2 Ground state energy, spectra, correlation gap and bandwidth	143
6.3.3 Summary - which kind of background potentials are suitable for calculating the electron-vortex distributions? . . .	146
6.4 About Electron - Vortex correlations and the persistence of the FQH state in systems subject to a random potentials	147
6.4.1 How does the size of an electron-vortex composite change? - Results for random potentials-	148
6.4.2 The size of the electron-vortex complex and the correlation length of the impurity potential	151
6.5 Summary, Conclusions and Discussions	153
6.5.1 Generalization of the results to systems with Coulomb Interaction	159
7 Summary of results	161
8 Outlook and future plans	163
A List of abbreviations, units etc.	164
B Details of perturbational calculus	166
B.0.1 The effect of a single impurity on the bandwidth	166
C Numerical precision of the employed algorithms and libraries	169
D Dependency of the vortex distribution on the symmetry of the sampling electrons	171
D.1 The sample electrons geometry	171
D.1.1 The symmetry of the electron configuration	172
D.1.2 Size of the sample electron configuration	172
E Some details about the evaluation of the electron-electron correlation	174
F The autocorrelation function	176
F.1 Outline	176
F.1.1 The case of constant potential	176
F.1.2 The case of a single gaussian potential	177
F.1.3 The case of a periodic potential	177

F.1.4	The case of white noise	178
F.2	Metropolis Algorithm	178
F.2.1	The algorithm	179
F.3	Statistical properties of the many impurity states	179

Chapter 1

Introduction

FQH and disorder.
What about local properties of a highly correlated state.

1.1 State of the art

Chern number analysis by Jain et.al.

Chapter 2

Previous Results and theoretical foundations

In this chapter of the work the important properties of the system under observation are presented and the relevant tools for its investigation are introduced.

We will start with a short historical tour through the different experimental results arising from ever thinner electron layers subjected to ever stronger magnetic field at ever lower temperatures. The more thorough introduction into the theoretical and conceptual basics of the Quantum Hall effects follows. We will start with an examination the two dimensional electron gas, followed by the study of the effect an magnetic field has on such a system. Some necessary reminders to gauge-invariance in quantum mechanics are given and the classical, integer and fractional quantum Hall effects will be introduced.

The localization of electrons in 2D systems will be studied and the method of exact Diagonalization (EXD), as a exact method to solve the Schrödinger equation, is introduced and some necessary background on the computational details will be given.

2.1 Phenomena of electrons subjected to a magnetic field - the Hall effects

In this part we will briefly review the different effects which arise from subjecting electrons in a thin layer (the exact meaning of thin will change throughout this section) to a magnetic field. The presentation follows the historical development of the experimental research - starting in the late 19th century to the present day.

We begin with studying a system of non-interacting electrons in a magnetic field within the framework of classical physics which reveals the classical Hall effect. In this framework (see e.g. [57]), an electron under the influence of a magnetic field $\mathbf{B} = (0, 0, B)$ and an electrical field \mathbf{E} is described by the following EOM

$$m_e \frac{d^2}{dt^2} \mathbf{r} = e (\mathbf{E} + \mathbf{v} \times \mathbf{B}) \quad (2.1)$$

This equation can be derived from an Hamiltonian function

$$H = \frac{(\mathbf{p} - e\mathbf{A})^2}{2m_e} + \mathbf{E}. \quad (2.2)$$

The vector-potential \mathbf{A} is connected to the actual measurable entity \mathbf{B} by the relation

$$\mathbf{B} = \nabla \times \mathbf{A}. \quad (2.3)$$

Every conservative potential function $\chi(r, t)$ can be added to the vector potential without any consequence for the magnetic Field B [57].

The solution of (2.1) gives the velocity

$$\mathbf{v}(\mathbf{r}, t) = \mathbf{r}_0 \omega_c (\sin(\omega_c t), \cos(\omega_c t) + \mathbf{v}_0, 0), \quad (2.4)$$

where $\mathbf{v}_0 = -\frac{\mathbf{E}}{B}$ is the drift velocity and $\omega_c = \frac{eB}{m_e}$ is the cyclotron frequency. Equation (2.4) describes a spiral trajectory of an electron, where the radius of the spiral is determined by the magnetic field and the translation in z-direction is governed by the electrical field.

The application of this theory to a thin metal sheet, where electrons are assumed to travel freely¹ under the influence of the potential V gives rise to the classical Hall [50] effect.

The text book explanation (see e.g. [57, 112]) goes as follows: **Hier einfach eine kurze Bemerkung zu ohmschem Widerstand rein** In a sample as depicted in Fig. 2.1 (right) with no magnetic field present, a current flows in x direction according to Ohms Law: $I = j_x db = \frac{U}{R}$. When switching on a perpendicular magnetic field $\mathbf{B} = B_z$, electrons experience a force in y-direction, deflecting them to one edge of the sample. This creates an additional voltage V_H , the Hall-voltage² across the sample (in y-direction). The voltage depends linearly on the magnetic field. $V_H = R_H \frac{BI}{d}$, where the Hall resistance is constant (and material dependent). In a stationary situation, the Lorentz force and the Coulomb force due to the perpendicular field cancel out, thus the current flows again in x-direction. The condition reads $\frac{V_H}{b} = \frac{B}{ne}$. Two different resistances can be derived from this line of thought, R_{xy} and R_{xx} , where $R_{xy} = \frac{V_H}{I}$ and R_{xx} is the voltage drop along the sample.

Ohms law in vector calculus reads

$$\mathbf{j} = n_e e \mathbf{v} = (0, -n_e e E / B, 0) = \underline{\underline{\sigma}} \mathbf{E} \quad (2.5)$$

where $\underline{\underline{\sigma}}$ is the conductivity tensor with the components $\sigma_{xx} = \sigma_{yy} = const.$ (where the actual value is independent of the magnetic field), $\sigma_{xy} = -\sigma_{yx} = -B/n_e e$.

The advent of semiconductors in the 1970s allowed people to make the thin sheet even thinner - practically confining electrons to two dimensions. The study of quantum effects in solid state materials has been greatly enhanced by the development of techniques to prepare confined electrons on interfaces. The preparation and characterization of those low dimensional systems are the subject of a vast body of literature nonetheless a short introduction of the experimental setup shall be given here.

¹neglecting scattering processes

²The sign of the voltage differs over a wide range of materials, something classical physics can not explain [62]

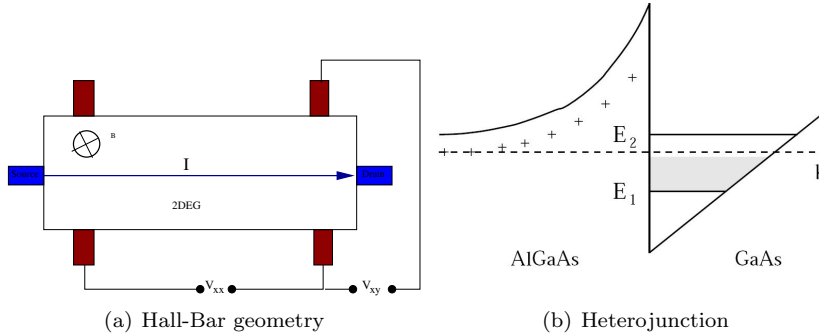


Figure 2.1: (a) Schematics of a Hall bar setup as used in the measurements of von Klitzing et al. (2.2) (b) Example potential profile of a hetero-junction. The cut is perpendicular to the materials interface, the electrons are located at the bottom of the potential minimum, moving only in 2 dimensions.

The basic setup to trap electrons at an interface can be realized by a so called hetero-junction (see Fig. 2.1(right)), which is heterogeneous in such a sense that two *different but-not-to-different materials* are grown on top of each other³. The 2 materials have a different band structure which must match at the interface. This leads to a spill-over of electrons into the region with the energetically lower band, thus creating a region of electrons apart from there donors and thus highly mobile. This region is confined along the main axis of material growth, leaving only 2 degrees of freedom for electronic translation.⁴

The result is the *Two (2) Dimensional Electron Gas (2DEG)* in which the electrons are highly mobile and move only in 2 dimensions. In typical samples used in present day experiments the electron density can be tuned over multiple orders of magnitude

The quantum mechanical EOM decouple into the z-dependent part and the x-y -plane motion,

$$\psi(\mathbf{r}) = \phi(x, y)\xi(z) = \exp(-ik_{x,y}(x + y))\xi(z), \quad (2.6)$$

where $\phi(x, y)$ are plane waves in the x,y directions. (**Das sind die die interessanten Teile**

The application of strong perpendicular magnetic fields onto such a 2DEG led to the discovery of the Integer Quantum Hall Effect (IQH). The famous experiments of Klitzing et al [67] were performed on a MOSFET (featuring a 2DEG) structure as depicted in Fig.2.1(right). A 2DEG under the influence of a strong magnetic field perpendicular to the electric field causing the current I shows (see Fig.2.2 left) a significantly different behavior from the classical (Fig. 2.1) linear dependency. In particular, at some magnetic field strengths (corresponding to integer⁵ filling factors), the Hall voltage has plateaus where the potential drop along the current direction is zero. Subsequent measurements showed that this

³The material pair GaAs/AlGaAs is often used as the lattice mismatch between these 2 materials is small enough

⁴Strictly speaking is this only true for $T = 0K$ where the next degrees of freedom in z-direction are not thermally excited.

⁵hence the name: Integer Quantum Hall Effect IQH

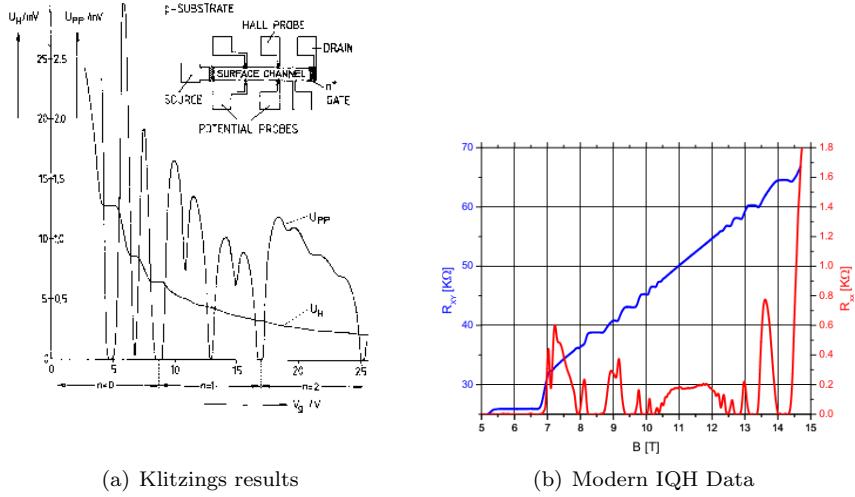


Figure 2.2: (left) Measurement of the Hall voltage and the Potential along the x-direction as measured by von Klitzing [67]. (right) The Hall resistance measured as function of B. The steps in R_{xx} and the plateaus in R_{xy} appear at certain discreet quantized values of the magnetic field (image taken from [112]). N.B.: The classical Hall effect would give a straight line starting at (0,0).

behavior is persistent for different field strength, geometries etc. and that the resistance value at $\nu = 1$ is constant to experimental precision (10^{-10}). In fact the use of those measurements to determine the fine-structure constant has been envisaged by Klitzing et.al at the beginning. Later on, the Hall resistivity at $\nu = 1$ became a constant in its own right. A detailed explanation is given below (Section 2.3, p.15 ff)

A few years after Klitzing's discovery of the IQH, an identical experimental setup was subjected to even higher magnetic fields, in search of a magnetically induced crystallization of the electrons in 2D. What Stoermer et al. [122, 115] found instead, were more plateaus in the Hall conductivity respectively minima in the longitudinal conductivity (see Fig. 2.2). These plateaus, very similar to the ones found by Klitzing et al., appear at rational (or as it was later called - Fractional) filling factors, most prominently at $\nu = \frac{1}{3}$.

The samples used were of high quality, in particular the electron mobility was enhanced by a large spatial separation of impurities in the bulk from the 2 DES and lower temperatures (compared to the IQH experimental setup). The overarching theme of this thesis - the question of how clean the samples were supposed to be in order to exhibit the FQH-like behavior was first encountered in those experiments.

The theory behind this effect is explained in more detail in the following sections (2.4, p. 20 ff.)

In the remainder of this section we plunge into the vast literature covering the origins and explanations of the Quantum Hall Effects. Instead of trying to write another textbook on the Quantum Hall Effects, only those features of the QHE which are of interest for the present work is given. For good textbooks the reader is referred to the books of eg. Yoshioka [135], Chakraborty [17], Jain

[58] and references therein.

2.2 Some reminders of the quantum mechanical description of electrons in strong magnetic fields

The use of a 2DEG and the low temperatures at which the measurements of Klitzing and Stoermer were performed, makes a treatment within the framework of quantum physics necessary. The quantum mechanics of electrons under the influence of magnetic fields is studied in this part.

2.2.1 The Aharonov Bohm Effect

A good starting point to elucidate the qualitatively different features of a quantum mechanical system in a magnetic field, is the Aharonov-Bohm Effect [5, 120, 81]. Here a vector potential, even if it is related to a vanishing magnetic field at the (classical) site of the electron, influences the phase of the electronic wave function. These changes give rise to measurable, B-dependent changes in the interference patterns (see Fig.2.3(left) and its caption).

To understand this, consider the Schrödinger equation of a free particle under the influence of an arbitrary vector potential,

$$\frac{1}{2m} \left(\frac{\hbar}{i} \nabla + \frac{e}{c} \mathbf{A}(\mathbf{r}, t) \right)^2 \psi_i = \epsilon_i \psi_i. \quad (2.7)$$

As the gauge invariance must be preserved in quantum mechanics, a gauge transformation must not only change the vector potential (and hence the Hamiltonian) but also the eigenstate ψ_i

$$\begin{aligned} \frac{1}{2m} \left(\frac{\hbar}{i} \nabla + \frac{e}{c} \mathbf{A}(\mathbf{r}, t) \right)^2 &\rightarrow \frac{1}{2m} \left(\frac{\hbar}{i} \nabla + \frac{e}{c} (\mathbf{A}(\mathbf{r}, t) + \nabla \chi) \right)^2 \\ \psi_i &\rightarrow \exp \left[\frac{ie\chi(r, t)}{\hbar c} \right] \psi_i \end{aligned} \quad (2.8)$$

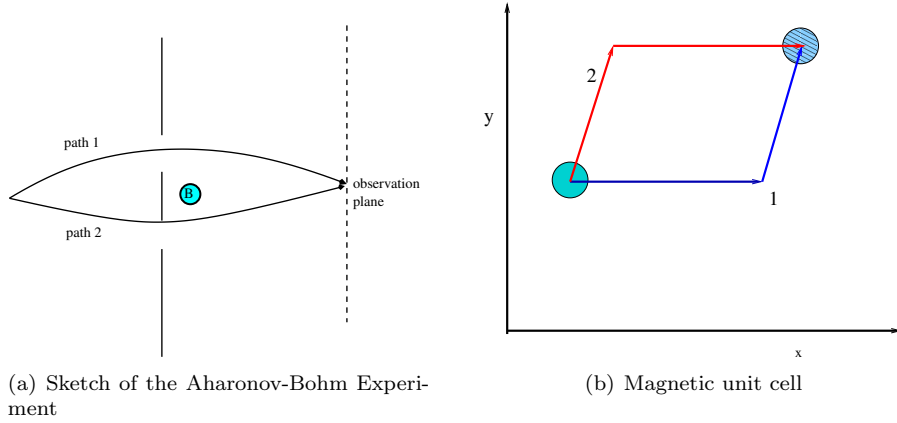
In the case $\mathbf{B} = \nabla \times \mathbf{A} = \mathbf{0}$, the vector potential can be written as a potential function $\mathbf{A} = \nabla \chi$. Applying this to (2.8) the function χ is determined by the integral $\chi(r, t) = \int_{\text{Path}} d\mathbf{r}' \mathbf{A}(\mathbf{r})$. As the vector potential can be gauged by an arbitrary potential function $\nabla \chi$ the phase change of the electron subjected to a translation is gauge dependent but persistent. Applying the Landau - gauge for a B field⁶

$$\mathbf{A}(\mathbf{r}) = \begin{pmatrix} 0 \\ Bx \\ 0 \end{pmatrix} \quad (2.9)$$

to a magnetic field $B(r) = (0, 0, B)^T$, we find the Aharonov-Bohm phase shift to be

$$\psi(x + a, y + b) = e^{\chi(a, b)} \psi(x, y) \quad (2.10)$$

⁶All results in this section are gauge independent - only convenience is dictating the choice of the gauge.



(a) Sketch of the Aharonov-Bohm Experiment

(b) Magnetic unit cell

Figure 2.3: (left) A wave function is split into 2 coherent parts before the slit. The separate beams propagate through the slit and are reunited in the observation plane. The magnetic flux is injected through the coil between the 2 beams, where the magnetic field is constricted inside the coil. However, the non-vanishing vector potential *outside* the coil affects the phase of the 2 beams and result in a B-field dependent interference pattern in the observation plane. The important point here is, that along the (classical) paths the magnetic field can be zero, only a local flux is present *somewhere inside* the path. (right) 1 and propagate to point 2 along the two possible trajectories.

The application of this phase shift to an arbitrary translation of the wave function combined with the constraint of the wave function to be single valued gives the connection of the magnetic unit cell and the magnetic field in flux quanta ϕ .

To see the resulting physics, we consider the "Gedankenexperiment" depicted in Fig.2.3 (right) where an electron propagates in 2 coherent paths from point 1 to point 2⁷. The electrons wave function acquires a general phase η along the 2 trajectories 1 and 2, however at point 2 they must be the same, thus giving a constraint to the phases picked up along the way. The phases can be calculated with the line integral.

$$\begin{aligned} \eta_1 &= \eta_2 & (2.11) \\ \int_1 \mathbf{A} d\mathbf{r} &= \int_2 \mathbf{A} d\mathbf{r} \\ \oint_{\text{any closed path}} \mathbf{A}(\mathbf{r}', t) d\mathbf{r}' &= \int_{\text{AreaS}} \nabla \times \mathbf{A} dS = \Phi \end{aligned}$$

The last line in (2.11) shows, that the unit cell which is impressed on the system by the magnetic field must contain a single flux quantum and has the area of $A_\Phi = 2\pi l_0^2$ [92]. It is worth noting, that the phase shift (and its implications) do not require the magnetic field to be > 0 in the paths of the electron. A

⁷This setup is realized in double slit experiments, where the interference pattern is measured at point 2.

single flux quantum inside this closed path has already the effect of changing the phase.

At second glance we recognize a similar structure in (2.10) and the gauge transformation(2.8). In both cases the original wave function is phase-shifted, either by the gauge phase or the translation.

2.2.2 Symmetries of the system - Translation operators

Symmetries are crucial properties of any physical system as they are related to eigenstates of the problem. They are particularly important when studying an infinite system in a finite model. The two characteristic entities for such a system (appearing in the Schrödinger equation (??)) are the cyclotron frequency

$$\omega_c = \frac{eB}{m_{\text{eff}}c}, \quad (2.12)$$

which is equivalent to the classical description above and the magnetic length

$$l_0 = \left[\frac{\hbar c}{eB} \right]^{\frac{1}{2}}, \quad (2.13)$$

which has the classical analogy of the Larmor radius. The magnetic length is a typical length-scale in the description of all phenomena in Quantum-Hall physics. It will be shown below, that the symmetry of a seemingly simple system reveals already a fascinating amount of physics. From a naive first approach one would not expect any differences from the symmetry of a free electron. The magnetic field is homogeneous and no boundaries are present in the system. However,

from the discussion of the Aharonov-Bohm effect we already learned, that even a zero magnetic field with a non-negative vector potential leads to phase shifts for electrons moving under its influence.

The Hamiltonian of such a (spin-polarized) system is

$$\hat{H} = \frac{1}{m_e} \left[\mathbf{p} - \frac{e\mathbf{A}(\mathbf{r})}{c} \right]^2 = \frac{1}{m_e} \pi^2, \quad (2.14)$$

where $\pi = m_e \mathbf{v} = \mathbf{p} - e\mathbf{A}$ is the dynamical momentum operator (\mathbf{p} is the canonical momentum operator).

To see the difference from the $\mathbf{A} = 0$ case, we start looking for a translation operator which transforms a wave function of a single particle at point \mathbf{r} to such a function for point \mathbf{r}' and commutes with the Hamiltonian in Landau gauge, yielding a new quantum number, analogous to k ⁸

Chakraborty und Daniela Habil noch mal gucken.

$$\hat{H} = \frac{1}{2m} \left[-i \frac{\hbar \partial^2}{\partial x^2} + \left(\frac{\partial^2}{\partial y^2} + eBx \right)^2 \right] = \frac{1}{2m} (\pi_x^2 + \pi_y^2). \quad (2.15)$$

The appropriate translation operator for a free particle without a vector potential reads $\hat{T}_{\text{free}}(\xi) = \exp i \frac{\xi k}{\hbar}$, where the kinetic momentum operator $\hat{\mathbf{p}}$ generates the translation. For the Hamiltonian (2.14) the commutator $[\hat{H}, \hat{T}_{\text{free}}]$ ⁹ is

⁸ $\mathbf{A} = \nabla \times \mathbf{B} = (\mathbf{0}, eBx, \mathbf{0})$, \mathbf{k} in normalen Systemen in denen der Impuls eine gute Quantenzahl ist

⁹ along the y-axis in the present gauge

not zero. This implies that the kinetic momentum is not a good quantum number/not conserved in our system anymore. However, it can be shown that the *canonical* momentum operator serves as a generator for the proper translation operator

$$\hat{T}(\xi) = \exp\left(-i\frac{\xi \dot{\mathbf{K}}}{\hbar}\right) = \exp\left[-i\frac{(\xi \cdot \mathbf{p}) - \mathbf{eA} + (\mathbf{eB} \times \mathbf{r})}{\hbar}\right] \quad (2.16)$$

with the commutation relations

$$[\hat{T}(a), \hat{T}(b)] = \exp\left[-i\frac{\mathbf{a} \times \mathbf{b}}{l_0^2}\right] \quad (2.17)$$

$$[\hat{H}, \hat{T}(b)] = 0. \quad (2.18)$$

2.2.3 Eigenfunctions and spectrum of noninteracting electrons in a magnetic field - Landau levels

Andere Eichung - Landau-Eichung only!(siehe Email von Daniela When confining charge carriers to two dimensional motions and treating them as quantum mechanical particles the QM analogon to cyclotron motions can be found, the *Landau Levels*. Apart from the spectrum and the eigenvalues the degeneracy of the eigenstates will be shown here. To understand this fundamental concept we follow [58] p.28 ff.

We consider electrons of equal spin, in the x-y-plane under the influence of a magnetic field $\mathbf{B} = B\mathbf{e}_z$, using the Landau gauge¹⁰ $\mathbf{A} = -By\mathbf{e}_x$.

The two characteristic entities for such a system are the cyclotron frequency

$$\omega_c = \frac{eB}{m_{\text{eff}}c}, \quad (2.19)$$

which is equivalent to the classical description and the magnetic length

$$l_0 = \left[\frac{\hbar c}{eB} \right]^{\frac{1}{2}}, \quad (2.20)$$

which has the classical analogy of the Larmor radius and is a typical length-scale in the description of all phenomena in Quantum-Hall physics.

The Hamiltonian reads

$$\hat{H} = \hbar\omega_c \left[\frac{1}{2}y'^2 + \frac{1}{2}\hat{p_y}'^2 \right], \quad (2.21)$$

with the further substitutions $y' = \frac{y}{l_0} - l_0 k_x$ and $p'_y = \frac{l_0 p_y}{\hbar}$, where $k_{x,z}$ are the eigenvalues of the momentum operators x-component. The analytical form of the Hamiltonian is the same as for an harmonic oscillator, hence the spectrum of our system is given by

$$E_n = \left(n + \frac{1}{2} \right) \hbar\omega_c \quad (2.22)$$

¹⁰The choice of the Landau gauge is most appropriate for numerical studies using periodic boundary conditions. Results for other gauges can be found i.e. in [58], p.28 ff.

with the eigenfunctions

$$\xi_n(x, y) = \frac{1}{\pi^{\frac{1}{2}} \sqrt{l_0 2^n n!}} e^{-\frac{1}{2} \left(\frac{y}{l_0} - l_0 k_x \right)^2} H_n \left(\frac{y}{l_0} - l_0 k_x \right) \quad (2.23)$$

$$\xi_{0,0}(\mathbf{z}) = \frac{1}{\sqrt{2\pi} l_0} e^{-\frac{|\mathbf{z}|^2}{4}} \quad (2.24)$$

$$\xi_{0,m}(\mathbf{z}) = \frac{1}{\sqrt{2\pi} 2^m m! l} z^m e^{-\frac{|\mathbf{z}|^2}{4}} \quad (2.25)$$

where H_n are the Hermite polynomials of order n . The last two eigenstates (in the lowest Landau Level) contain the introduction of complex coordinates $z = x - iy$ ¹¹. Since the spectrum in (2.22) does not contain an explicit dependence on x and z , the eigenstates (2.23) are degenerate in these coordinates.

In order to complete the description of the Landau-system we must account for this degeneracy, i.e. we need a complete set of observables.

Each state $|n, m\rangle$ is labeled by two quantum numbers n and m where the first distinguishes the Landau levels derived above, while the second gives the relative angular momentum of the state in the respective Landau level. The degenerate wave functions of quantum number m in the lowest Landau level are localized in a circle of radius $R = \sqrt{2m}l_0$.

When examining a sample of size $L_x \times L_y$, the degree of degeneracy can be determined to be [38]

$$N_L = \frac{L_x L_y}{2\pi l_0^2} = \frac{eBA}{hc}. \quad (2.26)$$

This is a large number for experimentally relevant systems which depends linearly on the magnetic field. The quantity $\nu = \frac{N_e}{N_L}$ is the *filling factor*, which defines how many of the available degenerate states are occupied by electrons. Values larger 1 suggest, that higher Landau levels are occupied, while All electrons residing in the lowest Landau Level have the same kinetic energy.

The picture is however not complete yet. In order to fully understand and explain the finite widths of the plateaus in the resistivity curve (and the appearance of those plateaus altogether) we need another ingredient. In particular we have not seen yet, why the Landau states should carry currents.

2.2.4 Localization

The Quantum Hall effect has to do with a current flowing through a sample and the electrons being deflected by the magnetic field. In order to have the ability to move freely (on a length scale much larger than the magnetic length) in the system, at least some electrons ought to be de-localized, which is by no means guaranteed in a two dimensional system. As the emergence of those delocalized or extended states is a hallmark of the Quantum Hall effects we shall detour briefly into the field of localization of charge carriers.

It has been shown very early by Aoki et al.[10], that the extended states must be in the center of the Landau band. The number of extended states in our system depends on the temperature and the precise properties of the impurity

¹¹which is different from the mathematical standard notation by the $-$ sign

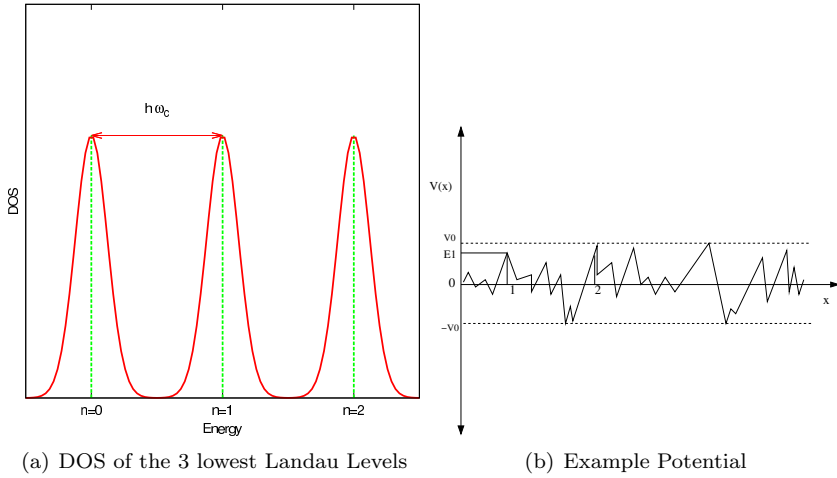


Figure 2.4: ((a) A schematic plot of the Density of states of the 3 lowest Landau levels. The green lines denote the degenerate Landau levels in a homogenous system (no impurities present). The red curve symbolically shows the Landau bands, caused by a small impurity which lifts the degeneracy. (b) 1D Example potential created by randomly distributed scatterer in the sample

potential.¹² When describing the movement of an electron by guiding center and cyclotron movement, the assumption [63] is, that only the guiding center part is coupled to the disorder potential, leading to a slow (when comparing the velocity to the cyclotron movement) drift through the sample along equipotential lines of $V(x, y)$. In the case of the strongly corrugated regime, the electrons would therefore move along closed equipotential lines around the extremal regions, thus remaining localized. In the weak corrugation regime, the equipotential lines stretch from one sample edge to the other, the electrons can now move through the sample - they become delocalized or extended and carry the current.

2.3 The Integer Quantum Hall effect

With the knowledge about Landau Levels on one hand and the localization phenomena on the other hand, we are now in a position, where we can explain the occurrence of plateaus in the resistivity curve. But beforehand let us restate the open questions:

- What is the origin of the plateaus in the resistivity curve and why do they have a finite width?
- Why does the longitudinal resistance vanish and why at the same values of ν ?
- Why is the effect so stable over a wide range of experimental parameters?

¹²It is interesting to note, that in the hypothetical case of a perfectly pure sample only 1 extended state exists in the center of each (degenerate) Landau Level, rendering the Quantum Hall effect “invisible”

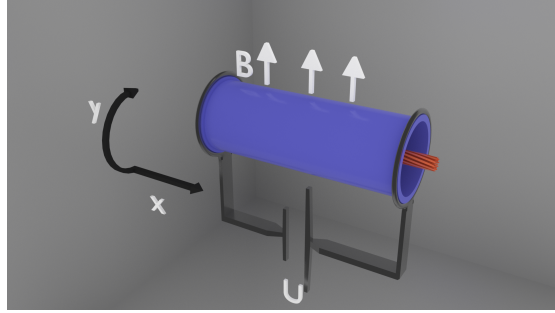


Figure 2.5: The picture for Laughlin's explanation of the IQH. The 2DEG is bent along the - equally bent - y-axis to form a tube (see 2.2 a). The y-axis is along the edge of the tube. The magnetic field points outwards (along the bent y-axis). The artificial flux is created by the solenoid in the center of the tube. The localized and extended states are depicted on the surface of the tube. The voltage is connected to the edges of the tube.

At least three different approaches have been used to explain the behavior (e.g. [71, 87, 116]). We shall follow the argument of Laughlin ([71, 135]) here, mainly due to their relevance for the FQH effect in the remainder of this work. The two other approaches will be mentioned briefly as far as they shed light on the topics of this thesis.

The argument of Laughlin relies on a *Gedankenexperiment*. The underlying geometrical setup is shown in Fig. 2.3 (p. 16). The Hall bar geometry (Fig. 2.2 a) has been bent into a cylinder, where the upper edges are glued together now. The drain and source are on the left and right edge of the cylinder. The magnetic field \mathbf{B} pierces the cylinder surface (the 2DEG of the original Hall setup) perpendicular at all places with a vector potential $A = (0, Bx, 0)$. The additional solenoid introduced into the geometry along the symmetry axis does not change the magnetic field outside its small circumference, however a vector potential $A_\Phi = (0, \frac{\Phi}{2\pi}R, 0)$ still exists and influences the 2DEG on the surface of the tube. The two possible types of electronic states (localized and extended) are shown on the circumference of the tube schematically.

To begin with, we acknowledge, that an extended state must match itself at the boundary, hence fulfilling the condition $\psi(x, y + 2\pi R) = \psi(x, y)$. Localized states¹³ do not fulfill this condition.

When introducing (adiabatically) an extra flux $\Delta\Phi$ in the solenoid, the vector potential at the surface changes by $A_\Phi = (0, -\frac{\Delta\Phi}{2\pi R}, 0)$ ¹⁴, the total vector potential now reads $\mathbf{A} = (0, B(x - \frac{\Delta\Phi}{2\pi}R), 0)$. Since the new flux in the solenoid does not change the magnetic field at the surface, we can interpret the change by A_Φ as a gauge transformation. This gauge transformation affects the phases of the wave functions, transforming them as $\psi(\mathbf{r}) \rightarrow \psi(\mathbf{r})e^{\frac{i\epsilon\chi(\mathbf{r})}{\hbar}}$ with $\chi(\mathbf{r}) = \frac{\Delta\Phi}{2\pi R}y$. We combine now the boundary conditions for extended states and the phase change due to the gauge transformation. The boundary condition must be met

¹³The wave function is not finite on a close path along the circumference of the tube

¹⁴using Stokes and Gauss theorem

regardless of the gauge transformation,

$$\begin{aligned}\psi(x, y + 2\pi R) &= \psi(x, y)e^{\frac{ieX(x, y+2\pi R)}{\hbar}} \\ &= \psi(x, y)e^{\frac{ieX(x, y)}{\hbar} + ie\Delta\Phi/\hbar} \\ &= \psi(x, y)e^{\frac{ieX(x, y)}{\hbar}}\end{aligned}\tag{2.27}$$

The last identity restricts the allowed values of the additional flux quantum $\Delta\Phi = \frac{\hbar}{e} \times \text{Integer}$, no continuous gauge transformation are allowed.¹⁵.

The effect of the gauge transformation is therefore none for localized states (only the unessential phase is changed) or a shift of the center of mass in x-direction (by a distance $\Delta x = \Delta\Phi/2\pi RB$) for all extended states, resulting in charge transport. Yoshioka likens this transport to a conveyor belt. The energy cost of transporting N electrons along the x-axis through sample is $\Delta E = eVN$, where V is the voltage between the 2 electrodes.

Calculating the current (in y-direction) yields

$$\begin{aligned}i_y &= \left\langle \sum_i \frac{e}{m_e} (p_y^i - eA_y(r_i)) \right\rangle / 2\pi RL \\ &= \frac{1}{L} \left\langle \frac{\partial}{\partial\Phi} \left[\sum_i \frac{1}{2m_e} (p_{x,i}^2 + (p_y^i - eA_y(r_i))^2) \right] + V_{imp}(r_i) \right\rangle \\ &= \frac{1}{L} \left\langle \frac{\partial H}{\partial\Phi} \right\rangle = \frac{1}{L} \left\langle \frac{\partial E}{\partial\Phi} \right\rangle.\end{aligned}\tag{2.28}$$

¹⁶ Since Φ can not change continuously, we can replace the derivative $\frac{\partial E}{\partial\Phi}$ by $\frac{\Delta E}{\Delta\Phi} = \frac{eVN}{\hbar/e}$. Thus the current reads

$$i_y = N \frac{e^2}{h} E_x = -\sigma_{xy} E_x\tag{2.29}$$

with the Hall conductivity

$$\sigma_{xy} = -N \frac{e^2}{h}.\tag{2.30}$$

This holds when extended states exist in the sample and these states (below E_f) are occupied which has been discussed in section 2.2.4, (p. 14).

The existence of the plateaus can be understood by assuming, that extended and localized states both exist in our sample. The extended states are energetically located in the center of the Landau bands (marked green in Fig. 2.2.3(b) while the states at the edge of each band are localized (marked red in the sketch). When filling the states now gradually with electrons, the following happens:

1. First the localized states are filled hence the Fermi energy lies in the region of the localized states. The effect of the extra flux is a simple gauge transformation with no charge transport. The current through the sample will remain constant, as will the resistivity - a **plateau in $\sigma_{xy}(B)$ appears.**

¹⁵For the localized states no such restriction exists.

¹⁶To get from the first to the second line, we use the fact that the current operator is the derivative of the (full) Hamiltonian, the last line expresses the equality of the expectation value of the Hamiltonian and the total energy.

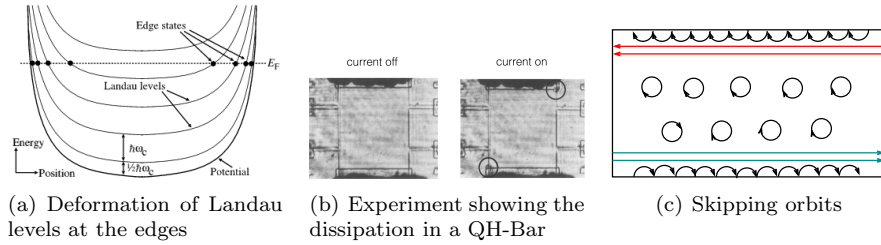


Figure 2.6: (a) Shows the energy levels for a system with finite width and the confining potential. (b) A Hall Bar (in the IQH regime). At the marked corners (where the electrons enter and leave the conducting channels, heat is dissipated due to the contact resistance. No dissipation occurs along the edges of the sample indicating dissipationless transport (Image taken from [126], see also [66]) (c) Shows a schema to explain the skipping orbits and the edge states in sample. In the bulk of the sample the electrons are confined to the circular Landau orbits, while at the edge of sample the "skipping" half circular orbits create the dissipationless edge states.

2. at some point, the first extended state becomes occupied. The electrons in these states will be carried along the x-axis. An extra net current will flow, the resistivity changes - we are between plateaus in the $\sigma(B)$ curve.
3. The next electrons will also occupy extended states, hence the current flowing through the sample will increase, as will the resistivity. The width of the plateau depends on the number of extended states and hence on the impurities which lift the degeneracy.

The discussion so far has explained the quantized values for the Hall conductivity. What is missing from the picture is the vanishing longitudinal resistance. To cope with this aspect, we need to introduce and study edges into our picture of the system. The effect of the edges on the energies of the Landau levels is depicted in Fig. 2.6(left). The energy of the Landau level is shifted to higher values at the edge of the sample, at some points being equal to the Fermi-energy. At this point the electrons can move along the x-axis. To understand the dissipationless transport the Fig. 2.6(right) may be helpful. In the bulk of the sample, the electrons move on their cyclotron orbits, no current is allowed and in the x-direction the bulk is an insulator. At the edges however, the electrons can not complete a full circle but are reflected at the edge and skips the upper /lower half of the circle - hence the term skipping orbits was coined. In our example, the electrons at the edge move to the left only (there are no channels for backward scattering), hence all electrons move from the left to the right, none is lost so no dissipation occurs. The Fig. 2.6(center) shows experimental evidence - the only points where energy is dissipated are the contacts of the edge states with the reservoir. This remains true as long as no scattering across the sample is allowed (which is experimentally true due to the large width of the sample).

This argument can be extended to the systems with edges (where the edge states are always extended and the bulk states localized) where different current distribution at the edges of the sample (Fig. 2.2 a) and in the bulk are observed.

This essential independence of the Hall conductance on the precise shape and quality of the sample came as a surprise (see [8], p. 489).

2.3.1 The Quantum Hall State as an example for a topological insulator

After some time it was realized, that the Quantum Hall Effect is an example of a newly discovered class of materials. These materials show the astonishing property to be insulating in the bulk region and conducting on the edges [6]. Although we will not make much use of topological arguments in the remainder of this work, a short detour into this fascinating field is appropriate here.

This alternative approach to explain the quantization of the conductivity is due to Kohomoto [68] and Thouless [120]. We follow them here to see how the conductance can be calculated from the linear response of the 2DEG to a small electric field and the relation of the quantized conductivity and the zeros of the wave function.

Again we start with the Hamiltonian (2.14) and note that the eigenfunctions can be written in the form of generalized Bloch functions as

$$\psi_{k_1, k_2}^\alpha = e^{i(k_1 x + k_2 y)} u_{k_1, k_2}^\alpha \quad , \quad (2.31)$$

where u_{k_1, k_2}^α are functions restricted to the Magnetic Brillouin Zone (MBZ). This symmetry allows us to rewrite the Hamiltonian as

$$\hat{H} = \frac{1}{2m} [-i\hbar\nabla + \hbar\mathbf{k} + \mathbf{eA}]^2 \quad , \quad (2.32)$$

with $\mathbf{k} = (\mathbf{k}_1, \mathbf{k}_2)$ and α being the Landau band index.

When applying Kubo's formula (see [38] for details) to study the effect of a small disturbance ϵE , the longitudinal conductivity evaluates to

$$\sigma_{xy} = \frac{e^2 \hbar}{i} \sum_E \frac{(\mathbf{v}_y^{\alpha\beta} \mathbf{v}_x^{\alpha\beta}) - (\mathbf{v}_x^{\alpha\beta} \mathbf{v}_y^{\alpha\beta})}{E_\alpha - E_\beta} \quad (2.33)$$

$$(v_{x,y})_{\alpha,\beta} = \frac{1}{\hbar} \left\langle \alpha \left| \frac{\partial \hat{H}}{\partial k_{x,y}} \right| \beta \right\rangle = -(E_\beta - E_\alpha) \left\langle \frac{\partial u^k}{\partial k_{x,y}} \right| \beta \rangle \quad (2.34)$$

which gives the conductivity per Landau band¹⁷ α as

$$\sigma_{x,y} = \frac{e^2}{\hbar 2\pi i} \int d^2\mathbf{k} \int d^2r \left(\frac{\partial u_\alpha^*}{\partial k_2} \frac{\partial u_\alpha}{\partial k_1} - \frac{\partial u_\alpha^*}{\partial k_1} \frac{\partial u_\alpha}{\partial k_2} \right) \quad . \quad (2.35)$$

The formal similarity of the integrand in (2.35) to a cross product encourages us to write the integrand as another vector field $\hat{B}(k_1 k_2) = \langle u_{k_1,2} \nabla_k u_{k_1,2} \rangle$. Recasting formula(2.35) with this vector field gives

$$\sigma_{x,y} = \frac{e^2}{\hbar 2\pi i} \int_{\text{MBZ}} d^2\mathbf{k} [\nabla_k \times \hat{B}(k_{1,2})]_3 \quad , \quad (2.36)$$

¹⁷Here we assume that the energy spectrum has gaps and that some disorder is present in the system which creates the Landau bands

where $[...]_3$ denotes the third component of the vector product. We shall pause here to remember, that the MBZ is (by virtue of the magnetic translation operators (2.16)) not a rectangle but rather a torus.¹⁸ The integral in (2.36) is 0 for any function without zeros because the torus has a boundary length of 0. Hence each non vanishing contribution must stem from the non-trivial geometry of the MBZ and the appearance of zeros in the wave function. The application of the theory of fiber bundles on this toroidal geometry ([120, 82]) leads to the identification of the integral (2.36) with the first Chern number C_1 of the principal fiber bundle.

If we are now interested in the evaluation of the integral (2.36) we shall remember, that the wavefunctions u have at least 1 zero in the MBZ thus the integral can not be evaluated at once but we have to use Stokes Theorem and integrate around 2 sections of the MBZ, one (I) with zeros of u and the other (II) without zeros. The integrals must be matched at the boundary between this areas (δH).

$$\sigma_{xy} = \frac{e^2}{\hbar 2\pi i} \left(\oint_{\delta I} dk [\hat{B}_I - \hat{B}_{II}] \right) \quad (2.37)$$

where the only difference between the 2 B is a phase change $B_I = B_{II} + \nabla \xi$ which reduces the conductivity to the integral

$$\sigma_{xy} = \frac{e^2}{\hbar 2\pi i} \int_{\delta H} dk \nabla_k \xi(k_{1,2}) = \frac{e^2}{h} n \quad (2.38)$$

where n is the count of zeros in region I.

This shows us, that the zeros of the wave functions - or equivalently - the Chern numbers are closely related to the physical property conductivity. This relation of geometry and physics leads to the stability of the quantization against changes of the system (size, disorder etc.)

2.4 Interacting electrons in 2D - The Fractional Quantum Hall Effect

While the Integer Quantum Hall effect has been predicted by theorists ([9]) for some time before Klitzing actually discovered it experimentally, the FQH has been quite a surprise. From all the work studied so far it should surprise everybody that minima (or plateaus) of the Hall resistivity appear anywhere else than at integer filling factors. However it turns out that the electron-electron interaction combined with the magnetic field gives rise to this effect. An illustrative picture to describe the new features of the FQH has been given by Zee [136]. When the electrons in the IQH regime can be described as dancers dancing in circles, the electrons in the FQH regime might be seen as dancers dancing in circles with the additional constraint of dancing only on white fields of a chessboard in order to prevent collision with other dancers. The theoretical background of the FQH effect is discussed in some detail in this section.

¹⁸One may imagine the construction of the torus by identifying the upper and lower edge of the MBZ, which leaves a tube and the left and right edge which leaves a torus (Fig. 2.7)

2.4.1 A closer look - The Hamiltonian with interaction term

To start with let us look at the Hamiltonian for a system of interacting electrons in a magnetic field. It reads

$$\begin{aligned}\hat{H} &= \hat{\Pi} + \hat{V}_{ee} \\ &= \sum_{i=1 \dots N_e} [\nabla_i + eA(\mathbf{r}_i)]^2 + \sum_{i,j}^{j < i} V(r_i, r_j) + V_{imp}(r_i),\end{aligned}\tag{2.39}$$

where the electron-electron interaction is not exactly specified here. To describe the solution of such a system many-particle techniques must be used. In order to write down a general fermionic many particle wave function (Slater determinant [39]) we need suitable single particle orbitals. It is reasonable to use the single particle wave function (2.23) here. We shall and can not restrict the filling factor to integer values any longer but shall allow any rational filling factor $\nu = \frac{p}{q}$ where $p, q \in \mathbb{N}$. In case $\nu > 1$ we are concerned with $\left[\frac{p}{q}\right]$ filled lower Landau levels and one partly filled Landau level which is highest in energy.

The Hamiltonian (2.39) extends the single particle Hamiltonian (2.14), hence the solutions (2.23), (2.22) represent a limiting solution to the FQH problem.¹⁹ However the Hamiltonian (2.39) is a fully fledged many particle Hamiltonian therefore no closed, analytical solution exists. Of course the reason for this is the interaction potential $V(r_i - r_j)$.

When looking at (2.39) and keeping in mind the degeneracy of the LLL-state, we recognize that it is impossible to treat the problem perturbatively in the sense that one might start with the IQH solution of (2.14) and treat the interaction operator in (2.39) as a perturbation. The reason can be seen either in the high level of degeneracy²⁰ or in the fact, that (in case only the LLL is considered) there is no small energy scale here. This is because the kinetic energy is quenched (all electrons have the same kinetic energy) and the only remaining part in the Hamiltonian is the non-local interaction term itself.

A first intuitive estimation as to at which filling factors the FQH can occur was given by Yoshioka [135] (p. 53 ff). The interaction energy U_0 depends on the average distance r_0 between electrons, which itself depends on the filling factor $r_0 \sim \frac{1}{\sqrt{n_e}} = \frac{\sqrt{2\pi l_0}}{\sqrt{\nu}}$ with $U_0 = \frac{e^2}{4\pi\epsilon r_0} \sim \sqrt{\frac{\nu}{2\pi}} \frac{e^2}{4\pi\epsilon l_0}$. The impurity potential is characterized by the splitting of the (degenerate states in the absence of the impurity) states belonging to a Landau level Γ . The 2 energy scales U_0 and Γ compete, if $\Gamma < U_0$ the interaction "wins", the electrons become delocalized and the conditions for a plateau are fulfilled.

Figure 2.7: A schematic depiction of the construction of a torus from a rectangular sheet with PBC. When the upper and lower edge coincide, a tube emerges, the equivalence of the left and right edge gives a torus

2.4.2 Additional symmetries and new translation operators

In the considerations above (see 2.2.2), we have shown symmetries emerging from the noninteracting electrons in a magnetic field. These symmetries are single-particle symmetries. When studying the FQH Hamiltonian, the question of many particle symmetries needs to be addressed as the relative positions of the electrons are essential for the interaction energy. For further usage in finite size systems we will employ a periodic system²¹ of size $L_x \times L_y$ with $N_e = pN$ electrons and $N_m = qN$ magnetic flux quanta in it.

Let us remark first that the single particle translation operator (2.16) does not commute with the Hamiltonian (2.39) which is reasonable as the change of a single electron position changes the electron-electron interaction and will therefore change the electron-electron interaction part of Hamiltonian. New many-particle symmetries are present in the system and we shall show them now. The symmetry analysis presented here is due to Haldane [47].

With an eye towards numerical analysis, we study the symmetries of a many particle system²² subject to periodic boundary conditions (PBC). We continue from the single particle translations (2.16) and their analysis from above. The application of the PBC onto the translation operators (2.16) gives a set of lattice vectors $\{L_{m,n}\}$ with

$$\{L_{m,n}\} = \{mL_1 + nL_2\} \quad n, m \in N \quad . \quad (2.40)$$

The Hamiltonian (as any physical quantity) must commute with the translation by one lattice vector and can therefore be constructed from states $|\alpha\rangle$, which are eigenstates of the translation operators with the eigenvalues $e^{i\theta_{mn}}$. The PBC translation operators (see sec. 2.16), (2.40) now read

$$t_i(L_{mn}) = e^{i\theta_{mn}} \quad , \quad \theta_{mn} = \pi mn N_m + m\theta_1 + n\theta_2 \quad . \quad (2.41)$$

We will now derive the 2 possible translations (collective and single particle²³) and will see, that all symmetries can be described by either affecting the center of mass of the electrons or the relative coordinates of the electrons.

The translation of all electrons by a vector \mathbf{a}

$$\hat{T}(\mathbf{a}) = \prod_{N_e} \hat{t}_i(\mathbf{a}) \quad (2.42)$$

¹⁹The IQH Hamiltonian (and hence the Landau levels developed in the previous section) are solutions to the FQH-Hamiltonian if the interaction term vanishes and the filling factor is not rational but an integer value.

²⁰With a 1 mm by 1 mm unit cell, we have typically 10^9 electrons with approx. 2.5×10^9 single particle orbitals (at $\nu \propto \frac{1}{3}$) and $10^{7 \times 10^8}$ distinct ground state configurations (according to Jain [58], p. 110

²¹Fig. 2.7 shows, how the use of PBC converts a rectangle into a torus.

²²using the Landau gauge

²³The former denoted by capital, the latter by lower case letters

shifts the center of mass along \mathbf{a} , where \hat{T} is the many-particle translation operator. At a moments thought it becomes clear that the single particle states of the system should not be affected by a mere translation of the *whole* system. To ensure this²⁴ we find that the "allowed" translation vectors are of the form $a = \frac{1}{N_s} mL_x + nL_y$, which is a translation by a lattice vector. The operators $\hat{T}_{x,y} \left(\frac{L_{x,y}}{N_\Phi} \mathbf{e}_{x,y} \right)$ do not commute, but obey the relation $\hat{T}_x \hat{T}_y = \hat{T}_y \hat{T}_x e^{-2i\pi/p}$. However, \hat{T}_x commutes with the Hamiltonian \hat{H} .

The relative translation of one electron i can be written as

$$\hat{T}_i^{rel}(\mathbf{a}) = \prod_j \hat{t}_i(\mathbf{a}) \hat{t}_j(-\mathbf{a}/N_e), \quad (2.43)$$

which is short for: move the electron in question in one direction and all the other in the opposite one, thus leaving the center of mass of the electronic system untouched. Rewriting the single particle translator (2.16) in terms of (2.43) and (2.42) gives

$$\hat{T}_i(\mathbf{a}) = \hat{T}(\mathbf{a}/N_e) \hat{T}_i^{rel}(\mathbf{a}). \quad (2.44)$$

In the wavefunction, this symmetry is reflected in a Bloch type relation

$$T_i^{rel}\psi = \exp(i\mathbf{k}^r)\psi, \quad (2.45)$$

where the wave vector \mathbf{k}^r sorts the Hamiltonian eigenstates. The values of \mathbf{k}^r are restricted to a Brillouin zone with

$$\mathbf{k}^r l_0 = \sqrt{\frac{2\pi}{N_m}} \quad (2.46)$$

After this description of the symmetries, it is clear, that the many-body wave function decomposes into 2 parts as

$$\Psi(z_1, z_2, \dots, z_{N_e}) = \Psi_{CM}(Z)\psi_{rel} \quad Z = \sum_i^{N_e} z_i. \quad (2.47)$$

When switching to a system subject to PBC, the spectrum of the Hamiltonian is independent from the parameters θ_{mn} and the momentum \mathbf{k} . The Hamiltonian can be split into a relative and a center of mass part $\hat{H}(r) = \hat{H}_{cm}(r_{cm}) + \hat{H}_{rel}(r_{rel})$, which factorizes the ground state to be $\Psi_{mp} = \Psi_{cm} \otimes \Psi_{rel}$. The center-of-mass (cm) wave function is essentially a single particle wave function with the characteristic form of a Landau wavefunction. It was shown, that it has q -zeros in the MBZ [96]. Since the center-of-mass part of the Hamiltonian commutes with T_x , the center-of-mass part of the ground state Ψ_{cm} is degenerate, Ψ_{rel} however is in general non-degenerate. **momentum in the state (Karels Diss, chapter 3.5.2, unter anderem : k^r als impuls zur relativbewegung, , Laughlin function und cm-wellenfunktion immer in der Loesung vorhanden, nur Laughlin (i.e. relativteil ist interessant**

For a short summary of the symmetry analysis we found that the ground state of the many-particle Hamiltonian for a system subject to PBC

1. is q-fold degenerate

²⁴by requiring $[\hat{T}(a), \hat{T}_i(a)] = 0$

2. and the spectrum has a gap.

The energy is classified by the Landau level index for \hat{H}_{cm} and is q-fold degenerate because Ψ^{cm} is simultaneously an eigenstate to \hat{H} and to the center of mass translation operator for the set of lattice vectors $\{T(q\frac{L_{mn}}{N_m})\}$.

It should be noted that the q-fold degeneracy of the ground state is no sign of a FQH system but is present in the system only because of the imposition of PBC's onto the system. It is present no matter what physical nature the ground state has²⁵.

For the relative part of the wavefunction it can be said, that k is the principal quantum number here.

Since our study is confined to electrons moving in the (x-y)-plane and the wave function is complex valued it is helpful to describe the positions of the electrons with complex variables z instead of (x, y) . The relations between the old and new variables read²⁶

$$\begin{aligned} z &= x + iy & \partial_z &= \frac{\partial}{\partial z} = \frac{1}{2}(\partial_x - i\partial_y) \\ \bar{z} &= (x - iy) & \partial_{\bar{z}} &= \frac{1}{2}(\partial_x + i\partial_y) \end{aligned} \quad (2.48)$$

When expressing the Hamiltonian (Eq.2.39)²⁷ with z, \bar{z} it takes on the form

$$\hat{H} = -\frac{1}{4}(\partial_z\partial_{\bar{z}} + z\bar{z}) + \frac{1}{2}i(z\partial_z - \bar{z}\partial_{\bar{z}}) \quad (2.49)$$

with the eigenfunctions

$$\psi_m(z) = z^m \exp\left(-\frac{1}{4}z\bar{z}\right) \quad (2.50)$$

2.4.3 Properties of the ground state

Without knowing an eigenstate to the Hamiltonian (2.39) it is possible to derive a few properties nonetheless.

When comparing the 2 Hamiltonians (2.39 and 2.14) the following argument can be made:

- The Landau Levels are spaced proportional to B (2.22)
- The difference between the 2 Hamiltonian is in the particle-particle interaction. The related energy E_{e-e} scales quadratically with the interparticle distance which can be approximated to $r \approx \frac{1}{\sqrt{n_e}}$. These two energies compete with each other. In the case that $E_{e-e} \ll \hbar\omega$ the next Landau level is far enough away to ensure that we can treat the system only in the frame of the LLL. **besser abschreiben!**
- As our system comprises impurities, leading to Landau bands with a width Γ **fehlt!**

²⁵In the remainder of this work, we will encounter systems which have a finite energy difference among the lowest states. In the thermodynamic limit however, the ground state splitting is zero again, despite the presence of disorder in the system

²⁶with the convention $\frac{\partial}{\partial z} = \partial_z$

²⁷In symmetric gauge and $l_0 = 1$

Incompressibility is one of the most often used terms to describe the Laughlin state. As its exact properties are not exactly straightforwardly generalized to finite system we shall go into some details here (see also [21], [4]).

In an infinite system the compressibility κ^{28} is defined [29, 65, 76] as the change of the pressure with regard to the volume which is in turn the change of the total energy with respect to the volume

$$\frac{1}{\kappa} \underset{T=0}{\underbrace{-V}} \left(\frac{dP}{dV} \right)_{N, E=E(n)} \underset{E=E(n)}{\underbrace{-V}} \frac{d^2 E_0}{d^2 n_0}. \quad (2.51)$$

When using this relation in a system of particles in their respective ground states with energy E the compressibility can be rewritten ([65, 21]) as

$$\frac{1}{\kappa} \underset{\mu=\frac{d}{dn_0}(n_0 E)}{\underbrace{n_0^2 \frac{d}{dn_0} \mu}}, \quad (2.52)$$

where the Seitz relation (see [21] eq. 5.1.5) has been used to link the particle number and the chemical potential²⁹. A system is said to be *incompressible* if the derivative in (2.51) is discontinuous at some density. In such a case, the process of adding and removing a particle would create a energy excess³⁰. In a semiconductor the creation of a particle-hole excitation therefore requires a finite amount of energy. This renders an incompressible state insulating [4].

The derivation above was made for systems in the thermodynamic limit. However in this work we deal with finite systems and are therefore interested in an expansion of the incompressibility concept to those systems. The work of MacDonald [4] is followed here.

Assuming a finite system with the chemical potential μ at a value where the incompressibility rule holds what is the effect of an infinitesimal change in the chemical potential? Firstly, there is no chance to generate additional free current-carrying charges in the bulk of the system as seen above, thus the current density in the bulk must remain unchanged. If there is any change in the current density at all, it must happen at the edge of the system. Assuming there is a change in charge density at one point, the conservation rules require a current to flow throughout the edge. The Maxwell equation for this current reads,

$$\delta I = \frac{c}{A} \delta M = \frac{c}{A} \frac{\partial N}{\partial B} \delta \mu \quad (2.53)$$

$$\frac{\sigma I}{\delta \mu} = c \frac{\partial n}{\partial B}|_\mu. \quad (2.54)$$

A closer analysis of the last line shows a rather different angle now. It is not *if there is a current* it must be in the edge, it is *if there is a magnetic field*

²⁸The compressibility term originates in classical thermodynamic, where the volume of a medium $\left(\frac{\partial V}{\partial P}\right)$ is changed by the application of pressure onto it. The compressibility is then the material property which describes the stiffness of the material towards this change. A material is said to be *incompressible*, if the volume is not changed when applying pressure, $\frac{dV}{dP} = K = 0$

²⁹See also [111] for a discussion of the definition of the chemical potential in a finite system

³⁰ $\mu^+ \neq \mu^-$, $\mu \in [\mu^-, \mu^+]$

dependent density there will always be an current. As the density of a Hall system is always dependent on the magnetic field this is a persistent feature of the FQH state.

How can we apply this to a finite system we are about to study? And what are the more obvious properties apart from the rather abstract (2.51)?

After these theoretical considerations it is worthwhile to mention, that the compressibility of a 2DEG in a FQH geometry has been determined experimentally (see e.g. Eisenstein et.al. [27]). The compressibility (K^{-1}) was measured for a range of filling factors where it was found that for strong magnetic fields and low temperatures the $K^{-1}(\nu)$ behavior shows irregularities around filling factors commensurate with the FQH-effect (namely 1/3, 2/3 and 2/5) Ilani et al. [98] measured the compressibility of a 2DEG in the Quantum Hall regimes locally³¹ and found (among other things) the coexistence of compressible and incompressible phases in the sample, very much as discussed in the section on localization.

There is still a gap!

As shown in the previous section, the conductance in the IQH-regime could be understood by using topological arguments: the conductance in this case is related to the Chern number of the corresponding ground state.

In the case of the FQH, it is not a-priori obvious, that a similar treatment could be successful, since the ground state is degenerate, and the existence of a gap was crucial for the argument above. However, Niu, Thouless extended the TKNdN-framework [119] to the FQH-regime [83]. The conductance formula (2.35) changes simply in such a way, that the conductance is obtained by summation over all (degenerate) ground states

$$\sigma_{xy}^{FQH} = \sum_{k=1}^D \sigma_{xy}^i \quad , \quad (2.55)$$

where the integral hidden in (2.55) is taken over the extended MBZ defined by the many particle symmetries. The integer Chern-Numbers are now carried by e.g. the threefold degenerate ground state in total.

2.4.4 The Laughlin wave function

The occurance of the FQH posed a big challenge to the theory developed so far when asking for an analytic form of the many-particle wave function. In fact the need was solved only by a brilliant guess by R. Laughlin [72]. The reasoning behind this guess and the properties of the Laughlin wave function are described in this subsection.

For a system of electrons in two dimensions under the influence of a magnetic field with flux according to $\nu = \frac{1}{m}$ where m is an odd integer number.

So the final guess for the ground state of a system of 2D electron system in a strong magnetic field given by the Hamiltonian 2.39 at a filling factor $\nu = \frac{1}{m}$ is

$$\Psi = \prod_{i,j} (\mathbf{z}_i - \mathbf{z}_j)^m \exp -\frac{1}{4} \sum_i |\mathbf{z}_i|^2 . \quad (2.56)$$

³¹Using a Single Electron Transistor

This is the celebrated Laughlin Ground State (LGS) a wavefunction guessed to be the ground state of a system described by the Hamiltonian 2.39. It contains the single particle functions of the lowest Landau level and a Jastrow factor of degree m .

Although the final form of (2.56) came from a guess, there are some reasons for its success. We will examine them here.

To start with, let us consider 2 limiting cases for the many-body problem, the case of a completely filled Landau band and the case of only two electrons in the Landau band. Both cases give interesting insights into the properties of the system and reasons for the success of (2.56).

2.4.4.1 Many body wave function for $\nu = 1$ - the completely filled Landau Level

In the case of a completely filled Landau band, all degenerate single-particle states in the Lowest Landau Band are filled. The degeneracy of this state is 0 as it is not possible to redistribute the electrons in the filled Landau level. The wavefunction can therefore be expressed as a single Slater-determinant. Using Landau gauge results (??) the determinant reads

$$\Psi = \frac{1}{\sqrt{N_e}} \begin{vmatrix} 1 & z_2 & z_2^2 & \dots \\ \cdot & \cdot & \dots & \dots \end{vmatrix}$$

or alternatively,

$$\Psi = \frac{1}{\sqrt{N_e}} \prod_{i < j} (z_i - z_j) e^{-\sum_i \frac{|z_i|^2}{4}} \quad (2.57)$$

which coincides with the Laughlin wavefunction (2.56) at $\nu = 1$ and is known as the Vandermonde determinant [123]. The electron-electron interaction plays no role in this state (as long as the excitation spectrum has a gap) because the single particle- states must be filled regardless of the interaction.

2.4.4.2 2 Electrons in the LLL - Haldanes Pseudo potentials

Another interesting limiting case is the situation, where we have only 2 electrons (at $z_{1,2}$ with angular momenta m (the relative momentum) and M (the center of mass momentum)) in a plane subjected to a magnetic field. We choose the strength of the magnetic field in such a way, that the electrons reside in the lowest Landau level.

The Hamiltonian for the kinetic energy only is

$$\hat{H}_{kin} = \frac{1}{2} [p_1 - eA(z_1)]^2 + \frac{1}{2} [p_2 - eA(z_2)]^2 , \quad (2.58)$$

An analogous treatment of this problem to the derivation of the single particle Landau level problem gives the eigenstates as

$$|mM\rangle = \Psi_{mM}(z_1, z_2) = (z_1 - z_2)^m (z_1 + z_2)^M e^{-\frac{1}{4}(|z_1^2| + |z_2^2|)} . \quad (2.59)$$

These 2 particle states reside completely in the LLL.

For any isotropic interaction (i.e. depending only on the distance between the 2 electrons), the Hamiltonian for the interaction (in the basis given above) is

$$\langle M', m' | V(r) | M, m \rangle = \langle M' | M \rangle \langle m' | V(r) | m \rangle \quad (2.60)$$

$$= \delta_{M'M} \delta_{m'm} \langle m | V(r) | m \rangle . \quad (2.61)$$

The last line shows, that an isotropic interaction conserves both angular momenta. The energy eigenvalues for the interaction Hamiltonian can be evaluated as

$$v_m = \frac{\langle m M | V | m M \rangle}{\langle m M | m M \rangle} , \quad (2.62)$$

and are independent of the total angular momentum. These energy eigenstates represent bound states of the repulsive potential.³² Those energies are referred to as Haldane's Pseudopotentials ([96, 121, 40]). The knowledge of those discrete values³³ describes the interaction completely, the actual form of $V(r)$ is not needed. The other way round: Each interaction producing identical values v_m is equivalent for the treatment of the FQH.

When examining the numerical values of the v_m it becomes apparent, that v_0 has the largest value. In numerical simulations one can test the influence of the individual pseudopotentials. In those calculations it was found, that even in the case of the infinitely wide-ranged Coulomb interaction, only $v_{1\dots 3}$ contribute significantly.

The fact that only discrete values are needed to specify the interaction has been used to construct artificial model interactions. One example (widely used in this study) is the Short-Range-Interaction (SRI) which has the coefficients $v_0 = 1, v_{1\dots\infty} = 0$, another is the Hollow-Core-Interaction ($v_0 = 0, v_{1\dots\infty} = 1$). It was shown ([49, 40]), that the Laughlin wavefunction (2.56) is an exact eigenstate for the many-Body-Hamiltonian (2.39), provided the interaction is of the SRI type.

2.4.4.3 Haldane's Pseudo-potentials in a PBC system

In order to derive some numerical values for our presently used model system we need to express 2.62 for our choice of wavefunctions. In the case of a system with periodic boundary conditions (torus) we have the difficulty to find suitable relative part wavefunctions³⁴ to replace ψ_m

A numerical evaluation of pseudo-potentials V_m gives (see [127]). It should be noted here, that the value of $v_0 = 1$ for the SRI is somewhat arbitrary. The corresponding value for the Coulomb interaction is about one third lower.

Raus wenn quantized charging verschwindet. Sonst richtig aufschreiben.
Wenn, dann auch die Abschnitte 3.34- 33.6 aus Karel's thesis

³²Without the magnetic field and the confinement of the states to the LLL, the spectrum of the interaction Hamiltonian would be continuous and no discrete states would be present.

³³Numbers for v_m can be found e.g. in [40] Fig. 2.

³⁴Note that m is not a good quantum number on a torus

2.4.4.4 Classical analogy - The One component plasma

Writing down the square modulus³⁵ of the Laughlin ground state (2.56) yields

$$|\Psi(z_1 \dots N_e)|^2 = \prod_{i < j}^N (z_i - z_j)^{\frac{2}{\nu}} \prod_{i=1}^N e^{-\frac{|z_i|^2}{2l_0^2}} \quad (2.63)$$

The classical probability distribution for a system of interacting particles is proportional to [29]

$$e^{-\beta U(z_1 \dots N_e)} , \quad (2.64)$$

with the inverse temperature $\beta = \frac{1}{kT}$ and U being a general interaction potential among the particles. The analogy is now to find a potential for which those two probability distributions (2.64) and (2.63) coincide. It was found by Laughlin [72] that the potential has the form

$$U(z_1 \dots N_e) = -M^2 \sum_{i < j} \ln |z_i - z_j| + M \sum_i \frac{z_i^2}{4} , \quad (2.65)$$

which has the interpretation of N point particles of charge M moving under the influence of the 2D coulomb interaction potential $\Phi(z_i - z_j) = \ln |z_i - z_j|$. With this analogy the first ground state energies and pair correlation functions were calculated. An interesting result was, that the classical analogy already predicts a homogeneous density for the ground state.

2.4.4.5 Electronic density

One of the first properties of the newly discovered FQH state was the charge distribution in the ground state. The two possible phases were the crystalline phase and the liquid phase. The former would exhibit clearly pronounced maxima and minima of the electronic density, while the latter would show no such clear maxima and rather a constant value. One might ask, why a crystalline state would at all be possible - when analyzing the Hamiltonian, the system shows perfect translational as well as rotational symmetries. The reason for the emergence of the Wigner crystal can be traced back to the magnetic field and its symmetry breaking properties³⁶. Early computer experiments by Yoshioka et al. [132] showed that the FQH ground state is „*a translationally invariant liquid*“

Some adaption to this statement must be considered in case the translational symmetry is broken or ”bent“. We will discuss those corrections later in this thesis, when addressing numerical results.

2.4.4.6 Electronic pair correlation

Another characteristical property of the ground state is the shape of the pair-correlation function

$$\hat{g}^2(r'', r') = \left\langle \frac{1}{N_e(N_e - 1)} \sum_{i \neq j} \delta(r' - r_i) \delta(r'' - r_j) \right\rangle_{GS} \quad (2.66)$$

³⁵we follow [38] here

³⁶Wigner crystallization an a 2DEG is indeed possible, but only at much higher magnetic fields.

and³⁷ its averaged form

$$\hat{g}(r) = \hat{g}(r + r', r'). \quad (2.67)$$

It describes the probability to find an electron at position r' in case there is an electron at position r'' . It is obvious that it must have a zero at the origin (the Pauli principle accounts for it). The probability to find one electron close to another however is smaller than in the case of the simple Fermi-Gas. It can be derived from Eq.(2.67) and (2.56) that the the averaged pair correlation $\hat{g}(r) \sim r^{2*n}$ or $\sim r^6$ for small values of r .

$$\int \Psi_{LGS}(r) \hat{g} \Psi_{LGS}^*(r) dr \sim |\Psi_{LGS}|^2$$

which vanishes as $(z_1 - z_2)^3(z_1^* - z_2^*)^3 = (z_1 - z_2)^6$ for $z_1 - z_2 \rightarrow 0$.³⁸

The long distance behavior of g tells us about the long-range structure. To understand this we discuss briefly the 2 alternatives to a liquid: the electron gas and a crystalline structure. In case of an electron gas, the correlation function shall exhibit no distinguishable feature apart from the correlation hole, while in the case of a crystalline structure somehow the periodicity of the system shall show up in the correlation function at some larger distances.

2.4.4.7 The properties: Vortices, zeros of the wave function and flux quanta

Since the Laughlin Ground State (2.56) is expressed as a complex valued function, the Fundamental Theorem of Calculus [36] tells us, that the number of zeroes of a complex valued polynomial of degree m is m , while the various integral theorems [2] of the complex analysis provides us with a priori insight on the line integrals in our 2D system. ?? We extract here only the polynomial part of the Laughlin Ground state (2.56) as the exponential part contributes no zeros

$$P(z) = \prod_{j=1}^N (z - \alpha_j)^{2m+1}, \quad m \in N \quad (2.68)$$

for which holds [20]

$$\frac{1}{i2\pi} \oint_C \frac{P'(z)}{P(z)} dz = \frac{1}{i2\pi} \Delta_c \text{arg} P(z) = \sum_{j=1}^N n_j \quad (2.69)$$

where n_j is the degree of the n -th zero of $P(z)$, $\Delta_c \text{arg} P(z)$ is the argument of $P(z)$ when evaluated around a curve C which encloses all zeros of $P(z)$. This derivation of the Cauchy-Argument connects the zeros of the wavefunction to the distribution of the electrons ($z_1 \dots z_M$ or equivalently to the phase an electron would acquire when moved along C).

In the literature the term *vortex*³⁹ is often used in order to describe the wave function. The definition of a vortex according to Halperin [51] is:

³⁷Where the expectation value is taken over the ground state

³⁸Only the polynomial part of the Laughlin ground state is taken into account here, as only this part provides the zeros of the wave function.

³⁹Sometimes the distribution of vortices is referred to as the *nodal structure* where a vortex is called a node.

A wavefunction $\Psi(z)$ has a vortex of vorticity n at z_v if (a) $\Psi(z_v) = 0$ and $\oint_C \Psi(z) dz = 2n\pi$.

A few remarks on this definition:

- All zeros of an analytical function are vortices.
- In non-analytic functions some zeros may occur with no phase change - which are called zeros, or with a negative vorticity which are called *anti-vortices*. In our systems this might occur for states which are not fully confined to the lowest Landau level.
- The effect of the vortex is the change of the wave functions phase after translation of an electron along a closed curve around the vortex
- The Laughlin Wavefunction (2.56) has the property, that it has only zeros at the position of each electron for which (2.68) vanishes. The Landau level function has no zero, hence the statement of Halperin that the Laughlin state has the feature of no wasted zeroes.

[2, 37, 20] A physical interpretation of the vortices links the topological entity vortex and the physical measurable quantity flux quantum is due to Laughlin **CITE!!**. Imagine a perfect 2DEG with a homogenous density and an infinitely long and narrow coil pierced through the plane at z_0 . Let us now increase the flux through the coil adiabatically by 1 flux quantum. The electrons feel a magnetic field $B(r, \phi) = (B, 0)^{-1}$ which pushes the electrons away from z_0 . If we now imagine a sample electron circulating around z_0 the wave function of this sample electron will pick up an Aharonov-Bohm phase of 2π for each flux quantum carried by the coil. From the argumentation above we learned that phase changes only occur for paths around a zero, hence we find that the flux quantum is tied to the zero of the wavefunction. This Gedankenexperiment is at the heart of the common equating of vortices and flux quanta in the FQH literature.

Another instructive way to see this feature is to follow the original Gedanken-experiment of Halperin. It is also worthwhile to review this as we will make use of it in the numerical part of this work.

Consider the ground state many particle wave-function Ψ which is a function of N_e complex space coordinates of the electrons. Now fix all electrons positions except 1 (say we keep the first electron and fix all the others). Now we retrieve an effective single particle wave function ψ which depends parametrically on the other electrons positions. To summarize this procedure

$$\Psi(z_1, \dots, z_{N_e}) \xrightarrow[\text{fix}]{\text{electrons}} \psi(z_1) \{ .z_2 \dots z_{N_e} \} \quad (2.70)$$

The first electron serves now as a sample electron when moved across the sample. At any other electrons position $z_{2\dots N_e}$ the reduced wave function has a zero **Erwaehne cm-vortices hier!** but nowhere else. When carrying the sample electron counterclockwise around one of those positions, $\psi(z_1)$ acquires an Aharonov-Bohm phase shift of 2π . This *Gedankenexperiment* provides us also with a method to find zeroes of the many particle wave function without studying the minima of a function of $2N_e$ variables.

2.4.5 Topological conductance

No introduction to the theory of the Quantum Hall effects would be complete without at least mentioning⁴⁰ briefly the topic of *Topological conductance*. In one sentence: for some classes of systems, the conductance is not primarily defined by the particular form of the particle-particle interaction and/or an external potential, but rather defined by the geometry (and in particular symmetries) of the system. Typical features of the conductance stay constant over a wide range of systems particularities.

In order to convince the reader (who is referred to [83] for details and further references) we show briefly a derivation of the Hall conductivities for IQH and FQH systems without using the particular forms of the electron-electron interaction or the substrat (i.e. external potential). In this work we will be concerned with the Chern numbers which arise

2.4.6 Excitations to the Laughlin ground state

It is possible to classify the excitations (see e.g. Yoshioka [134]) of the FQH system⁴¹ as to whether they are related to a change of the number of flux quanta (and hence a change in the effective size of the system) or not. We shall start with describing the former excitations.

2.4.6.1 Elementary excitations - quasi-particles

We will discuss the creation of quasi holes into the system and show their charge and the changed wavefunction. In order to change the filling factor of the system (which might be realized by a change in the density and/or the magnetic field) one may create additional flux quanta⁴² The change of the wave function from Ψ^q to Ψ^{q+1} goes as follows. To see that this adds an extra flux quantum to the system we rewrite the Laughlin Ground state as

$$\begin{aligned}\Psi_{LGS}^q &= \prod (z - z_i)^q \exp - \sum \frac{z_i^2}{4} \\ &= \sum A_{m_1} \cdots A_{m_{N_e}} z_1^{m_1} \cdots z_{N_e}^{m_{N_e}} \exp - \sum \frac{|z_i|^2}{4} \\ \Psi_{LGS}^{q+1} &= \sum A_{m_1} \cdots A_{m_{N_e}} z_1^{m_1+1} \cdots z_{N_e}^{m_{N_e}+1} \exp - \sum \frac{z_i^2}{4}\end{aligned}\tag{2.71}$$

⁴⁰in particular since the Nobel prize 2016 was awarded to Haldane, Thouless and Kosterlitz for theoretical discoveries of topological phase transitions and topological phases of matter [1]

⁴¹Strictly speaking we treat the LGS as the exact solution to the FQH ground state which is only true in an approximation

⁴²A Gedankenexperiment which illustrates the process goes as follows:

1. start with a homogeneous state at $\nu = \frac{1}{q}$ on a disc,
2. insert an infinitely small solenoid at the center (z),
3. switch on the solenoid adiabatically to create a localized flux Φ_0 at z . The gap guarantees, that the system remains in an eigenstate.
4. due to the resulting change of the vector potential, the electrons get pushed outwards, thus increasing their angular momentum.
5. at the center a charge deficiency (a hole) is created.

This operation introduces a zero in the wave function at the origin - or by replacing Z_i by $(z_i - z_0)$ - at a chosen point z_0 . The distribution of the electrons is changed by moving each electron from state m_i to m_{i+1} . An interesting feature of this zero is that the resulting charge deficiency results in a positive charge localized at z_0 and spread around on a radius l_0 . The single flux quantum attached leaves an Aharonov-Bohm phase of 2π . Again, we find a connection between a zero in the wavefunction (with a Aharonov-Bohm phase) and a localized magnetic flux quantum.

To establish which charge this *quasi-hole* carries, we perform another *Gedanken-experiment*. We introduce now q zeros into the sample at z_0 . The wavefunction is now multiplied by $\prod_i(z_i - z_0)$. If we now introduce another electron at z_0 , the resulting state is the same as the original one, exhibiting a uniform density. Therefore q quasi-holes are neutralized by 1 electron, the charge of a quasi-hole is therefore $e^* = \frac{-e}{q}$.

The conjugated, negatively charged, excitation is the *quasi-particle* (or quasi-electron) which is introduced by the operator

$$\hat{\prod}_i \left[e^{\frac{-|z_i|^2}{4}} \left(2 \frac{\partial}{\partial z_i} - z_i^* \right) e^{\frac{-|z_i|^2}{4}} \right] \quad (2.72)$$

The new quasiparticle carries a charge of $e\nu$ and contributes with -2π to the Aharonov-Bohm phase.

The introduction of an isolated quasi-particle (either hole or electron) costs a finite amount of energy, i.e. the excitations are separated from the ground state by an energy gap. This is a direct consequence of the incompressibility of the Laughlin state.

2.4.6.2 Quasiparticle-Quasihole pairs

In order for the excitations to remain charge neutral, a particle-hole pair must be considered as the appropriate excitation.

- Energy
- Density

2.4.6.3 Low lying collective excitations - density response

Another class of possible excitations are those which do not change the size of the system (by introducing extra flux quanta) or create an excess charge in the system (by introducing quasiparticles), but are generated by redistributing the electrons inside the LLL (making it intra-LLL excitations). Those excitations are of the density wave type [40, 135]. In this subsection we will establish the fact, that the creation of those excitations (taking the LGS as the ground state) costs a finite amount of energy too.

A approximation to the energies needed to excite the system is given by the Single Mode Approximation (SMA) by virtue of the variational principle. A short outline of the SMA is given below (following [34], [135], [104]). The theory relies on the textbook knowledge of Fermi-Liquids (see for example [69, 74, 3]) which have low lying excitations of phonon and roton type.

2.4.6.4 The single mode approximation

The question at the heart of the SMA is the following: What can we gain from our (nearly) exact knowledge of the FQH ground state for the description of the excitations.

It is reasonable to assume, that those excitation are not too different from the ground state. Because the wave function (2.56) was not derived from the Hamiltonian 2.14, we cannot use perturbation theory to study the gradual change of the ground state.

An elegant solution has been proposed by Platzman et.al. [42] by adaption of an older method used by Feynman [34], [35] to study the properties of liquid helium. It uses an Ansatz which states that the low-lying excitations are of a density-wave type. This requires local changes in the density of the system which are possible even for our incompressible system at hand. (see below for numerical "proof")

Since we know that the Laughlin state describes a Fermi liquid we can apply textbook techniques to its analysis (see for example [32]). It is reasonable to formally describe the low lying excitations as

$$\Psi_{\mathbf{k}} = \frac{\hat{\rho}}{\sqrt{N}} \Psi_{GS} \quad (2.73)$$

with the operator $\hat{\rho}_k = \sum_{j=1\dots N} \exp(-ik\mathbf{r}_j)$ ⁴³ being the Fourier transform of the standard density operator $\hat{\rho}$.

The variational principle provides an upper bound to the energy of a state

$$E_{GS} = \frac{\langle \Psi_k | \hat{H} | \Psi_k \rangle}{\langle \Psi_k | \Psi_k \rangle} + \Delta(\mathbf{k}) \quad (2.74)$$

$$\Delta(\mathbf{k}) = \frac{\langle \Psi_k | \Psi_k \rangle}{\langle \Psi_k | \Psi_k \rangle} - E_{GS} = \frac{f(k)}{S(k)}, \quad (2.75)$$

where $\Delta(\mathbf{k})$ is the excitation energy. The \mathbf{k} -dependence stems from the initial assumption that the excitations are of density fluctuation type ([17], p. 177 ff).

When plugging in 2.73 into 2.74 we find

$$\Delta(\mathbf{k}) = \frac{\mathbf{f}(\mathbf{k})}{\mathbf{Sk}} = \frac{\langle \psi(\mathbf{k}) | \psi(\mathbf{k}) \rangle}{\langle \psi(\mathbf{k}) | \psi \rangle} \quad (2.76)$$

$f(k)$ is being referred to as the oscillator strength, while the entity $S(k)$ is known as the structure factor of the system under study. It can be measured experimentally (as has been done for liquid He [35], [34]) or can be calculated once the ground state is known to a sufficient degree of accuracy. The latter is the case here, the ground state (2.56) is known and can be used to calculate both the excitation energy and the shape of the excitations. When doing so a few adaption must be made to exploit the most from our previous analysis⁴⁴

The first assumption is that the ground state is entirely in the lowest Landau Level and that the next Landau level is of no interest due to the energy gap¹². Therefore we can replace the density operator with its projected counterpart

$$\hat{\Lambda}_k = \hat{P}_0 \hat{\rho}_k \hat{P}_0 \quad (2.77)$$

⁴³The sum is not an integral because of the periodic boundary conditions applied here.

⁴⁴Replacing the density operator ρ_k with a LLL projected operator $\Lambda_k = P_{LLL} \rho_k P_{LLL}$.

¹²Ist das der "Roton" state [69]? Check in Abrikosov

where P_0 are projection operators to the LLL.

The derivation of the excitation energy so far has been restricted to a static structure factor $S(q)$ which is an Ansatz, as in general the full structure factor $S(q, \omega)$ must be used. The approximation that only one frequency is relevant here is hence called the Single Mode Approximation [38].

Making use of the LLL projection, the gap between ground state and the lowest lying excited many-particle state can be calculated by a modified Feynman-Bijl formula

$$\Delta(k) = \frac{f(k)}{s(k)} \quad (2.78)$$

where $f(k)$ is the projected oscillator strength and $s(k)$ is the projected static structure factor of the lowest Landau level. The evaluation of the excitation energy was performed using numerical methods and can be found e.g. at p. 78 (Fig. 4.7) of [135], see also [43, 40]. For all values of k (and in particular for the interesting values $k \rightarrow 0$), the excitation energy remains finite (appr. 0.15 enu at $k \rightarrow 0$) and shows a minimum at $k \approx 1l_0$. This particular excitation is called a magneto-roton in keeping with Feynmans description of He^4 atoms moving in ring-like structures.

What does this tell us about densities?, zitiere auch Girvin und dessen Excitation spectrum [42]

2.4.7 Liquid state vs. insulator

This section shall be concerned with deviations from the FQH ground state which are stronger than those discussed in the previous section.

Here we discuss in particular the influence of disorder potentials stronger than those needed to provide for the steps in the $\sigma_{xx}(\nu)$ curve.

- Liquid to insulator transition
- Gap closing
- Transitions between plateaus (Kosterlitz Thouless)

Let us recall the intuitive picture given to us by experimentalists (see Fig.2.2 (a)). We find the plateaus in the Hall resistivity σ_{xy} and the regime of zero longitudinal resistivity σ_{xx} . Let us look now at the other parts of the curve and ask the question what the ground state is like for a system with $\nu \neq \frac{1}{2p+1}$.

We know already two limiting cases for the ground state:

- For large B and finite disorder we find the Laughlin liquid with zero resistivity
- For $B \approx 0$ and a finite disorder we find an insulator due to the Anderson localization

What happens now if we a) turn up the magnetic field to decrease the filling factor or b) reduce the field to drive the filling factor into a region where no Quantum Hall effect is present.

In the first case the electrons form a crystalline structure known as the Wigner crystal (WC). It is known that this happens for $\nu > \frac{1}{7}$ (experimental work [89] shows the melting of the WC for filling factors of $\nu > \frac{1}{7}$).

But also for a filling factor of $\nu = \frac{1}{3}$ the WC has been observed experimentally by Pan et.al. [88] who added a vertical magnetic field to the already existent $\nu = \frac{1}{3}$ field which rendered the system insulating at certain strength of the vertical component. They identified the new state as a Wigner crystal.

For even filling factors $\nu = \frac{1}{2p}$ metallic phases have been If the magnetic field tends to zero, the gap will close and the state is rendered insulating.

The situation becomes more even involved with more than the lowest Landau level populated.

What do we expect as a general rule?

[26]

2.4.8 The Composite Fermion

Despite the fact that the Laughlin wave function provided a resounding success, it left the question whether one could find a more systematic way to solve the FQH puzzle posed by (2.39). Several attempts have been made mostly in the direction of gauge transformation of the Hamiltonian (compare [80] for a review). The Composite-Fermion approach in particular makes us of the knowledge about the form of the Laughlin-wave function (see 2.4.4.7, p. 30) - and the 3 fold vortex at each electrons position in particular. This approach recasts the Hamiltonian into a simpler form for electrons confined to the Lowest Landau Level.

A very popular approach in many particle physics is to transform an intractable many particle problem into a seemingly simpler one by creating new types of "dressed particles" see [22, 59] One such attempt was made with the construction of Composite Fermions by Jain [58]. The essence of this approach is a *transformation from strongly interacting electrons in a strong magnetic field to weakly interacting (composite) particles in a weak magnetic field*. We shall give a brief overview of the essentials of the Composite Fermion (CF) theory. For a more detailed review read the Book by Jain [58] or one of the many review articles.

The advent of the Composite Fermion CF came when the resistivity curves from IQH and FQH measurements were compared. With the removal of the scale of the magnetic field the curves look alike. This led Jain to the idea that the FQH effect is just the the IQH effect of other particles. Those are constructed by attaching an even number of vortices to each electron in an adiabatic process⁴⁵ The attachment of an even number of flux quanta to the electrons ensures that the statistics of the composed entity is fermionic as an even number creates a phase for the wavefunction of integer multiples of 2π ⁴⁶. A sketch of the vortex attachment is given in Figure 2.4.8(a). Vortices are attached to electrons, resulting in Composite Fermions (1 electron and an even number of vortices) experiencing a weaker magnetic field.

If this whole procedure can be successfully implemented, we end up with new particles (composite fermions) who themselves live in a (significantly weaker) magnetic field in which they occupy again Landau Levels (CF- Landau levels

⁴⁵Note that this vortex attachment is purely virtual, in contrast to i.e. superconductors. The measurable magnetic field remains homogeneous throughout the sample. To verify that this attachment does indeed have a physical meaning, experiments with the composite Fermions themselves have been performed.

⁴⁶The phase change of the wavefunction is a result of the Aharonov Bohm phase of the external field and the Berry phase which is due to particle statistics

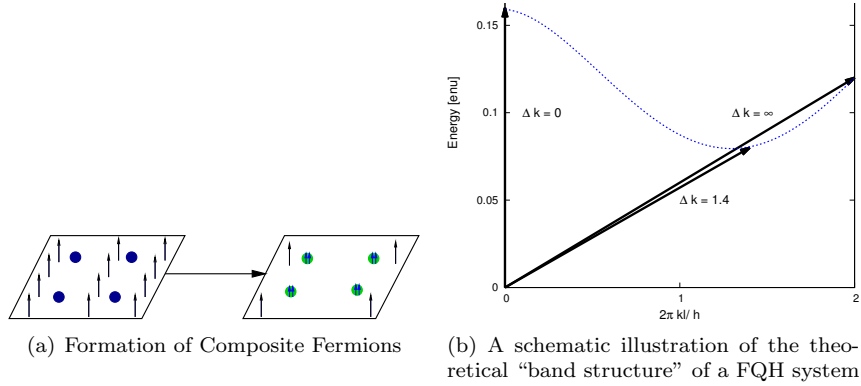


Figure 2.8: (left) Formation of Composite Fermions by attachment of 2 vortices to each electron. The remaining 3 flux quanta symbolize the residual (weaker) magnetic field. (right) A schematic illustration of the theoretical “band structure” of a FQH system. Shown is the energy of the first excited state ($E(k)$). The 3 typical excitation scenarios are marked. The exact shape of the calculated curve can be found eg in [135], p. 78.

/ A-Levels). The filling factors of the CF-LL and the electronic LL correspond to each other as $\nu_{CF} = \frac{1}{2p+1}$. The CF LL are fully occupied thus curing the problem of the high degeneracy of original problem. In particular, in case of the $\nu = \frac{1}{3}$ the corresponding CF-LL is fully occupied and the filling factor $\nu_{CF} = 1$. The non-degeneracy and the weakness of the magnetic field makes the problem for the CF tractable by mean-field approaches.

2.4.8.1 The Composite Fermion (CF) and the FQH in some detail

A good starting point for an explanation here is the lowest Landau Level. When we are interested only in the FQH effect itself and do therefore assume that only the lowest (electronic) Landau level is occupied ($B \rightarrow \infty$) the Hamiltonian (2.39) reduces in the following way:

- The kinetic energy is a constant of value $\hbar\omega_c$ and can be ignored
- the impurity background potential $V(r)$ is set to zero and can thus be ignored too.

When skipping both contributions to the Hamiltonian, the resulting Hamiltonian of electrons in the lowest Landau Level reads

$$\hat{H}_{LLL} = \hat{P}_{LLL} \sum_{j < k} \frac{1}{r_j - r_k} \hat{P}_{LLL} , \quad (2.79)$$

where the projection to the LLL (encoded in the operator \hat{P}_{LLL}) is a non-trivial exercise.

A Composite Fermion (CF) is now defined as a bound state of an electron and an even (in the case of $\nu = \frac{1}{3}, 2$) number of vortices or flux quanta.

The flux attachment conducted is more formally described as a gauge transformation of Chern-Simons style, where the vector potential that does the binding is

$$\begin{aligned} a(r_i) &= \frac{2p}{2\pi}\phi_0 \sum_j^{j \neq i} \nabla_i \theta_{ij} \\ \theta_{i,j} &= i \ln \frac{z_j - z_k}{|z_j - z_k|} . \end{aligned} \quad (2.80)$$

In Eq. (2.80) the angle $\theta_{i,j}$ is the relative angle between 2 particles (electrons). The vector potential generates a delta-peaked magnetic field

$$b_i = \nabla \times a(r_i) = 2p\phi_0 \sum_{i,j \neq j} \delta^2(r_i - r_j) , \quad (2.81)$$

which is not visible to any other electrons than the one where the flux is attached to. The resulting Hamiltonian for CFs in a mean field approximation reads therefore

$$\hat{H}_{MF} = \frac{1}{2m_b} \sum_i \left(p_i + \frac{e}{c} A^*(r_i) + \frac{e}{c} a(r_i) \right)^2 , \quad (2.82)$$

where the gauge transformation (2.80) is incorporated into the Hamiltonian resulting in the changed vector potential A^* ⁴⁷. It should be noted here, that there is no formal connection to the stripped FQH-Hamiltonian where only the electron-electron interaction in the LLL were present. In fact, no CF interaction is present in this Hamiltonian - although it is possible to treat CF interactions - and the kinetic term is the only one present. The Schrödinger equation for this Hamiltonian can be traced back to the Schrödinger equation of non-interacting particles by virtue of the gauge potential 2.80. When "gauging away" the unphysical vector potential $a(r_i)$ Was fehlt hier? Noch mal Jain gucken

Wavefunction of a CF!

2.4.8.2 Successes of the CF theory

With the relation of CF-Landau levels and electronic Landau levels it is easily explained why the FQH effect occurs at more than the Laughlin fractions. In particular the filling factors $\nu = \frac{1}{2p+1}$ can easily explained with this model (and they have been found experimentally). Other fractions can be explained when inter-CF interactions are taken into account.

The usage of the CF wavefunctions in a mean-field approach (where the CFs are treated as particles in a weak magnetic field) gave good reproductions of the spectra and gaps.

In the present work we will not make any direct usage of the Composite Fermion approach. However, we will be concerned with vortices/flux quanta

⁴⁷The reader should be warned, that it is not obvious from the short run through given here, whether or not the physics captured in the original Hamiltonian (2.79) is still present after the transformation. The procedure described here is in fact not invariant of the physics - the argumentation to motivate its validity relies on the gapped ground state and the expectation, that the "adiabatically" performed flux attachment does only change the form of the Hamiltonian, but not the essential physics.

bound to electrons (a complex which might with some right be called a Composite Fermion).

As mentioned above it is to some degree a matter of taste whether we consider our system to consist of Composite Fermions (with an even number of vortices bound to each electron) or of Composite Bosons (with an even number of vortices). Additionally the fractional Quantum effect at a filling factor of $\frac{1}{3}$ at which most of the analysis in this work will be carried out, can be explained to a sufficient degree without invoking the CF theory. We shall therefore proceed with our numerical experiments with an open eye for the implications of our results for the CF theory.

2.5 Exact Diagonalization

An exact first-principles⁴⁸ approach to finite system is provided by the exact numerical solution of the Schrödinger Equation (2.39). Although this method lacks the beauty of a generic approach and the application of the derived results to infinite systems need carefully considerations, it is widely used.

In this section the method of the ***EXact Diagonalization*** is presented. Two popular alternatives for the model system geometries (disk-shape vs. torus-shaped) are discussed and the possibilities to compare results are analyzed. Implementation details of the computer code used in our investigations are shown

2.5.1 The geometry - Disk world vs. Torus

In order to diagonalize an operator we need a basis. The choice of a suitable basis allows for different classes of problems to be tackled and may reduce the numerical effort. In our case we assume (as stated above) that we are only concerned with states in the LLL. States localized in the subspace of the LLL are therefore a suitable choice. This signals already the size of the problem, the size of the basis (and therefore the rank of the matrix-representation of the Hamiltonian operator)

2.5.1.1 The choice of geometry

In the literature 2 common choices for the geometry of our system can be found. The system with periodic boundary conditions (PBC) which is equivalent to a toroidal geometry and the disk shape geometry. The advantages of the latter is that the momentum is a good quantum number and no edge effects must be studied. This is in turn a disadvantage in our case as we are interested in edge effects. This leaves us with the system which is subject to periodic boundary conditions.

$$\hat{H} = \hat{H}_0 + V(r_i) \quad (2.83)$$

Continue from the symmetry part here, verknuepfung herstellen!!

Assume now that we consider a system with N_e electrons confined in a box. How do we construct a basis set suitable for exact diagonalization? First we

⁴⁸Where the term *exact* refers to the character of the solution itself, not notwithstanding the fact that substantial approximations must be made to state the problem in a suitable form.

shall formulate the PBC mathematically, they read

$$\Psi(x_0, y) = \Psi(x_0 + a, y) \quad (2.84)$$

$$\Psi(x, y_0) = \Psi(x, y_0 + b)\Phi(b) \quad (2.85)$$

which is correct only in Landau gauge. The Aharonov-Bohm phase in Eq. (2.84) suggests, that we choose a combination of plane waves in x- direction and Gaussian centered at the y-values where the phase shift is constant. The states read

$$\Psi_{0,k_y} = e^{\left(-i\frac{k_y y}{l_0}\right)} e^{-\frac{(x+k_y)^2}{2l_0}}. \quad (2.86)$$

We turn now to the x-direction symmetry which can be incorporated into Eq.(2.86 as $\Psi(x, y) \rightarrow \Psi(x + a, y) + \Psi(x + 2a) \dots$ where $x \in [0, a]$. Putting these together Yoshioka developed the basis functions

$$\phi_j = C \times \sum_{-\infty}^{\infty} \exp \left(iy \left(\frac{j}{m} + k \right) \zeta - \frac{1}{2} ((x - \frac{j}{m} + k) \zeta)^2 \right), \quad (2.87)$$

where $\zeta = \sqrt{\frac{a}{b} 2\pi m}$

The basis states (2.87) are periodic both in modulus and phase. It was however discussed in the literature that the periodicity of the modulus should be sufficient for our needs leaving two phases $\Phi_{1,2}$ as arbitrary parameters in the basis. These parameters have been shown to have physical significance in so far as they have the same effect as a time dependent electrical field ([53]).

The most general choice of a system with PBC studied so far is the parallelogram where the opposite edges are related by the relations ... Rezayi and Haldane [96] developed the basis states as

$$\Psi(x, y) = e^{\frac{x^2}{2}} e^{ik_z} \prod_{l=1}^m \theta_1 \left(\frac{\pi(z - z_l)}{b} |i\rangle \right), \quad (2.88)$$

where the first theta function θ_1 [75] is used.

Verweis nach oben, in der Lsung sind immer relativ und cm Anteile vorhanden, interessant Physik steckt nur im relativteil, auch die Nullstellen und den Zusammenhang mit der cm-wfct. zeigen [96]

2.5.2 Computational details

In this section a short overview is given on the Implementation and performance of the package developed to study the systems sketched above.

The package implements (roughly) the following algorithm:

- Initialization with the geometrical and physical properties of the system (i.e. size of the unit cell, electron-electron interaction type, number of electrons and filling factor).
- creation and population of the Hamiltonian Matrix
- diagonalization of the matrix
- check of the eigenvectors and storage of eigenvectors and eigenvalues.

The eigenvectors obtained here are postprocessed in order to calculate the electronic densities, vortex correlations, pair correlations and the like. Parts of the package was developed and used in other projects [127, 53].

The most time and memory consuming part of the algorithm is the diagonalization part. A multitude of packages provide the necessary functionality (, The algorithms used for diagonalization (sparse matrix/full matrix, Lanczos). We use two different algorithms (and implementations) to diagonalize the Hamilton matrices constructed in the previous section. The first algorithm (**F02HCF**) is used for smaller systems (matrix dimension of up to 3000 x 3000 complex elements) and is described as a "Black Box algorithm" In this algorithm the matrix is handled "fully" ⁴⁹ therefore expected to be of high precision when compared to other algorithms. For a comparison and for portability the diagonalization routine was also implemented using the **GSL**-library [44, 55] which is based on the LQ decomposition and subsequent diagonalization of the upper triangular matrix. The differences were comparable to machine precision.

The second algorithm ([85], **F02FJF**) is of the Lanczos type [118] and makes use of the sparsity ([16] of the Hamiltonian matrix. It is considered to be less precise than the "full" algorithm but can handle larger matrices because of its smaller memory footprint. Another algorithm used for the diagonalization of sparse matrices is the **FEAST** algorithm, provided in the **MKL**, [55] library.

A comparison is provided in the appendix (see C, p. 169).

As a rule of thumb, we will use the Lanczos algorithm only when needed, i.e. when the memory consumption of the LR algorithm exceeds the available memory. Typically this is the case for systems with more than 5 electrons at $\nu = \frac{1}{3}$. For all other cases the matrix will be diagonalized using the "Black Box method".

The package is written in C++ and built using either the **gcc** or the **icc** compiler.

2.6 Alternative approaches

[Follow Karel here \[127\]](#).

Density Renormalization Group ... [33]

⁴⁹In the sense that a) all matrix elements are used, (b) a full factorization of the matrix is performed and (c) that (in principle) all eigenvalues/eigenvectors are calculated.

Chapter 3

The homogenous FQH system

3.1 Preliminaries

We shall start our investigation by establishing the key features of a FQH-system as we see them in our model system. The spectrum, the gap, and the electronic densities are presented here in relation to previous work found in the literature. Special emphasis will be given to the issue of errors encompassed in the choice of the method (EXD), the geometry (PBC) and the finite system size (number of electrons).

At the very beginning of this numerical investigation, it must be checked whether the approximation of a real-world FQH system (with many electrons) by a periodically repeated unit cell with few electrons, is valid. Such an approximation and the application of a numerical solver introduces a number of simplifications and error sources, which comprise:

1. the finite size of the unit cell - which is tied to the finite number of electrons dictated by the available computer power
2. the confinement of the basis to the lowest Landau level
3. the approximation of an infinite thin 2DES
4. the accuracy of the numerical tools

In order to find the influence of those errors and to judge whether our approach delivers meaningful results, we will discuss a number of studies already available in the literature. A few results are known from analytical work, which we will use as a benchmark to judge the precision of our method. The same is done for numerical results from other authors. We attribute to the first type of results a higher accuracy as they do not suffer from numerical imprecisions and are mostly valid for infinite systems.

3.1.1 Organization of this chapter

After a successful calculation of a many-particle wave function ([58]), one is left with the knowledge of the complete state represented by projections on the

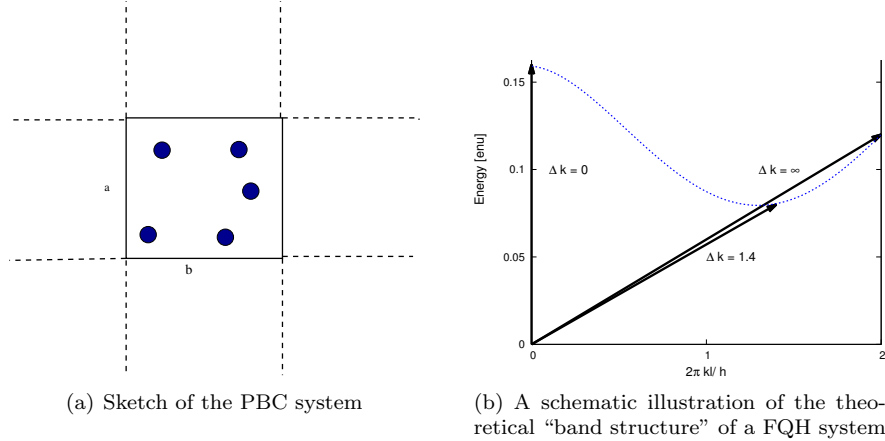


Figure 3.1: (a) Shows a scheme of the unit cell with 5 electrons, subject to PBC.
(b) Shows the band structure of a FQH system (see text)

the basis of the high dimensional Hilbert space, but without any real physical insight. Therefore the state must be analyzed by calculating quantities which can be interpreted physically. The major part of this chapter is dedicated to this analysis.

The remainder of the chapter is organized as follows: we start with the analysis of the spectrum of the homogenous system and derived energetic values (gap and degeneracy) in section 3.2. In order to proceed from global properties to local ones we calculate and analyze the electronic density (sec. 3.3) and the electron-electron pair correlation.

3.2 The spectrum of the homogenous system and derived values

In this section we study the spectrum obtained by diagonalizing the Hamiltonian (2.39) by means of the EXD method. After presenting the spectrum itself, along with a discussion of the degenerated many-particle ground-state, we continue with the analysis and discussion of the gap.

3.2.1 The spectrum of the homogenous system

We start out with a clean system (i.e. no impurity) and study the influence of the system size. The ground state energy, the energy gap as well as the degeneracy of the ground states are scrutinized.

To show the results for the largest system studied in this work, we turn to Fig. 3.2.1 (a,b). Shown are the spectra of a homogeneous system containing 7 electrons and 21 flux quanta for both types of interaction. The diagonalization was performed by virtue of the Lanczos algorithm (see 2.5.2). The plot is limited to the 2 energetically groups of eigenstates¹.

¹Plots with more states are provided in the appendix (Fig. B.1, p. 168)

Analysis of the spectra demonstrates clearly the energy gap between the states ϕ_3/ϵ_3 and ϕ_4/ϵ_4 . This essential feature was predicted and discussed i.e. in sec. 2.4.3, p. 26 ff. The gap is significantly (approximately three times) larger for the SRI system when comparing it to the Coulomb case.

The insets show enlarged the energies of the quasi-degenerate states $\phi_{1\dots 3}/\epsilon_{1\dots 3}$ and $\phi_{4\dots 6}/\epsilon_{4\dots 6}$ respectively. In contrast to the expectations formulated previously² - the ground state is supposed to be threefold degenerate due to geometrical arguments - the states show a small (10^{-7} enu) but finite difference in energies for the larger system. The same is true for the next higher state, the energy split among the lowest 3 states is approximately 100 times smaller as for the first states above the gap for the SRI system. Surely this finding deserves some more scrutiny, which we will provide below.

The spectrum of the Coulomb system is shifted to lower energies when compared with the SRI type system. This can be understood when keeping in mind that the Madelung energy for the system with hard core interaction is zero³, while it contributes negatively in the case of Coulomb interaction.

3.2.2 The ground state energy.

The energy of the ground state is calculated in this subsection and compared with results from previous studies. Although the ground state energy is not a measurable quantity, it is often used to compare different phases of solid state systems (which we shall not do in this work) and hence values are given in the literature, to which we compare our values.

In Fig. 3.2.1 (a) we present the spectra obtained for increasing system sizes. The ground state energy calculated by Rezayi et al is shown as a benchmark. Fig. 3.2.1 (b) shows the ground state energy for systems of different sizes (equivalent to increasing particle numbers). The ground state energy increases with increasing system size. If one is interested in the value for $N_e = \infty$, Zhao et al. [138] performed a finite size scaling analysis of their results for systems of finite size. From the shape and the scarcity of the available data a similar analysis here will obviously yield rather unreliable results. However, a quadratic fit yields a thermodynamical limit ($E(N_e \rightarrow \infty)$) of -0.409 enu, while a linear fit yields 0.414 enu.

For reference we provide a compilation of literature values along with our results in Tab. 3.2.2⁴. We discuss the values and its interpretation in what follows.

The ground state energy for a FQH model system with few electrons has been calculated by many authors. For the toroidal system the work of Yoshioka [135], Fano et al. [30], Pfannkuche et al. [93], Wan et al. [129] and Haldane et al. [48] are most important and shall serve as a reference here.

Wan et al. [129] calculate the ground state energy for a number of system sizes and extrapolate to the thermodynamical limit at which the energy is ≈ 0.4

²see section 2.4.1

³The Madelung energy here is an energy contribution caused by the periodic superstructure imposed by the PBC. It adds an interaction energy term for the Coulombic case introduced by the artificial interaction of the electrons in different unit cells. This contribution is not present for the short range interaction since the electrons don't "see" each other.

The ground state energy is reduced by approx. $0.2 \frac{\text{enu}}{\text{particle}}$ in a 5-15 system

⁴In the case of a SRI system we expect the ground state energy to be 0, hence all comparisons with literature values are given for the Coulombic system only.

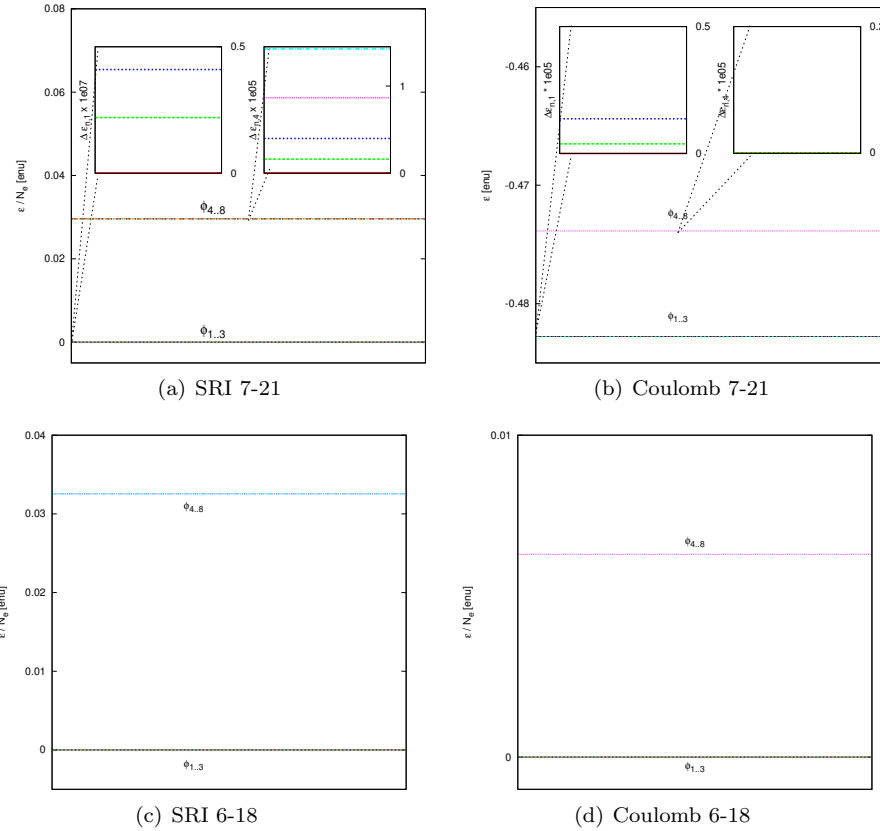


Figure 3.2: The energy spectrum of a $N_e = 7$, $N_m = 21$ (top/ a-b) and $N_e = 6$, $N_m = 18$ (bottom/ c-d) homogeneous system. (a) Short-Range interaction. The insets shows a zoom of the energy spectrum to see the degeneracy. Energies in the insets are given with respect to the energetically lowest state in the respective band. (b) shows the same for a Coulomb system. (c) and (d) show the spectra obtained for smaller systems, matrix diagonalization was performed for the full matrix.

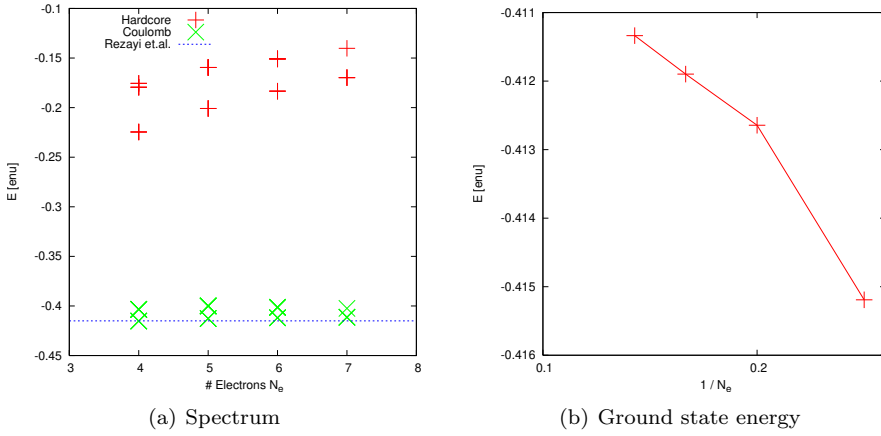


Figure 3.3: (a) Lowest energies of homogeneous FQH systems with 4 to 7 electrons. The lowest state is 3 fold degenerate (cf. Fig. 3.2.5.1(a)). (b) Ground state energy for a Coulombic system with up to seven electrons at $\nu = \frac{1}{3}$.

enu. Our values are in close agreement (3 percent larger) with those from Wan, in particular when taking into account the fact that we report only energies for finite systems, which are expected to be slightly larger than those for the infinite system.

Haldane's work [48] was performed on a spherical geometry and yielded a ground state energy of -0.415 enu⁵ in the thermodynamical limit. For a finite system with 4, 5, 6 and 7 electrons they calculate 0.48, 0.46, 0.45 and 0.44 enu respectively. Their values are in good agreement with ours, the thermodynamic limit value being 0.005 percent larger than our $N_e = 7$ value. As they performed an analysis of the system size effect, we refer the reader to Fig. 3.2.1 (b). The ground state energy increases with system size in both calculations which agrees with the results of Haldane.

The closest similarity in respect to the system and method is with Pfannkuche et al [93], where a PBC system with 4 electrons was investigated. Their value is as close as +0.1% to our result for 4 electrons. Yoshioka [133] performed a numerical study with 4 - 6 electrons on a torus. Our values deviate less than 0.5 %. In contrast to our calculations they used a unit cell with an aspect ratio of 4:1. The investigation of the aspect-ratio's influence showed a weak dependency with a minimum at the ratio 4:1.

Laughlin [71, 72] found the ground state energy by virtue of the hypernetted chain calculation to be 0.449 enu for an infinite system. The comparison shows that the values calculated here are within a reasonable margin of error with values found in the literature. A similar calculation is reported by Morf et al. [78]. Here the ground state energy is calculated by numerical evaluation of the energy expectation values of the quasi-hole and quasi-particle state for different system sizes in a spherical geometry. Besides the ground state energy of 0.41 enu, they report a system size dependence to the ground state energy of $E(N_e) \propto E_\infty + \frac{1}{\sqrt{N_e}} - N_e$ which results in a decrease of the ground state energy

⁵energies are given in convenient units enu = $\frac{e^2}{el_0}$

with particle number. This qualitative result is not reproduced by us (see Fig. 3.2.1 (b)). We find a slight increase in the ground state energy with increasing system size instead. However, in both cases the energy converges to the ground state energy of infinite system with increasing system size.

Other approaches to the ground state energy emerged from the analysis of finite electron layer width ([18, 41]). Those studies have been performed using the Hypernetted Chain Calculation (HNC) method. In both works the ground state energy is slightly larger than the EXD values by less than 1 per cent. Later on the DRMG method was employed by Zhao et al. [138] in order to calculate the ground state energy. The authors perform a finite scaling analysis on their results and estimate the ground state energy to be -0.410 enu.

Fano et al [31] developed a technique to combine calculations for the disk and the torus systems. In what they called Configuration-Interaction calculations, they obtained the ground state energy and the correlation gap for systems with up to 10 electrons. Their linear extrapolation to infinite systems yields - 0.4116 enu which is 0.6 % larger than our value for 7 electrons. For finite systems however, their values for e.g. the 6 electron systems are approx 10 % larger than ours.

Finally the ground state energy was also calculated by means of the Composite Fermions method (Jain et al. [61]). Their results are consistently larger than those derived from all other methods.

To give a benchmark on the accuracy of our numerical results, the ground state energy value for infinite systems is plotted in Fig. 3.2.1 (a) as a line at -0.4155 enu as calculated by Haldane et al. [97]. The margin of error for 5 and 6 particle systems when compared to the value of the infinite system is comparable and in the range of 0.18 %. Since we want to reduce the cost of the numerical calculations, we shall reduce the system size to a reasonable small value. Judging the obtained precision from the convergence tests performed above, we shall reduce our systems size to 5 -6 electrons.

3.2.3 The Correlation Gap

We shall now discuss a critical property of every FQH system - the size of the gap. We calculate a particular gap and compare our values to those found in the literature (experimental as well as theoretical, Tab. 3.2.4). But before exploring the gap in the homogenous system, it is necessary to discuss, which experimental gaps exist and to which data we shall compare our results.

3.2.3.1 Gaps measured in the experiments

It is well established (see eg Girvin et al. [43] and Wu et al. [131]), that a FQH system exhibits not only a gap, but also a gapped band structure ($E(k)$). A sketch of this band structure is shown in Fig. 2.4.8. As with other semiconductors too, this gapped structure gives rise to various experimentally obtainable gaps. We shall classify them by the momentum transfer needed to create an excitation. From the “band structure” (see Fig. 3.2.1(b)) of the homogenous system, we distinguish 3 different classes of excitations, those with

1. $\Delta k = 0$, we shall call it the optical or the correlation gap [93],
2. $\Delta k \approx 1.4l_0$ the magnetoroton gap

Reference	System size (electrons)	$ E_0 $ [enu]	
this work	4 - 7	0.41264 - 0.41133	Coulomb interaction
Yoshioka [133]	4 -6	0.4152 - 0.4128	Torus
Morf [78]		0.410	Monte Carlo calculation
Fano [31]	∞ (limit)	0.4116	Config. Inter. calculation
Wan et al [129]	∞	0.41	Spherical geom.
Pfannkuche et al. [93]	4	0.416	EXD, PBC
Laughlin [73]	N/A	0.449	no HNC calculation
Haldane et al. [48]	∞	0.415	EXD
Chakraborty [18]	N/A	0.41	HNC calculation
Mac Donald et al [41]	N/A	0.41	analytical calculation
Jain [61, 60]	∞	0.409828	CF theory, thermodynamic limit
Feiguin et al [33]	∞ extrapolation	0.41010	DMRG

Table 3.1: Ground state energies per particle computed in this work for systems with Coulomb interaction and reference values from literature

3. $\Delta k > 1.4l_0$, the transport gap ($\Delta k \approx \infty$).

The $k = 0$ excitation have been measured using optical techniques by eg Pinczuk et al. [94]. The excitation and decay process involved is a multi step decay and it therefore required quite some experimental skill to obtain the results for the $k = 0$ gap. This gap is measured to be 0.084 enu (which corresponds to a gap of 14.1 meV in the experiment, Platzman et al. [95]).

The gap at $k \approx 1.4l_0$ is substantially smaller than the gap at $k = 0$. It corresponds to the magneto-roton minimum in the spectrum. The corresponding excitation can be envisaged as a many-particle excitation with rotating (quasi) particles in the first excited and the the ground state.

The creation of an independent quasiparticle-quasihole pair is connected to an excitation across the gap with $k \approx \infty$. Those gaps are most frequently measured with transport experiments. Typical results for this gap are e.g. found by Wakabayashi et al. [128] are of the size of 0.062 enu and hence smaller than the $k = 0$ gap. See also the work of Willet et al [130] for a comparison among the 2 different excitation types. Those results do not compare directly to the results presented later in this chapter, as they suffer strongly from the influence of disorder in the sample.

3.2.3.2 Calculated gaps from the literature

In order to compare our values with numerical values found in the literature we must discuss the different approaches used in those works and the models employed. The correlation gaps for different system sizes along with a comparison to literature values is given in Table 3.2.4.

3.2.3.2.1 Other EXD results

Closest to our work are results from few-particle exact diagonalization calculations. Apart from the influence of the system size (i.e. number of electrons), the precise interaction is of the essence. While we use a model where the 2DEG is exactly 2D, Zhang et al have calculated a correction to the energies and gaps for the case that the electron gas has a finite z-extension. In this case, the electron-electron interaction is different from ours and consequently their energy values deviate from ours. Other authors estimated the impact of finite temperatures onto the gap.

As for the strength of the magnetic field B , two limiting cases are discussed in the literature. The lower limit does not protect the system from LL mixing, where numerous authors showed (see eg. [45]) that the influence of higher Landau levels reduces or closes the gap altogether. The other limit is given by Wigner crystallization, where a very high magnetic field makes the Wigner crystal state energetically favourable over the FQH state. We do not expect to find a breakdown due to the strength of the magnetic field, as B does not enter our calculations directly but only through the number of flux quanta. With the assumption of no LL-mixing our system is “protected” against the low B limit.

3.2.3.2.2 Results for $k \approx \infty$

In order to calculate the energy needed to create a quasi-particle / quasi-hole pair (ϵ_p, ϵ_h) , which is perceived as the lowest excitation, Chakraborty et al [17] calculated $\epsilon_p + \epsilon_h = 0.025 + 0.026\text{enu}$. A slightly different method was applied by Laughlin which yielded $\epsilon_p + \epsilon_h = 0.025 + 0.0276\text{enu}$. Those results compare not directly to our value for the HC system which are roughly 2 times larger.

3.2.3.2.3 Results from variational and other methods

Briefly we discuss the results obtained with other methods below. Girvin, Mac Donald et al [42] calculate the gap in the framework of the Single Mode approximation (compare Eq. 2.78). Their value of 0.079 enu compares to our results for the Coulombic system. The gap they calculate is taken at the magneto-roton minimum (the magneto-roton gap) at which the excitation spectrum of the SMA shows a minimum at $k \propto 1.4l_0$. As discussed above, this gap is expected to be substantially smaller than the optical gap at $k = 0$. The values range from 0.15 enu at $k = 0$ to 0.06 enu at the magneto-roton minimum. Inclusion of the effect of finite thickness of the 2DES accounts for a reduction by a factor of two for the gap at $k = 0$.

Within the framework given by the theory of Composite Fermions, the gap was calculated too, e.g. Bonesteel [15]. He calculates a gap of 0.1 enu for a SRI system which is a comparable value to those of Morf et al. [79]. Jain et al. [61] estimates the $k = \infty$ gap at the thermodynamical limit to be approx 0.1 enu.

3.2.4 Results for the $k = 0$ gap obtained in this work

We are now ready to present and interpret the results calculated in the course of this work.

We calculate the gap between the ground state (ϵ_1) and the first excited state (ϵ_4)

$$\Delta_{\text{corr}} = |\epsilon_1 - \epsilon_4| , \quad (3.1)$$

which is depicted in Fig. 3.2.1 ($k=0$ excitation)⁶. This gap (or a related gap as will be discussed below) is one of the key ingredients for the FQH-effect and has therefore attracted a lot of interest, in both theoretical as well as experimental studies. We report our results and compare them extensively to literature values of both kinds.

For the largest accessible systems, we calculate the gap to be 0.2 enu (SRI) and 0.062 enu (Coulomb interaction respectively)⁷. The size of the correlation gap we obtain gets smaller with larger systems (by $\approx 10\%$). When comparing the interactions, we find the gap to be substantially smaller for the Coulomb interaction. This can be explained in the following way. In the SRI-case, the interaction energy is smaller because the electrons “see” each other only on very small distances. This is not the case for the Coulomb interaction, here the interaction energy is proportional to the average distance (and hence the electronic density) $n(r) E_{\text{interaction}} \propto \sqrt{n}$

The calculated sizes of the correlation gap for several system sizes and interaction types is shown in Figs. 3.2.4, 3.2.4 and Tab. 3.2.4.

The direct comparison of the 2 interaction types in Fig. 3.2.4 shows for both interaction types a reduction of the gap size with system size. The changes are more drastic for the SRI system.

For both interaction types, the gap size is reduced somewhat for larger systems, however no drastic change occurs. When comparing the numeric value of the correlation gap of the 2 interaction types, we find the gap for the SRI to be approx. 3 times larger than the coulomb type gap. This is in agreement with the fact, that the ground state in the SRI approximation is (due to the tailor made pseudopotentials) a true ground state of the FQH system,

When studying the values in Tab. 3.2.4 a wide spread (appr. 25%) among the multiple theoretical values as well as between the experimentally measured activation energies and our numerical values becomes apparent. Therefore a few comments are in place to convince the reader that our calculations are consistent with respect to the correlation gap.

We shall approach this problem in two steps. First we shall analyze and compare the different theoretical methods and their results, while in the second step we shall discuss the differences among the experimental results and those from theoretical work.

Let us start by comparing our findings with those of other theoretical works. We shall present a wider range of benchmark results from different approaches.

The first computations of the correlation gap have already been given by Laughlin [73], other results were provided e.g. by Morf et al [78]. He used the method of the Hypernetted chain (HNC) which models the system as a 2D plasma of particles with logarithmic interaction. His work is fully analytical and does thus not suffer from the finite size restriction of our model. His value is appr. 10 per cent smaller than ours.

⁶Sometimes the same value is referred to as the *Spectral Gap* [129]. Another common definition of the correlation gap is $\frac{\Delta_{\text{corr}}}{N_e}$

⁷Since some authors give the gap size per particle, the SRI gap per particle is appr. 0.048 - 0.02 enu while in Coulombic case the gap energy per particle is between 0.03 and 0.006 enu.

Reference	System size (electrons)	E_{gap} [enu]	
this work	4 - 7	0.195 - 0.2	Short Range Interaction
this work	4 - 7	0.1179 - 0.062	coulomb interaction
Pfannkuche et al [93]	4	0.05	coulomb interaction
Haldane et al [48]	4-8	0.13-0.118	coulomb interaction
Girvin et al. [42]	-	0.06 - 0.15	Single Mode approximation
Girvin et al.[43]	-	0.079	SMA with disorder
Wan et al. [129]	6	0.04	coulomb interaction
Laughlin [73]	N/A	0.056	no HNC calculation
Morf [78]	N/A	0.099	HNC calculation
Morf [79]	therm. limit	0.102	EXD study
Jain [61, 60]	8, 10	0.106	coulomb interaction, CF theory
Fano [31]	∞ (limit)	0.0766	Configuration Interaction calculation
Feiguin et al [33]	∞ extrapolation	0.1010	DMRG
Gold [45]		0.1	analytical work
Platzman et al. [95])	N/A	0.084	Raman scattering. $k = 0$ (see text)
Wakabayashi [128]	N/A	0.062 / 0.036	experimental. work (see text)
Khrapai [64]	N/A	0.05 - 0.06	exp. work, dependent on B-Field (see text)
Boebinger et al [13]	N/A	0.01 - 0.03	experimental work

Table 3.2: Energy Gap sizes computed in this work and reference values - both experimental and theoretical - from the literature. See text for a discussion and comparison of different methods.

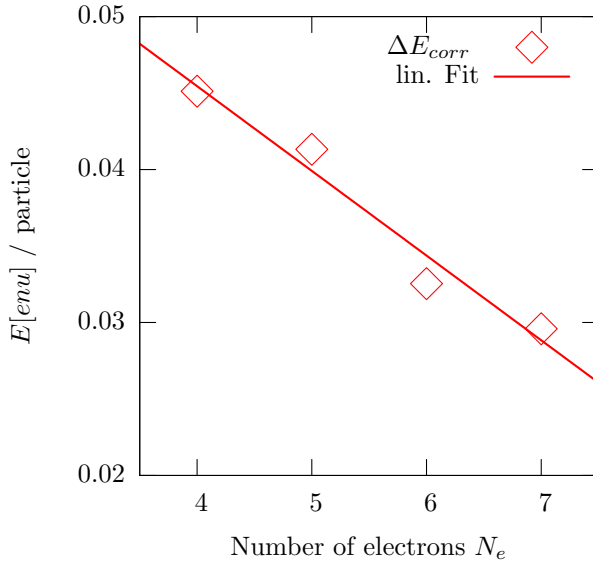


Figure 3.4: Correlation gap of a homogenous system with 4-7 electrons, Short Range Interaction.

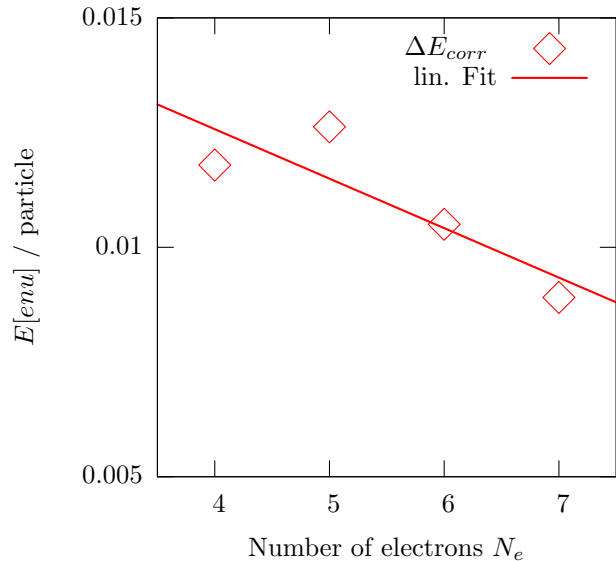


Figure 3.5: Correlation gap of a homogenous system with 4-7 electrons, Coulomb interaction

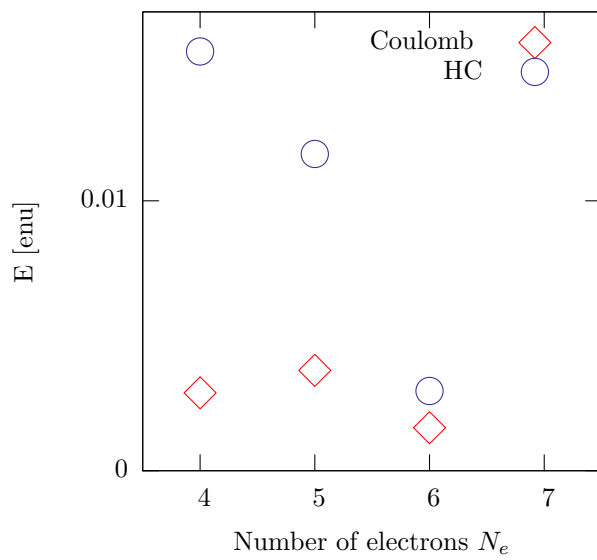


Figure 3.6: Change of the correlation gap relative to the value at the largest system size (7 electrons) for coulomb and Short-ranged interaction

Morf et al. [78] estimate the gap by direct numerical calculation of the energy expectation value from the excited states wavefunctions. They find the gap to be 0.0999 enu in the thermodynamical limit.

The studies that are most similar to ours are other EXD studies performed either on the torus or the disk geometry. The results, e.g. of Haldane et al [96, 97] and Pfannkuche [92, 91] are consistent with our results within the limits of numerical precision.

Wan et al. [129] calculate the gap for the coulombic interaction and study the influence of finite layer width and disorder on the spectral gap. Since they use a different pseudopotential ($V_0 = 0$) we do not expect perfect conformity of our respective results, our results are in reasonable agreement.

Haldane et al.[48] calculate the gap for different values of k , we compare their results at large k and infinite particle number which is $\propto 0.105 \pm 0.005$ enu with our coulomb gap results. A subtle point here is the different way the charge background neutralizations handled by the authors.

Jain et al. [61] calculated the transport gap employing the CF-approach. The values for finite systems and the estimation of the value in the thermodynamical limit are . There estimate for the thermodynamical limit is to be compared with our coulomb values and is slightly larger.

Halperin [52] gives an estimate for the transport gap at filling factors $\nu = \frac{1}{2n+1}$ as $E_g = \frac{C}{2n+1}$ enu which in the case of $\nu = \frac{1}{3}$ yields a gap of approx. 0.1 enu⁸.

The calculations of Girvin et. al were performed in the framework of the Single Mode Approximation and yield hence the gap at the magnetoroton minimum. As discussed earlier, we expect those results to be significantly smaller than our $k = 0$ results. Let us now turn to the comparison of our theoretical⁹ and experimental results which exhibit a larger discrepancy as shown in Tab. 3.2.4. As we discussed before, a multitude of experimentally accessible gaps exist in an FQH sample, hence a great many measurement techniques have been applied to the problem. We will later introduce another possibility to define an activation gap. [45]

The earliest experimental works measured the resistivity from transport experiments at different temperatures. Unanimously an activated behavior of the $\sigma_{xx/xy}(T)$ was found and an activation energy was deduced by applying a fit to an Arrhenius function [130, 13]. The excitations seen by those experiments can not be of the charge neutral type as those will not significantly contribute to the conduction process. The relevant energy gap hence is related to the creation of a quasi-particle/quasi-hole pair, to which we will refer as Δ_{qp}^3 .

In the work of Boebinger et al. [13] the excitation energy is derived from activated transport measurements and compared to results from theoretical work (much the same as ours). It is found that the measured activation energy is appr. 10 times smaller than Δ_{qp}^3 from numerical investigations. To reconcile this large discrepancy several investigations were performed mainly to quantify the effect of the assumptions made in the theoretical work. Sasaki et al. [105, 28] have used the results from Boebinger and performed a semiclassical analysis of

⁸The value of the constant C was estimated from numerical studies and taken to be 0.301. The gap estimated here is in our terminology a $k \rightarrow \infty$ gap, hence we do not expect a precise reproduction of the value in our calculations.

⁹We compare the gaps calculated with Coulomb interaction

the gap size. They conclude that the gap size in the absence of disorder is $\propto 0.065 \text{enu}$.

The effect of a more realistic 2DEG which has a *finite width of the electron gas* has been studied by a number of authors [45, 18]. It is reported consistently that the effect of such a finite width accounts for a reduction of the correlation gap by 50 percent. The origin of this rather drastic change is the different analytical form of the interaction which has its origin in the extra degree of freedom accessible to the electrons¹⁰.

According to Boebinger et al. [13, 14] the accessible activation energy derived from transport measurement is no "universal quantity" but depends on the sample quality, the magnetic field and the experimental technique used. We compare our values to those from high-field measurements which guarantees the reduction of the LL-mixing in the real system, thus matching the no-Landau-Level-Mixing assumption made in our calculations. Willet et al. [130] attribute a further decrease of 20 per cent of the theoretical value to LL mixing in the experimental system.

Another early determination of the activation gap based on transport measurement was given by Wakabayashi et al. [128]. They find an activation energy of appr. 0.036 enu in the low temperature regime. After consideration of the effects of finite thickness and LL mixing they estimate the "bare" correlation gap to be of 0.062 enu.

The influence of *disorder* (incorporated not in the EXD calculations but used to correct the values of the EXD are in the same order then the finite width corrections) accounts for another reduction of Δ_{qp}^3 , [45].

Let us now discuss the experimental results given in Tab. 3.2.4. A different approach based on thermal excitation of the system is the measurement of the specific heat of the 2DEG (e.g. Schulze/Wischeler) which yields comparable results to the abovementioned transport experiments.

The measurement of the activation energy by optical probing was performed by Schueller et al [106]. They determined the quasi-hole creation energy as 0.0136 enu, which compares i.e. to the HNC results by Laughlin and Morf. Other optical gap measurements were performed by Platzman et al. [95], yielding a gap of 0.08 enu. Those measurements are best to compare with our $k = 0$ gap.

Yet another method to measure an activation energy includes the direct measurement of the compressibility, e.g. by Eisenstein et al. [27] or the chemical potential (Khrapai et al. [64]). Eisenstein et al. find the chemical potential at $\nu = \frac{1}{3}$ to be of the order of 0.05 enu, while Khrapai et al. [64] found a transport gap of approx 0.064 enu for the highest magnetic field used in their study (12 T)

Another controversial issue was the B-field dependency of the activation energy (gap) which we will only shortly discuss here as we are bound to a $\nu = \frac{1}{3}$ system. As the main effect of an increasing B-field is the increase of the gap between the lowest and higher Landau levels our approximation of no Landau-Level mixing becomes more valid. Hence we should compare our data with experimental measurements at higher magnetic fields rather than with low field measurements.

¹⁰If the electrons are no longer confined to the x-y plane but can also move in a thin but finite layer of width z , the electron-electron interaction is reduced since the electrons have another dimension to avoid each other. The strength of the repulsion is therefore reduced and the interaction has a logarithmic form.

interaction	no electrons	full matrix (NAG)	sparse matrix (Lanczos / FEAST)
Coulomb	4	0	6×10^{-9}
Coulomb	5	0	1.06×10^{-6}
HC	4	0	3×10^{-9}
HC	5	0	1.04×10^{-6}

Table 3.3: Bandwidth E_b (see text for definition) calculated with the Lanczos and the NAG black-box approach for 2 system sizes. Coulomb and short Range interaction. The system sizes used here are the only ones which are accessible to both diagonalization routines.

Other measurements have been performed to study the influence of a finite Zeeman-energy. Dethlefsen et al. [23] determined a B-field dependend gap by activated transport measurements. They find 2 regimes in the $\Delta(B)$ characteristic which are identified with 2 different regimes. The low field excitation is characterized as a skyrmion.

However, as experimental data do necessarily include the impact of disorder, finite temperatures and finite width of the 2DEG, it is reasonable to expect the experimental values to be smaller than those gained from computer experiments where those factors have been excluded. The computed gaps are expected to be larger than those measured experimentally (Ref. [61]).

3.2.5 The degeneracy of the ground state - band width E_b

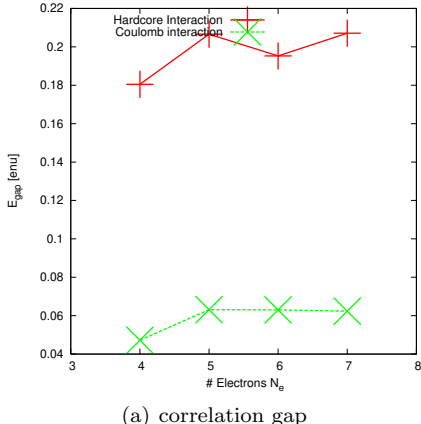
Let us return to the degeneracy of the ground state which we expect to be perfect (i.e. the energy difference between the 3 ground states should be 0) for infinite systems. We define the band width $E_b = \epsilon_3 - \epsilon_1$ as the energy difference between the energetically lowest state and the energetically highest state in the lowest band in accordance with Wan et al. [129]. cf. Fig.3.2.1

From the symmetry analysis discussed in Sec. (2.4.2) we expect the degeneracy to be perfect, i.e. $E_b = 0$ for both interaction types. We want to verify this numerically and shall use potential errors as hints to the precision of the method.

The degeneracy is perfect - i.e. below the threshold of numerical error- for all calculations performed with the "full-matrix-approach" (see sec. 2.5.2, p. 40) for system sizes of up to 5 electrons and 15 flux quanta. The bandwidth becomes finite once we use the "sparse method" to diagonalize the Hamiltonian. In order to compare both approaches we calculate the spectrum for both method for intermediate systems sizes in Table 3.2.5. E_b is finite for all system sizes, although its relative value is smaller than 10^{-5} . The apparent value is nearly constant among the different interaction types, underpinning the notion of this effect to be purely numerical.

3.2.5.1 Some remarks on the numerical precision

The numerical results presented in this section are subject to numerical errors due to the implementation of the diagonalization routines. The precision of



(a) correlation gap

Figure 3.7: (a)(b)Gap in the homogeneous ground state for 4-7 electrons, coulomb and hard core interaction results are shown respectively.

the eigenvector Ψ_i scales inversely with the gap to the energetically closest eigenvector Ψ_j [85, 44], while the accuracy of the eigenvalues is bound by

$$\|H\|_2 \times \epsilon , \quad (3.2)$$

where ϵ is the machine precision¹¹, The actual precision value must not worry us when considering the energies or the correlation gap. The situation is different for the bandwidth where inherently small energy differences ($\approx 10^{-7}$) are combined with an increasing error margin. A clear numerical effect is observed, when employing different matrix-storage schemes (full vs. sparse) and hence results obtained by different diagonalization techniques must be interpreted in the light of possible artifacts introduced by those storage schemes.

3.3 The electronic density

After having studied global energetic properties of the FQH ground state, let us now turn to the electronic density of the FQH (ground) states. This quantity will provide us with an insight into the local structure of such an FQH state. We will compute the electronic density from the EXD-calculated ground state(s) and compare again the effect of different electron-electron interaction.

As we saw in section 2.4.4.5 (p. 29), the density of the homogenous FQH state is supposed to be uniform due to symmetry considerations. However, deviations from this constant behaviour arise when using finite systems. We discuss those deviations and their origins in detail below.

An example plot of a electronic density distribution for a system with 5 electrons interacting via the SRI is shown in Fig. 3.8. Two defining features are prominent:

1. the constant (background) density with a value of $N_e = 5$ and

¹¹Machine precision is $\approx 1.210^{-16}$

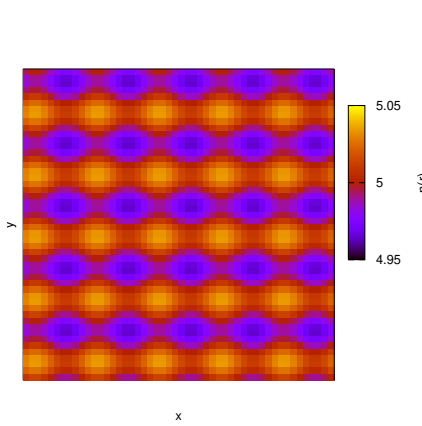


Figure 3.8: Density of a homogeneous system with 5 electrons and $\nu = \frac{1}{3}$ interacting via the SRI. The electronic density was calculated for 1 of the 3 degenerate ground states.

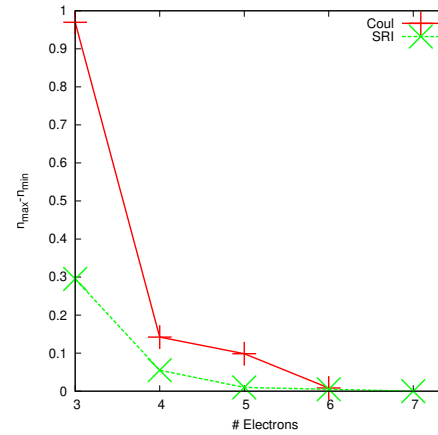


Figure 3.9: Magnitude of density oscillations in the energetically lowest state for different system sizes. Calculated for a system with SRI and coulomb interaction respectively.

2. a periodic superstructure with a spatial periodicity of $a/5$ and $b/5$ (approx. $2 l_0$) in x and y - direction respectively.

The homogenous density fits nicely with the expectations formulated in the theoretical section (cf. Sec.2.4.4.5).

However, the periodic structure of density maxima and minima of ca. 1% of the average density must be explained. We call these maxima the *finite size wiggles* which must be taken into account when analyzing density plots later on. Vyborny [127] analyzes the density of an homogenous state in a finite system. He tracks the origin of the finite size wiggles to the center-of-mass part of the ground state wave function (cf also section 2.5.1), we follow his argument here.

The wavefunction we retrieve from our calculation decomposes (symbolically) into a relative and a center-of-mass part and can be written as the product of the center-of-mass part (in torus geometry) and the relative part as

$$\Psi_{\frac{1}{3}} = \underbrace{F(Z) \exp\left(-\frac{|Z|}{2l_0^2}\right)}_{\Psi_{CM}} \times \underbrace{\exp\left(-\frac{1}{4} \sum_{i=1 \dots N_e} |z_i|^2\right) \prod_{i < j} (z_i - z_j)^3}_{\Psi_{rel}} , \quad (3.3)$$

where the center of mass variable Z is $Z = \sum_{i=1 \dots N_e} z_i$ and $F(Z)$ is an analytical function of Z with 3 zeroes in the unit cell.¹²

The calculation of the density of the state 3.3 can be expressed symbolically as

$$n(z) = \int d[\tilde{z}] |\Psi_{CM}(N_e z - [\tilde{z}])|^2 |\Psi_{rel}([\tilde{z}])|^2 , \quad (3.4)$$

where \tilde{z} is used as an abbreviation for the relative coordinates.

¹²Of course we restrict ourselves to the $\frac{1}{3}$ state here.

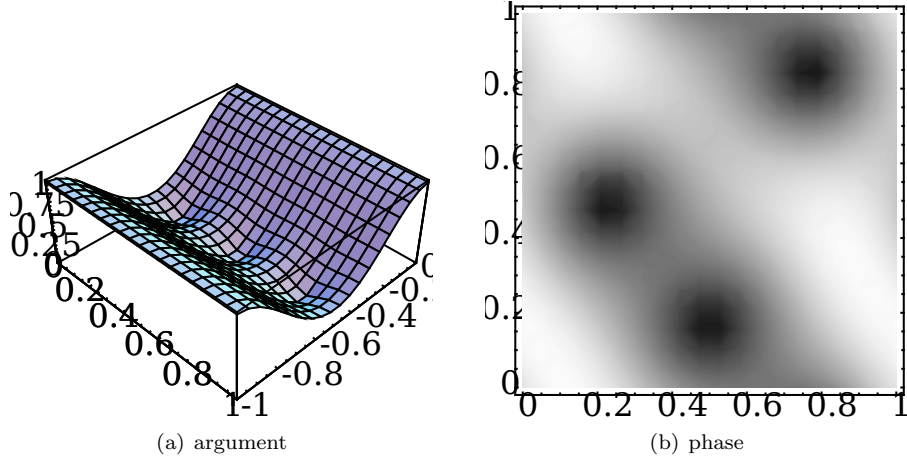


Figure 3.10: Examples of center-of-mass wave function. Note the 3 minima of the wavefunction which create the finite-size wiggles later on.

Following the work of Haldane and Rezayi [49], we will use odd elliptic theta functions $\theta_1\left(\frac{\pi(z-z_i)}{L}|\tau\right)$ as the most general form of the $F(Z)$ function. The z_i are supposed to be positions of $\frac{1}{\nu}$ flux quanta. In pursuing this approach, the authors verified the degeneracy of the many-body ground state. The precise analytical form of the center-of-mass wave function is not uniquely defined. When using the freedom to choose the cm-wavefunction (the positions of the zeros of the center of mass wave function can be chosen freely), one could place the cm-flux quanta either all onto one position¹³ or e.g. on a straight line. For the coherent states, the resulting wavefunctions have zeros on a grid in the unit cell - “the charge density of the state will essentially be constant, but with a small superimposed periodic component that is minimized at these positions, and vanishes as $N_e \rightarrow \infty$ ” [49]. In Fig. 3.3 we show an example of such a function for 3 flux quanta.

Analysis of Eq. (3.4) leads us to expect the following qualitative features of the electronic density:

1. The density contribution of the relative part Ψ_{rel} contributes a constant value of N_e , e.g. 5.
2. The density contribution due to center-of-mass part Ψ_{CM} contributes the oscillatory part of the overall density, which
3. has a periodicity of $1/N_e$ in a quadratic unit cell and
4. vanishes for $N_e \rightarrow \infty$

We discuss those expectations in the light of our EXD results now. To verify the first two expectations, we refer the reader to Fig. 3.8. The electronic density is in this case 5 with a 5% fluctuation.

¹³called *coherent states*

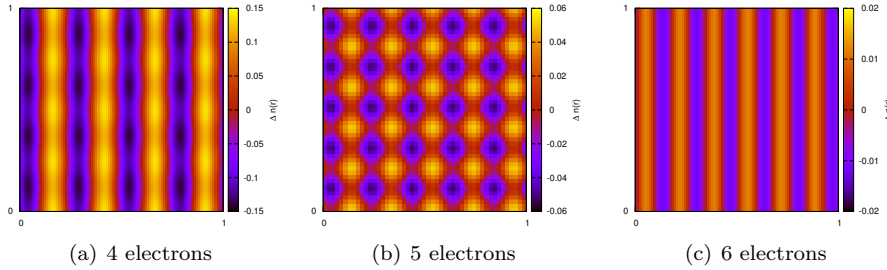


Figure 3.11: Fluctuations of the electronic densities of the ground state (one of the threefold degenerated states), calculated for 3 different system sizes, SRI. Note the periodicity of the finite size wiggles.

The third expectation is verified in Fig. 3.3, which shows the density fluctuations¹⁴ for 3 different system sizes. The periodicity of the finite size wiggles is 4-5-6/cell size in x and y direction respectively. The distance between 2 neighbouring extrema is $\frac{\sqrt{2\pi N_m}}{N_e}$ which is approx. $2l_0$ for $N_e = 5$.

The validity of prediction (4) can already be seen in Fig. 3.3 and has been verified numerically (see Fig. 3.9) in accordance with the work of aldane and Rezayi [96]. The density fluctuations do vanish within numerical precision for values $N_e > 7$.

Since in the case of the SRI the calculation yields a 3-fold degenerate ground state, the averaged density over all 3 ground states has been calculated (Fig. 3.3). In all 3 cases the density shows a strong periodicity of $\propto \frac{1}{5}$ cell size in x-direction. The periodicity is the same for all 3 states, the “phase shift” of the modulating function is $\frac{1}{15}$ cell size. A periodic superstructure in y-direction is superimposed. The amplitude of the former is larger as for the latter one, the periodicity is the same.

In Figure 3.3(left) the averaged density created from all 3 states is shown.¹⁵. The density fluctuations are reduced drastically. This reduction can be qualitatively understood from Eq.(3.4). The positions of the cm zeros are shifted by one third unit cell for each of the degenerate ground states. Its superposition account for a partial cancellation of the finite size wiggles

We shall now compare the effects of the electron-electron interaction. In Fig.3.3 the densities from the 2 interaction types can be compared directly. Shown are the differences between the averaged densities of the 3 lowest states ($\frac{1}{3} \sum_{i=1}^3 n_i - n_{homo}$) and the expected value of the homogenous density (5). It is obvious, that in both cases the density is constant to a precision of 10^{-6} .¹⁶. When comparing the density of the ground states directly, the symmetry of the finite size wiggles as well as the average density are identical for both interactions¹⁷ In Fig. 3.9 the size of the density fluctuations can be compared between the 2 interaction types. Small systems ($N_e < 5$) with coulombic

¹⁴Please note, that the density fluctuations are shown from hereon unless otherwise noted.

¹⁵The density is calculated by averaging over the 3 densities generated from the 3 degenerate ground states. An alternative approach would be to create a linear combination of the 3 ground states $\Psi_{GS} = \alpha\Psi_{GS}^0 + \beta\Psi_{GS}^1 + \gamma\Psi_{GS}^2$ and calculate the density of this state.

¹⁶We shall assume this value the obtained numerical precision.

¹⁷This persists for all 3 lowest states, although the ground state is non-degenerate in the case of the coulomb interaction.

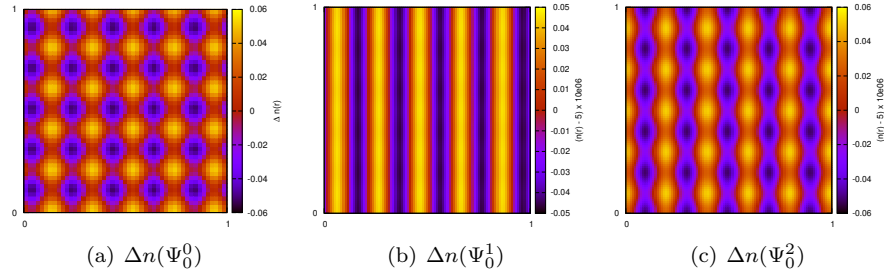


Figure 3.12: Fluctuations of the electronic densities calculated from the 3 perfectly degenerate ground states of a homogenous system with $N_e = 5$, $N_m = 5$ with SRI

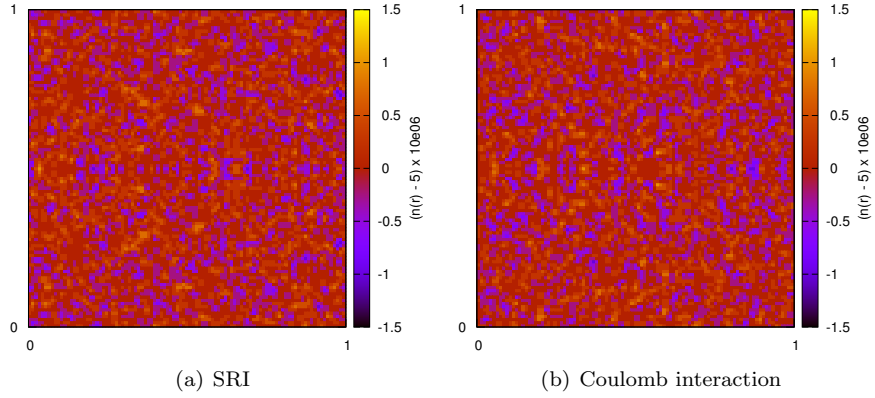


Figure 3.13: Electronic density fluctuations ($\Delta n = n(x, y) - 5$) calculated from the ground state of a $N_e = 5$, $N_m = 15$ system. (a) shows the SR-interaction, (b) the coulomb interaction. The images show the averaged density over the lowest 3 states. Note the factor (10^6) used to make the fluctuations visible.

interaction show stronger density oscillations than those with SRI. However, for systems with more than 4 electrons, the fluctuations are comparable in size. This is consistent with the statement, that the finite-size wiggles are caused only by the center-of-mass wavefunction of the wave function to which the interaction does not contribute.

3.4 Electron-Electron correlation in the homogeneous ground state

Let us now turn our attention to another quantity derived from the ground state wavefunctions - the (two particle) electron-electron correlation $g(r'', r')$ ([21] p.400 ff), introduced in sec. 2.4.4.6. Calculating $g(r)$ from the Laughlin ground state for small values of r gave a r^6 characteristic. With the further analysis of this quantity we will reinforce the notion of the ground state of the homogenous system as a liquid-like state.

In the literature we find the density-density correlation function for an inte-

ger QH state at filling factor $\nu = n$ to be [127]

$$g(r) = 1 - \frac{1}{n^2} \exp(-[(rk_F)^2]/4n) \left[L_{n-1}^1 \left(\frac{(rk_F)^2}{4n} \right) \right]^2 , \quad (3.5)$$

where $L_{n-1}^1(x)$ are the Laguerre polynomials. Using the fact that the Fermi vector $k_F = \sqrt{2\nu}l_0$ and taking the limit $n \rightarrow \infty$ (which is $B \rightarrow 0$) gives the correlation function of free electrons in a 2D system, namely

$$g_{FS}(r) = 1 - \left[\frac{2}{k_F r} J_1(k_F r) \right]^2 . \quad (3.6)$$

The correlation function for $\nu = \frac{1}{3}$ systems however, is not analytically¹⁸ known. We formulate a few additional expectations regarding the qualitative form of $g(r)$, based on the known properties of the Laughlin ground state. We showed already the r^6 characteristic for small r . This feature should be present in our calculations too, regardless of the finite size of our system. As we expect the Laughlin ground state to be an electron liquid, we expect $g(r)$ to be isotropic for distances outside the correlation hole. The other possible phases could be crystalline (the Wigner crystal) and a charge density wave (CDW). Both would exhibit a $g(r)$ with a clear periodic structure (see [135] p. 62)) and possibly some directional preference in $g(\mathbf{r})$. Whether or not we would find conclusive proof of such a homogeneity in our *finite* systems is questionable.

3.4.1 Results

We have calculated the electron-electron correlation functions of Coulombic as well as short-range interaction type ground states for four and five electrons respectively. Fig. 3.14 shows a 2D plot of $g(r)$. Clearly visible is the correlation hole around the fixed electron position (located in all 4 corners due to the PBC). In Fig. 3.14(a) and (c) the constant value of $g(r)$ outside the correlation hole becomes prominent, while in Fig. 3.14(b) and (d) the size of the correlation hole (measured as the distance from the sample electron to the first maximum of $g(r)$) is prominent. In this representation no major difference is visible between the two interaction types.

In order to further investigate the differences caused by the different interaction types, a diagonal cut through the unit cell ($g(x, y) \stackrel{!}{=} g(r)$) is shown in Fig. 3.15. The region of isotropic behaviour $g(r)$ is visible in the center of the unit cell, however it is small due to the small size of the system (NB the symmetry of $g(r)$ created by the PBC). When comparing different system sizes (Fig. 3.15 (a,b)), we find that the maximum position of $g(r)$ is at $\approx 4.5l_0$, regardless of the system size and interaction type. This distance can be interpreted as the typical interparticle distance in the homogenous ground state. The comparison of the two interactions is given in Fig. 3.15(c) shows that the qualitative behaviour is the same for both interactions beyond the interparticle distance, the short range interaction showing a slightly more isotropic behaviour. Due to the limited system size however, a conclusive statement about the isotropy of $g(r)$ for $r > 4.5l_0$ cannot be made. Vyborny [127] calculated correlation functions

¹⁸in the sense of a closed formula

for systems with 10 electrons and made a more conclusive statement about the isotropy.

The characteristic for small values of r is shown in Fig.3.15 (d), where $g(x)$ is shown on a double logarithmic scale along with a function $\sim r^6$. In this presentation the SRI state shows a better 6-th order behavior than the Coulomb system. The later shows a qualitatively different characteristic near the origin. To further investigate this finding, we compare $g(r)$ (Fig. 3.4.1) with 2 fitted polynomials. We find $g(r) \sim r^2$ in the immediate vicinity of the sample electron - which is similar to the correlation of the free electron gas. At larger distances ($r > 0.4l_0$) the correlation shows the same r^6 characteristic as expected in the Laughlin ground state (and as in the short -range interaction depicted above). It seems, that the characteristic correlation of the Laughlin ground state is destroyed on short ranges by the long-range Coulomb interaction.

Summarizing the analysis of the electron-electron correlation function we conclude, that the ground state of the SRI system shows features - in particular the liquid like state and the $g \propto r^6$ behavior - which are similar to those of the Laughlin ground state. Some deviations are observed for the coulomb ground state however, which will be addressed later again.

3.5 A short first summary

In the preceding section we presented numerical evidence that our method yields physically meaningful results when studying the homogenous 2DEG. Comparison with previous works - analytical, numerical as well as experimental - shows no unexplicable or unreasonable differences with our results.

The influence of the geometry and the resulting finite system size used and the numerical methods employed can be estimated to be in the range of less than 1% for the ground state energy. The perfect degeneracy of the 3 lowest eigenstates in smaller systems, regardless of the interaction type, as well as the apparent lifting of this degeneracy in the case of larger systems are well understood and match previous results from the literature.

The electronic density calculated from the ground state shows an essential constant value with some modulations which we trace back to the symmetry imposed by the PBC. The size of those modulations is reduced for larger systems and we expect it to vanish in the thermodynamical limit. The attainable precision of the density is $\propto 10^{-6}$.

The investigation of the two particle electron correlation shows the expected Laughlin-type $\sim r^6$ characteristic near the origin and an liquid-like isotropic behavior at larger distances. Comparison of the two interactions showed significant differences near the origin. The maximal repelling property of the Laughlin state is not found for homogenous systems with coulomb interaction at short distances.

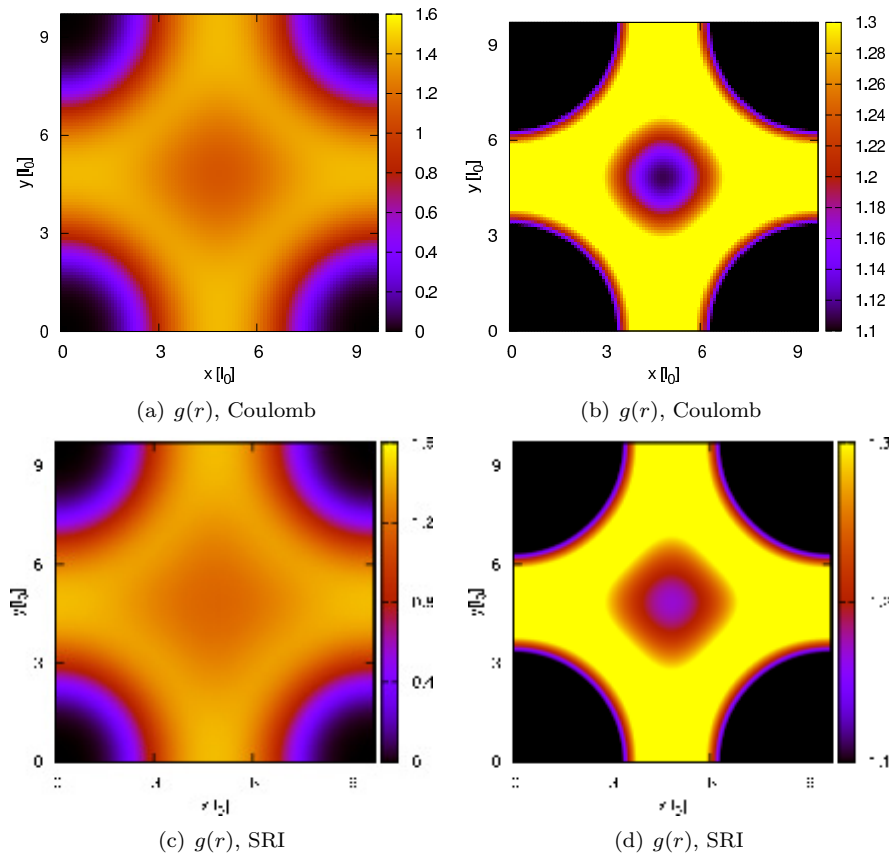


Figure 3.14: Electron-electron correlation $g(r)$ calculated from the ground state of an homogeneous system (5-15) with **coulomb interaction** (upper row) and **short ranged interaction** (bottom row) (b) and (d) show a different color range to amplify the visibility of the maximum at $\approx 4.5l_0$. The position of the fixed electron is at the corner of the unit cell (remember that the unit cell is periodically repeated).

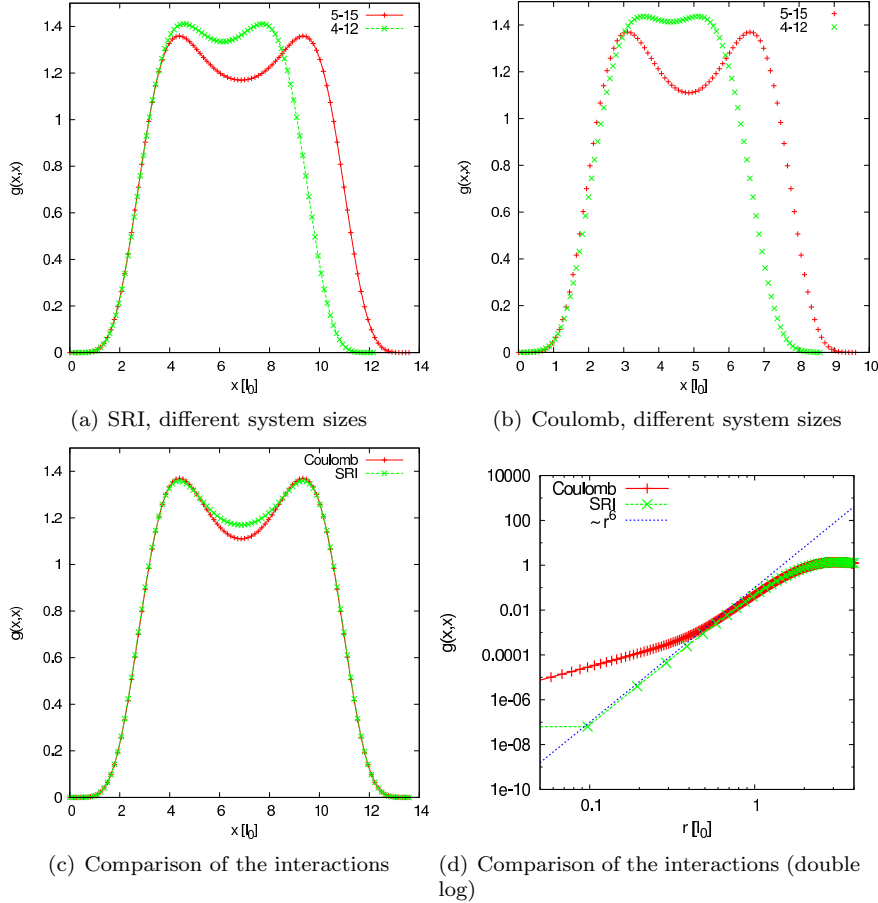


Figure 3.15: Electron-electron correlations along a diagonal cut through the unit cell (cf. Fig. 3.14) ($g(x,x)$). Top row ((a) and (b)) shows the comparisons between different system sizes for short range interaction (a) and Coulomb interaction (b). A direct comparison of the two interaction types is shown in the bottom row (c) . (d) shows the same as (c) near the origin, plotted on a double logarithmic scale . For comparison a fitted 6th order polynomial is provided. ($N_e = 5$, $N_m = 15$)

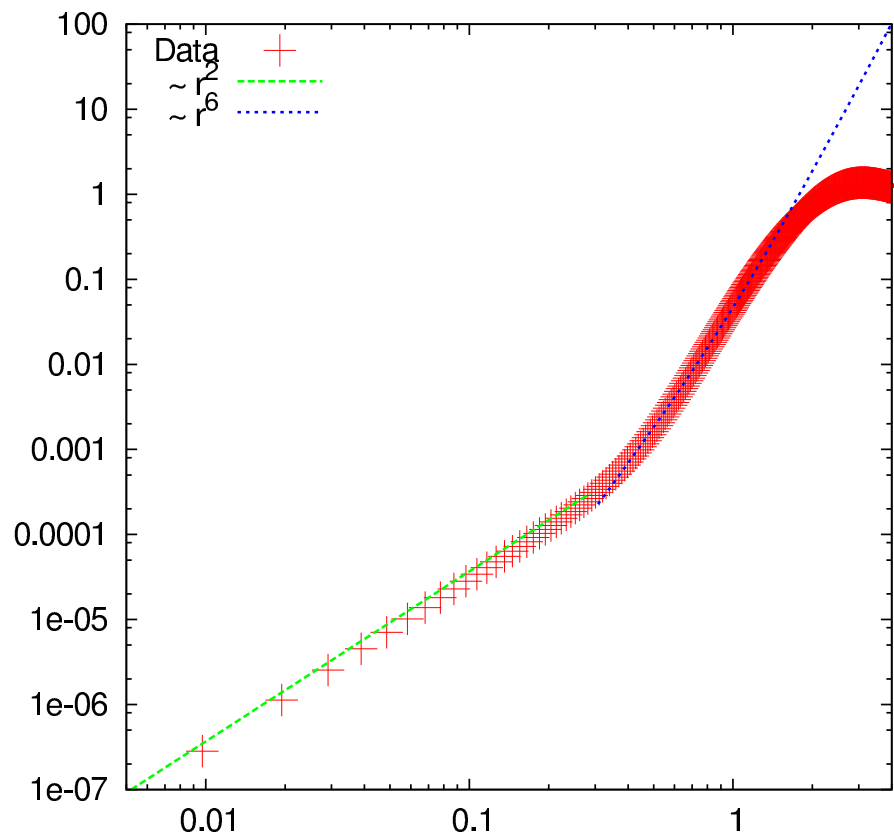


Figure 3.16: $g(x,x)$ for the ground state of a homogeneous system with **Coulomb interaction**. Provided are also fits in different regions (r^2, r^6). Note the logarithmic scales.

Chapter 4

Investigating the inner structure of the electron-vortex complex

Having established global properties of the homogeneous FQH-system, we turn now to a somewhat more local property of the ground state - the positions of the wave functions vortices in the unit cell.

To see, why those positions are of interest, let us recall the arguments set forth in sec. 2.4.4. The Laughlin wave-function (2.56) has a peculiar property, it has zeroes at the positions of the electrons only. In the CF-theory, this peculiarity is used to construct composites of electrons and flux quanta¹

We shall make use of the changes in the vortex positions, under the influence of external potentials, to distinguish between incompressible FQH states and disturbed, compressible states. We expect this feature of the ground state to be more sensitive towards impurities and more significant with regard to the incompressibility of the disturbed state than e.g. the gap. We will investigate this special property in what follows for the homogeneous state, later on we will extend this analysis to inhomogeneous systems.

In this chapter, we introduce a method to calculate the positions of the wave-functions vortices and extend it to the calculation of correlations between electrons and vortices. After laying the necessary foundations, we discuss the actual implementation of the algorithm and its margin of error. Finally, we apply the method to homogeneous systems with Coulombic and short-ranged interaction respectively.

¹Remember the equivalence of magnetic flux quanta and zeroes. Remember also, that an analytic function is fully determined by the distribution of its zeroes.

4.1 Background and some details of the calculations - How to find vortices in a many-particle wave function

The problem we face is the following: the many particle wave function $\Psi(\mathbf{z}_1 \dots \mathbf{z}_{N_e})$ is a function of $2 \times N_e$ real variables (10 -12 in our case). Finding the vortices of this wave function² would mean to sample or search a 12 dimensional phase space. Even if we would find zeros in this phase space, no clear physical interpretations could be developed from those zeros.

We follow a slightly different approach here. Let us recall the argumentation by Halperin about the meaning of the vortices in the Laughlin ground state. It was shown that, in the Laughlin ground state, all zeros are to be found at the place of the electrons³.

To “see” the zeroes in the wave function, the idea of a sample electron was introduced, which can be moved through the sample and around the other ($N_e - 1$) fixed electrons. In this approach, the phase space has been reduced to a mere 2 dimensional one, easily accessible to present day minimax routines (compare [16]).

Recalling the structure of the many particle wave function (3.3) and its decomposition to be

$$\Psi(z_1 \dots z_{N_e}) = \Psi^{CM}(z_1 \dots z_{N_e}) \times \Psi^{rel}(z_1 \dots z_{N_e}), \quad (4.1)$$

and fixing the position of all electrons but one at $\{z_2 \dots z_{N_e}\}$, we obtain an *effective single particle* wave function $\Phi(z_1, \{z_2 \dots z_{N_e}\})$. Φ also decomposes into a center of mass part and a relative part,

$$\Phi(z_1, \{z_2 \dots z_{N_e}\}) = \Phi^{CM}(z_1, \{z_2 \dots z_{N_e}\}) \times \Phi^{rel}(z_1, \{z_2 \dots z_{N_e}\}) \quad (4.2)$$

$$= \underbrace{F(z_1, \{z_2 \dots z_{N_e}\})}_{\frac{1}{\nu}(3) \text{ vortices}} \times \dots \times \underbrace{\Phi^{rel}(z_1, \{z_2 \dots z_{N_e}\})}_{N_m - \frac{1}{\nu} (12,15) \text{ vortices}}. \quad (4.3)$$

As we discussed earlier, Ψ^{CM} is determined by the positions of the electrons center of mass ($Z = \sum_{i=2, N_e} z_i$). The center of mass part (Φ^{CM}) in

(4.2) contributes 3 vortices to the overall N_m vortices, which are not bound (in the sense described above) to the individual electron positions $\{z_2 \dots z_{N_e}\}$ and do not contribute to the repulsion of the electrons.

In a Laughlin state, we will therefore find 2 different types of zeros in the reduced wave function, (i) those located at the electrons positions and (ii) zeros not bound to any electron position. Only the first type of zeros is due to the polynomial part of (2.56) and Φ^{rel} in (4.2) and causes all other electrons to see a zero at this particular position. Those zeros are related to charge deficiencies and create an phase shift of $2m\pi$ in the wave function. We denote them *vortices* in agreement with Graham et al. [46] (see also section 2.4.4.7).

From this observation the following algorithm has been developed to find vortices of the wave function:

²i.e. those points $r_{1 \dots N_e}$ at which $\Psi(r_{1 \dots N_e}) = 0$ and $\oint_{\epsilon} \Psi(r_i) dr = 2\pi \cdot N$.

³thus enhancing the repelling interaction among the electrons and force them “more” apart, than the Pauli principle and mere electrostatics would do.

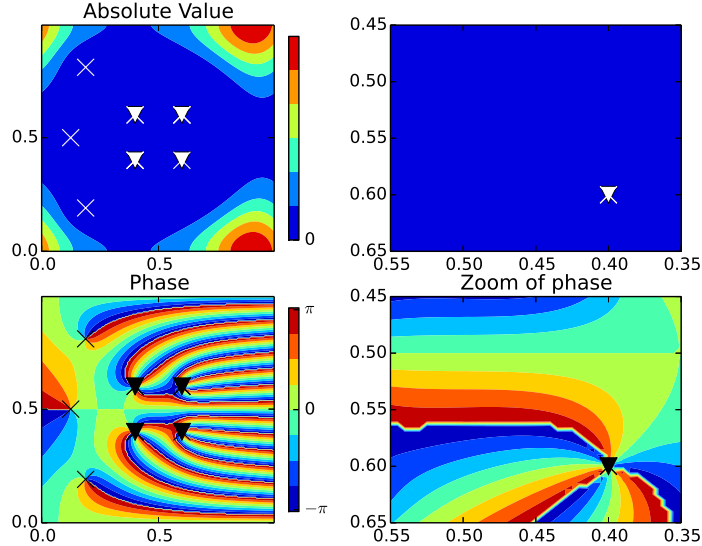


Figure 4.1: Top row shows $|\Phi(z_1)|$, bottom row shows the phase of $|\Phi(z_1)|$. The sample electrons are marked with ∇ , the vortex positions with \times . The right column shows a magnified region around a single sample electron for the same homogeneous system with $N_e = 5$ and **short range interaction**

1. Start with a many particle wave function $\Psi(z_{1\dots N_e})$ from EXD calculations
2. create a spatial electron configuration for $N_e - 1$ electrons $\{z_{2\dots N_e}^e\}$
3. Use those positions to create a reduced many particle wave function $\Phi(z_1) \{z_{2\dots N_e}\}$ which depends parametrically on those positions
4. Find the zeros $(\mathbf{r}_{1\dots \frac{N_e-1}{\nu}})$ of the reduced wave function Φ ,
5. Calculate the phase shift associated with a translation around each \mathbf{r}_i . If it is an integer multiple of 2π , we found a vortex at \mathbf{r}_i .

The results of this algorithm are shown in Fig.4.1 for a system with short range interaction and Fig.4.2 for a system with Coulomb interaction. Both figures show the modulus of the effective single particle wave function ($|\Phi(r)|$) (generated from a set of symmetrically arranged electrons (∇)) in the respective top row and the phase of $\Phi(r)$ in the bottom row. The vortices calculated by the aforementioned algorithm are shown as \times . For both interactions, each electron binds at least one vortex (bottom left of Fig. 4.1 shows nicely the phase change of 6π when going around the electron position). The Coulomb system shows 2 vortices in the vicinity of each sample electron, while the short range system binds the vortices at the electron positions.

A few remarks are in place concerning the ramifications of this calculational method and the interpretation of the vortices.

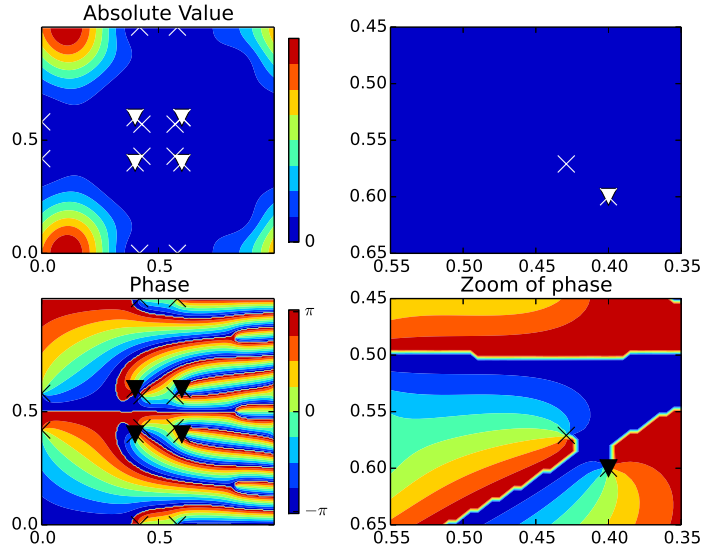


Figure 4.2: Figure shows effective single particle wave function for a homogeneous system (**Coulomb interaction**). See also caption of Fig. 4.1

- The reduced wave function (Φ) is always generated from the same many particle wave function. The fact that we use different electron positions means merely that we sample points in the Hilbert space, where the probability of the many particle wave function is different. The maximum probability is always attained at configurations for which the electrons are kept apart ([101, 99]).
- The vortices of the reduced wave function are not visible in the electronic densities, as they represent points of *conditional* zero probability to find an electron. This is clear, as the many particle wave function could be written as a (weighted) superposition of effective single particle wave functions. This superposition leads to a homogeneous density (in the case of a clean system).

4.1.1 Previous results from the literature

The position of vortices in FQH-systems have been studied in a few other works, notably by Tavernier et al. [117] and Saarikoski et al. [101, 99]. As these studies relate directly to our work, we describe them shortly here. A review is given in [100].

Tavernier et al. followed the same approach to calculate vortices from many particle wave functions calculated by Exact Diagonalization. They investigated electrons (2-4), interacting via the SRI, in a quantum dot (simulated by a confining parabolic potential with rotational symmetry), subject to a magnetic field. The authors calculated the positions of the vortices at different filling factors,

for comparison we use their results for $\nu = \frac{1}{3}$. The wave function has 3 vortices per electron. One is bound to each electron as prescribed by the Pauli principle, while the remaining 2 vortices are symmetrically displaced in the vicinity of the electron. They observed a tendency of the vortices to repel each other, hence avoiding the emergence of higher order vortices. The special geometry of the sample electrons forces the vortices to “move” away from the electron cluster. Upon variation of the potential strength, the position of the vortices changed in such a way, that their distance to the next electron is enlarged. The impact of the configuration of the sample electrons was studied and a substantial influence was found.

Saarikoski et al. [101, 99] also studied a few electron system (6 electrons in an elliptical or rectangular trap) under the influence of a strong magnetic field. To find the vortices they used a mean-field approach (SDFT) [102] as well as ED and the reduced wave function (as we do). They observed with both methods the emergence of vortices with increasing magnetic field and claimed, that the MDD shows features of a correlated quantum liquid of electrons and point-like vortices. At the positions of the vortices (EXD) the mean field results showed a circular current as well as a vanishing electronic density. The latter was not found with the EXD method. Again, the positions of the vortices depend strongly on the shape of the confining potential and no higher order vortices have been observed.

4.2 The vortex distributions in a homogeneous state

In Fig. 4.3 we show the vortex distributions⁴ for the Coulombic and the SRI homogeneous ground state. The figure shows the expected attachment of the vortices to the electron positions.

The SRI state binds 3 vortices on-top of the electrons⁵ while 3 remaining vortices - those due to the center of mass wave function - are scattered across the unit cell. Yoshioka [133] mentions the vortex distribution they encounter in the homogeneous state, which is that all electrons bind 3 vortices giving a ” 6π vortex” at each electron position. This is in excellent agreement with our results as well as with the expectations formulated in Sec. 2.4.4.7 where the Laughlin state with its perfect attachment was found to be the exact ground-state of a SRI system, as well as with the expectation derived analytically by Halperin.

The Coulombic state binds 1 vortex on-top of the electron (representing the Pauli principle) while 2 vortices can be found in the vicinity of each electron at a distance of $0.29 l_0$. Again 3 center-of-mass vortices are distributed throughout the unit cell. The displacement of the 2 off-electron vortices is roughly symmetric along the symmetry axis cutting through the periodically repeated impurity and the sample electrons⁶. The displacement is of the same order of magnitude for all 4 electrons. We find again the Coulombic ground state to be similar⁷ to the Laughlin state where a few expectations needed relaxation.

⁴for a single configuration of electrons

⁵That is, the line integral $\oint z_i^e dz$ yields 6π . The spatial resolution of the vortex positions is better than $0.001 l_0$.

⁶A similar geometry was found by Tavernier et al.

⁷In the sense that the vortices are located in the vicinity of the electrons.

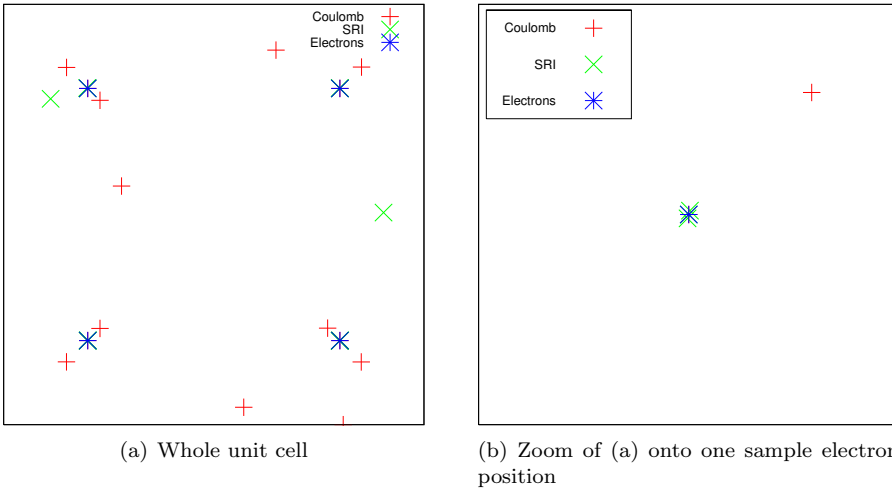


Figure 4.3: Vortex distributions across the unit cell for the homogeneous ground state (SRI and Coulomb interaction). Electron positions are marked by asterisks while vortices are denoted by red crosses(+), while the vortex positions for the 2 different interaction types are marked green and blue. (b) shows a more detailed distribution around 1 sample electron.

A schematic sketch of the electron-vortex geometry is given in Fig. 4.4, where the detachment vector ξ is introduced. The size of the electron vortex complex in the Coulombic case (for the given sample electrons configuration) is hence $2\xi_{\text{coul}} \sim 0.6l_0$, while $\xi_{\text{SRI}} = 0$.

4.3 Eliminating the impact of the sample electron configuration - Electron vortex correlations $g_{ev/vv}$

The method developed so far however has a serious shortcoming - its results are dependent on the actual positions of the sample electrons (see App. D, p. 171 and [101]). This clearly unphysical behavior can be cured by averaging over all possible sample-electron configurations as we will show next.

To this end we repeat the search for a large number of sample electrons configurations, thus "ironing out" the influence of the geometry. By recording the vortex displacement for each of the configurations we arrive at a representation of the vortex detachment which is independent from the geometry.

In this section we will introduce, test and apply this method to the ground state of homogeneous systems. A description of an automated evaluation method is also given.

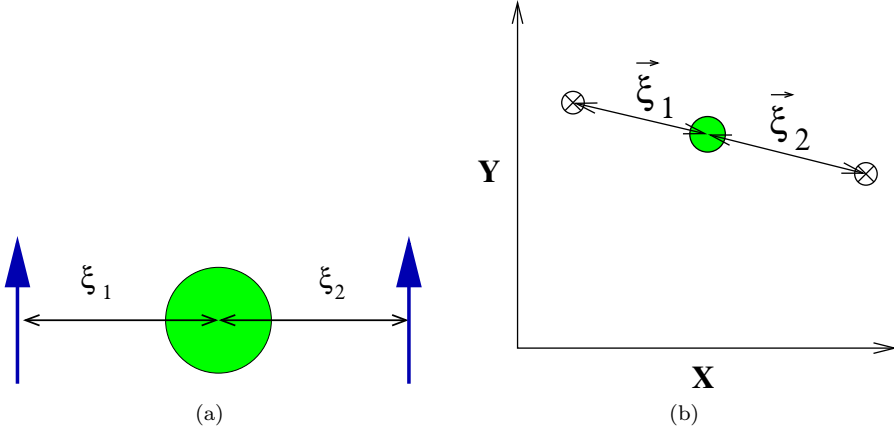


Figure 4.4: How to measure the flux attachment/detachment in an electron-vortex complex. 2d geometry (b) and 1d geometry (a). The quantity ξ is the electron vortex distance.

4.3.1 Methodical considerations

The new quantities we will analyze from here on are the vortex-vortex correlations

$$\begin{aligned} g_{vv}(z) &= \langle\langle \Psi | \delta(z_i^{\text{vortex}} - z_j^{\text{vortex}}) | \Psi \rangle\rangle_{\text{elec. pos.}} \quad (4.4) \\ &= \frac{1}{N_{MC}} \sum_{i=1}^{N_{MC}} \sum_{j,k,j < k}^{\#\text{vortices}} \Theta_\epsilon((z_j^{\text{vortex}} - z_k^{\text{vortex}}) - z) \dots \end{aligned}$$

and the electron-vortex correlation

$$\begin{aligned} g_{ev}(z) &= \langle\langle \Psi | \delta(z_i^{\text{vortex}} - z_j^{\text{elec}}) | \Psi \rangle\rangle_{\text{elec. pos.}} \quad (4.5) \\ &= \frac{1}{N_{MC}} \sum_{i=1}^{N_{MC}} \sum_{j=1}^{\#\text{vortices}} \sum_{k=1}^{N_e} \Theta_\epsilon(z_k^{\text{electrons}} - z_j^{\text{vortex}} - z) \dots \end{aligned}$$

where the expectation value $\langle\rangle$ in (4.4) and (4.5) is calculated from averaging over the ground state.

The second lines in (4.4) and (4.5) give a numerical description of the correlations where Θ_ϵ is the rectangular function of width ϵ . To extract these quantities from the ground state wave function the algorithm reads

1. Diagonalize the Hamiltonian Eq.(2.39). Extract the ground state $\Psi_0(z_1 \dots N_e)$
2. create a random distribution of $N_e - 1$ electrons $z_2 \dots z_{N_e}$ by virtue of a weighted Metropolis - Monte Carlo method [110].
3. calculate the reduced wave function $\psi_0(z_1)$ using the positions generated in step 2.
4. find the minima $r_{1\dots(N_m-3)}$ of $\psi_0(z_1)$ and calculate the residuum of the complex valued ψ_0 . If it is a multiple of 2π count it according to (4.4) and (4.5)

5. remove the Pauli vortices
6. Repeat from step 2 until N_{MC} (convergence is reached at $N_{MC} = 1000$).

In order to sample the ground-state configuration space in a physical way, the Metropolis algorithm is used to determine the sample electron configurations for step (2). This algorithm favors the sample electrons to be well separated but allows for other configurations with a finite probability. A deeper description is given in the appendix (F.2.)

The way the data are generated and analyzed is depicted in Fig. 4.5. The two dimensional distribution $g_{ev}^{2D}(\mathbf{r})$ is shown in Fig.4.5(a) (difference vectors are plotted here, hence only a single vortex electron complex is shown). The two dimensional distribution shows very nicely the symmetrical localization of the vortices around the electrons. The 2D distribution is consolidated into the angle averaged $g_{ev}(r)$ (Fig.4.5(b)). The position (r_{max}) of the maximum of $g_{ev/vv}(r)$ is extracted. We identify this position with the size of the electron-vortex composites (ξ). The size of this composite will be dependent on the interaction type and some parameters of the potential and will be studied later as sketched in (Fig.4.5(c)).

A subtle point not to be overlooked is the relation of g_{ev}, g_{vv} to the pair correlation functions discussed in chapter 3.4. At first glance the observed quantities are equivalent: the pair correlation function shows the probability to find an electron at point r if there is one at r_0 . g_{ev} shows the probability to find ***no electron*** at point r if there is one at r_0 . Why should we find new physical insight as these two quantities look complementary?

The difference is in the positions and type of the vortices. For the case of a homogeneous SRI system, the 2 quantities should give the same information, all vortices - save the unessential CM-vortices - are bound to the electrons, i.e. the sample electron finds a 3 fold vortex, or the pair-correlation function decays with $r^{\frac{2}{\nu}}$. The situation is different for the case where the vortices are displaced from the electrons. They do still mark points where no other electron can be found, BUT it is not because at this point is already one electron. In fact there are points where no electron can be found although the Pauli-principle does not require it. These places are "seen" by the correlation functions g_{ev}, g_{vv} but not by the pair correlation function ($g(r)$) directly⁸.

4.3.2 Analysis of the distributions principal properties

Let us now scrutinize the actual shape of the correlations. To start with, let us recall what the argument of Halperin predicts for the electron-vortex correlations. Because all the vortices are fixed on top of an electron the electron vortex distribution should show a delta peak at the origin for the system with hard-core interaction as sketched in Fig.4.6(a). Depending on whether the Pauli-Vortex is counted or not the value for g_{ev}^{homo} should be 3 or 2. The geometry of the unit cell should give a non-zero contribution for $r > 0$ ⁹. The vortex-vortex distribution has the same shape for the homogeneous system with an unessential difference in the total count value.

⁸We postpone a deeper discussion to a later part (see p. 112)

⁹Vortices belonging to the randomly distributed "other" electrons with a peak at the average interparticle distance at $\approx 4.5l_0$. This finding matches nicely with the intra particle distance extracted from the electron-electron correlations.

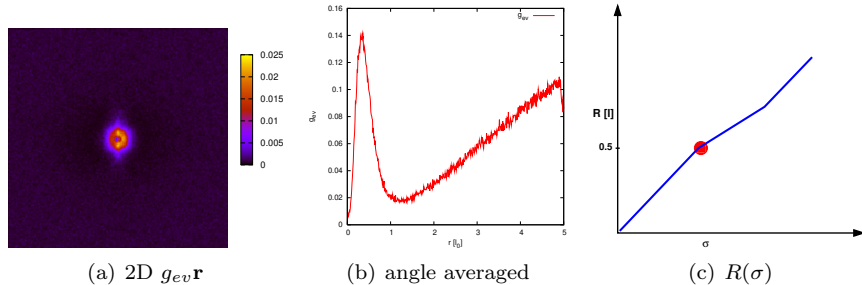


Figure 4.5: Schematics of data consolidation. In Fig (a) the raw 2d distribution is shown. The maximal distribution of vortices in the center of the unit cell is obvious. (b) shows the angle averaged g_{ev} . (c) represents the last state where the maximum value from (b) is plotted in a $R(\sigma)$ plot. (The same could of course be done with the maximal count of (b)). State with 5 electrons $\nu = \frac{1}{3}$, single impurity with $V_0 = -0.3$, $\sigma = 1l_0$.

4.3.3.1 Comparison of the different interaction types - Coulomb vs Short Range Interaction

In Fig. 4.3 it was found already, that for the Coulombic interaction the non-Pauli vortices are not fixed to the electron but are found in the vicinity of the electron position. This must be found for the distributions too. In Fig. 4.6 (a and b), we show the electron-vortex correlations for both interactions. While for the SRI (Fig. 4.6(a)) the maximum of $g_{ev}(r)$ is essentially at 0 (with a small finite value for $r < 0.05l_0$), the Coulomb interaction (b and c) shows the maximum at $\approx 0.6l_0$.

When recalling the section on electron-electron correlations (sec. 3.4, p. 60) we found, that the electron-electron correlation for a homogeneous state with Coulomb interaction showed a quadratic dependence ($g(r) \propto r^2$ near the origin). We analyze therefore also the analytical shape of g_{ev} calculated from a Coulombic ground state for small r . In Fig. 5.40 a double logarithmic plot of the same data as in Fig. 4.3 is shown. The numeric evaluation of the fits to polynomial functions give a good agreement to $\sim r^2$ which is in good agreement with the slopes found for electron-electron pair correlations (cf. 3.4, in particular Fig. 3.4.1, p. 65 and the discussion thereof).

With the introduction of g_{ev} and the connected geometrical interpretation (vortices at a finite distance from the electron) we interpret now the two different slopes in the electron electron correlation $g(r)$ of the Coulomb ground state as shown in sec. 3.4, (p. 60ff and Fig. 3.4.1). Imagine 2 electrons (with their attached vortices), one at $r = 0$, the other at r (as depicted in Fig. 4.8(b)). We can distinguish now two scenarios, in the first the two electrons are farther away than the average electron vortex distance in the second the two are closer than that. In the former case, the electrons “see” each others three vortices, giving a r^6 repulsion, while in the latter the electrons experience only the Pauli r^2 repulsion. For the short ranged interaction, the electron binds all three vortices, therefore the other electron sees 3 vortices at $r = 0$, hence the r^6 repulsion over the whole range of r . The involved distances here are the size of the electron-vortex complex (approx. $0.7 l_0$) and the distance below which

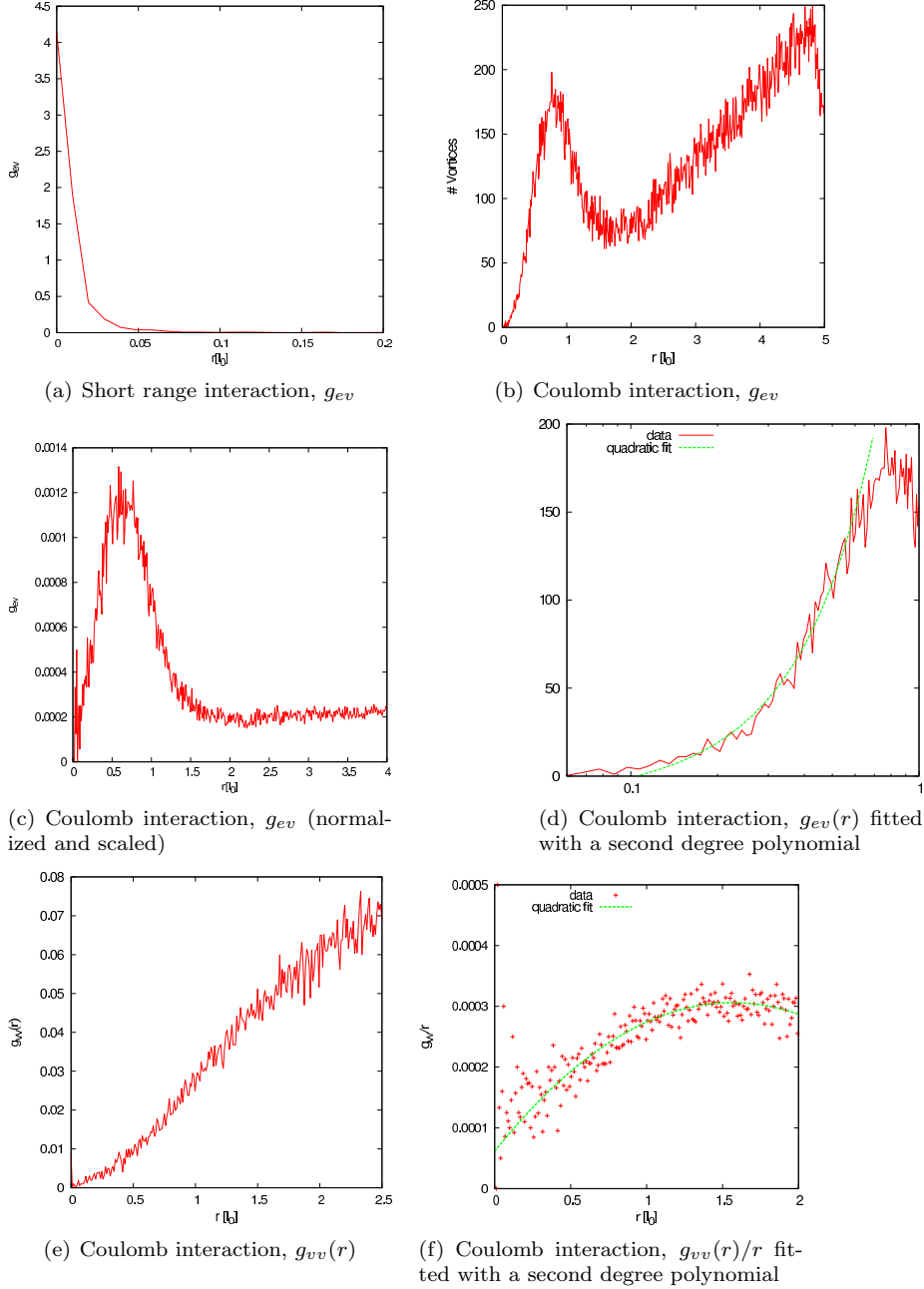


Figure 4.6: This picture summarizes the various electron/vortex -vortex correlations (g_{ev}, g_{vv}) for the two interaction types. The top row shows the electron vortex correlation (g_{ev}) for the **Short Range Interaction** and g_{ev} for the **Coulomb interaction**. The second row shows g_{ev} for the Coulomb interaction (c) together with a fit to a second degree polynomial (d). The bottom row (Figs. (e) and (f)) shows the vortex-vortex correlation ($g_{vv}(r)$ and $g_{vv}(r)/r$ with a fit to a second degree polynomial), Coulomb interaction. Comparison of the two fits ((d) and (f)) shows, that for g_{ev} the quadratic regime is prevalent, while for g_{vv} the linear coefficient is three times larger than the quadratic coefficient. All correlations were calculated from the respective ground state of a homogeneous 5/15 system.

$g(x, x) \sim r^2$ which is approximately $0.3 l_0$.

To reinforce this notion we show the individual vortex distribution calculated for a particular electron configuration, in which the electrons are pairwise close to each other in Fig. 4.8(a)). The vortices are not situated between the two electrons, hence the electrons “see” only the single on-top vortex. This interpretation is summarized in the sketch provided in Fig. 4.8(b), at larger distances the electrons “see” each others 3 vortices, while at small intra-electron distances the non-Pauli vortices of the two electrons repel¹⁰ each other. This leads to the configuration where no vortices are between the two electrons, hence the electrons “see” only the other electrons pauli vortex, thus the $\sim r^2$ regime.

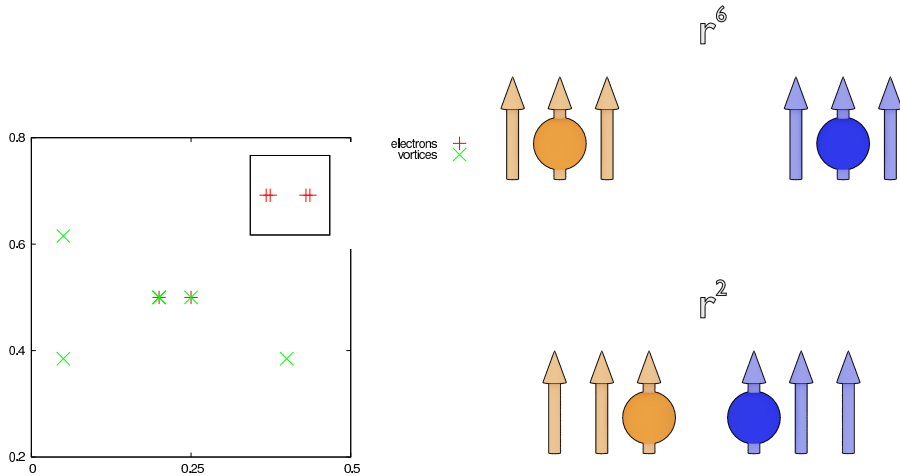


Figure 4.7: Vortex distribution

Figure 4.8: (a) Vortex distribution calculated from a homogeneous Coulomb ground state and a single electron configuration in which the electrons are pairwise close to each other (shown in the inset). In (b) we show a sketch of the situation of the two regimes as described in the text.

4.3.3 Aspects of computer based evaluation of g_{ev} and g_{vv}

In later parts of our work we will be concerned with the analysis of many electron-vortex and vortex-vortex correlations. This analysis was performed automatically. We give here only a short introduction of the underlying algorithm.

Given the typical shape of $g_{ev/vv}$ (see e.g. Fig.5.38, p. 118) the following algorithm was used to extract the quantities ξ and the width of the peak.

1. The distribution was normalized (e.g. $g*_{ev} = \frac{1}{N_{MC}} g_{ev}$)
2. the distribution was smoothed, using a polynomial of sixth order ([86], [108]),

¹⁰a finding similar to the vortex distributions encountered by Tavernier et al.

3. the maximum value of this smoothed distribution and its position (ξ_{ev} were recorded)
4. the width of the peak was estimated as the distance where g_{ev} falls off to 10 % of its maximal value
5. the same procedure was repeated for g_{vv} , resulting in ξ_{vv}
6. the normalized distributions were fitted to a polynomial (degree 8)¹¹ and the maximum of the polynomial was calculated.
7. ξ was calculated as the average value of all ξ_{ev} and $\frac{1}{2}\xi_{vv}$

Summarizing we should note that the position of the maximum can be taken as a defining property of those distributions. Furthermore, the results gathered in the previous section and the results presented so far allow us, to conclude that both distributions reveal the same physical properties where only numerical convenience gives preference to one or the other. We will use results from both distribution types from here on.

4.4 Electron-vortex correlations in homogeneous system

We summarize now the findings for the electron-vortex and vortex-vortex correlations for homogeneous systems with SRI and Coulomb interaction. The fact, that with SRI the electrons bind all vortices on top (as shown above) translates into a delta peak in g_{ev} as shown in Fig. 4.6(a). The finite value of g_{ev} for $r < 0.05l_0$ ¹² is due to the finite sampling of the unit cell and gives an indication of the method's precision. The vortex-vortex correlation ($g_{vv}(r)$, not shown here) for the SRI system has the same feature, a strong delta-shaped peak at the origin.

The findings are different for the Coulomb system (see Fig. 4.6(b,c,d)). The results were calculated after averaging over 5000 electron-configurations ($N_{MC} = 5000$)¹³. The electron-vortex correlation shows a maximum at $\approx 0.7l_0$, while a less pronounced maximum¹⁴ has been found for g_{vv} at approx. $1.4 l_0$.¹⁵ The electron-vortex correlation shows a strong quadratic dependence near the origin, while the vortex-vortex correlation is essentially linear in this region.

The minimum at $g_{vv}(0) \approx 0$ can be interpreted in such a way, that the vortices effectively avoid each other - similar to the findings of Tavernier and Saarikoski discussed above. A possible underlying mechanism is the repulsion of the current vortices¹⁶ via their magnetic repulsion as discussed by Saarikoski. Without such a repulsive vortex-vortex interaction, the shape of the 2D g_{ev}

¹¹This fit serves also as a reassurance, as we find that both g_{ev} and g_{vv} are of sixth order for all SRI-distributions analyzed in this thesis

¹²In the calculation this is equivalent to all entries in the electron-vortex distribution being zero, except the first (the origin) and the second.

¹³Normally $N_{MC} = 1000$ provides sufficiently well converged results.

¹⁴The numbers are inconclusive here as to whether g_{vv} is constant for $r > 1.4l_0$

¹⁵The maximum near the origin in Fig. 4.6(c) is caused by the small value of r and not present in the raw data, cf. 4.6(b) and can therefore be neglected as an numerical artefact.

¹⁶in the effective single-particle wavefunction, see sec. 4.1.1

as shown in Fig. 4.5 could also show a more homogeneous distribution of the vortices, exposing a disk-like characteristic as opposed to the ring-like shape found in Fig. 4.5. Such a repulsive interaction among macroscopic vortices was observed in superconductors by Chaves et al. [19].

This vortex-vortex repulsion is in stark contrast with the vortices in the SRI system, where no such behavior is observed. The vortices are bound to the electron and show no repulsion in our calculation. Assuming that the repulsive interaction prevails also for the microscopic vortices, the shape of g_{vv} and the apparent absence of such an interaction for the SRI, could be explained by two opposing mechanisms - the effectively attractive pinning of the vortices to the electrons - having its origin in the lowest component of the pseudopotentials¹⁷ - and the repulsion of the microscopic vortices having its origin in the higher order components of the Coulombic pseudopotentials. The observations by Saarikoski et al. (in particular the current vortices) can provide another intuitive picture of two magnetic dipoles repelling each other.

The maximum position at $r \approx 1.4l_0$ in g_{vv} is consistent with a symmetric displacement of the vortices around the electron. The

Calculations for $g_{ev,v}(r)$ were carried out for each of the 3 degenerate ground states with no difference. This is consistent with the notion, that only the electron-electron interaction determines the vortex displacement, which makes $g_{ev}(r)$ a good candidate to study the collective properties of their ground state.

4.5 A short summary

In this section we developed a method which allows us to gain microscopic insight into the structure of the wave function. Based on previous work, we calculate the positions of the vortices in the wave function.

The results shown in this section of the wave functions are in agreement with previous analytical work and in other EXD studies. The new quantities g_{ev} and g_{vv} have been introduced and thereby an intuitive picture of the vortex distribution in the respective ground state was developed. The results were used to interpret the different regimes in the electron-electron correlation functions.

It was found, that even in homogeneous systems with Coulomb interaction, the vortices avoid each other, showing the signature of a repulsive vortex-vortex interaction.

¹⁷which is present in both types of pseudopotentials

Chapter 5

Introducing disorder - The system with a single Gaussian impurity

After the introduction of our methods and the presentation of the results obtained from the analysis of the homogeneous systems, it is worthwhile to pause here and summarize the results. We found thus far no apparent contradiction with previous results from the literature - experimental as well as theoretical. In particular, the ground state shows a large gap between the first three (degenerate) states and the energetically neighbouring states. This gap is a crucial necessity for the system to be incompressible. However, we expect the gap to be reduced once impurities are introduced into the system. We expect the system to be compressible (and insulating) once the gap is closed, however it is not clear whether the gap really needs to be closed completely. Moreover it is not clear, whether the gap-size alone is a sufficiently fine indicator of the compressibility of the ground state. To the contrary, previous results (summarized below) hint, that rather the positions and localization of the vortices should be used as such an indicator. In this spirit we will study, whether it is possible to characterize the state by the localization of the vortices around the electrons. With this tool, we will establish a relation between the gap-size, the vortex positions and the incompressibility of the ground state.

5.1 Preliminaries and results from the literature

As we have seen in sec. 2.2.4, disorder plays an important role in understanding the physics of the FQH-effect. On one hand “some” disorder is needed for the emergence of the plateaus in the $\sigma_{xy}(B)$ characteristic. On the other hand, the application of percolation theory showed that a “too strongly fluctuating” disorder may render the state insulating, destroying the incompressible ground state. The necessity of balancing the strength and fluctuations of the disorder became already manifest in the first experiments - Störmer et al. [122] had to use high mobility samples to discover the FQH-effect in the first place. [experiment + theory](#)

The disorder-driven collapse of the FQHE was studied before, mainly in two works by Arovas et al. and Sheng et al. As some ideas for our study originate from those works, it is appropriate to summarize them here.

At the heart of the work by Arovas et al. [11] is the following question: "Can one reproduce the assumption of extended states in the middle of the Landau band by first principle based computer experiment?". To answer this question, they studied IQH systems with impurities by means of ED. The system was constructed using twisted PBC, $T(L_j)\phi(r) = e^{i\theta_j}\phi(r)$, where the change of the parameter θ is equivalent to an external potential (see e.g. Helias [53]). The positions of the vortices of the exact single particle states $\phi_{1\dots 7}$ were studied over a wide range of boundary conditions θ . They found that, for the energetically lowest and highest states, the vortices were located in narrow stripes inside the unit cell, while for the state in the middle of the Landau band ($\phi_{3,4}$, the vortices were found all over the unit cell. Since the positions of the vortices uniquely define the wave function, the authors concluded that the lower states are localized, while the middle states are extended. Subsequent calculation of the Hall conductivity by virtue of the Chern-numbers (see sec. 2.3.1, p. 19), delivered the result, that only the extended state(s) contribute to the Hall conductivity (only the middle states have a non-vanishing Chern number).

An extension of this study - in the sense that the analysis of the Chern numbers was used as a telltale for the existence of the FQHE- was done by Sheng et al. [109]. As discussed earlier (see sec. 2.4.3, p. 26), the Chern number 1 is obtained, when summing over all $\frac{1}{\nu}$ degenerate ground states in the homogenous ground state. Sheng obtained the many-particle ground state by EXD, studying systems with up to 8 electrons and a tunable white-noise gaussian impurity potential. The Chern numbers were calculated not only for the near-degenerate 3 ground states but also for the higher groups of states (see spectrum in Fig.3.2.1, p. 45). They found, that also the higher states carry a Chern number of 1 for weakly disturbed systems. After increasing the strength of the impurity potential, the authors found the Hall conductivity of the ground state - again calculated by virtue of the sum over the Chern numbers- to be smaller than 1 - the ground state is not incompressible anymore. The authors conclude that the destruction of the FQH regime is a continuous process.

5.1.1 Organization of this chapter

In this chapter we shall present our results in the order described below. We will start our investigation by introducing a model for the disorder present in experimental samples. This model shall enable us to study the influence of disorder on a finer scale than those early models which accounted for disorder by a single heuristic parameter. We discuss several options and present our model of randomly distributed gaussian scatterer. In this chapter, our calculations will be restricted to systems with a *single impurity* of varying strength and shape. We start with a thorough investigation of the spectra, bandwidths and correlation gaps of disturbed systems. In particular, we will establish a good understanding of the closing of the correlation gap, which is a crucial precondition for the FQH state. Since we are interested in other effects than the mere destruction of the incompressibility by closing the correlation gap, we ensure thereby, that in later calculations the correlation gap remains present.

By employing perturbation theory onto the center-of-mass part of the wavefunction, we shall establish the origin of the increasing bandwidth. By investigating the electronic density response to the impurity, we shall find traces of the incompressibility in the density response of our finite size system.

In the last part of the chapter we will present the electron-vortex correlations as a finer measure for the quality of the FQH-state. All results will be presented for the Coulombic and the short ranged interaction.

5.1.2 How to model disorder - Introducing the model system

The first task is to find an appropriate model of the real world system which does not exceed the available computer power on the one hand and recovers all essential physical properties on the other hand. The real world problem can be described as electrons confined to 2 dimensions moving under the influence of a weakly modulated stochastic electrostatic potential. The origin of the potential are the donor ions located in the bulk of the semiconductor at a relatively large distance from the 2DEG. *Präzisierung auf Störstellen, die normalen Störstellen gibt es in hochreinen Proben nicht mehr. Long range Coulomb. Warum erst die Energien? Erst das gap kleiner machen, FQH so zerstören?)* A wide range of disorder models suitable for numerical studies can be found in the literature. The models fall roughly in 3 categories,

- disorder is modelled by the superposition of many randomly distributed single-particle potentials (think of them as the potentials of impurity ions)
- disorder is constructed from other random processes (Random Matrix approach [54]), or
- disorder is treated by a single additional (global) parameter in the Hamiltonian as it was done in the early works of Laughlin and Morf.

In this work we will follow the first approach to model the disorder by an external field, generated from an array of individual scatterer. We consider this approach to be intuitive (in contrast to the Random Matrix approach) on the one hand and to provide insight into local properties in contrast to the treatment by a single disorder parameter.

To motivate our particular choice of the individual potential, we note, that some work is reported in the literature for a range of potential types (gaussian, delta or parabolic [125]). It has been shown, that a reasonable model for this system is to put multiple scatterer at random positions in the sample , [7, 54].

The construction from Gaussian scatterer gives (according to Huckestein [54]) a similar random potential when used instead of the delta potentials while reducing the calculational effort. For this reason we will construct our potential from many Gaussian scatterer.

In order to pursue a methodical approach, we are well advised to start with a simple system, containing only a single Gaussian scatterer in this section and proceed to random potentials in Section 6.

The system to be studied in this chapter is depicted schematically in Fig.

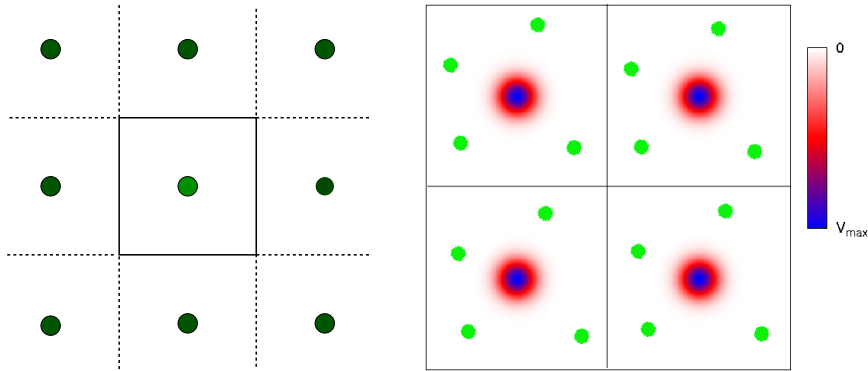


Figure 5.1: Schemes of the single impurity system(a)Schematic plot of the periodically repeated unit cell. The green dots denote the positions of the Gaussian impurity and (b) Example of the effective potential $\sum_{\text{cells}} V(\mathbf{r}_{\text{cell}})$ in the unit cell created by an array of attractive Gaussian scatterer. The effect of the neighboring scatterer amounts to less than 1% for $\sigma < 1l_0$ of the overall impurity potential. The green circles denote arbitrary electrons positions.

5.1. The unit cell is quadratic¹ with a single Gaussian shaped impurity,

$$V(z) = V_0 \exp -\frac{(z - z_0)^2}{\sigma^2}, \quad (5.1)$$

in the center of the cell at ($z_0 = (L_x/2, L_y/2)$) and is periodically repeated. The strength and the width of the impurity can be tuned individually. The electrons are assumed to be fully spin polarized (large Zeeman energy) and the magnetic field is sufficiently strong to ensure the validity of the LLL-approximation.

5.2 Global properties - Spectra, energetics and overlaps

In this section the global energetic properties of the many particle wave functions are discussed that were calculated using the EXD method. In particular, the energy spectrum, the excitation gap and the degeneracy of the ground state are studied. A first evaluation of the effect of the finite size is given and the influence of the used model is addressed. Two interaction types will be studied in this section - the Hardcore Interaction² as the interaction type for which the Laughlin state is a perfect solution and the Coulombic interaction

5.2.1 Weak impurities

To veer away from homogeneous systems, we gradually switch on the impurity and vary its strength (V_0) and width σ independently. We will study weak³ attractive as well as repulsive impurities. We compute spectra, correlation gaps

¹with $L_x = L_y = \sqrt{2\pi N_m} \approx 10l_0$ for $N_e = 5$

²or the Short Range Interaction SRI)

³where weak is loosely defined as $V_0 < E_{\text{gap}}^{\text{homo}} \approx 0.1enu$ at this point

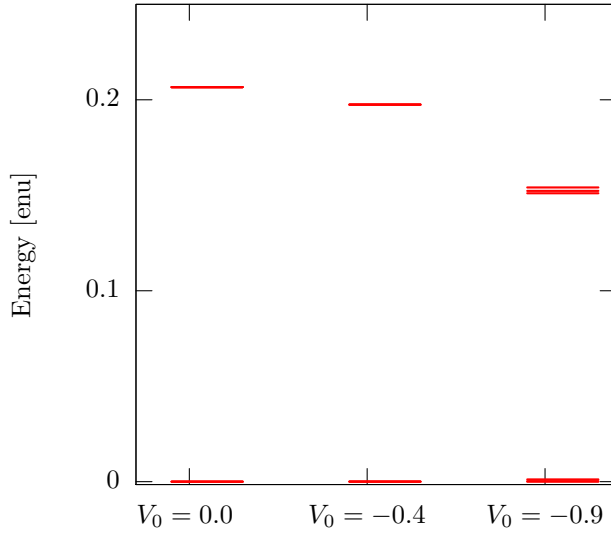


Figure 5.2: Lowest states of the many particle spectrum of a 5-15 system, three choices of V_0 , $\sigma = 1l_0$ - SRI. The energies are given relative to the respective ground state energy. The splitting of the 3 lowest lying states is not visible on this scale.

and the bandwidth and compare the influence of the 2 interaction types for systems with 5 electrons at $\nu = \frac{1}{3}$ only.

5.2.1.1 The principal shape of the spectrum

Let us first discuss the basic properties of the spectrum for 3 different strengths as depicted in Fig. 5.2. When comparing the spectra for $V_0 < 0$ with the spectrum of the homogeneous system, we find the spectral gap to be smaller (although still present) and the degeneracy of the ground state and the first excited state to be lifted. The gap is further reduced and the degeneracy further lifted for the stronger impurity.

At this point we shall pause to recapitulate the main question of this thesis. With regard to Fig. 5.2 we ask, whether the existence of the gap in the spectrum for $V_0 = -0.9$ is sufficient to render this state to be of the FQH-type. Or is the existence of the gap not a conclusive indicator for the FQH character of the state?

In Fig. 5.3, we show the development of the spectrum for a range of impurity strengths. The normalized Plot (c) shows a symmetric behaviour of $E_{1\dots 5}$ around $V_0 = 0$. Generally speaking, it can be observed, that in all cases the correlation gap is preserved - although somewhat reduced - and the degeneracy of the 3 lowest states is nearly preserved. The finer and subtler aspects of those spectra are discussed below in detail.

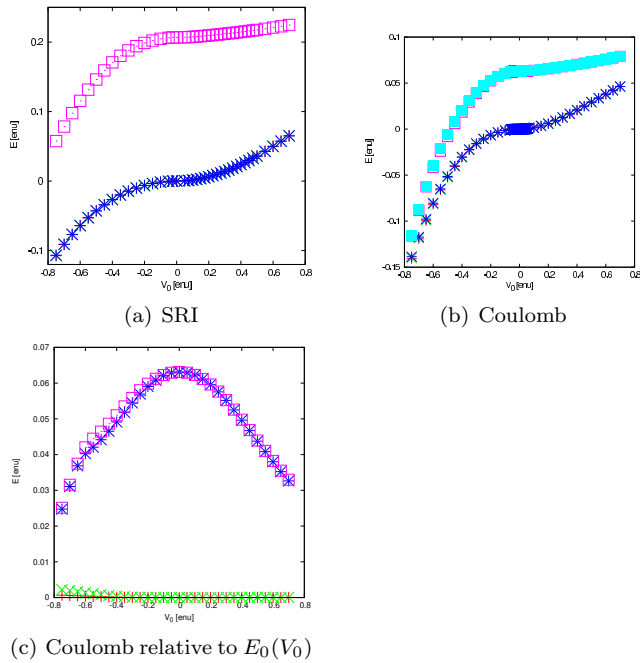


Figure 5.3: Spectra of the lowest 5 eigenstates of a 5/15 system, normalized to the ground state energy of the homogeneous state ($E_0(0)$) (a) SRI, (b) Coulomb interaction. (c) Spectrum normalized to the respective lowest energy ($E_0(V_0)$), Coulomb interaction. $\sigma = 1l_0$. The lifted degeneracy of the ground state is too small to be seen on this scale.

5.2.1.2 Analysis by means of perturbation theory

Although it has been stated above that it is impossible to employ perturbation theory in the FQH context, we must differentiate here somewhat. The statement should read more precisely: It is not possible to use perturbational calculus to find the eigenstates of the FQH-system as there is no small parameter which could serve as the expansion coefficient. However, once we know the ground state and start to perturb it with a small (local) potential the situation changes. Qualitative results can be extracted from a perturbation-like approach. Those results are useful as a reference for comparison with numerical results.

It is known both from symmetry analysis (see 2.5.1) as well as from numerical results (see sec. 3.2.5), that the ground state of a FQH system in a PBC geometry is degenerate. When taking into account a small impurity potential to the Hamiltonian $\hat{H} = \hat{H}_{FQH} + V(\mathbf{z})$ we find (following standard text-book procedure, e.g. [39, 70]) that the degeneracy is lifted and the energy of the splitting is proportional to V .

In the analysis of the homogenous states E_b we verified, that the ground state of a $\nu = \frac{1}{3}$ is exactly threefold degenerate, independent of the electron-electron interaction (see 3.2.5, p. 55) and nearly degenerate for larger Coulombic systems. In this section we analyze the lifting of the degeneracy of the ground state under the influence of an impurity. We will determine the exact meaning of **strong** and **weak** impurity.

We remember,

- that the ground state wavefunction decomposes into a center-of-mass part and a relative part and
- that the degeneracy of the ground state is solely due to the center-of-mass part of the Hamiltonian,

The impurity potential can now be treated as a small perturbation to the CM part of the Hamiltonian. It is expected to lift the 3-fold degeneracy of the homogenous ground state (cf Fig. 5.2). **Idee CM nur angucken, Annahme!, Potential symmetrisch als translation...** Applying the perturbation theory of degenerate states ([70, 84]), we find that the coupling between the degenerate ground states accounts only for a partial lifting of the degeneracy. The detailed analytical calculations can be found in the appendix, sec. B.0.1, p. 166.

5.2.1.3 Ground state energy

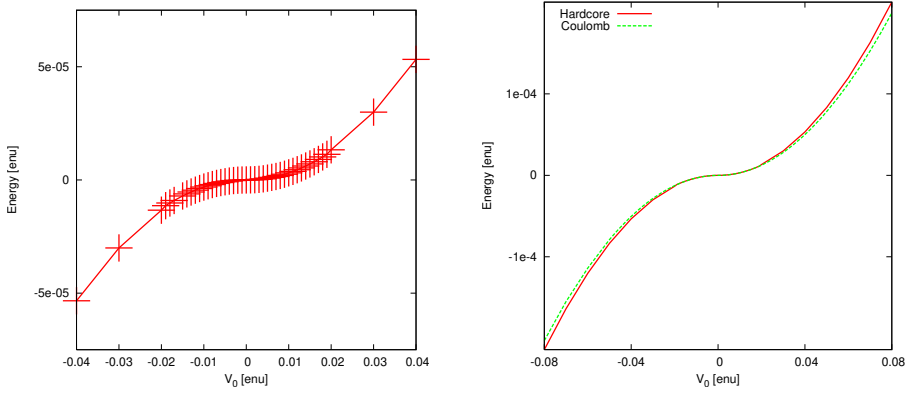
We shall now begin to analyse the development of the ground state energy E_0 with V_0 and σ , obtained by EXD calculations⁴. The first dependency we shall establish, is the dependency $E_0(V_0)$, to this end we fix $\sigma = 1l_0$ and calculate the ground state energy (cf. Fig. 5.4). In accordance with basic quantum mechanical considerations we find $E_0 \sim V_0$ and $\text{sign}(E_0 - E_0^{\text{homo}}) = \text{sign}(V_0)$ ⁵

Upon closer examination of Fig. 5.4 (a) and Fig. 5.7 (a) we find:

- $E_0(V_0) = -E_0(-V_0)$ for $|V_0| < -0.08\text{enu}$,

⁴For convenience we define $\Delta E_0 := E_0(V_0, \sigma) - E_0(0, 0)$

⁵In the Hamiltonian (2.83) the impurity adds a negative/positive single particle contribution, hence the ground state energy is lowered/raised with impurity strength.



(a) Energy of the lowest lying state of a system with 5 electrons and $\nu = \frac{1}{3}$, SRI depending on the strength of the impurity with $\sigma = 1l_0$.

(b) Ground state energies for Coulomb and SRI system

Figure 5.4: (a) Ground state energy of depending on the strength of impurity with $\sigma = 1l_0$ 5 electrons and $\nu = \frac{1}{3}$, hard-core interaction(b) Comparison of the ground state energy change(ΔE_0) for the coloumbic and the short range interaction.

- 2 regimes of $E_0(V_0)$ become apparent
- For $|V_0| > 0.02\text{enu}$ $E(0)$ follows $V(0)$ linearly, whereas
- for $|V_0| < 0.02\text{enu}$ a $E(V)$ shows a non-linear characteristic. The latter can be explained with the help of perturbation calculus of degenerate states.

All features are independent of the interaction type, although the quantitative findings may change slightly (cf Fig. 5.4 (b)).

As is shown in the appendix (sec. B.0.1), the calculation of the energy corrections by means of the perturbation theory requires the first and second order of perturbation theory. The latter contributes a V_0^2 term to the energy correction. In Fig. 5.5 we show the ground state energy (calculated by the EXD method) for negative values of V_0 along with a fit to a quadratic function. The fit reveals the quadratic behavior of the $aV_0^2 + bV_0$ type expected from the perturbation calculus. When evaluating the fit, we find that the quadratic term dominates the energy correction for values $V_0 < 0.085$ in accordance with the observations made above from visual inspection. These 2 coinciding results - the first obtained from the EXD calculations and the latter from analytical perturbation theory - fit nicely. **schoener**

Not a great many authors have published numerical results which we could use as a direct benchmark. Pfannkuche et al [91] study a system under the influence of a periodic (cosine) potential with an average potential $\oint_{cell} V(r)d^2r = 0$. They find the ground state energy to be lowered with increasing impurity strength. Obviously we do not expect quantitative agreement with their results as we did i.e. for the gap of the homogenous system. However we note, that the decrease of the ground state energy for an attractive impurity is reproduced in our calculations for both interaction types.

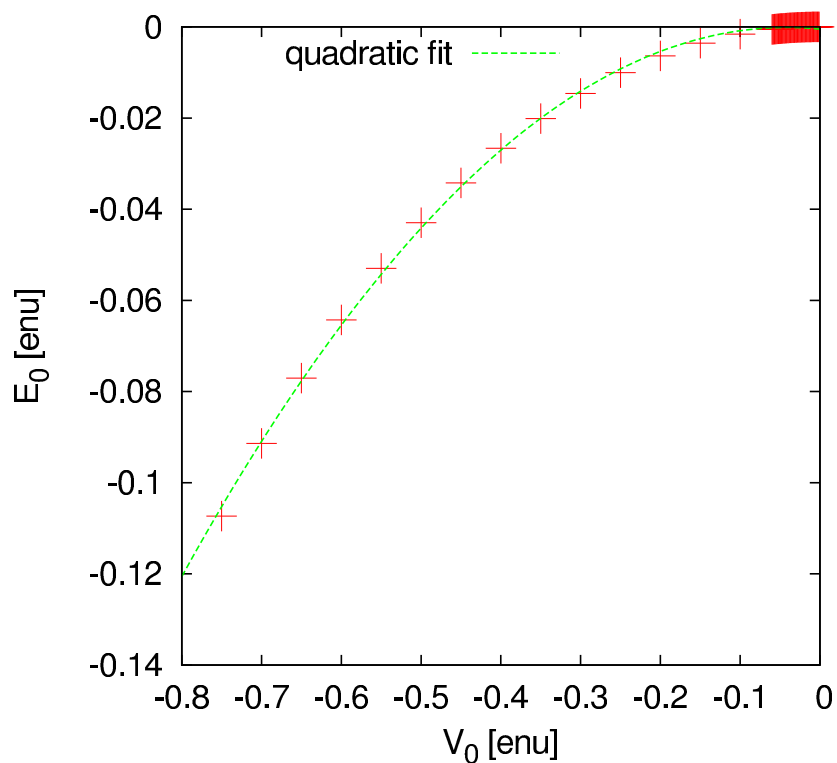


Figure 5.5: Ground state energy of a 5-15 SRI system with an attractive ($V_0 < 0$) impurity, fitted to a quadratic function $E_0(V_0) = -0.209V_0^2 - 0.017V_0$.

5.2.1.4 Correlation gap

We shall discuss now the change of the correlation gap⁶ when an impurity is present.

The gap size is reduced by an impurity, irrespective of its attractive or repulsive character (cf. Figs.5.6(b), 5.7 (b) and 5.9) while the clean system has the largest gap. A quantitative analysis is shown in Fig. 5.6(b). The fit to a quadratic function shows nearly perfect quadratic dependence $\Delta E \propto aV_0^2$.

When comparing the 2 interaction types (Figs 5.6 vs. Fig.5.7 (b)) the same analytical form of $E_{corr}(V_0)$ becomes apparent. In Fig. 5.9 we show the relative change of the correlation gap for our 2 interaction types. The rate of change is significantly larger for the Coulombic system. This higher susceptibility of the correlation gap towards disorder agrees with the smaller overall value of the correlation gap. The different susceptibility of the correlation gap for the 2 interaction types solidifies also the expectation, that the gap is due to the interaction part of the wavefunction and hence no artefact of our PBC system.

The asymmetric characteristic of $E_{corr}(V_0)$ is due to the asymmetric change of the excited states energy. It has its origin in the energy of the higher states being not altered symmetrically as is demonstrated in the spectra shown in Fig. 5.3 (a,b).

Bessere Logik - homogen. Gap ist zu groß, der Klammerterxt verwirrt. For the homogenous system, we studied the discrepancy between measurement of the activation energy and theoretical studies of the correlation gap. Here we extend this analysis by referring to some theoretical work which improved the theoretical results (in the sense that the discrepancy between the measurement and the theory is reduced).

The most direct comparison can be drawn to the work of Zhang et al [137]. They calculate the change of the correlation gap under the influence of a point charge Z for different geometries using the EXD method. For the toroidal symmetry they calculate the gap in the presence of a point charge in a unit cell with 4 electrons. Although only a few points of the $V(Z)$ have been calculated a non linear $E_{corr}(Z)$ can be seen. The change of E_{corr} is approx -20% of the homogenous value.

Girvin et al. [42] give an evaluation of the change of the magneto-roton state with disorder generated by an ionized impurities in the bulk of the system at a comparatively large distance from the 2DES in the frame of the Single Mode approximation.

When comparing our results qualitatively with the experimental studies by Boebinger et al. ([13], Sec. B and C) we find a consistent decrease of the gap with increasing disorder. They find a linear correlation of their qualitative disorder parameter and the activation gap. Other authors [45, 77] found also a decrease of their respective gaps⁷ with increasing impurity strength and a critical magnetic field below which the FQH state will disappear.

Although no quantitative evaluation of our results can be given from the comparison with literature, we find the trend of a shrinking correlation gap with stronger impurities / disorder to be in accordance with the literature as

⁶For convenience we define $\Delta E_{corr}(V_0, \sigma) = E_{corr}(V_0, \sigma) - E_{corr}(0, 0)$ as the difference of the correlation gap size w.r.t. the correlation gap of the homogeneous system. N.B.: Since the correlation gap is reduced in the presence of an impurity, $\Delta E_{corr}(V_0, \sigma) \leq 0$.

⁷regardless of the particular type of gap

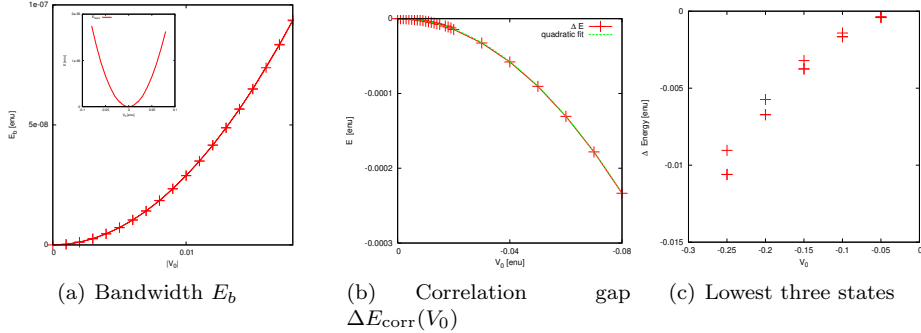


Figure 5.6: Changes of the band width E_b (a) and the correlation energy gap ($\Delta E_{\text{corr}}(V_0)$) fitted with a quadratic function (b) for a system with a gaussian impurity. Varying strength of the impurity V_0 with $\sigma = 1l_0$. **SRI**). (a) shows an inset for a larger range of impurities both for attractive and repulsive impurities. System with 5 electrons and $\nu = \frac{1}{3}$, **SRI** (c) shows the energies of the three lowest lying states (**SRI**). The ground state is twofold degenerate.

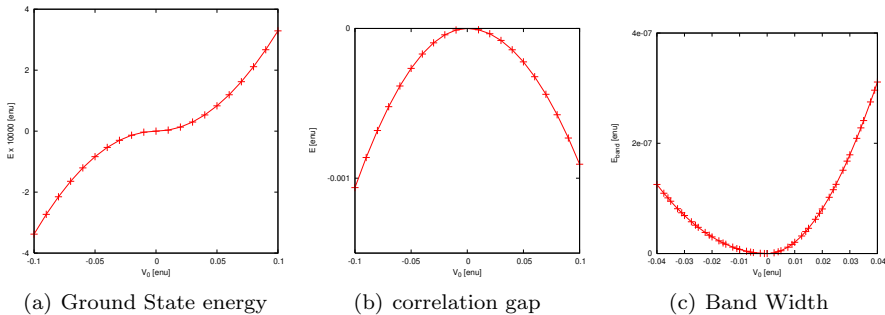


Figure 5.7: Change of the ground state energy (a), Correlation Gap (b) and Bandwidth (c) relative to the homogenous systems values. $N_e = 5$, $N_m = 15$ system with **Coulomb interaction**, $\sigma = 1l_0$

well as with results from perturbation theory.

5.2.1.5 Ground state degeneracy - Bandwidth

Since we find the degeneracy to be eventually completely lifted, it must be the result of coupling between the ground states and the higher excited states. This coupling emerges in second order of perturbartion theory and occurs at energies $|V_0| > 0.6 \text{enu}$. We denote impurities of strengths absolut values larger than 0.6enu as **strong**.

A quantitative analysis of this effect is shown in Fig. 5.6(a) which shows the widening of the bandwidth with increasing impurity strength ⁸. The effect is symmetric in V_0 , i.e. is the same for repulsive and attractive impurities.

⁸The calculations have been performed using the full matrix approach. Calculations with the sparse matrix approach show the same qualitative results but are prone to numerical imprecisions

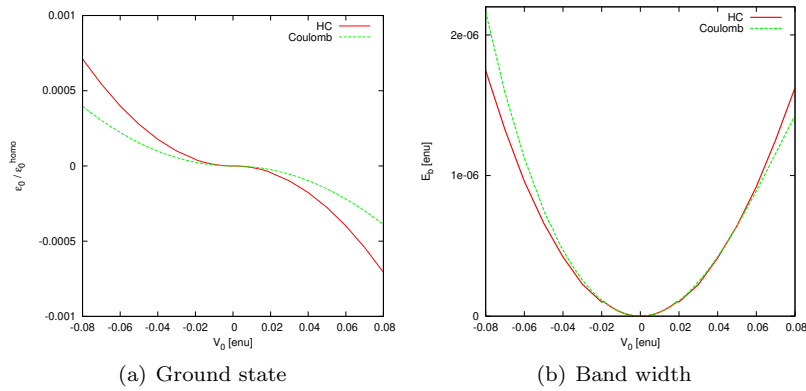


Figure 5.8: Comparison among the two interactions of the relative changes of the ground state energy (a) and of the band width (b).

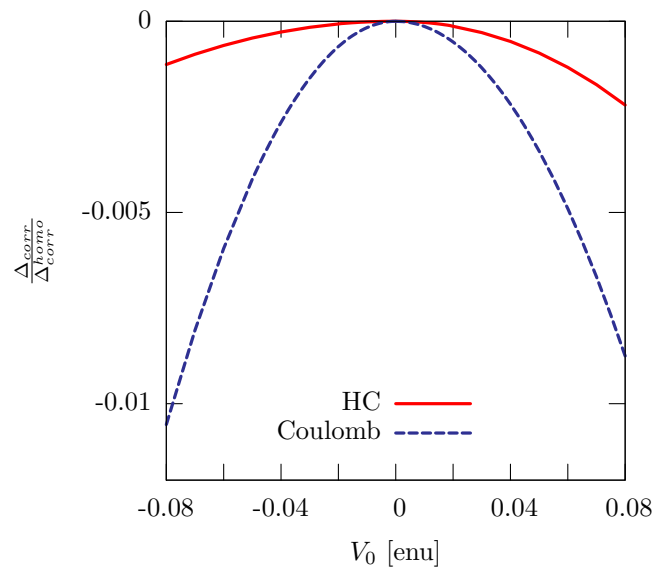


Figure 5.9: Comparison of the relative change of the correlation gap for HC and Coulomb interaction.

We expect a quadratic dependence $E_0 \sim V_0^2$ because of the second order in perturbation calculus, which is responsible for the lifting of the degeneracy. In Fig. 5.11 the asymmetric widening of the ground state “band” is shown - the 2 lowest states are less separated than the upper 2. An example spectrum is given in 5.11(b), where the lifting of the degeneracy is shown. In all cases the (degenerate) ground state is separated by a gap from the higher excited states, a key requirement for the FQH effect to survive.

5.2.1.6 Results from the literature

We come back to the work Sheng et al. [109] and their expectation of the bandwidth to decrease exponentially with system size (??) and to vanish in the thermodynamical limit. To check whether our method shows a similar result for a single impurity (they used a random potential) we embark on the same mission for verification purposes. We calculate E_b for the same weak impurity in unit cells with up to 7 electrons and compare the results. The results are summarized in Fig. 5.10 where the Coulomb (b) and SRI (a) results are given respectively. When comparing our results to those from Sheng, we find a drastically different behaviour. A bandwidth which increases with system size is found instead of a recovered degeneracy. When comparing the absolute values of the bandwidth we find a much smaller bandwidth (about 5 orders of magnitude) than Sheng. Again, E_{band} is about 2 orders in magnitude larger for the Coulombic interaction.

A possible reason for this discrepancy is the different potential used by us and Sheng. Sheng uses a random potential which does not introduce any further (artificial) symmetries into the system, whereas the single impurity preserves (as shown) several rotational symmetries for a finite number of electrons. We shall also keep in mind, that this effect is well in the range of the diagonalization methods numerical error-

However, at this point we can not resolve the apparent contradiction with the work of Sheng et al.. We will come back to this problem later when we tackle random potentials.

When comparing the effect of the different interaction types (Fig. 5.8(b)) we find the effect of the interaction potential on the bandwidth to be small for weak impurities. For both interaction types the bandwidth increases for small values of V_0 . This changes however slightly for $|V_0| > 0.04$. For those values the coulombic systems shows an asymmetric behavior where an attractive impurity has a stronger influence than a repulsive interaction. This can readily be explained considering second order perturbation effects go with the gapsize, which is significantly smaller for the coulomb interaction.

5.2.1.7 Shape of the impurity

So far we have restricted the analysis to impurities with a characteristical width of $1l_0$. The dependency of the correlation gap with varying width and fixed strength is the subject of this section.

In Fig. 5.12 we show the correlation gap calculated for a weak impurity ($V_0 = -0.05enu$) and a range of σ for both interaction types. The analysis of the graph shows the following prominent features

- The correlation gap varies weakly (1 %) with σ

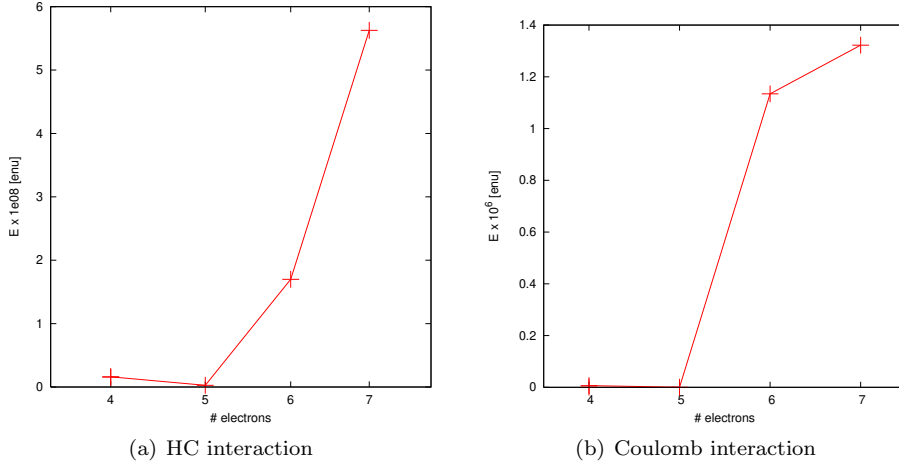


Figure 5.10: E_b calculated for systems with a single impurity of $V_0 = 0.001$, $\sigma = 1l_0$ and different system sizes. SRI (a) and Coulomb interaction (b).

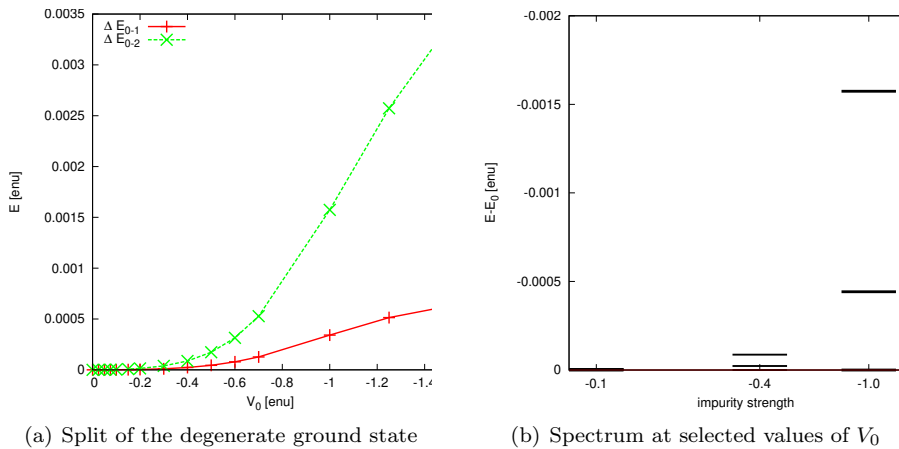


Figure 5.11: (a) Energy differences of the lowest and second and third lowest states respectively. (b) provides an example of the spectrum at selected values for V_0 . The energies relative to the respective lowest state are shown. The energetically lowest state is twofold degenerate for small values of $V_0 \approx 0.1$. All calculations performed for 5-15 state with SRI

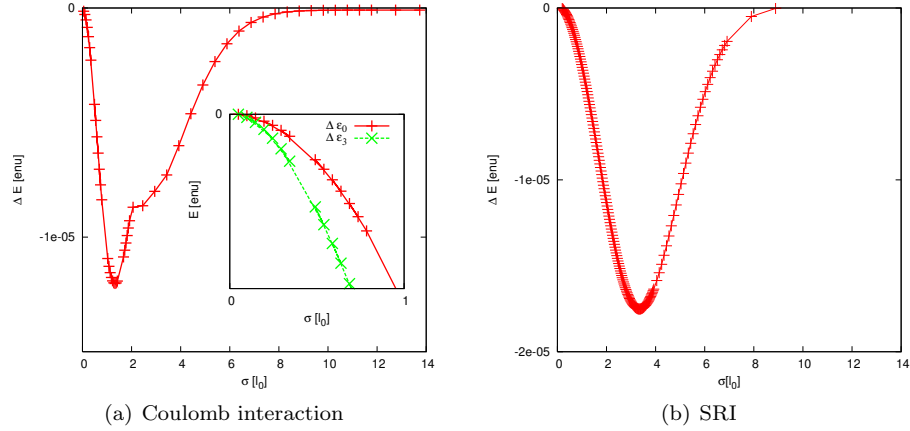


Figure 5.12: $\Delta E_{corr}(\sigma)$ calculated for a system with $V_0 = -0.01$ enu, 5 electrons and 15 flux quanta. (a) coulomb interaction with an inset showing the change of the ground state and the third excited state. (b) same parameters as in (a), SRI

- the overall change of the correlation gap is approx. 1 order of magnitude larger for the SRI system.
- At a characteristical width of $\approx 1.5l_0$ $E(\sigma)$ has a sharp minimum.
- For values larger 3 (SRI) or $1.5 l_0$ the gap opens up again and regains its value from the homogeneous system at widths comparable to the cell size ($\approx 8l_0$ for both interaction types).
- For $\sigma < 0.25l_0$ a different regime for the $E_{corr}(\sigma)$ is found.

Let us analyze those findings on a qualitative level. The fact that the gap regains its homogeneous state value for wide impurities can easily be reconciled with the expectation that very wide impurities have essentially the effect of an additional constant background charge which does not change the physics of our system. Therefore it is also not sensible to analyze the ground state energy as it will be lowered/raised by such an impurity.

Differences start to appear, when comparing coulomb and short-ranged interaction (apart from the overall value of the gap). The different shape of $E(\sigma)$ for values of $2-3 l_0$ deserves further analysis. We show the energy changes of the respective states with respect to the homogeneous-state value and find, that the "kink" in $E_{corr}(\sigma)$ is due to an higher sensitivity of the excited state towards the impurity. Although this behavior might be interesting to study, we will not pursue this here. We will mostly be concerned with the ground state of the system in the further analysis on the one hand, on the other an impurity of an effective width of a half cell is too wide to use as a building block for random potentials as we envision them. However, an analysis will be given in section 5.2.2.

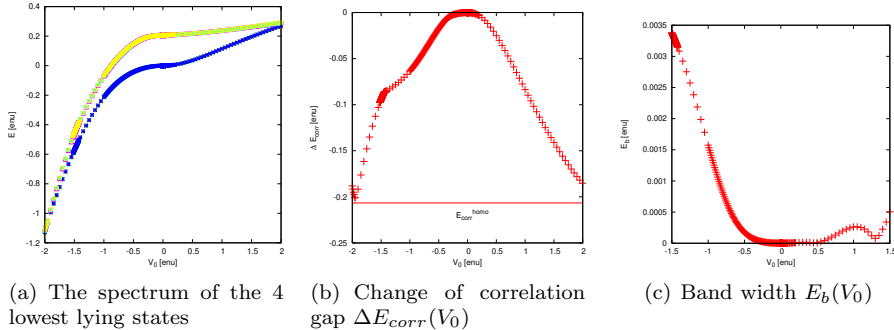


Figure 5.13: Study of a system with $V = -V_0 \exp -\frac{z-z_0}{\sigma}$ where $\sigma = 1l_0$, 5 electrons 15 flux quanta and SRI. In Fig. (b) the value for E_{corr}^{homo} is given to show the closing of the gap.

5.2.2 Strong impurities

Having explored the influence of weak impurities we shall now proceed to the analysis of stronger⁹ impurities and their influence on the spectra and the derived characteristical energies.

5.2.2.1 Ground state energy

Let us begin by extending the analysis of the $\epsilon_0(V_0)$ characteristic. In Figs. 5.13 (a) and Fig. 5.14 (a) we show the evolution of the 4 lowest lying states of the many particle spectrum with increasing impurity strength. For both interaction types the relation $\epsilon_0 \sim V_0$ holds throughout the value space.

Analyzing the overall shape of the $\epsilon_{1,4}(V_0)$ characteristic we find an asymmetric behavior for $|V_0| < 0.8$ and $|V_0| < 0.2$ for the HC and coulomb interaction respectively. This asymmetry is present in the ground state and in the excited states likewise. Outside this regions of V_0 we find $\frac{\partial \epsilon}{\partial V}|_{\epsilon < V_{T,-}} > \frac{\partial \epsilon}{\partial V}|_{\epsilon > V_{T,+}}$. In Fig. 5.15 (a) we show the different characteristics of the ground state energy for $V_0 >< 0$.

Analyse fehlt

Mehr Daten, anfang liegt in rawdata singleimpurity, slave03 rechnet (symmetrischer Plot)

5.2.2.2 Correlation gap and bandwidth

In the same spirit as in previous sections we study the energies bearing the most physical significance in the spectra. We focus first on the case of short-ranged interaction, the correlation gap and the bandwidth.

The E_{corr} is shown in Fig. 5.13(b). We see that for stronger impurities than ± 1.9 enu the correlation gap is completely closed while for ± 1.5 enu it is reduced by a factor 2. The increasing bandwidth E_b does not play an important role in the closing process i.e. the group of the lowest states remain close in energy.

The slope of the $E_{corr}(V_0)$ curve has three different regime which are clearly distinguishable. For weak impurities ($V > 0.5$, Region I) the slope is quadratic

⁹where strong is defined as $|V_0| > E_{gap}$

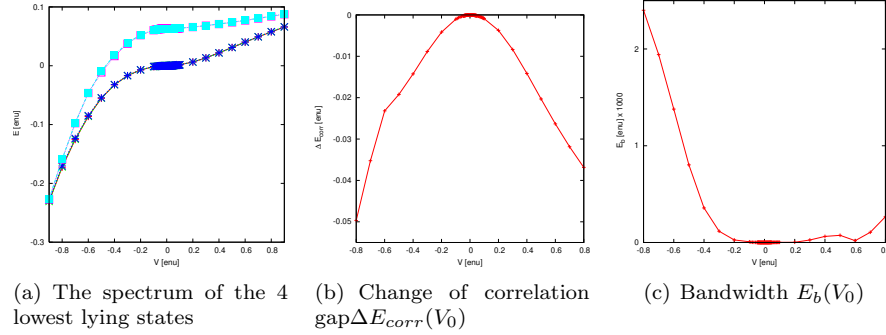


Figure 5.14: Spectrum of the 4 lowest lying states (a), correlation gap (b) and bandwidth E_b of a system with *coulomb interaction*. All other parameters as in Fig.5.13

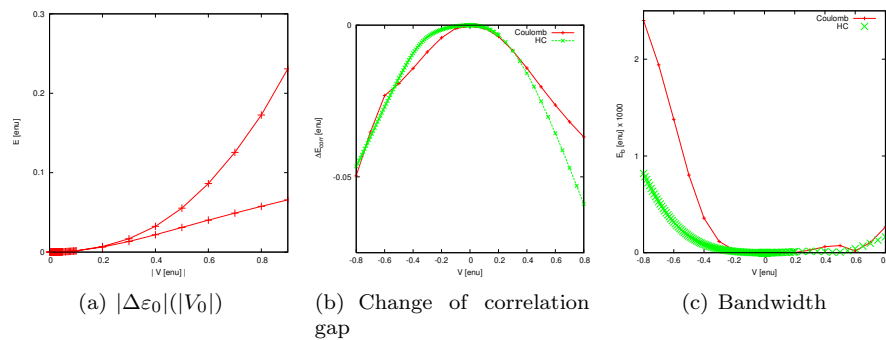


Figure 5.15: Figure (a) shows the asymmetry of the ground state energy to the impurity strength for a coloumbic system. Fig (b) and (c) show a comparison of bandwidth change and correlation gap change between coulombic system (cf. Fig. 5.14) and short range interaction (cf. Fig. 5.13).

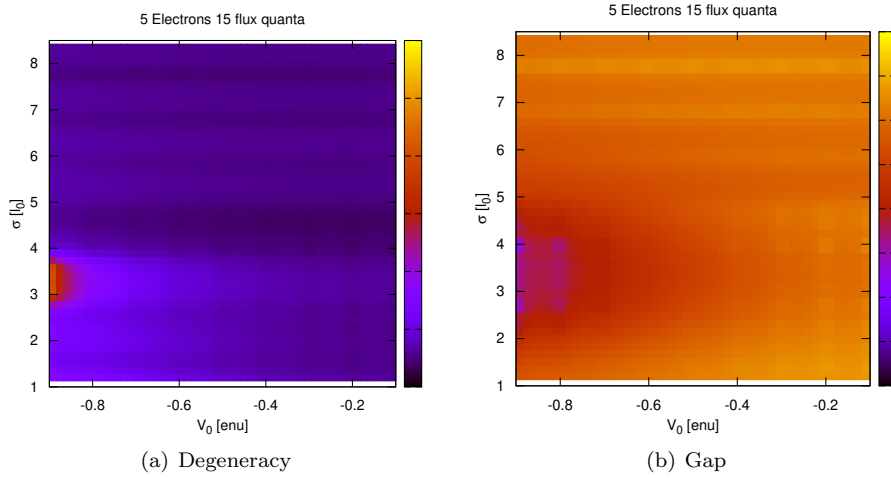


Figure 5.16: (a) Energy gap between lowest state and highest state of the semi degenerate states and (b) Energy gap between lowest state and fourth state for a system with 5 electrons and for a system with 5 electrons and $\nu = \frac{1}{3}$, SRI, and varying repulsive Gaussian impurities

where for V_0 - Region II - values the slope is linear. At $V_0 \approx -1.5$ - Region III - an inflection point is found and the gap closes rapidly.

In the case of coulomb interaction we see a qualitatively different behavior. The gap between the Landau levels is closed at far weaker impurities (appr. 0.8 enu, cf. Fig.5.14(a, b)). This leads us to the first conclusion for the breakdown of the FQH regime: For energies larger than 0.8 enu the FQH state ceases to exist, as one of its key features is not present anymore.

The characteristic of the band width is shown in Fig. 5.13(c) and Fig.5.14 (c) respectively. The overall shape is similair and strikingly different from the correlation gap symmetry. E_b increases much stronger for repulsive impurities ($V_0 < 0$) than for attractive impurities with the final value being approx 2 times smaller for repulsive impurities. Another representation of this fact is given in Fig. 5.15 (a) where the absolute value of the ground state energy is given. The resulting bandwidth is

When studying the slope of the curve, again 3 different regimes are prominent. Analysis of this plot shows different regimes with respect to the impurity strength. For impurities stronger than 0.5 enu we find a larger

We shall conclude this section with a discussion of the influence which the interaction type has on the energies. In Fig. 5.16 (b) and (c) we show a comparison of the energy changes for the 2 interaction types studied here. The entity ΔE_{gap} shows an asymmetry for $|V_0| > 0.2$ enu for both interaction types. The change of the correlation gap itself is approximately the same for both interaction types - keep in mind that the gap close for the coulomb interaction at appr. ± 0.8 enu. This explains also the larger value of ΔE_{gap} st $V_0 > 0.5$ enu the correlation gap is simply larger for the case of SRI.

Concluding we remark that the minimum requirement of the FQH effect - the correlation gap - vanishes in systems with impurity strengths above 2 enu and 0.8 enu in the case of short range interaction and coulomb interaction

respectively. In such systems we do not expect to find an incompressible liquid anymore, the fractional quantum Hall state has been destroyed, thus we will confine further analysis to values below this threshold.

The regime of nonlinear response extends to values of appr. 0.4 enu for short range interaction and 0.1 enu for coulomb interaction. In this region the gap is still very much open (within a few percent of the homogeneous value) and thus we have hope that we might find an FQH state in this range.

5.2.3 Shape of the impurity

In this section the impact of the spatial extension of the scattering potential is analyzed, comparable to the analysis in section 5.2.1. To further motivate the need for such a study consider that the extension of an electron with 3 attached flux quanta is of the order of $\frac{1}{\nu}l_0$ and the size of the density depletion is of the order of $1l_0$. A potential which is constant on this length scale will most likely have a different effect than a potential which varies considerably.

When analyzing the effect of different impurity sizes we use 2 different strengths (V_0) which represent the two cases of "weak" and "strong" as used in the previous sections. For the "strong" impurity we shall use values for which the correlation gap is preserved for $\sigma = 1l_0$. We compare the ground state energy, the correlation gap and the bandwidth with changing widths of the impurity.

5.2.3.1 The correlation gap

Let us start with the analysis of the change of the gap size (see Figs. 5.17 (a,b)). For both interaction types the gap size is reduced for stronger impurities. When turning to the 0.5 enu impurity in Fig. 5.25(c), we find roughly 3 different regimes. For $\sigma < 0.8l_0$ we see a linear behavior. At $\sigma = 1.14l_0$ a deflection point is found where we see a local minimum. Can this be attributed to the magnetoroton minimum at $1.4l_0$? The third regime is again a linear one starting at $1.2l_0$ with a saturation. The saturation can be explained with the following argument: When the impurity becomes wider or comparable to the unit cell size the neighboring cells start to contribute substantially, in the limit it generates a constant potential background which in turn should not change the FQH state at all, therefore the gap should return to the homogeneous system value. This expectation is validated with the analysis of E_0/σ shown in Fig.5.18(a) where the effect of very wide impurities (more than $5l_0$) is just an additive constant to the ground state energy. The correlation gap is shown in Fig. 5.18 and Fig.5.18 where the correlation gap shows a minimum at approx $4l_0$ and returns to the homogenous value for $\sigma = 20l_0$.

5.2.3.2 The bandwidth

The bandwidth has been studied for the sake of completeness. Again curves for both interaction types were calculated and are shown in Fig.5.17(c) and Fig. 5.18 (a). We reproduce again the results from the analysis of the correlation gap, where we found that the gap recovers its homogenous system value for very wide impurities. **Referenz Stimmt nicht!!**

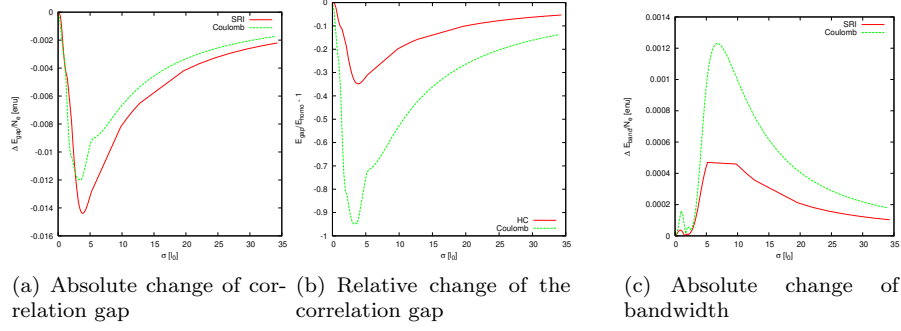


Figure 5.17: Comparison of the Coulomb interaction and Short range interaction when varying the width of the impurity σ . (a) Relative Change of the correlation gap to the homogeneous ground state (b) Relative Change of the band width relative to the homogeneous ground state band width

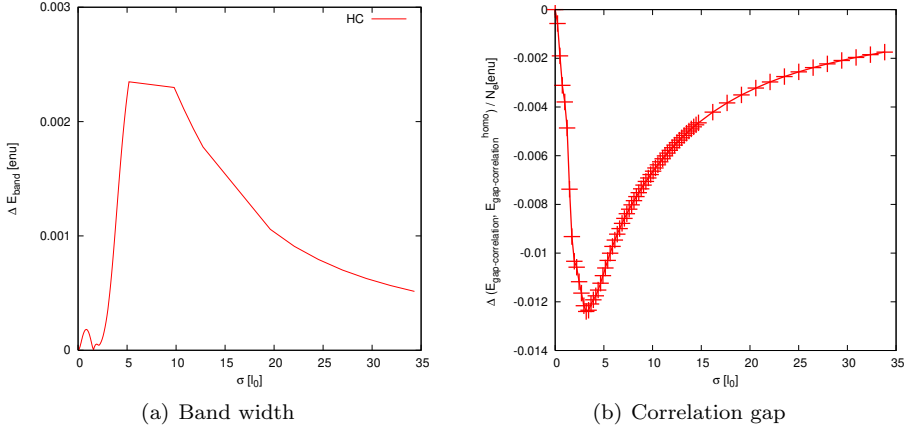


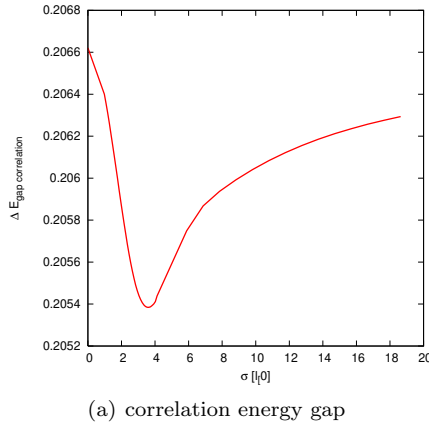
Figure 5.18: Energy changes with σ , 5/15 system , $V_0 = 0.5\text{e}\nu$, coulomb interaction. The gap size is calculated relatively to the gap of the homogeneous system. The cell size is appr. $10 \times 10l_0$.

5.2.3.3 The influence of electron-electron interaction

When comparing the relative change in the gap energy (i.e. $E_{\text{gap}}^{\text{homo}} - E_{\text{gap}}(\sigma, V_0)$) for the two interaction types (Fig. 5.17 (a, b)) we find another puzzling property at the same σ value where the minimum was found in the gap plot. The change of the gap (i.e. the deviation from the Laughlin ground state) is nearly the same for coulomb and SRI. This is contrary to previous findings where we always found the hard core interacting system to be more Laughlin-like than the coulomb state . Clearly the value range around $\sigma = 1l_0$ deserves further investigations.

5.2.3.4 Linear Response in the FQH?

For a system with a gapped ground state (i.e. a finite amount of energy is needed to excite the system) no linear response behavior is expected. In particular, a weak impurity should not change the ground state of the system linearly



(a) correlation energy gap

Figure 5.19: Energy changes with σ , 5/15 system , $V_0 = 0.5 \text{enu}$, *short range interaction*. The gap size is calculated relatively to the gap of the homogeneous system. The cell size is appr. $10 \times 10 l_0$.

($E_0 \propto V^n$ where n is not 1). This has indeed been found in all calculations presented so far. For each entity the deviation from the homogeneous state value is non linear.

5.3 Electronic Density

In the previous section (3.3, p. 56 ff), we studied the electronic density of the homogeneous state. We established the homogenous density of the ground state and the effects of the systems geometry (and size) which result in small density fluctuations, the *finite size wiggles*. In the following part we study the influence attractive and repulsive impurities exert onto the electronic density. Again we will study the effect of the 2 tuning parameters σ and V_0 independently and compare the 2 electron-electron interaction types.

5.3.1 Expectations based on literature: Response to an impurity

Let us first recall some results from earlier work which have studied the impact of impurities - modelled by their electrostatic potential $\phi(\mathbf{r})$ on the 2D electron gas, the 2D electron gas in a magnetic field and the 2D electron liquid.

5.3.1.1 The response of the 2DEG in the absence of a magnetic field

It is well established, that in the presence of mobile charge carriers, a scattering potential $\phi(r)$ is screened by electrons rearranging in such a way, that the potential felt by the electrons beyond a distance ξ_{SC} approaches zero. This fact is well known as screening and has been studied by a lot of authors ([12, 113, 114]). It is found that the relation between the electronic density induced by the charge (ρ^{ind}) and the potential can be written as $\rho^{ind}(\mathbf{q}) = \xi(\mathbf{q})\phi(\mathbf{q})$. The calculation of the screening function ξ needs - as long as no full quantum mechanical

approach is used - modelling and hence further approximations. Two popular choices of further approximations are the Thomas-Fermi approach and the Lindhard screening.

When applying those two approximations to a 2 DEG, Stern *et.al.* [113, 114] found the static response function to be of the shape

$$\xi(r) \propto 2\pi n(r) J_0(k_f r) N_0(k_f) , \quad (5.2)$$

where $J_{0,1}$ is the Bessel function. [103]

Another, purely quantum mechanical, effect are the Friedel oscillations [56]. These density - oscillations persist on larger length scales then the semi-classical screening length and are of the form $\Delta n(r) \propto \frac{\cos(k_f r)}{r^2}$.

5.3.1.2 The response of the 2DEG in the presence of a magnetic field- Previous results and derived expectations

When discussing the properties of the FQH Groundstate, we found that the Laughlin Groundstate (2.56) makes the electrons avoid each other "more effectively" than the mere Pauli principle requires. Having that said, we expect different electron-electron correlations and perhaps different electronic densities compared with the simple electron gas on one hand and the Laughlin ground state¹⁰ when subjecting our system to impurity potentials.

The electronic density of $\frac{1}{3}$ FQH systems has been studied before by e.g. Rezayi et al. [96] and Zhang et al [137]. Both authors studied the impact of the impurity by EXD - methods (Rezayi used the spherical geometry, while Zhang studied both symmetries). Both authors agree, that the density changes in the presence of an impurity (δ shaped in [96]), extra charge is accumulated at the site of the (attractive) impurity and the induced charge oscillates on a length scale of $1.45l_0$. Since the oscillations are independent of the systems size (except for finite size effects at the edges), the authors conclude, that "*the occurrence of a local charge density wave around the impurity is a general feature of the (FQH) system*" [137] ¹¹.

Rezayi [96] coined the term of no net-screening to describe this effect which is different from both, the free 3D electron gas (where the density oscillations vanish at some distance from the impurity) as well as from the 2DEG without a magnetic field. They performed numerical studies of the influence of delta-shaped impurities on the electronic density. They conclude, that the amplitude of the impurities over a certain threshold is constant, hence claiming that the effect of strong delta impurities with finite impurities is essentially the same as that of indefinite delta impurities.

Efros et al.[24] applied the Thomas Fermi approach to a system with a random impurity distribution, subjected to strong magnetic fields. The authors demonstrated, that the density response differ qualitatively for filling factors commensurate with the Quantum Hall states and for magnetic fields resulting in other filling factors. For the latter case, they calculated screening lengths and found the Thomas-Fermi approach to be meaningfull. At e.g. $\nu = \frac{1}{3}$ however, the Thomas-Fermi approach is not applicable, the authors predicted

¹⁰In Sec. we found that the ground state of homogeneous system with short range interaction is a very good finite-size approximation to the LGS.

¹¹Note that those oscillations would vanish at large distances for the free-electron gas

a coexistence of compressible areas (with $\nu \neq \frac{1}{3}$ locally) and incompressible regions (with a local filling factor of $\frac{1}{3}$) of a characteristic size of $R \propto \sqrt{\frac{\Delta E_{\text{gap}}}{W}}$, where W is a measure for the strength of the random impurity. From this approximation Efros predicted a path to the estimation of a maximal value of W , however this path has not been followed up to the knowledge of the author.

5.3.2 The density response of the 2 DEG in the presence of a magnetic field - Results

In this subsection, we present the numerical results obtained from the EXD-wavefunctions. The impact of the various geometrical shapes of the impurity is analyzed and the differences among the 2 interaction types are discussed. The incompressibility of the ground state is demonstrated by analyzing the density response.

5.3.2.1 Principal shape of the density response

To begin with, we show in Figs.5.20 (a) and (b) the response of the electronic density to a weak attractive impurity located at the unit-cells center. Note that the change of the density with respect to the ground state density is shown. The potentials characteristic width is $1l_0 \approx 0.1[\text{c.u.}]$. The density shows a symmetrically shaped maximum at the potentials maximum, surrounded by ring shaped depletion at a distance of 0.25 unit cells ($\approx 2l_0$). Beyond this depletion zone, the density approaches a constant value¹².

The principal shape of $n(r)$ is the same for all (attractive) potentials studied in this section with deviations for very wide impurity potentials. The shape of $n(r)$ is moreless constant - regardless of the prevailing electron-electron interaction. In Fig. 5.21 we show a comparison of the 2 interactions for the same shape of an impurity. In both cases, the density response is fitted to a Bessel-function $n(z_0)J_0(bx + c) + d$. The obtained width parameters b of the functions are constant among the 2 fits ($b = 12.9878 \frac{1}{l_0}$ (SRI) and $b = 12.9223 \frac{1}{l_0}$ (Coulomb)). When comparing the maximal amplitude of the density response ($n(z_0)$)¹³ it becomes obvious, that the Coulomb system is more susceptible to the impurity (the maximum value is approx. 2 times larger than for the SRI state¹⁴). A direct comparison of the density response is shown in Fig. 5.23.

In contrast to the results of Zhang [137], we do not find clear evidence for density oscillations. The fitted Bessel-type shape of the density function has an wavelength of appr. $\frac{1}{2}$ cell size - making conclusive statements on the persistence of those oscillations at larger distances impossible. The predicted size of the oscillations (with a characteristic size of $1.45 l_0$) can not be reproduced due to the limitations of the geometry, although the first period of the Bessel function is comparable in size with the results of Zhang.

¹²In Fig. 5.20 (a) a ring shaped structure of finite size wiggles is visible. These wiggles are residuals of the finite size wiggles and are of no interest.

¹³The value $n(z_0)$ will be referred to as n_{\max} , the maximal value of the density.

¹⁴One reason for this could be the factor 3 among the 2 different values of the lowest pseudopotentials (see sec. 2.4.4.3)

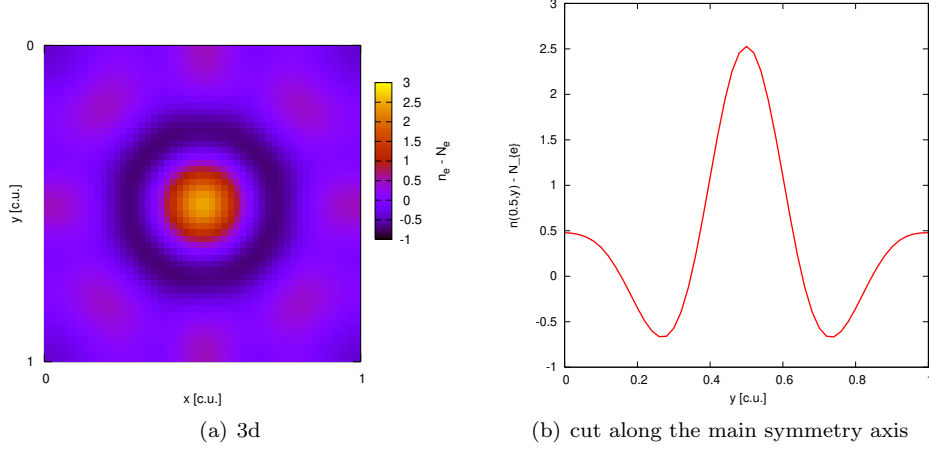


Figure 5.20: Electronic density of a system with $V_0 = -0.3$, $\sigma = 1l_0$, $N_e = 6$, $N_m = 18$ state with coulomb interaction. (a) map of the unit cell, (b) cut along the main symmetry axis

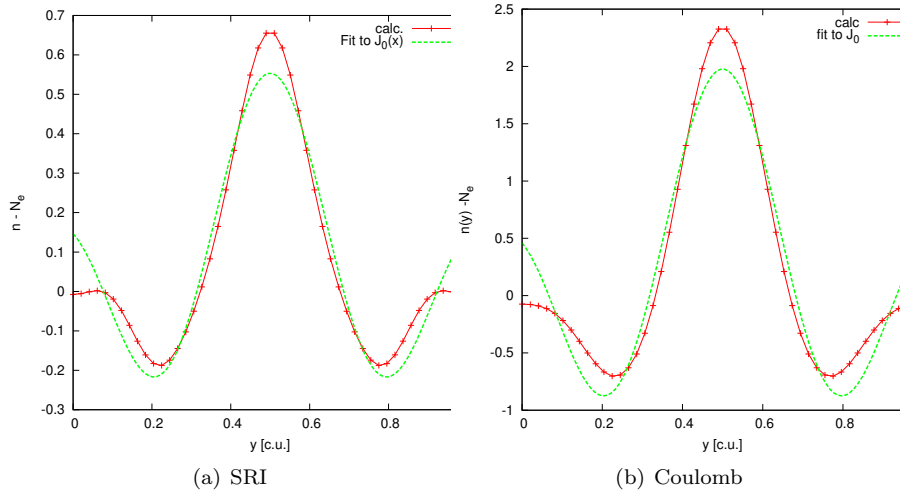


Figure 5.21: Density response for an impurity ($V_0 = -0.3$, $\sigma = 1l_0$) shown for the 2 interaction types. In both plots a fit to a Bessel function $n(y) = aJ_0(by+c)+d$ is provided.

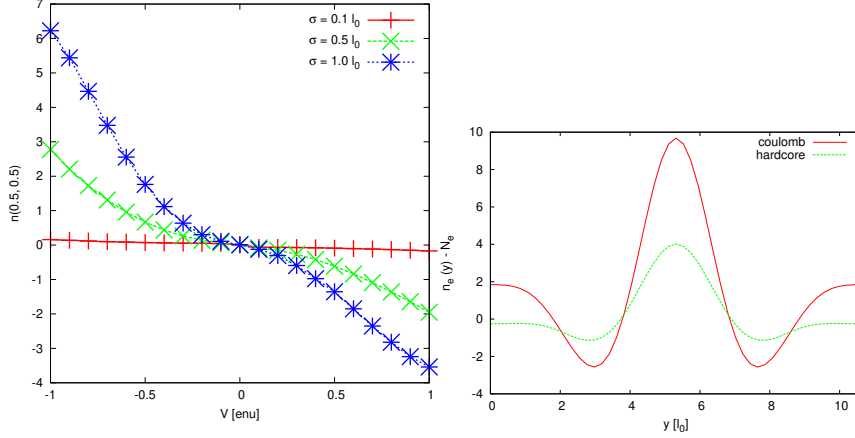


Figure 5.22: Density response for a Figure 5.23: Comparison of the $N_e = 5, N_m = 15$ state with SRI disturbed by an impurity with variable SRI width σ and strength. $\sigma = 1 l_0, V_0 = -0.7 tenu$

5.3.2.2 $n_{max}(V_0)$ - The effect of the impurities amplitude

In the next step, we vary the strength of the impurity and record $n_{max}(V_0)^{15}$ for 3 choices of σ (Fig. 5.22). Examination of the results show the expected charge accumulation at attractive impurities and charge depletion caused by repulsive ones. The effect is quadratic in V_0 for larger values of V_0 and σ . However, the effect is not symmetric for $|V_0| > 0.5$, which is easily explained by the finite size (and the finite number of electrons) in our system.

What is striking here is, that the width of the Bessel shaped density response - or the area of charge accumulation around the impurity - is nearly constant for a fairly wide range of potentials. This is also found in the literature ([96, 124]).

Both findings have been explained by Girvin et al [104, 42], the validity of the single mode approximation - developed in [104] - and shown in (2.4.6.4) - (assuming that the excitation of the ground state can be modelled by a single density wave is verified here numerically.

5.3.2.3 $n_{max}(\sigma)$ - Response in k-space...

It could be seen from the SMA that the density response depends not only on the strength of the potential but also on its shape. In particular we expect the density response to be more or less constant for all values below some critical value σ . Intuitively we can equate this critical length with the diameter of an electron with 3 flux quanta attached (if assumed to be circular) of $3 l_0$.

In Fig. 5.25(a) we show the density response of the system to a weak impurity with varying width (σ). The maximum change of the density is appr. 5% of the homogenous systems value and occurs at $\sigma \approx 1.45 l_0$. Above this value, the density returns more less to its homogeneous value. The same picture presents itself for weaker impurities (Figs. 5.25 (c) and (d)), only the actual value of the maximal density differs (as we have seen already in sec. 5.3.2.2, p. 103).

¹⁵or n_{min} in case of a repulsive impurity

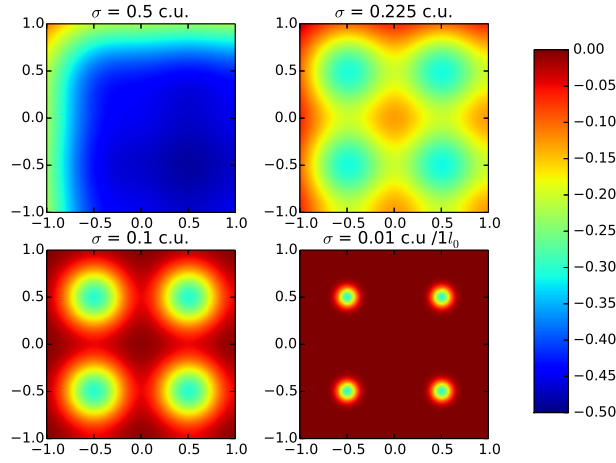


Figure 5.24: Shown is an enlarged detail of the potential created by superposition of four gaussian potentials ($V_0 = -0.3$) in four neighbouring cells of the PBC grid. The length scales are given in cell units, for $N_e = 5, N_m = 15$ is $0.1 \text{ c.u.} \approx 1l_0$. The four different values of σ are displayed over each pane.

When comparing the actual shapes of the density profiles (Figs. 5.25 (b) and (d)) a somewhat different behavior appears. In the case of the weak impurity, a different structure presents itself for larger values of σ . A density suppression at the center of the cell is present, surrounded by 2 symmetrically located maxima at a distance of apr. $0.7 l_0$. The density suppressions value is in the range of the finite size wiggles, the geometry of the substructure is not.

The steep decline at $\sigma \approx 1.5l_0$ can be understood when comparing with Fig. 5.25(b). It appears that a wide impurity (of diameter $> 3l_0$) captures a second electron in the center of the cell. The corresponding many-particle spectra shows no peculiarity, the gap is still present and the bandwidth is small

(*Ist das ein Elektron auf einer cyclotron bahn?*

Spektren nochmal angucken - insbesondere die Fig. 5.17 bei kleinen σ

5.3.2.4 Incompressibility revisited

We apply now the theory developed in sec. 2.4.3, p. 25 to our numerical results. In that section it was demonstrated, that the incompressibility ($\kappa = 0$) is a result of the second derivative $\frac{d^2 E_0}{dn^2}$ being infinite around the energy of the homogeneous ground state. At the same time, the chemical potential must have a finite value, i.e. $\frac{d\mu}{dE} = \frac{dE}{dn}$ must be finite. When studying the density response of a FQH system it is reasonable to ask whether the incompressibility of the FQH ground state can be seen in weakly disturbed system's densities of finite systems too. To this end, we show in Fig. 5.26(a) the $\Delta n(E_0)$ behavior of a system with 5 electrons. The density was taken at the position of the potentials maximum (z_0) and the difference to the homogeneous values are shown. Thus we try to reduce possible masking effects of the finite size wiggles discussed above.

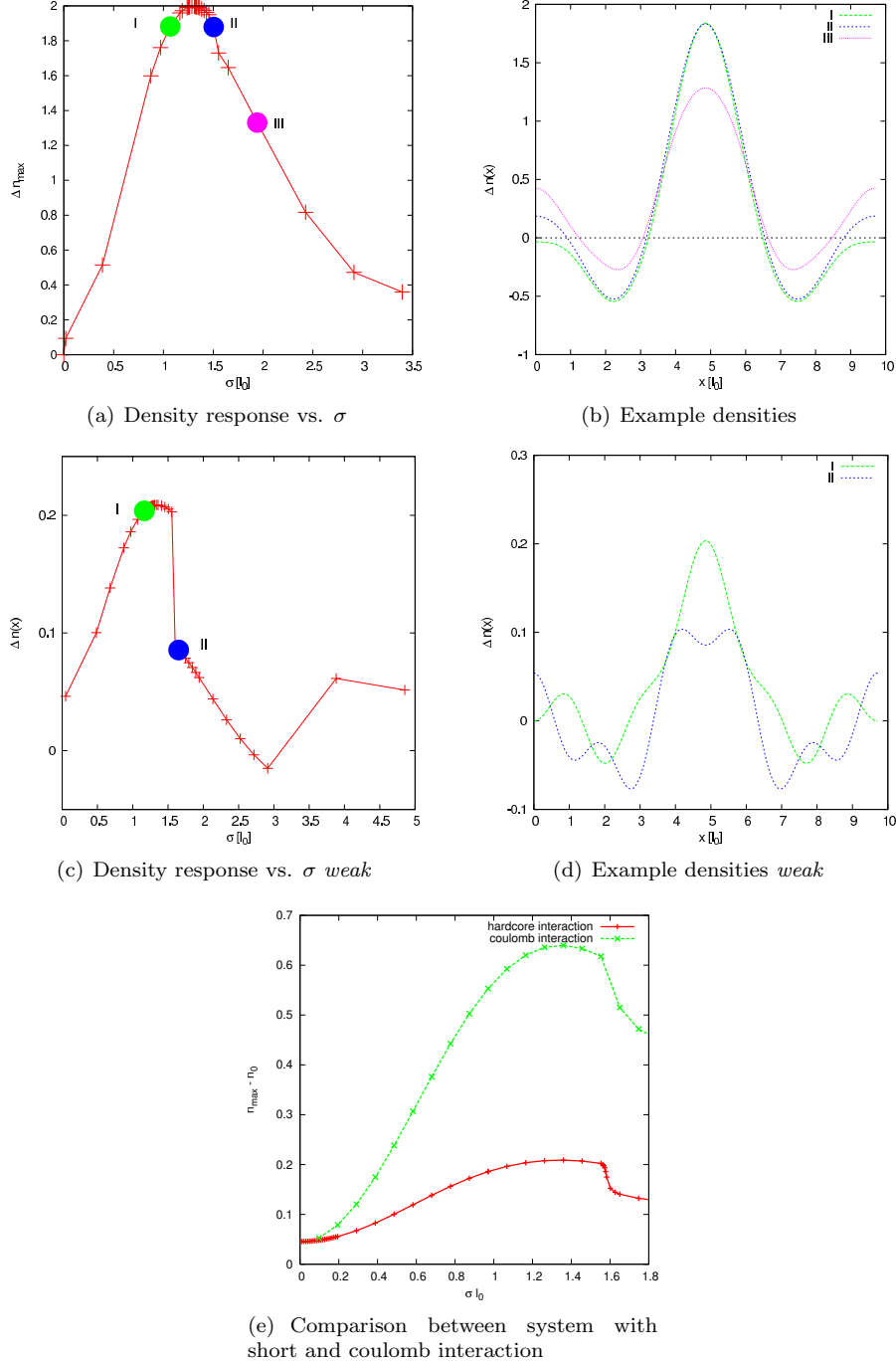


Figure 5.25: Density response of a 5/15 system - SRI. The impurity strength is -0.5 enu (a) maximal density response. (b) Cuts along the y-axis for 3 choices of σ as depicted in (a). In Figs. (c) and (d) the same setup is shown for *weaker* ($V_0 = 0.15$ enu) impurities. (e) Comparison between systems with hard core and coulomb interaction

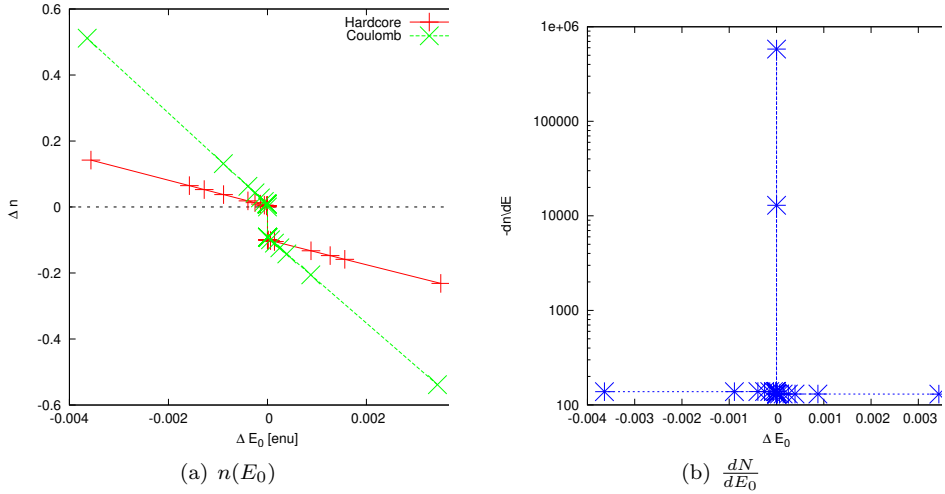


Figure 5.26: Left: $\Delta n(E_0)$ calculated for a 5-15 system subject to weak impurities (attractive and repulsive). Both interaction types are shown. The density was taken at the position of the maximum of the impurity (r_0). The energies and densities are shown relative to the values for a homogeneous system. (Right): The numerical evaluation of $-\frac{dN}{dE}$ for the coulomb interaction on a logarithmic scale.

The calculations were performed for both, the SRI and coulomb interaction. The $n(E_0)$ results show the expected cusp at energy values near zero - corresponding to the homogeneous FQH value.

Apart from the cusp at $\Delta E_0 = 0$, the first derivative exists (Fig. 5.26(b)) (being nearly constant for $\Delta E_0 \neq 0$).

The effect is present for both interactions. Further comparison of the interactions shows, that the slope of $n(E)$ is steeper for the coulomb interaction, while the discontinuity at the homogeneous value is of the same size. When fitting a linear function to the $n(E)$ distributions, we obtain values of -38 ± 2 (SRI) and -138 ± 4 (coulomb interaction). A classical interpretation of the relation of the 2 values implies, that the change of the interaction from SRI to Coulomb makes the system more compressible, changing the electronic density costs less energy. This can also be seen in Fig. 5.25(c) , where the same impurity changes the density more drastically in the case of Coulomb interaction. The maximal density change for the coulomb interaction is about 3.5 times higher¹⁶ than for the SRI case - corresponding to the values for $\frac{1}{\kappa}$ extracted from the linear interpolation performed in this section.

5.3.2.5 The effect of long-range interaction / Coulomb interaction

The Laughlin state is exact for hard core interaction systems only. The study of the more realistic coulomb system (see Figs 5.21, 5.23,) shows the following differences between the two interactions examined:

¹⁶This factor is in the same order of magnitude as the factor between the $L = 0$ components of the pseudopotentials.

- No significant differences in the shape of the density profile (see Fig. 5.23) have been found.
- The change of the interaction potential leads to significant changes in the absolute density values at the impurities maximum.

The stronger influence of the impurity in the case of the coulomb interaction can be readily understood by invoking the argument of the long-range character of the coulomb interaction. On the other hand is the LGS exact only for systems with SRI, thus we expect (and find) the density response in the case of Coulomb interaction to be significantly different for weak impurities.

To summarize the observations made in this section, we find that the densities from our finite size studies resemble well the expected forms from analytical studies ([112]). The correlation functions show a deeper hole around zero electron distance (compared with the simple electron gas).

5.3.3 Electron-electron correlations

As we did for the homogeneous systems in sec 3.4 (p. 60) we shall analyze the pair correlation function ($g(r)$) for inhomogeneous systems. For homogenous systems we found the correlation function to be liquid-like with a pronounced maximum at $\approx 4.5l_0$ and an r^6 characteristic in the vicinity of the sample electron.

In Fig. 5.27 we show the electron-electron correlations for two choices of V_0 , corresponding to a strong attractive and repulsive impurity respectively. For comparison $g(x, x)$ of the respective homogeneous system is provided. When comparing the coulombic and SRI plots (Fig. 5.27(a), (b)) we observe clearly a stronger deviation from the homogen system for Coulomb interaction. To better quantify the change of $g(r)(V_0)$ we calculate the average pointwise difference between the correlations obtained from the homogeneous and the disturbed system respectively¹⁷,

$$\Delta g(r)(V_0) = \overline{g(r)(V_0) - g(r)(0)} \quad . \quad (5.3)$$

The results are shown in Fig. 5.28. For the hardcore interaction (a) we find a roughly symmetric dependence on the impurities strength V_0 . A small asymmetry is found for stronger impurities, where the response of attractive impurities is slightly smaller than for the repulsive impurity. This symmetry is not found for the coulomb interaction (b). Instead a clear asymmetry is apparent, the attractive impurity changing the correlation much stronger (visible also in Fig. 5.27 (b)). It seems, that the longe range repulsive interaction is suppressed by the effect of the attractive impurity. The position of the maximum of $g(r)$, interpreted as the average interparticle distance, remains constant over the range of V_0 tested here. However, this method of comparison is rather crude and we refrain from drawing too strong conclusions at this point.

Another way to quantify the change of the correlations is shown in Fig. 5.30 (a). We recall, that the electron-electron correlations for small r are quadratic (for coulomb systems) and $\sim r^6$ for short range interaction. The Figure shows

¹⁷we average over approx. 100 values of $g(x)$, each data point in Fig. 5.28 describes the deviation of ther particular states electron electron correlation from the homogeneous state.

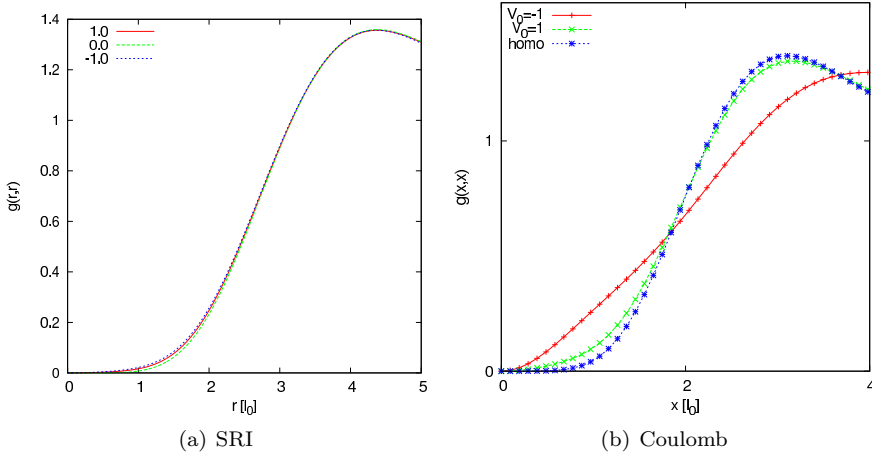


Figure 5.27: Electron-electron correlations ($g(x,x)$) for 2 choices of V_0 . The characteristic of the respective homogeneous state is provided for comparison. ($5/15$, $\sigma = 1l_0$)

electron electron correlations for weak ($V_0 = -0.15$) as well as the second derivative $\frac{d^2g(x)}{dx^2}$ of attractive impurities for both interaction types. The correlation of the Coulomb interaction shows a quadratic dependence for $r < 0.3l_0$ while the extension of the quadratic regime in the SRI-correlation is only vanishingly small (for $|V_0| < 0.15$ no quadratic behavior is found up to numerical errors). The extension of the quadratic regime in the correlations has been extracted and is shown in Fig. 5.30 (b) for systems with coulomb interaction. It is striking, that the correlations change abruptly at $V_0 \approx |0.3|$. This discontinuity is not found in any other of the tested properties.

Another complementary evaluation is shown in Fig. 5.29. We fit the electron-electron correlation onto a polynomial in the vicinity of $x = 0$ and extract the quadratic and $\sim r^6$ coefficients. The change of these coefficients with regard to the homogenous state are plotted vs. V_0 . For both interactions the quadratic component changes more drastically than the 6-th power component. When comparing the two interactions, we find the change to be an order of magnitude larger for the coulomb case when comparing with the SRI case. For $|V_0| < 0.3$ the changes are essentially zero for both interactions, as found already in the former analysis.

More details concerning this particular method are given in the Appendix E (p. 174).

5.4 Discrete charging of a single impurity potential

Since the model allows us to tune the strength and shape of the impurity potential at will, it is possible to generate deep and wide density holes in our system and study the behavior of such a quantum well as a spin-off result of the work performed so far. Experimental work on such systems has been done by many

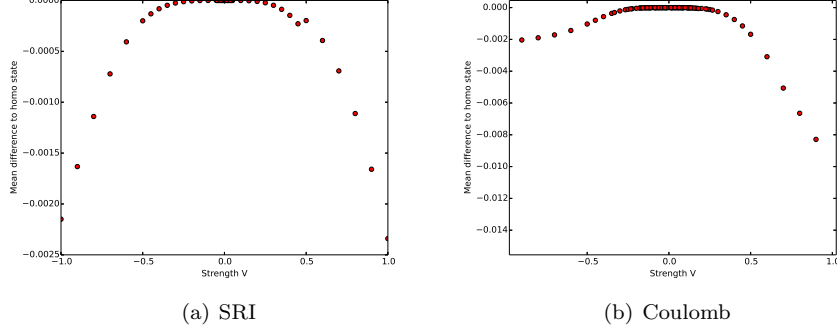


Figure 5.28: Shown is the mean difference of the electron-electron correlations of the disturbed states ($\sigma = 1l_0$), $g(x, x)$ and the electron-electron correlation of the homogenous ground state $g_{\text{homo}}(x, x)$. Left pane shows short range interaction, right pane the coulomb interaction.

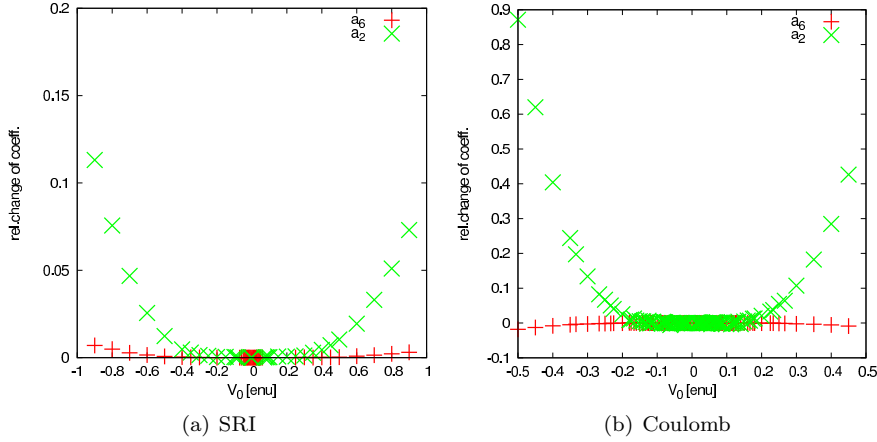


Figure 5.29: The figure shows the relative change of the electron-electron correlations quadratic and $\sim r^6$ component as obtained from fitting $g(x)$ to a polynomial $f(x) = \sum_{i=0}^8 a_i x^i$. More details in the text.

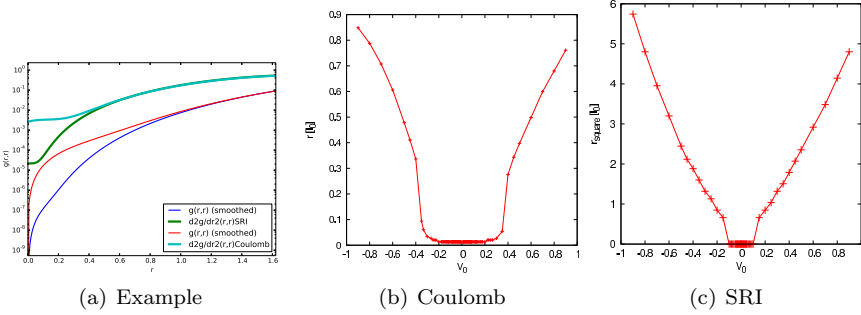


Figure 5.30: The figure shows the electron-electron correlation ($g(x,x)$) and the second derivative $\frac{d^2g}{dx^2}$ calculated from the ground state of a 5-15 system with $V_0 = -0.15$ for both interactions. The blue line shows $g(x,x)$ of the SRI interaction, green the coulomb interaction. (b) Shows the expanse of the $\sim r^2$ regime in electron-electron correlations (see text), Coulomb interaction, (c) shows the results for Short range interaction. The results depicted in (c) are less precise for small values of x due to the employed method.

groups (see e.g. work by Heitmann et al. [107]). The electronic structure of the electrons trapped in such a Quantum Well (QW) or Quantum Dot (QD) resembles that of an atom, hence the term “artificial atom” has been coined for such an arrangement.

We study here a 5-15 system with an attractive single Gaussian impurity at the center of the unit cell. The electrons interact via short ranged interaction. When tuning the strength of the impurity over a wider range than in (5.3) we find the following.

1. The electronic charge is accumulated at the position of the impurity with a surrounding depletion area (see Figs. 5.31(a, b)).
2. For an impurity strength of approx. 1.9 enu the density response shows a deviation from the linear regime.

The electronic charge in the area where the density exceeds the homogeneous equilibrium value is evaluated. The diameter of this charge accumulation is of the order of a 3 magnetic lengths (????).

For a wider range of impurity strengths the density response stays more less constant. However at an impurity strength of approx. -1.8 enu an abrupt change is observed, where the charge in the accumulation area increases by 1. We see a single electron entering the quantum dot. A similar effect is found for the coulomb interaction at an impurity strength of appr. 0.9 enu (see Fig. 5.32

How can this abrupt, quantized charging be explained? From the discussion of the ground state properties (namely the “size” of a flux quantum) we saw that the size in a 1/3 state is appr. $3 l_0$. Inside this region only a single electron is allowed. The ground state can therefore not be a FQH state anymore. Instead we see 2 electrons in the region of the impurity (we call it a Quantum well) well disconnected from the rest of the system. This makes it possible to use the same model as above (2 electrons in the lowest Landau Level). We learned there that the Haldane pseudo potential depends only on the relative angular momentum and To summarize, we need the following conditions to hold:

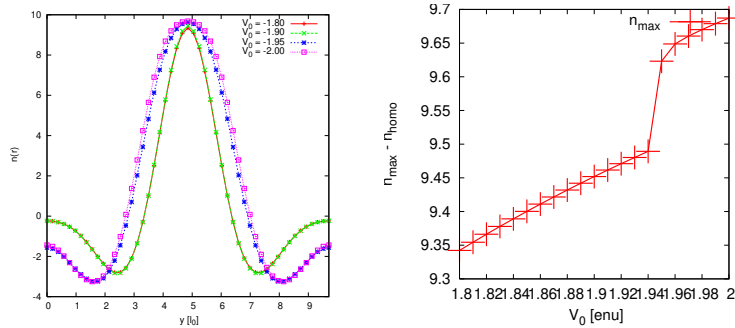


Figure 5.31: Schemes of the single impurity system(a)Schematic plot of the periodically repeated unit cell. The green dots denote the positions of the Gaussian impurity and (b) Example of the effective potential $\sum_{\text{cells}} V(\mathbf{r}_{\text{cell}})$ in the unit cell created by an array of attractive Gaussian scatterer. The effect of the neighboring scatterer amounts to less than 1% for $\sigma < 1l_0$.

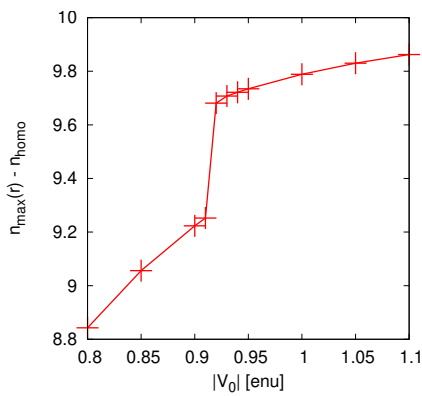


Figure 5.32: Maximal density response of a 5/15 system to different impurities ($\sigma = 1l_0$).

1. The impurity must destroy the FQH state, thus allowing 2 electrons to be closer than $3 l_0$
2. The impurity must be stronger than the l -dependent repulsion from the pseudo potential.
3. If these preconditions are met, an additional electron may enter the Quantum Dot, visible both in the electronic density profile and in the vortex distribution.

This "sudden rearrangement" of charge in the Quantum Well has also been found by Rezayi et al. [96] for system with coulombic interactions in a spherical geometry. No further analysis there.

5.5 The inner structure of the electron-vortex complex

So far we have studied the effect of impurities on global properties of the 2DEG, but no conclusion as to which strength/shape of impurity destroys the FQH state has been drawn. From previous work it is known, that the existence of a gap is a necessary but not a sufficient condition for the FQH effect to occur. We will use the electron-vortex correlation as described in sec. 4 as a better, finer measurement to distinguish states within the FQH regime and those outside.

The method mainly used in this section is described in 4.2 and 4.3 , (p. 70 ff.). In that part we have shown the attachement of vortices to electrons and the subsequent characteristic shape of the vortex distributions in homogeneous systems. In this section we study the changes in those individual electron vortex composites under the influence of external potentials.

The section is organized as follows: we start with the description of the vortex distribution for a fixed configuration of sample electrons, while the examination of the electron-vortex correlations g_{ev} , g_{vv} is provided in the following section.

5.5.1 Vortex distribution: The disturbed system

Let us first analyze the change in the vortex distribution for a single configuration of sample electrons (a square geometry with a size of $5 l_0$).

The situation for the homogeneous system is described in section 4.2, the vortices are placed exactly (for the SRI case) at the electrons positions and are slightly displaced from the electrons in the Coulomb case (cf Fig.4.3). The situation is different when analyzing the ground state of systems with $V_0 \neq 0$ as shown in Fig. 5.33 (a) . Two of the 3 vortices move away from the electrons under the influence of the impurity, but remain attached to the electrons at some small distance ($0.5 l_0$ in the example shown). The third vortex - representing the Pauli principle - remains at the electron position. The center of mass vortices are located at the border of the sample, one vortex is bound to each of the sample electrons and the remaining vortices are located in the vicinity of the electrons. We choose $V_0 = -0.8$, a value where the gap is still present but the ground state degeneracy is already lifted.

Recurring to Fig.4.4 and the geometrical parameters introduced there, we will use the detachment vectors ξ magnitude ξ to characterize the detachment process quantitatively.

We shall analyze again the influence of the 2 parameters strength (V_0) and width σ separately. The configuration of the sample electrons is the same for each analysis, thus leaving possible effects of changing sample geometries minimal.

Fig. 5.33(b) shows the dependency of ξ on the parameter V_0 for displacement values of up to $2 l_0$. Throughout this region a linear dependence of ξ on V_0 is characteristic (cf. the densities and gap changes which are non-linear for small values of V_0 , cf. Fig. 5.22 and 5.15). As the average electron-electron distance is of the order of $5l_0^{18}$, the detachment of $2 l_0$ is about the maximal distance at which we can still find an unambiguous relation between a vortex and an electron, i.e. it becomes less obvious to find the electron to which the vortex belongs.

The situation is somewhat different for the case of coulomb interaction (cf. Fig. 5.34). The vortices “move away” from the sample electrons for $V_0 < 0.6$, where the electron and the 2 next vortices are located on a line. However, for stronger impurities, the vortices do “move back” toward the electrons. This is consistent with the findings of Tavernier et al. (see 4.1.1). They found an apparent repulsive interaction among the vortices when they added a new vortex into their system. The mechanism underlying the vortex dislocation has therefore two components, the repulsion of the vortices from their electron and the intra vortex repulsion. Hence $\xi(V_0)$ has a maximum at $V_0 \approx -0.6$ as shown in Fig. 5.34 (b). Further comparison of the 2 interaction types shows, that the vortex displacement is larger for all coulombic systems and the increase of the vortex displacement with the impurity strength is much stronger in coulombic systems for small values of V_0 . These findings are in keeping with previous results which show the system with coulomb interaction to be less “Laughlin-like” than the SRI systems.

We turn now to the influence of the impurities width σ . In Fig. 5.35 we show $\xi(V_0)$ curves for 3 choices of σ . In all cases the dependency $\xi(V_0) \sim V_0\alpha$ is linear with an increasing slope α May be we shall try $V_0\sigma$ too here!. The direct analysis of $\xi(\sigma)$ is shown in Fig. 5.35. We compare the 2 different interaction types in Fig. . For both interaction types we find the same principal relationship:

- the displacement approaches the value for clean systems for wide and very narrow impurities.
- a local maximum of the displacement is observed in both cases at values of about 1.5-2.0 l_0 .
- for values of $\sigma \geq 2.5l_0$ the absolute values for ξ are constant among the 2 systems.

Differences between the interaction types are the magnitude of the (relative) change of ξ , with σ the absolute value for the homogenous state. The maximal value of the displacement is appr. 50 percent larger for the coulomb system with approx. the same width.

The finding for values of $\sigma > 3.5l_0$ is again, that the property under investigation - the vortex displacement- approaches the value of the homogenous state.

¹⁸depends on N_m how?

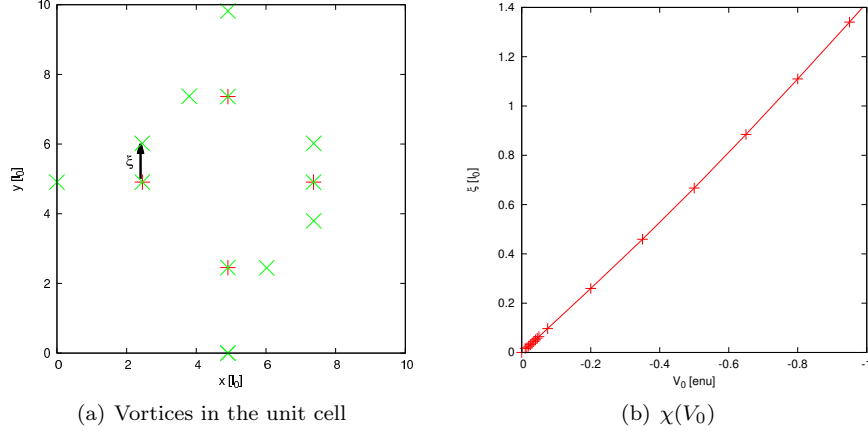


Figure 5.33: (a) Example distribution of vortices in the unit cell. The positions of the sample electrons are marked (+). $V_0 = -0.8$. The particular displacement ξ is also shown. (b) Shows the magnitude of the vortex displacement ξ over the strength of the impurity potential V_0 , **SRI**

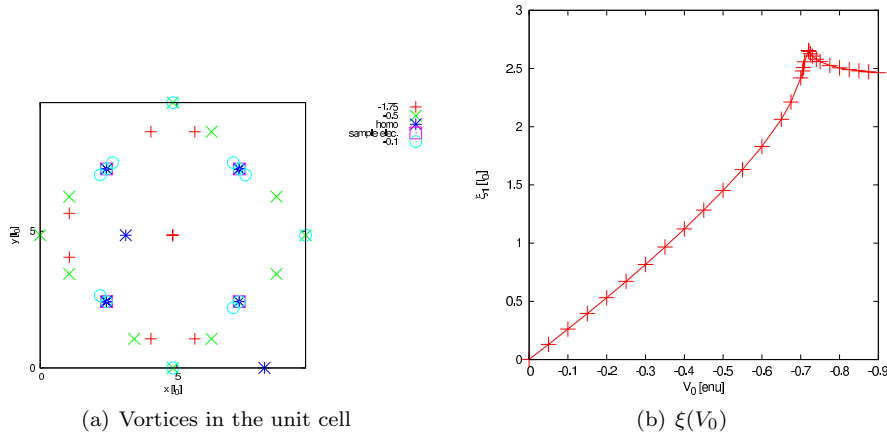


Figure 5.34: (a) Example distribution of vortices for some selected values of V_0 in the unit cell. The distribution of vortices for the homogeneous Coulomb system is provided for comparison (blue stars, the displacement is not visible on this scale). The positions of the sample electrons are marked (+). (b) Shows the magnitude of the vortex displacement ξ over the strength of the impurity potential V_0 , **coulomb interaction**. The finite value for $\xi(0)$ is not visible on this scale.

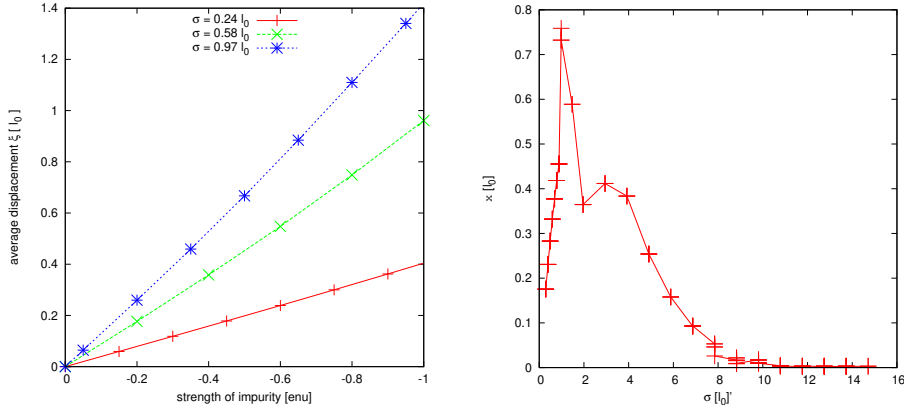


Figure 5.35: (a) $\xi(V_0)$ for 3 choices of σ . (b) $\xi(\sigma)$ for a single Gaussian impurity **SRI**, $V_0 = -0.3$

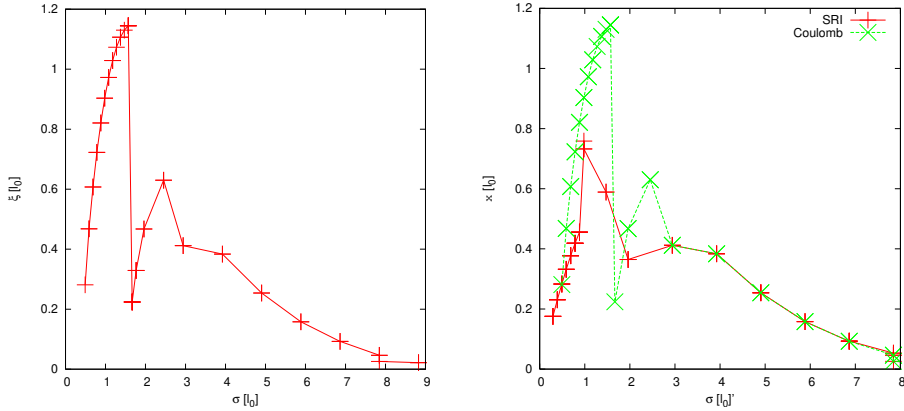


Figure 5.36: (a) $\xi(\sigma)$ for a single Gaussian impurities (Parameters as in Fig. 5.35), coulomb interaction (b) comparison of $\xi(\sigma)$ for coulomb and short range interaction, same parameters as in (a) and Fig. 5.35

The wide potential adds nothing but an more-less constant background potential. The situation is different for values $\sigma \in [0, 2l_0]$. The average displacement decreases sharply by appr. 50 .percent with a minimum at $\sigma \sim 2l_0$.

From the analysis described in this section we draw 2 important conclusions

1. The distance ξ from electron to vortex is a good candidate for a sensitive quantity to study the destruction of the FQH property in a ground state wave function.
2. A relation can be established between the strength and the corrugation of the scattering potential and the displacement- hence with the assumption that a scatterer disturbs or destroys the FQH state- it may serve as an quantitative indicator of the FQH quality.

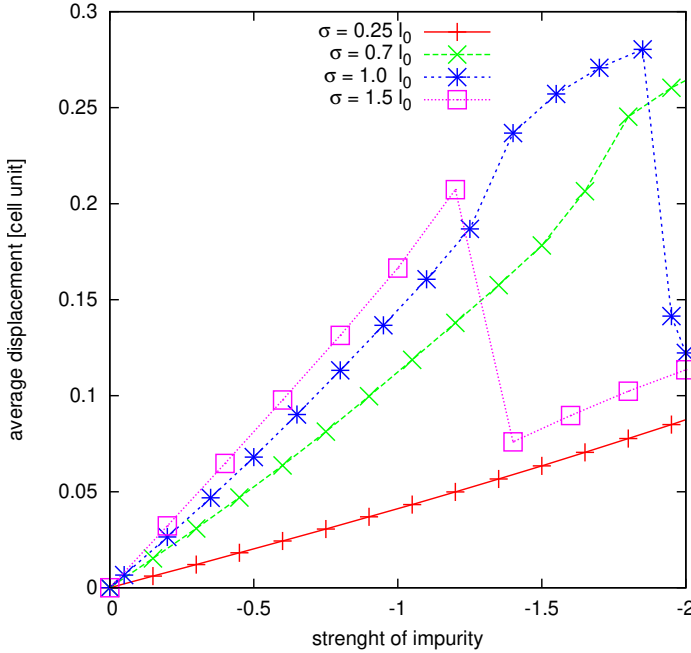


Figure 5.37: Vortex displacement for different strengths and sizes of a Gaussian impurity potential.

5.5.2 Quantized charging revisited

Having applied the vortex search algorithm to a number of systems we shall apply it now to the same system as in Section 5.4.

In Fig.5.37 the displacements of the vortices from sample electrons arranged in a square pattern along the symmetry axis at a distance of $2.5 l_0$ is shown. For narrow impurities the vortices "move" away from the electron positions when increasing the potential strength. For impurities of characteristic width $1 l_0$ the vortices "move back" toward the electrons at some larger values of V_0 . The value of V_0 is the same as for which the single charging of the quantum well occurs (see above, Sec.5.4). We may therefore interpret this "movement" of the vortices as an indication of a local restructuring of the electron system in the outside the quantum well. This rearrangement seems to reinforce the binding among electrons and vortices and might be interpreted as a recovery of the FQH phase. **CAREFULL HERE!**

Efrov verarbeiten. Vielleicht ist es ja so, dass man die incompressiblen Pfäützen sehen kann? [25], [24]

5.5.3 Conclusion

In this section we found, that the positions of the vortices with respect to the electron do indeed depend on the characteristics of the impurity potential, regardless of the electron-electron interaction type. The distance between vortices and their corresponding electrons increases with stronger impurities. Taking the attachment of all vortices to electrons as another peculiarity of the LGS, it is

reasonable that this feature vanishes with the other defining, global features as seen in the closing of the correlation gap and changes of the electronic density.

However it turns out (compare section 4.3), that the effects of different distances of the sample electrons from the impurity is canceled or even superseded by purely artificial geometry effects. In the following section we shall therefore calculate the averaged displacement in order to obtain quantitative results.

5.6 Correlations and many body properties of the disturbed state

We shall now use the electron-vortex and vortex-vortex correlations ($g_{ev/vv}(r)$) as developed before (section 4.3, p. 71 ff.) to study the electron - vortex complex in inhomogeneous systems. We found earlier, that both correlations exhibited a delta peak shape at $r = 0$, $g_{ev/vv}(r) = \delta(0)$, reflecting the perfect binding of the vortices to the electrons in the SRI wave function. The correlations generated from the homogeneous Coulomb ground state reflected the positions of the vortices in the vicinity of the electrons by showing a peak in g_{ev} at $r_{max}^{coul} \approx 0.7l_0$, the particular shape of g_{vv} was interpreted as a tendency of the vortices to avoid each other.

In this section, we will study the influence of the impurity strength and width on the electron-vortex complex. An examination of the two correlations analytical properties, performed at selected correlations, is followed by an investigating the size of the electron vortex complex over a wide range of impurities. Based on this analysis, we shall make a first statement about the physical property of the underlying many-body state, in particular about the resemblance to the incompressible FQH ground state.

5.6.1 Analysis of general features and properties of g_{ev} and g_{vv}

We continue the analysis of the principal properties of the correlations g_{ev} and $g_{vv}(r)$ as begun in section 4.3.2 and extend the analysis to inhomogeneous systems here.

At first, we study the correlations calculated for systems with weak attractive impurities and short range interaction. Those systems showed a large degree of similarity with the Laughlin groundstate (the spectrum shows a gap, the ground states are nearly degenerate, the density is nearly homogeneous and the electron-electron correlations are essentially identical to LGS electron-electron correlations).

Let us first analyze the electron-vortex correlation (g_{ev}) in such inhomogeneous SRI systems as shown in Fig. 5.38 (a) and (c). Most prominent is the fact, that g_{ev} has its maximum no longer at the origin, the vortices are found in the vicinity of the electron instead. The position of the maximum (r_{max}) increases with V_0 ¹⁹, the same effect was observed already for the single electron configurations studied in the previous section.

The peak in g_{ev} has a finite width, unlike the δ -peak observed in homogeneous systems. The peak widens with stronger V_0 (cf Fig. 5.38 (a), we interpret

¹⁹We choose $\sigma = 1l_0$ in all calculations unless otherwise noted.

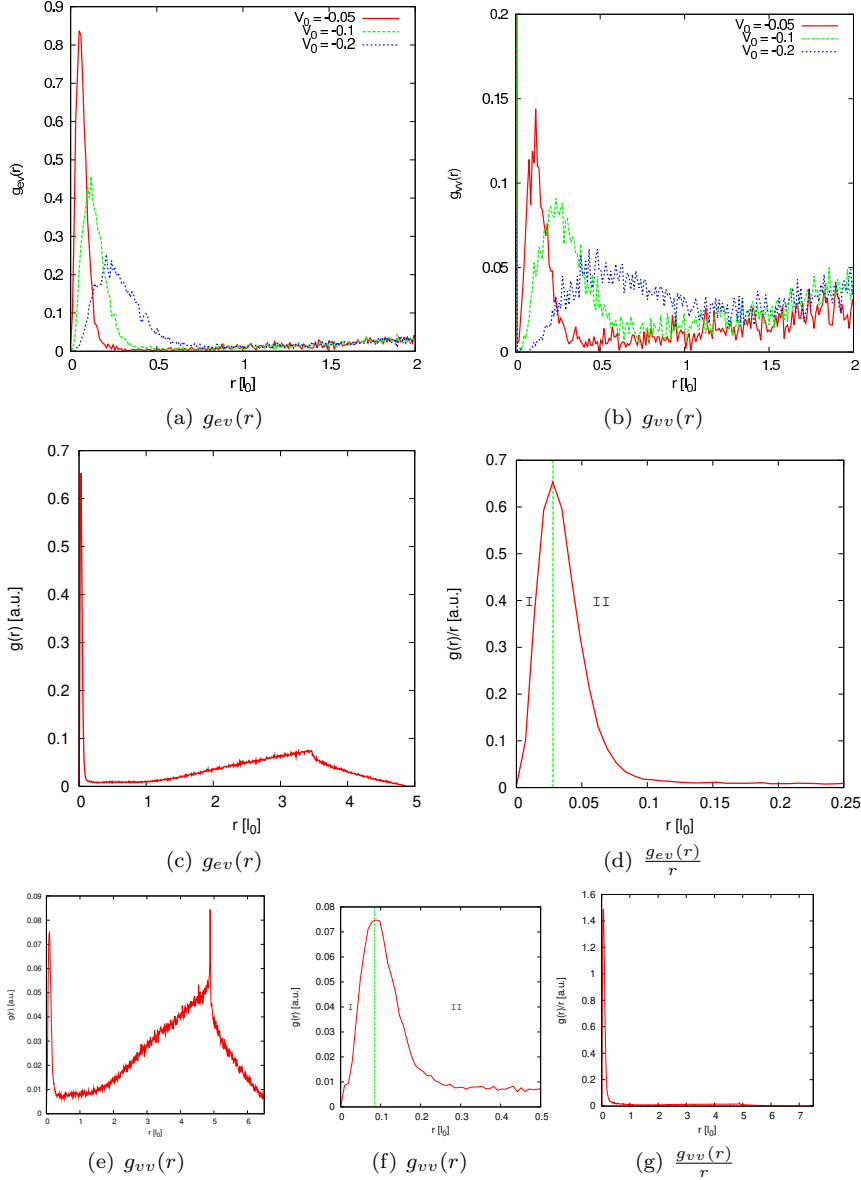


Figure 5.38: Electron-vortex and vortex-vortex correlations for weakly inhomogeneous **SRI** systems. First row (a) and (b) show g_{ev} and g_{vv} for 3 choices of V_0 . Second row (c) and (d) shows electron-vortex correlation and normalized electron-vortex correlation for a $V_0 = -0.04$, $\sigma = 1l_0$. Third row (e-g) shows vortex-vortex correlations for the said system ((f) shows the data from (e) on a smaller scale). (g) has been normalized to the area of the sampled circle ring.

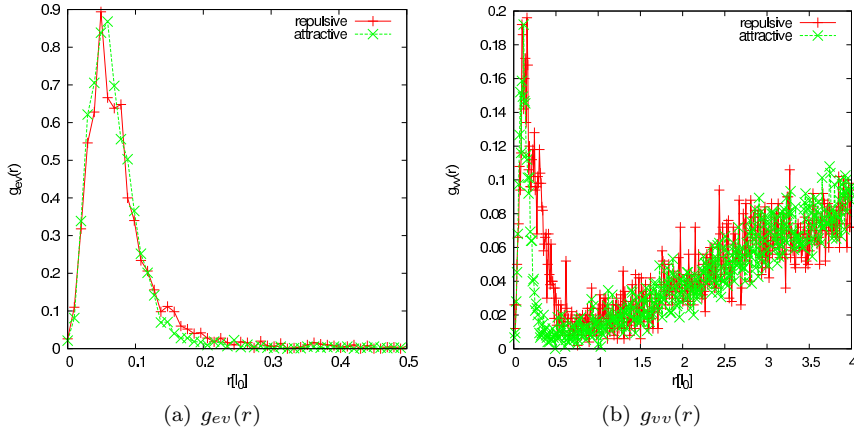


Figure 5.39: Electron-vortex correlation ($g_{ev}(r)$) (a) and vortex-vortex correlation ($g_{vv}(r)$) (b) . for weak attractive and repulsive impurities ($V_0 = \pm 0.05$), SRI.

this as the effect of the tendency of vortices to avoid each other in accordance with the findings for the homogeneous Coulomb System²⁰. While the width of the peak increases with V_0 , the height ($g_{ev}(r_{max})$) decreases with V_0 , this effect is complementary to the larger width of the distribution under the condition of a finite number of vortices ($\approx (\frac{N_e}{\nu} - 1) N_{MC}$).

A quantitative analysis of the slope of the electron-vortex correlation²¹ reveals three different regimes. For $r < r_{max}$ - Region I in Fig. 5.38 (d) - the correlation shows a (somewhat inconclusive) cubic dependence as shown in Fig. 5.40 (a). This characteristic is persistent over a wide range of V_0 . For $r > r_{max}$ two further regimes present themselves, the falling edge of the maximum (region II in Fig. 5.38 (d)) with an r^{-3} dependence and the subsequent rising regime ($r > 1l_0$ in Fig. 5.40 (d)) with a $r^{\frac{3}{2}}$ characteristic. A further peak appears at $r \approx 4.5l_0$. This secondary peak is caused by the Pauli-vortices of the nearest-neighboring electron, the distance is compliant with the average electron-electron distance extracted from the analysis of the electron-electron correlations (Sec. 3.4).

When increasing the strength of the impurity to a value where none of the conditions for the FQH state is fulfilled (the gap is no longer present) a weak maximum can still be observed at larger distances, approximately at half electron-electron distance (Fig. 5.41). The mere existence of a maximum is hence no clear criterion for the incompressibility of the respective state.

Since the examination of the homogeneous Coulomb system revealed, that the vortex-vortex correlations (g_{vv}) provide additional insight into the vortex-vortex “interaction”, we study those correlations also for the same weakly inhomogeneous SRI systems as before. Some exemplary results are shown in Fig.5.38(b). Similair to g_{ev} , the vortex-vortex correlations are no longer of $\delta(0)$ type, but exhibit a peak with a finite width at finite distances r_{max}^{vv} . The po-

²⁰For a quantitative analysis of the broadening of g_{ev} , we define the width of the peak as $\Delta_{g_{ev}} = r_{0.75}^+ - r_{0.75}^-$, the difference in r at which the correlation reaches 75% of its maximum value, $g_{ev}r_{0.75}^+$ $g_{ev}r_{max}^-$.

²¹Note that the correlations presented so far, are not normalized to the sampling area!

sition of the maximum (r_{max}^{vv}) increases with V_0 . The width of the peak is consistently larger than in the case of $g_{ev}(r)$. The positions of the two maxima ($r_{max}^{vv} = 2r_{max}^{ev}$) are consistent with a symmetric displacement of the vortices from the electrons.

When performing an analysis of the slopes of g_{vv} (Fig. 5.38(b)), the result is less conclusive than for the electron-vortex correlations. $g_{vv}(r) \sim r^{\pm 3}$ holds only for very small values of r on the rising edge and on the falling edge of the peak. At the maximum - where most vortices are found - the tendency of the vortices to repell each other is weaker, resulting in a $\sqrt{r^3}$ characteristic in the vortex-vortex correlation (Fig. 5.40(b, c)).

It is worthwhile now to explore the influence of the impurity type (attractive vs. repulsive) on g_{ev} . We show the results in Fig. 5.39(a). The position of the maxima in both correlation types is nearly identical for both types of impurities, where the electron-vortex correlations are essentially identical throughout the unit cell. The vortex-vortex correlation however, shows a qualitatively different slope for $r > r_{max}^{vv}$. We may attribute this difference between attractive and repulsive impurities to the sampling algorithm by invoking the following argument: remember that the sampling algorithm favours electron configurations where the electrons are kept apart. A repulsive impurity in the center of the unit cell creates an area of depleted electron density in the center of the unit cell, quite the opposite effect is observed for an attractive impurity. The Monte Carlo algorithm samples more configuration with larger intra-electron distances in the former case, with smaller ones in the latter case. This may be the reason for the different slope of the falling edge in g_{vv} . However, the position of the maximum is not affected by the type of the impurity.

5.6.1.1 The effect of the electron-electron interaction onto the correlations.

So far, we have restricted our discussion of $g_{e,v/v}(r)$ to SRI systems. We incorporate now the influence of the electron electron interaction by comparing SRI systems to those with Coulombic interaction. While the homogeneous SRI system shows $g_{ev}(r) = \delta(0)$, the situation is different for the Coulomb interaction. The homogeneous Coulomb system shows already a finite value for $r_{max}^{ev/vv}$. In order to better understand the prevailing mechanism - in particular the different effects of the electron-electron interaction and the effect of the impurity onto the system, we compare the correlations calculated from inhomogeneous states with Coulomb interaction.

When subjecting a Coulomb system to a weak impurity, the maximum position of the peak is driven farther away from the origin as shown in Fig. 5.43 (a-c). The characteristic shapes of g_{ev} and g_{vv} are not altered by the impurity (cf. Fig. 5.43 (a, b)).

Having seen now, that an impurity in our sample forces the vortices away from the electrons for systems with SRI, we compare the electron-vortex correlations of a homogeneous Coulomb system, where the distribution is not δ -like, with an inhomogeneous SRI system in order to see, whether the effect of the long range electron-electron interaction can be substituted by the effect of the local impurity potential.. We choose the impurity strength for the SRI system in such a way, that r_{max} is nearly identical for both interaction types. We compare the characteristics for small values of r in Fig. 5.42. The compari-

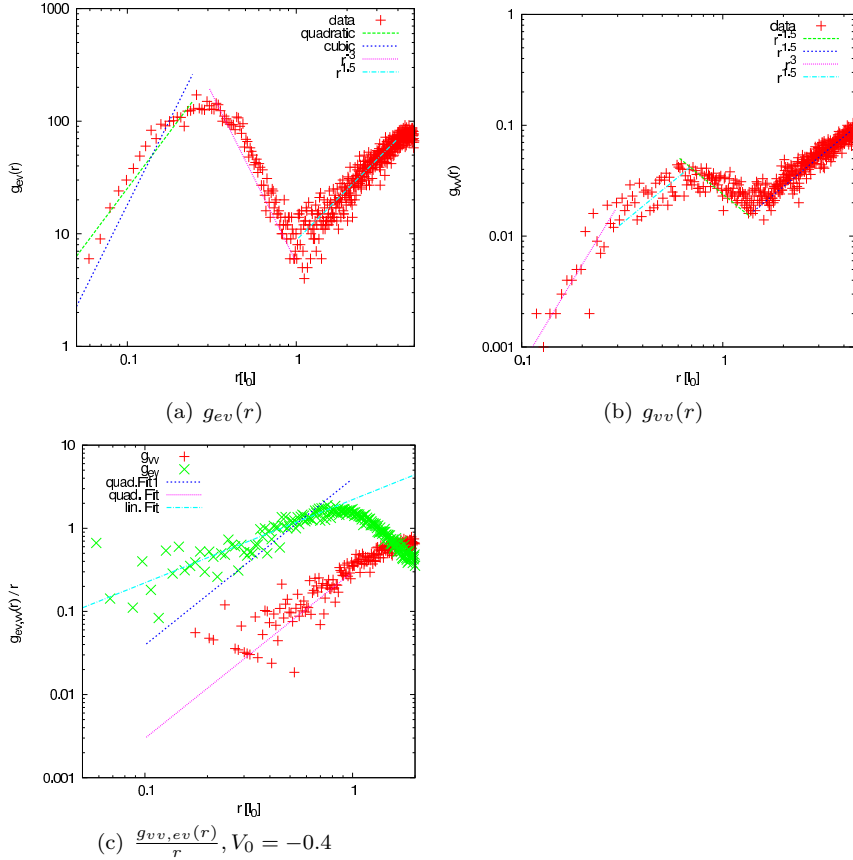


Figure 5.40: Electron-vortex and vortex-vortex correlations, calculated from the ground state of a SRI-system ($V_0 = -0.25$), shown on a double logarithmic scale. Fig (a) shows the electron vortex correlation, fits to a quadratic function and a cubic function are provided as guide to the eye (confined to $r < r_{ev,vv}^{max}$). In panel (a) a fit to a \sqrt{r} function is provided for $r > r_{max}$. Fig. (b) shows the vortex-vortex correlation for the same system. As guide to the eye fits to cubic functions and $\sqrt{r^{\pm 3}}$ are provided. Bottom row shows a comparison of the normalized correlations for a stronger impurity. As guide to the eye quadratic fits and a linear fit are provided on a larger scale (for $r < r_{max}^{ev,vv}$).

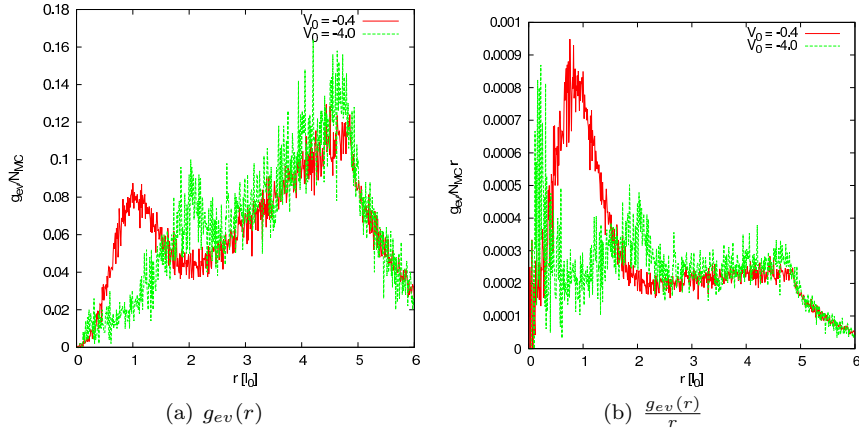


Figure 5.41: Electron-vortex correlations for two choices of V_0 , representing weak ($V_0 = -0.4$) and strong ($V_0 = -4.0$) impurities. Left pane shows the raw data, while the right pane shows the area-normalized distributions. The apparent maximum for the strong impurity in the right pane is due to numerical errors (see text and compare to left pane). The spectrum for the (too) strong impurity shows none of the features of the FQH state - namely neither are the lowest three states degenerate, nor is a gap between the third and fourth state present. See text for an discussion of the different behavior of g_{vv} for $r > 0.2$.

son of the electron-vortex correlations is somewhat inconclusive (Fig. 5.42(a)) (g_{ev}^{SRI} is not unambiguously $\propto r^3$)²² The results for the vortex-vortex correlations have clearly different characteristics. The homogenous Coulomb system has a quadratic behavior, while the inhomogeneous SRI system has a cubic behavior (Fig. 5.42(b)). This underpins the conclusion, that g_{vv} is in general more susceptible to the long range parts of the interaction and/or the impurity. Apparently the long range impurity and the long range electron-electron interaction have a different effect on the vortex-vortex correlation. It is hence not promising to replace the impurity by an effective (shielded) interaction or vice versa while keeping all of the the many-particle properties.

We shift our attention now to strong impurities in Coulombic systems. We will study now the slope of g_{ev} and g_{vv} for larger values of V_0 in order to explore whether the impact of the impurity changes this general characteristic of the respective correlations. In Fig. 5.43 we calculated the correlations for inhomogeneous Coulomb systems and extracted their respective slopes. The r^2 characteristic prevails over a wide range of impurity strength, regardless of the repulsive or attractive character of the impurity.

For a preliminary conclusion, we state that the dependence of r_{max} on the impurity strength can be interpreted as the result of two opposing mechanisms, the binding of the vortices has its origin in the pseudopotentials of the SRI²³, while the electron-vortex repulsion is due to the long range character of the impurity. The vortex-vortex correlation is more susceptible to the influence of the impurity (foremost seen in the comparison of the attractive and repulsive

²²To emphasize this ambiguity a quadratic fit is provided for the SRI system as well as a cubic fit.

²³More precisely in the absence of any higher order contribution in the pseudopotential

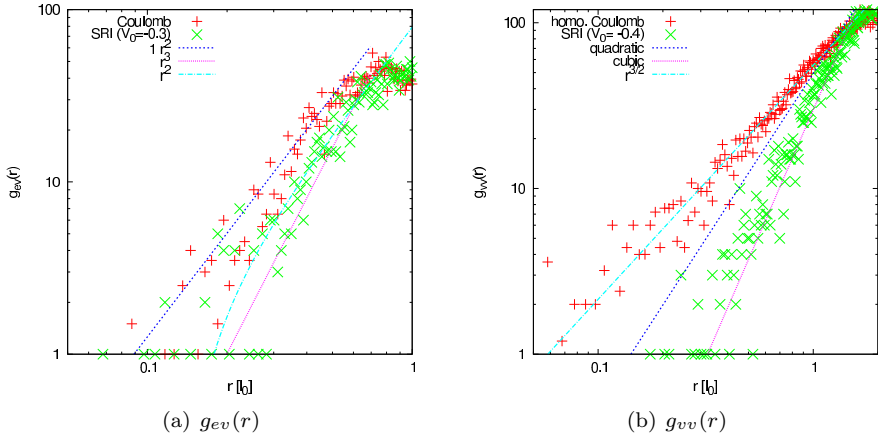


Figure 5.42: (a) Electron vortex correlations for an homogenous Coulombic system and a disturbed ($V_0 = -0.3$) HC system on a double logarithmic scale. Along with the raw data, fits to r^2 and r^3 are provided. Fig (b) shows the vortex-vortex correlation for the same systems, along with fits to r^2 , r^3 and $\sqrt{r^3}$. See discussion in text!

impurities and in the comparison of the two interaction types). After the analysis of the correlation shapes we conclude, that the peaks position ($r_{\max}^{ev/vv}$) can be used as an indicator for the deviation of the particular system from the LGS and hence as a criterion for the incompressibility of the respective state.

5.6.2 Quantitative exploration of the Electron-Vortex complex in inhomogeneous systems

Having established now the peculiarities of the different correlations, we aim now at the dependence of the correlations peaks on the strength and shape of the impurity for systems, which display some or all of the macroscopic features of the FQH ground state. All systems studied in this subsections show a gap, a small bandwidth and comparitively homogenous electronic density. In what follows we show the radius of the electron-vortex complex ξ which we extract from the maxima of the electron-vortex and vortex-vortex correlations respectively ($\xi = \frac{2r_{\max}^{ev} + r_{\max}^{vv}}{2}$)²⁴

We start with the analysis of the electron-vortex complex' size ξ , extracted from similair calculations as those shown in Fig.5.38(a,b) for weak repulsive impurities and Short Range Interaction. The results are presented in Fig. 5.44 (a), where $\xi(V_0)$ is shown along with a fitted linear function. The radius ξ increases linearly with the impurities strength with the slope being strongly σ dependend as shown in Fig. 5.44 (b). Again we find, that narrow (nearly δ -shape) impurities have a small impact on the system, in this case g_{ev} remains essentially of the $\delta(r)$ form.

Investigations of $\xi(\sigma)^{25}$, as shown in Fig. 5.45 (a), reveal different regimes.

²⁴For stronger impurities the determination of r_{\max}^{vv} becomes less precise - in those cases only r_{\max}^{ev} will be used.

²⁵Essentially testing the dependency of $g_{e,vv}$ on the shape of a weak impurity

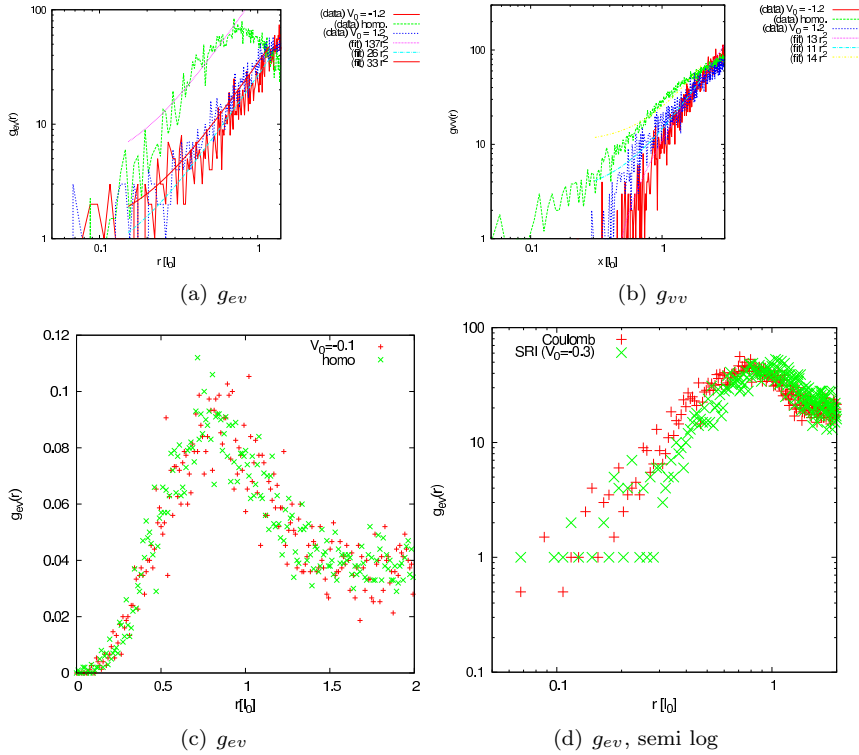


Figure 5.43: Shown are the electron vortex correlations (a) and the vortex-vortex correlations (b) for the homogeneous and two strongly inhomogeneous ground states of a system with Coulomb interaction on a double logarithmic scale. To guide the eye, fits to quadratic functions are provided for each data set, the quadratic coefficients are provided as well. The panel (c) shows a comparison of the electron vortex correlations of a homogeneous and weakly ($V_0 = -0.1$) inhomogeneous state.

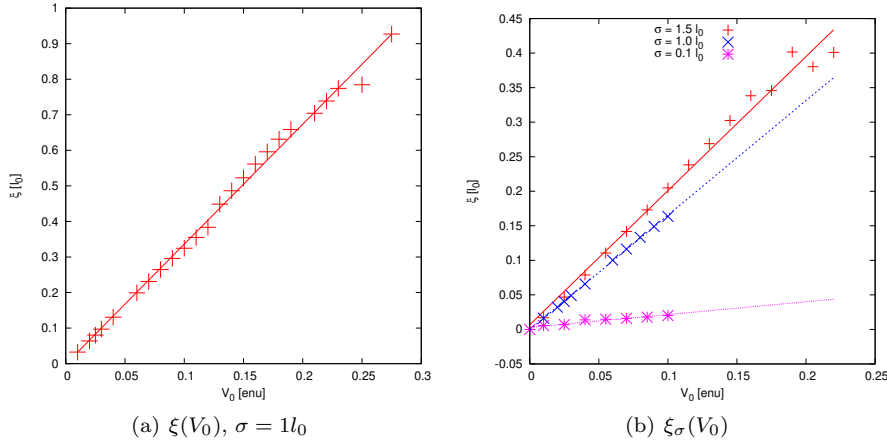


Figure 5.44: (a) $\xi(V_0)$ for weak repulsive impurities with $\sigma = 1l_0$. (b) Shows 3 choices of σ and the resulting CF size ξ , **SRI System**, weak repulsive impurities.

For very narrow impurities ($\sigma > 0.15l_0$), the electron vortex complex is enlarged by the impurity. For an extension of $\sigma \approx 2.25l_0$ the electron-vortex complex has its largest size while at larger values the system retains the same property as in the homogeneous case, the electron vortex complex contracting rapidly with σ . We may interpret the sudden contraction of the electron-vortex complex as an effect of the PBC. The potentials of neighboring unit cells begin to overlap substantially and at some value of σ the potential felt by the electrons in the unit cell changes its character from being locally repulsive to an extended, periodic type. In this case the actual character (repulsive or attractive) of the impurity can not be clearly distinguished any longer. (see Fig. 5.24, p. 104).

To create an overall picture of the electron vortex complex size and the impurity characteristic, we show $\xi(V_0\sigma)$ for different choices of σ in Fig. 5.45 (d). $V_0\sigma$ is used as a measure for the overall entry of energy into the system caused by the impurity ($\int V(x, y) dx dy \propto V_0\sigma$). For small values of this entry a linear characteristic is found.

When extending the analysis to systems *subject to repulsive and attractive impurities* respectively, we find (see Fig. 5.45 (b)) a linear characteristic ($\xi \propto V_0$) for weak impurities regardless of the impurities type. The sensitivity of the Electron-Vortex complex is the same for weak repulsive and attractive impurities. The situation changes somewhat if we analyse stronger impurities where we find a maximal size $\xi_{max} \approx 1.1l_0$ for short range interaction and a strong attractive impurity. For strong impurities this V_0 symmetry is no longer present, the repulsive impurity has a different effect than the attractive one. A similar behavior was demonstrated for the characteristics of g_{vv} (see Fig. 5.39 and discussion thereof), which was explained by the peculiarities of the sampling algorithm.

When investigating the *effect of the electron-electron interaction*, we find (see Fig. 5.45 (c)) a nearly identical characteristic for weak impurities of both interaction types. The slope ($\frac{\partial \xi}{\partial V_0}$) is identical ($\pm 1\%$) for both interactions and impurity types in the weak impurity regime.

In order to draw conclusions with regard to a lower limit of the maximal

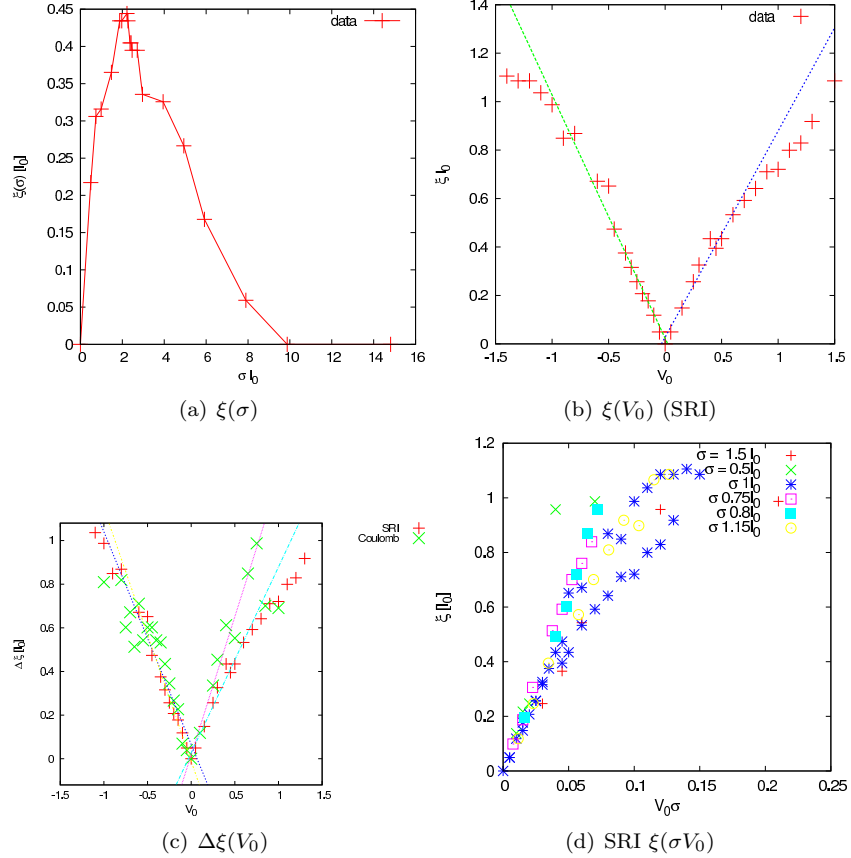


Figure 5.45: (a) Shows the response of ξ to impurities with different extensions. $\xi(\sigma)$, ($V_0 = -0.3$). Line is a guide to the eye - SRI. Pane (b) shows the size of the electron-vortex complex over impurity strength, SRI and $\sigma = 1l_0$. (c) Shows a comparison of the change of the electron vortex composite's size for the two interactions ($\sigma = 1l_0$). NB the size of the composite is $0.7 l_0$ for the homogeneous system with Coulomb interaction. A linear fit is provided as guide to the eye which makes the symmetry in V_0 more striking (the slope is equal for both interaction types to a precision of less than 1%). Picture (d) shows $\xi(V_0\sigma)$ generated from 3 choices of σ .

complex size, we show the dependency of ξ on the correlation gap (Fig. 5.46) for both interaction types. Analyzing the data, we find two regimes, for weak impurities (corresponding to a vanishing bandwidth - not shown here) the Electron vortex complex expands very easily, while for stronger impurities (where the coupling over the gap comes into play) the complex remains stable. This allows us to draw two conclusions, the size of the electron vortex complex is indeed more sensitive to the influence of disorder than the (global) correlation gap. Secondly, we conclude that $\xi \approx 0.4l_0$ is commensurate with an incompressible state for the SRI. For Coulombic interaction this finding changes slightly. As it is known from experiment, the Coulomb interaction renders the FQH state to be more stable than for the SRI. We can therefore state, that a change of $0.4l_0$ - giving a maximal size of $1.1l_0$ - is still commensurable with the existence of the FQH properties in such a system.

To find an upper limit of ξ for which it would still be reasonable to expect features of incompressibility is more involved. The first (conservatively high) limit can be obtained from the average electron-electron distance as calculated from the electron-electron correlations (sec. 3.4, p. 60, in particular Figs. 3.4 and Fig. 5.27). The distance estimated is $r_{ee}^{avg} = 4l_0$, half that distance is a - comparitively large upper limit to ξ .

5.6.3 Bridge the gap between global and local properties by virtue of the electron-vortex correlations

So far we have calculated and studied mostly global properties of the system, in particular all the correlations studied thus far are global properties of the 2DEG. However, it is well established that the FQH state contains localized and extended states, hence some investigation of local correlations in our unit cells is desirable.

Experimental works by Ilani et al. [98] - performed on systems with $\nu = 1, 2$ and partly at $\nu = \frac{1}{3}$ as well as theoretical investigations by Efros [25, 24] for integer filling factors within the framework of Thomas-Fermi theory predict the existence of compressible and incompressible domains in samples under the influence of an external electrostatic field. The former study established the existence of localized states bound to maxima and minima²⁶ of the electronic density by measuring the local compressibility of the electrons. Since we made the claim that an incompressible state is related to a strong localization of vortices at the electrons, it is worthwhile to attempt a connection between some form of local electron-vortex correlations and the local incompressiblity of our system.

Let us first - before presenting the actual methods and results - adress the following question: Given that we perform calculations in a unit cell with a finite size and given that the only local property studied so far - the electronic density $n(r)$ - shows typical extensions of $1l_0$ around the impurity, what resolution do we expect from a further analysis of local properties? Since the electronic density accumulation is located in an area of a size $\approx 1l_0$, moreless regardless of the impurity potentials width and - in a single electron picture - the extension of the electron states is of the same order of magnitude- we do not expect a finer resolution than $1l_0$.

²⁶quantum wells and quantum dots

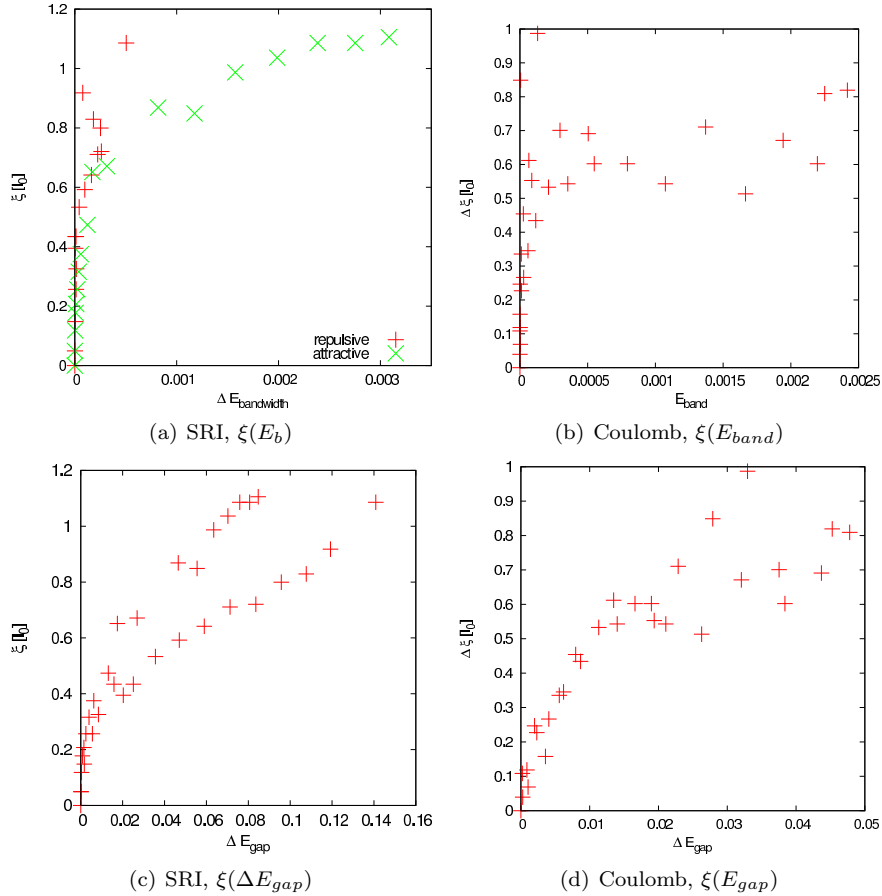


Figure 5.46: Both panes show the change of the Electron-Vortex complex size (ξ) over the change of the correlation gap with respect to the value for the homogeneous system. For the interpretation of (a) keep in mind, that the gap size corresponding to the set in of coupling to higher states is at approx. $\Delta E = 0.002$ in this scale. (b) Shows the change of the electron-vortex complex with respect to the homogenous size of $\approx 0.7l_0$ over the change of the correlation gap.

5.6.3.1 Local electron-vortex correlations as a possible indicator for local properties of the system

In subsection 4 (p. 66 ff.) we introduced the electron-vortex correlation $g_{ev}(r)$ after having made the observation that the vortex distribution obtained from a single electron configuration is sensitive towards the distance of the sample electron to the impurity. We expand this finding now and calculate a local electron-vortex correlation by keeping the position of one electron at a fixed place r_0 in the sample and calculate $g_{ev}^{loc}(r_0)$ by performing many Monte Carlo runs. The remaining $N_e - 2$ electrons are placed in the unit cell according to the sample algorithm described above. We evaluate the electron-vortex distribution ($g_{ev}^{cond}(r)$) only for the fixed electron after removing the Pauli vortices and extract the position of the maximum, $\xi_{loc}(r_0)$.

Let us now examine the properties of the extracted correlations and $\xi_{loc}(r)$. In a homogenous system we expect and find this quantity to be independent of the sample-electrons position, regardless of the electron-electron interaction type. The SRI system shows delta-peak shaped correlations, for the Coulomb interaction $\xi_{loc}(r) = 0.7l_0$ for r varied within the unit cell.

Upon introduction of an impurity (again at the center of the unit cell), the conditional correlations change their shape, depending on the sample point r . An example of those changed conditional distributions $g_{ev}^{cond}(r)$ and the unconditional distribution $g_{ev}(r)$ for a weakly disturbed system is shown in Fig. 5.47 (a). The position of the maxima in $g_{ev}^{loc}(r)$ ($\xi_{loc}(r)$) changes with the position of the sample electron, taking values larger and smaller than ξ_{uncond} . Since we found earlier, that a homogenous state shows an homogenous electronic density and perfect $\nu = \frac{1}{3}$ correlations one could expect the local correlations to be $\frac{1}{3}$ like²⁷ in regions with a constant density. A comparison of $\xi_{loc}^{loc}(r)$ with the electronic densities ($n(r)$) as shown in Fig. 5.47(b) shows no such behavior. Instead the vortices are weakly localized in regions, where the gradient of the electronic density is large.

A possible interpretation of the observed ξ^{loc} characteristic can be drawn from the inversion of the statement related to the $\xi(E_{band})$ characteristic as shown in Fig. 5.46 and discussed before in section 5.6.1. The inverted statement reads: changes of $\xi^{loc}(r)$ on scales $< 0.4l_0$ do not signal a qualitative change of the electron-vortex correlations. This interpretation provides us also with an error margin for $\xi^{loc}(r)$.

The analysis of the global correlations provided us two regimes - described by the correlations being either globally of $\nu = \frac{1}{3}$ type or not²⁸. Let us now analyze local correlations calculated for systems chosen to cover the following three regimes, where :

- the system shows global $\nu = \frac{1}{3}$ correlations ($\xi < 0.4l_0$, $V_0 < 0.25$),
- the system shows no global $\nu = \frac{1}{3}$ correlations ($\xi \approx 0.4l_0$, $V_0 > 0.5$) or
- the intermediate regime $0.25 < V_0 < 0.5$, where the global correlations show no clear global $\xi > 0.4l_0$, $\nu = \frac{1}{3}$ correlations.

In Fig. 5.48 we show conditional correlations for representations each regime for both interaction types. For all states the vortices are stronger localized for

²⁷ ξ^{loc} is smaller at a distance from the impurity.

²⁸The former showing $\xi < 0.4l_0$, the latter $\xi > 0.4l_0$

positions far away from the impurity. At intermediate distances, the deviations of ξ^{loc} are significantly larger than the limit ascribed to $\frac{1}{3}$ correlations. In close proximity of the impurity the vortices are strongly localized at the sample electrons (with the exception of very strong impurities).

For small values of V_0 we find $\xi^{loc}(r) < 0.4l_0$ throughout the unit cell. Together with the analysis of the unconditional correlations, we conclude that those states show the typical $\nu = \frac{1}{3}$ correlations locally as well as globally.

For $V_0 \approx -0.3$ the local correlation lengths are beyond the margins of $\nu = \frac{1}{3}$ correlated state and show, by our definition, no fractional correlations. only in a certain region of the unit cell ($r > 1l_0$). The size of this region grows with the strength of the impurity. The most significant finding of this analysis is, that with impurity strengths in the range of $0.4 < V_0 < 0.7$, we find domains of different correlations in the unit cell. We conclude, that those states show $\nu = \frac{1}{3}$ correlations only locally. This finding parallels the coexistence of compressible and incompressible domains (see Ilani et al. [98]) or FQH and IQH domains (see Pardiso et al. [90]) as shown in experiments.

Further increase of the impurity strength renders the area of $\nu = \frac{1}{3}$ correlations smaller until those correlations are not present at all.

After this analysis it is justified now (with some caution) to make a statement about the correspondence of the electron-vortex correlation lengths and experimental quantities. We expect a system with global and local correlations with $\xi > 0.4l_0$ to show none of the typical characteristics of the Fractional Quantum Hall Effect. As many authors have named those states compressible we shall use this term (and its opposite) as a shorthand for the electron-vortex correlations are (or are not) of the $\nu = \frac{1}{3}$ type.

When comparing the effect of a repulsive and attractive impurity we find a nearly identical characteristic (Fig. 5.49(a)). The impact of the impurity's geometry is tested in Fig. 5.49(c). The extension of the compressible region is identical for both choices of σ .

The effect of the two interactions was studied for systems belonging to the intermediate regime as shown in Fig. 5.49(b)). We find the effect of the impurity to be of the same order of magnitude with regard to the absolute values of $\xi^{loc}(r)$. The size of the areas with $\nu = \frac{1}{3}$ correlations are identical within the margin of the numerical error. This underpins the notion of the decay of the electron-vortex complex to be caused exclusively by the impurity.

Summarizing the results set forth in this section, we find that the incompressible $\nu = \frac{1}{3}$ state - as determined by the electron-vortex correlations is destroyed gradually with stronger impurities. The coexistence of compressible and incompressible domains in the unit cell is shown. The compressible domain appears at distances of $\approx 1.5l_0$ from the impurity and expands over the unit cell with larger amplitudes of the impurity.

5.7 First Summary and Conclusions

After having studied both the homogeneous system and inhomogeneous systems disturbed by a single Gaussian impurity of different width and maximal value it is time for a first summary before continuing with the examination of systems disturbed by many impurities.

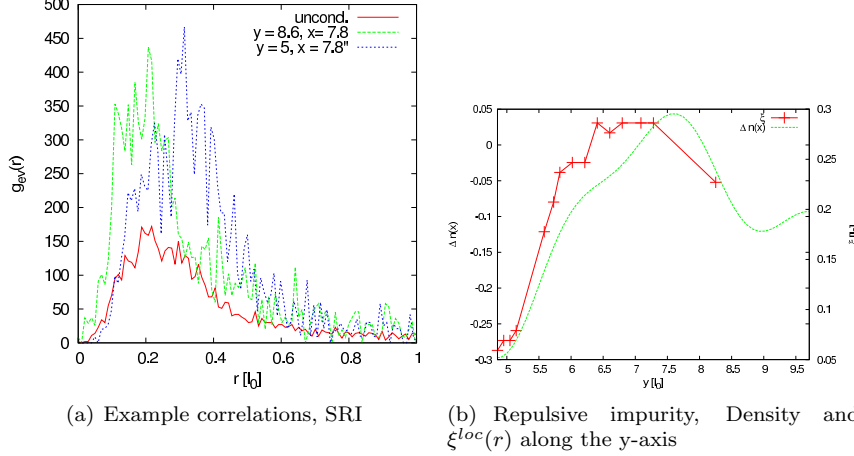


Figure 5.47: Left: example correlations $g_{cond}^{ev}(r)$ along with the electron-vortex correlation ($g_{ev}(r)$) calculated at two different places in the unit cell, weak (-0.2) attractive impurity. Right: density (difference to the homogenous systems value) and local correlations maxima ($\xi_{loc}(r)$) calculated for weak repulsive impurity ($V_0 = 0.2$) and SRI. Shown are values for a cut along the y-axis.

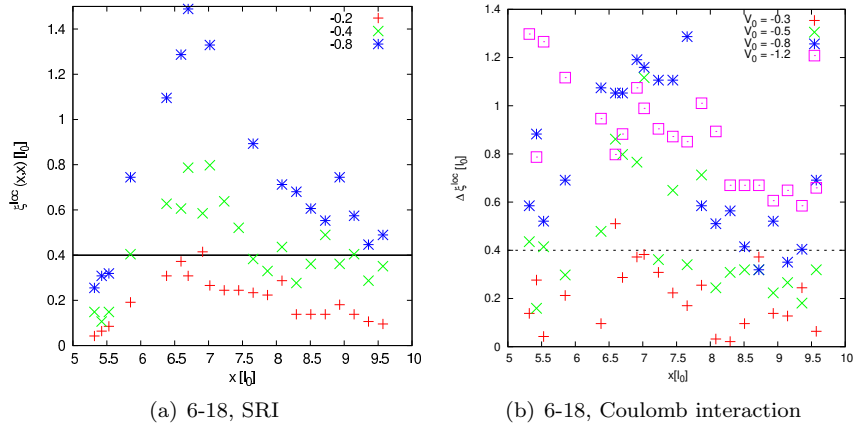


Figure 5.48: (Left) $\xi_{loc}(r)$ for three choices of attractive impurities. SRI (Right) Shown are the differences of $\xi_{loc}(r)$ and the extension of the electron-vortex complex as extracted from the unconditional electron-vortex correlation. V_0 have been choosen in such a way, as to pick a representative of each regime (see text). Coulomb interaction. Shown are values for $\xi_{loc}(r)$ along the diagonal through the unit cell. The impurity has its maximum at $x = 5$ in these figures.

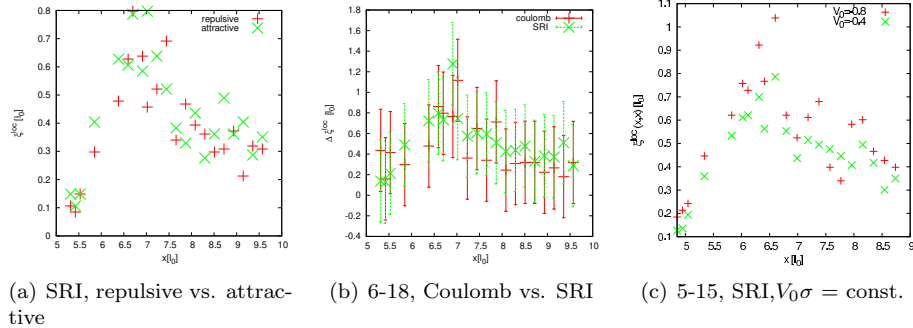


Figure 5.49: (Left) $\xi^{loc}(r)$ calculated for a repulsive and attractive impurity of equal strength ($V_0 \pm 0.4$). (Center) Shown are the relative changes of ξ^{loc} with respect to the unconditional electron-vortex correlations for Coulomb and short range interaction respectively. $V_0 = -0.5$, see text for a discussion of the errorbars. (Right) $\xi^{loc}(r)$ for two choices of the impurity width σ with $V_0\sigma$ constant. (all) Shown are values for $\xi^{loc}(r)$ along the diagonal through the unit cell. The impurity has its maximum at $x = 5$ in these figures.

In this section we calculated the spectra and derived energies of a disturbed system. We found the ground state energy to increase and the correlation gap to decrease with the impurity strength. The threefold degeneracy of the ground state is lifted with an impurity present, for weak impurities only partially and fully for strong impurities. The latter has its origin in coupling between the ground state and higher states with the correlation gap being the relevant energy scale. This finding gives a criterion to distinguish weak ($V_0 < 0.3$) and strong impurities.

The examination of the electronic density shows a charge depletion or accumulation at the position of the impurity. The shape of the density profile could be matched with a Bessel-function as expected from the literature. Calculating the compressibility of the state shows clear signs of the incompressibility of the homogeneous ground state.

The calculation of the two-particle electron-electron correlation shows no significant change of the average inter-particle distance, however the analytical shape of the correlation changes from the homogeneous r^6 character to a r^2 type.

The electron-vortex and vortex-vortex correlations shape deviate clearly from the δ shape of the homogeneous state. This deviation allows us to assign a finite size to the electron-vortex complex (possibly the Composite Fermion) in an inhomogeneous system. Putting the energies (as global properties) and the size of the CF (as a local property) in connection, gives a first idea of the persistence of such a complex in inhomogeneous systems. We shall use this size ξ as a benchmark for the incompressibility of the respective many-particle state from here on.

The findings sketched here encourage us to continue with the work. We have analyzed the building blocks and may proceed now to the "real thing".

Chapter 6

Multiple impurities - localization and scaling in the FQH regime

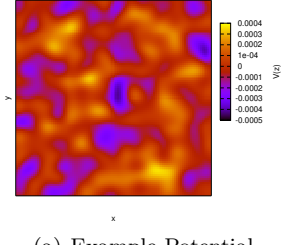
6.1 Introduction and organization of this chapter

The situation experimentalists encounter when studying the disorder potential in there samples is clearly different from the toy-model studied in Section 5. Instead of a single, well defined potential the 2DEG is subject to a random potential landscape with certain stochastic properties, resulting from numerous scatterers of different strengths, located at different distances from the electron gas. To cope with this situation, we must improve our model system. As discussed above (sec. 2.2.4, p. 14) the properties of the impurity potential are crucial for the existence of delocalized states and hence for the emergence of the Quantum Hall effect.

In the following section we study systems composed of many Gaussian scatterers, using much the same methodology as for the homogeneous system (sec. 3) and the system with a single impurity (sec. 5). First we will introduce the model system. The characteristics of the potential landscape will be studied in detail. After the establishment of the potential landscape's properties, we shall proceed with the analysis of the correlation gap and the band width. Finally the electron-vortex and vortex-vortex distributions will be studied for a wide range of potentials (section 6.4).

6.2 Creation and characteristics of the random potential

In this section we create and analyze random electrostatic potentials, which are generated by superimposing many Gaussian scatterers. The section is organized as follows. At the beginning we describe the method used for the creation of the potential landscape. The stochastic properties (variance and correlation



(a) Example Potential

Figure 6.1: An example potential generated from 30000 impurities. The potential was sampled over the unit cell on a 100×100 grid. ($\sigma = 0.75l_0$)

length) of the potential are investigated and the impact of the parameters used in the construction process are studied. Furthermore we study the effect of the potential on the energies of the system (using analogous methods as in section 3.2). We find a unifying value for the three parameters σ , V_{max} and N_{scatt} .

6.2.1 The generation method

In order to simulate a potential landscape we follow the work of Huckestein [54] and create it from a superposition of Gaussian scatterers with a constant width (σ) and varying strength which reads

$$V_{rand}(\mathbf{r}) = \sum_{i=1}^{N_{scatt}} V_i(V_{max}, \mathbf{r}_i) = \sum_{i=1}^{N_{scatt}} V_0^i \exp\left(-\frac{(\mathbf{r} - \mathbf{r}_i)^2}{2\sigma^2}\right). \quad (6.1)$$

We shall use a random distribution of the individual V_0^i with $V_0^i \in [-V_{max}, V_{max}]$ normalized by the condition $\lim_{i \rightarrow \infty} \sum_i V_0^i = 0$. This choice guarantees that no extra charge accumulation is introduced into the system as we studied this case essentially in the previous section. According to Huckestein et al. [54] (p.366) such a symmetric potential guarantees, that a possible percolation occurs at the band center. The center positions r_i of the individual scatterers are randomly distributed throughout the unit cell, the width σ is fix for each individual run. The resulting overall potential landscape for such a scatterer distribution is shown in Fig. 6.1.

6.2.2 The random electrostatic potential and its statistic properties

Before starting with the calculation of ground states of the FQH systems, it is necessary to understand the properties of the random potential used to simulate the background. We shall also try to define the meaning of *varying slowly on a given scale*¹ more quantitatively.

In order to characterize a randomly distributed potential, we use two different quantities, the variance²

$$var(V) = < |V(r) - < V(r) >|^2 | \quad (6.2)$$

¹a term found often in the literature to characterize a well behaving potential for which the FQH regime is expected to exist in the sample

² $< V > = 0$ within the precision imposed by the discrete sampling.

and the correlation length l_{corr} which we discuss below. The former describes the amplitude of the potential's fluctuations while the latter describes the length scales on which those fluctuations occur.

Let us briefly discuss which different regimes of the potential can be obtained by the construction procedure (Eq. 6.1). Few isolated impurities (corresponding to small values of N_{scatt}) result in a potential with a small variance and a small correlation length. Upon increase of N_{scatt} we reach the regime where the potentials overlap substantially, the variance increases further and we expect the potential to have an increasing, finite correlation length.

Therefore, the impact of the local parameters³ N_{scatt} (number of scatterers), σ (the width of the individual scatterer) and V_{max} (the maximum strength value) on the global properties of the background potential (defined by Eq. 6.1) needs to be established.

Before doing any actual calculations, we discuss existing works in order to establish a first idea of the order of magnitude for those parameters. As to the number of scatterers used in the generation process, the literature ([7, 54]) gives impurity concentrations $c_i = 2\pi l_0 n_i \approx 40$ for a potential which is "sufficiently random". In the case of a 5/15 system (area of approx 95 l_0^2) this corresponds to 4000 scatterers of delta shape. For impurities of Gaussian shape this number is reduced according to Huckestein by a factor of $\sqrt{1 + \frac{\sigma^2}{l_0^2}}$ which is nearly identical to 1 for $\sigma < 1l_0$, hence 4000 is supposed to be a good value for the impurity number for the non interacting (IQH) regime.

The reasoning behind this value was given by Ando [7] for the numerical analysis of the IQH system. It was found that the number of impurities must be larger than the number of single electron states. Although this argument was made for systems in the IQH regime (hence with neglected electron-electron interaction), we can to some extent transfer it to the system at hand. If all the single electron states were trapped by the impurities, their mutual interaction would be significantly changed which in turn would render the state insulating as all states are localized at an impurity. By virtue of this argument, we take the value of 4000 impurities as a first guess for the impurity number.

Another - very crude - first approximation of the number of necessary scatterers can be made from simple geometrical considerations. If we expect no significant overlap of the potentials, it is reasonable to model the potentials as circles with radius σ in such a way, that the unit cell can be (nearly) covered with those circles. In order to cover the whole unit cell we need approximately $N_{scatt} = \frac{2\pi N_m}{\sigma^2} \sim 30000$ for impurities with $\sigma = 0.001l_0$ and approx 10000 impurities for $\sigma = 0.1l_0$.

6.2.2.1 The auto correlation function (ACF)

While the variance provides a global measure of the fluctuations of the potential, we are however interested in the length scale on which the potential fluctuates. The appropriate quantity to study is the correlation length l_{corr} which we introduce now.

We study the auto-correlation function (following [54]) of the potential, in order to calculate such a unifying parameter distinguishing the potentials. For

³parameters defining the individual scatterer

an infinite system the auto-correlation function (ACF) is defined as

$$ACF(\xi_x, \xi_y) = \int_{-\infty}^{\infty} \int_{-\infty}^{\infty} V(x, y) V(x + \xi_x, y + \xi_y) dx dy . \quad (6.3)$$

In the study of finite systems, the integration is performed over the unit cell only, hence

$$ACF(\xi_x, \xi_y) = \int_0^a \int_0^b V(x, y) V(x + \xi_x, y + \xi_y) dx dy . \quad (6.4)$$

(see Appendix F for more details).

The calculation of the auto-correlation function was performed in the following way:

1. Generate an array of N_{scatt} Gaussian scatterers $v_i(\sigma, V_{\max})$ randomly distributed throughout the unit cell
2. Calculate the resulting potential $V_{\text{rand}}(r) = \sum_{i=1}^{N_{\text{scatt}}} V_i(r)$ (left of bottom row in Figs.6.2 and 6.3))
3. take a sample of $V^{\text{rand}}(r)$ on a regular 100 x 100 grid, $V^{\text{rand}}(\{R_k\})$
4. calculate the 2D ACF (6.4) of $V^{\text{rand}}(\{R_k\})$ using standard routines [86] as shown in the right images of the bottom rows of Fig.6.2 and 6.3, extract the 1D ACF along the x-axis as shown in the respective top row image.
5. fit the 1D ACF to a Gaussian ($\propto e^{-\frac{1}{\sigma_{\text{ACF}}^2}}$), extract the width σ_{ACF} . (top of Figs.6.2 and 6.3)
6. the steps are repeated with identical sets of parameters to calculate the mean value of σ_{ACF} .

For a suitable potential we expect the auto-correlation function to exhibit a finite correlation length⁴ in the range of $1l_0$ and the system size and hence the potential to have a smooth behavior on length scales larger than one magnetic length and in the range of the system size.

The auto-correlation function is calculated and shown in Fig.6.2 and Fig.6.3 for 2 choices of $V(z)$. We find in both cases the pronounced Gaussian shape of the ACF which allows us to equate the correlation length of the potential with the width of this Gaussian $l_{\text{corr}} = \sigma_{\text{ACF}}$. In Fig. 6.3 however, the ACF starts to deviate from a purely symmetric Gaussian. We will discuss those deviations in the next part.

6.2.3 Numerical results for the variance and the correlation length of the random background potential

Let us now discuss the numerical results obtained for the variance and correlation length as shown in Fig. 6.5 and 6.6 respectively. Summarizing the findings shown in Fig. 6.5, which show the variance ($\text{var}(V(r))$) of the potentials, we find the variance to depend linearly on the number of scatterers. The influence

⁴Note that the ACF of a single Gaussian is again a Gaussian.

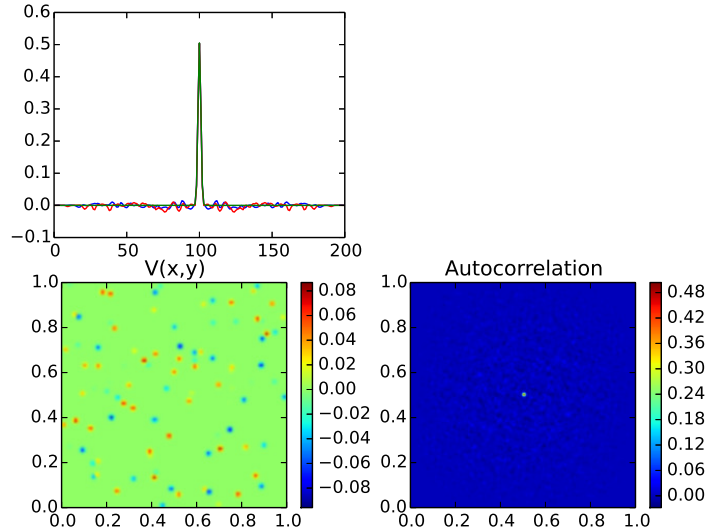


Figure 6.2: The picture shows: (bottom left) the electrostatic potential $V(x, y)$ generated from 500 scattering potentials. Bottom right: The auto-correlation function $ACF(\xi)$ of $V(x, y)$. The 2D plot in the top row shows cut $ACF(x, y = const.)$ $ACF(x = const., y)$ respectively, fitted to a Gaussian function.

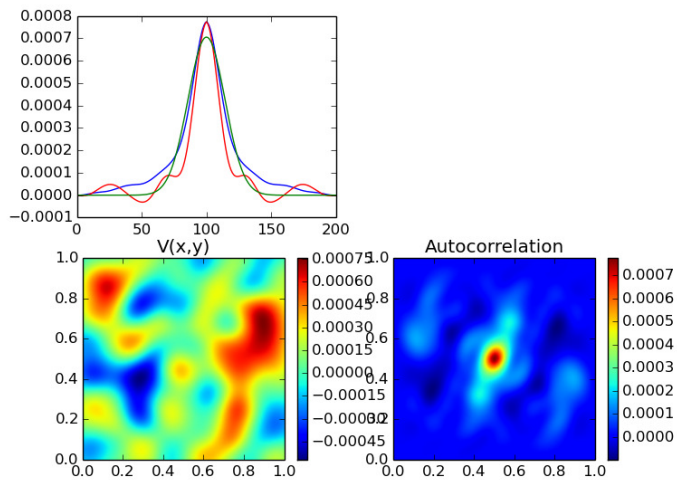


Figure 6.3: The layout of the image is the same as in 6.2. Shown are the results for 4000 impurities with $\sigma = 1l_0$

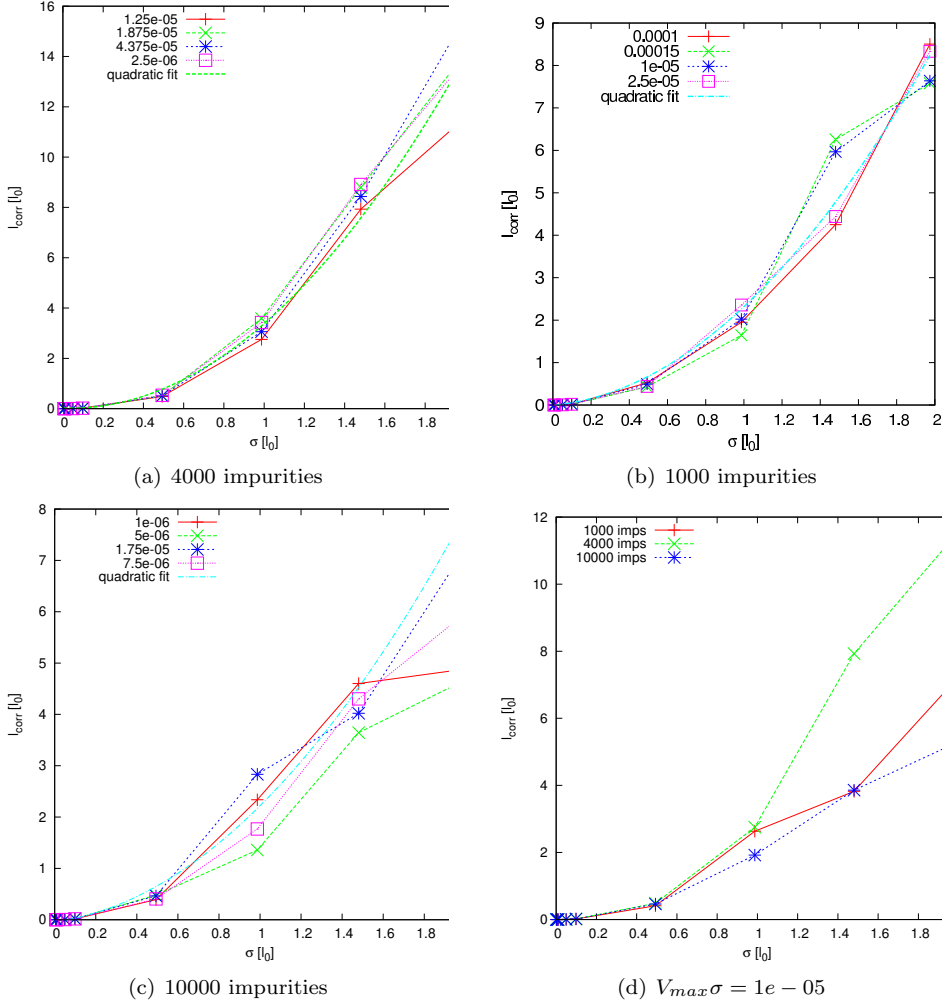


Figure 6.4: Top row: Correlation length of the background potential (fitted with of the Gaussian shown in Figs. 6.2 and 6.3) vs. σ for a selection of impurity strengths. Potentials created from 4000 impurities (left), 1000 impurities (right) and 10000 impurities (bottom left). Shown are results for some choices of $V^{\max}\sigma$. Bottom right pane shows the change of correlation length vs. σ for the values of N_{scatt} used in (a-c), $V_{\max}\sigma = 1e-05$.

of the width of the individual Gaussian (σ) and the maximal potential V_{max} is quadratic within the tested parameter range. Invoking the analytical property of the variance $var(\alpha V(\mathbf{r})) = \alpha^2 var(V(\mathbf{r}))$, we can interpret the quadratic behavior as a result of gradually increasing the overlapp of the individual Gaussian scatterer. The latter parameters (σ and V_{max}) are hence the determining values for the variance of the background potential.

The results obtained for the influence of the parameters on the correlation length l_{corr} are presented in Figs. 6.4 and 6.6. The results show clearly a negligible effect of the amplitude and number of the scatterers (V_{max} and N_{scatt}). The correlation length depends most strongly on the width (σ) of the individual scatterer. The dependence is linear up to correlation length of approximately 1/3 of the unit cells size. Although the correlation length shall be calculated for each electron-vortex distribution, we find a linear relation $l_{corr} = \alpha\sigma$.

We address now the errorbars in Fig. 6.6(e). They represent the fluctuation of l_{corr} for potentials generated from identical parameters σ , V_{max} and N_{scatt} . The fluctuation is negligible for small values of σ ($< 0.4l_0$). For wider individual impurities however, this fluctuation increases significantly. To interpret this finding, we refer to Fig. 6.7, where we show examples of the full two dimensional ACF (2Dacf) calculated from identical parameters where l_{corr} is extremal. Striking is the observation, that the 2Dacf does not exhibit a circular symmetric Gaussian shape for wider impurities anymore. Instead the 2Dacf is distorted and exhibits a preferred direction which changes randomly within the sets of the calculated correlations. To quantify this feature, we show in Fig. 6.8 a measure of the symmetry of the autocorrelation function around the origin. This asymmetry is the main reason for the strong fluctuations of l_{corr} ⁵.

We use these results now to distinguish between the two regimes of isolated, strongly peaked potentials and those potentials which show a significant overlapp. As discussed before, the ACF of a single Gaussian is itself a Gaussian which is symmetric. The fact that the shape of the 2Dacf deviates strongly from this symmetric characteristic leads us to the conclusion, that the regime of smooth, weakly modulated potentials is marked by asymmetric 2Dacf functions.

Summarizing the analysis described in the section so far, we conclude that potentials constructed by superimposing 1000 - 10000 Gaussian scatterers provide us with a good approximation of a random potential as encountered in experiment. The variance of the potential is determined by the width (σ) and the maximal strength of the impurities, while the correlation length is determined by σ only.

6.3 The electronic properties under the influence of a random background potential

We investigate in this section the ground state energy, the correlation gap and the bandwidth for systems subject to random potentials. The analysis is similar to the investigation of the homogeneous system (see sec. 3.2, p. 43) and the system with a single impurity (see sec. 5.2, p. 82). Although the parameter space is enlarged by the inclusion of N_{scatt} now, the results presented in the

⁵extracted by virtue of fitting a 1D slice of the full 2Dacf to a Gaussian as discussed above

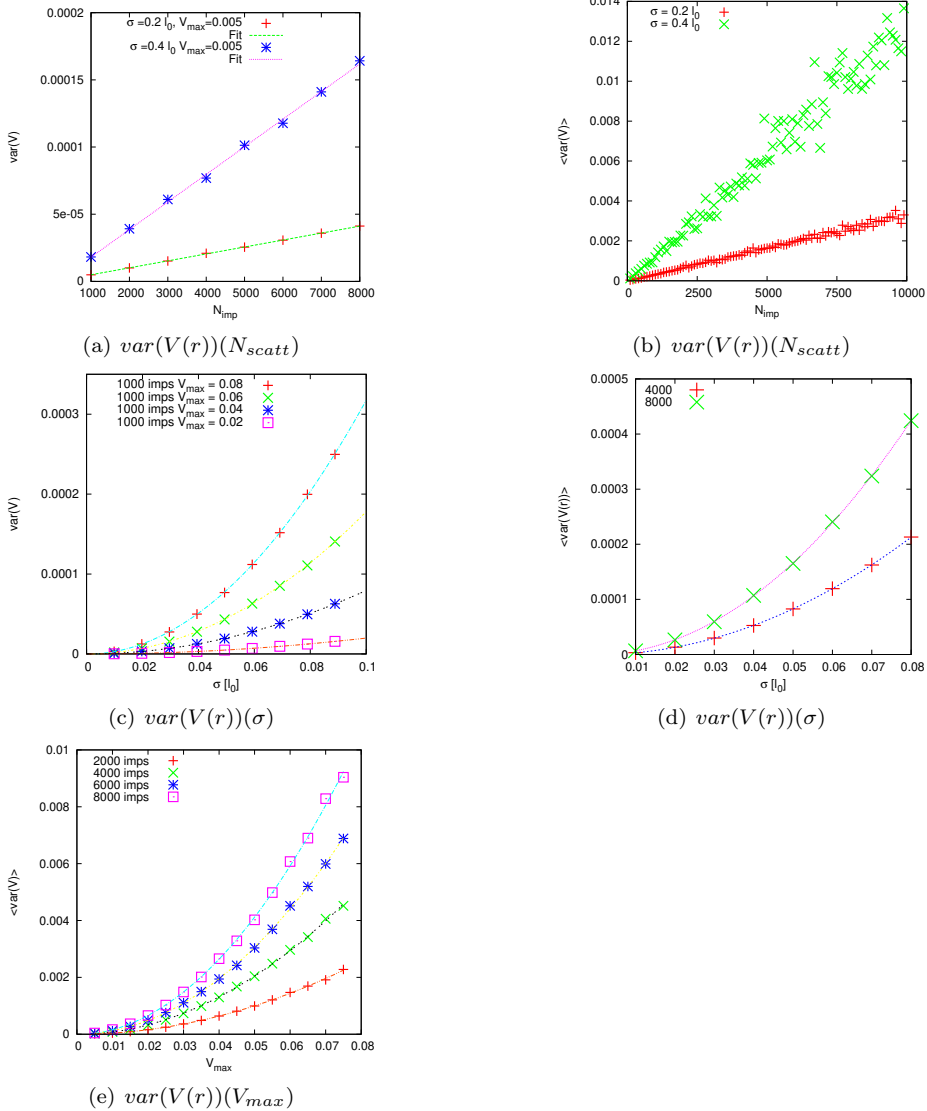


Figure 6.5: This image summarizes the variance (see Eq.6.2) of the randomly generated electrostatic potentials. The variances are evaluated for the three parameters of Eq.(6.1) ($N_{\text{scatt}}, \sigma, V_{\text{max}}$) individually. The top row shows $\text{var}(V)(N_{\text{scatt}})$ for two choices of σ and V_{max} , linear fits are presented as a guide to the eye. The left pane shows the variance on a finer scale for two choices of σ . In the second row the $\text{var}(V)(\sigma)$ characteristic is shown. The left pane shows results calculated with 1000 impurities and choices of V_{max} , while the right pane shows results for some choices of N_{scatt} and smaller values of σ . Fits to a quadratic functions are provided as guide to the eye. The third (bottom) row shows $\text{var}(V)(V_{\text{max}})$. Each datapoint was generated from averaging the variances over 200 random potentials generated from the same set of the individual parameters. The potentials were generated for a 5-15 system and sampled on a regular 100×100 grid. NB: Due to the generation method the expectation value $\langle V \rangle$ is not always zero. However it is multiple orders of magnitude smaller than V^{max} (typical values of 10^{-6} enu).

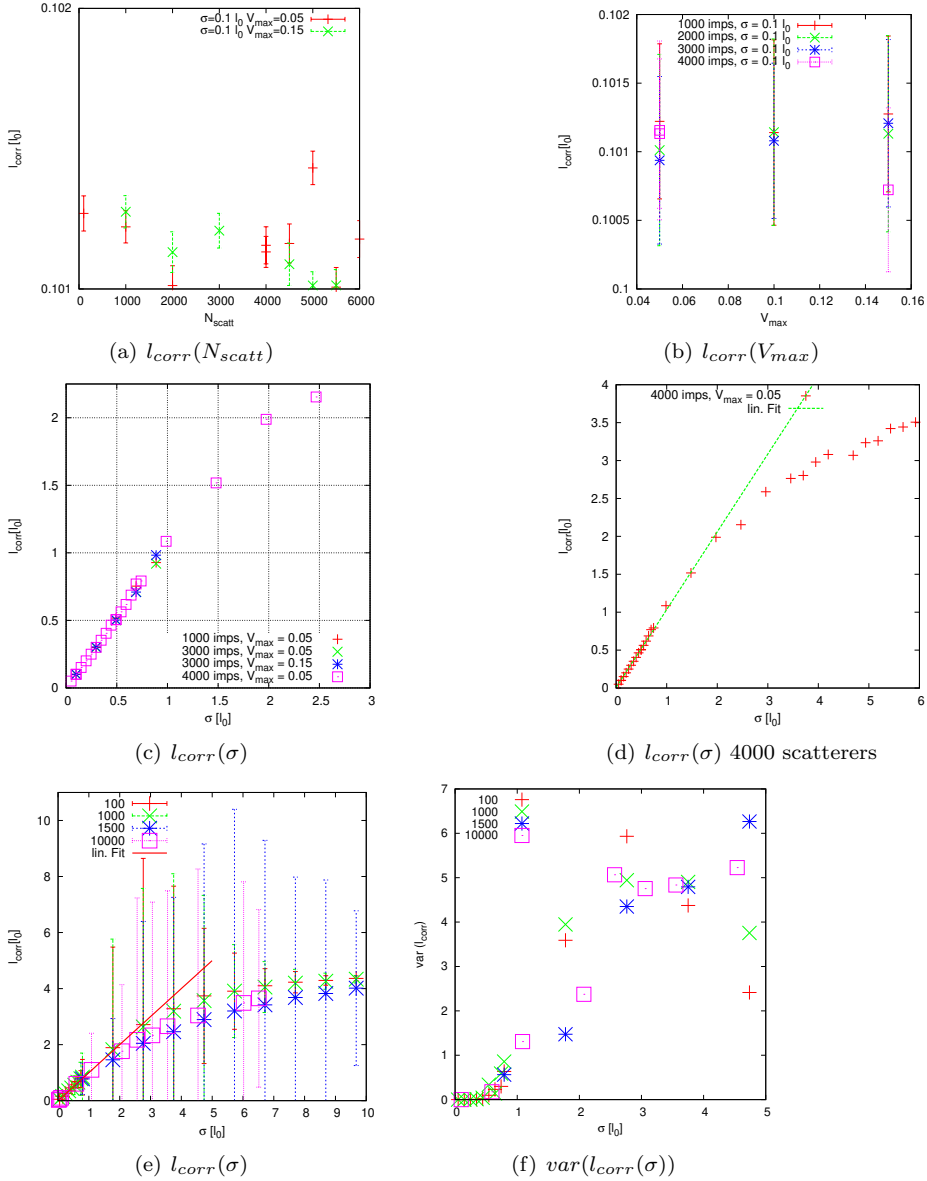


Figure 6.6: This image shows the correlation length's (l_{corr}) dependency on σ , N_{scatt} and V_{max} respectively. Top row left: correlation length vs. number of impurities for two choices of V_{max} . Top row right shows the influence of V_{max} for three choices of σ and N_{scatt} . The second rows shows the correlation length dependence on the width (σ) of the individual scatterer. Right pane shows the σ -dependence for four choices of N_{scatt} . As a guide to the eye, a linear function (fitted to the curve for 100 impurities for $\sigma < 1l_0$) is provided. Bottom row plot provides a linear fit to the $l_{corr}(\sigma)$ characteristic for 4000 scatterers as a guide to the eye. The smaller gradient's value for $\sigma > 2l_0$ is inconclusive here, the best fit produced a $\sigma^{0.8}$ dependency. Errorbars have been omitted for reasons of legibility, the fluctuation increases drastically for values of $\sigma > 1$ for all data presented as shown in the bottom right pane. The data were averaged over 200 random configurations created from identical sets of σ, V_{max} and N_{scatt} . The errorbars denote the standard deviation.

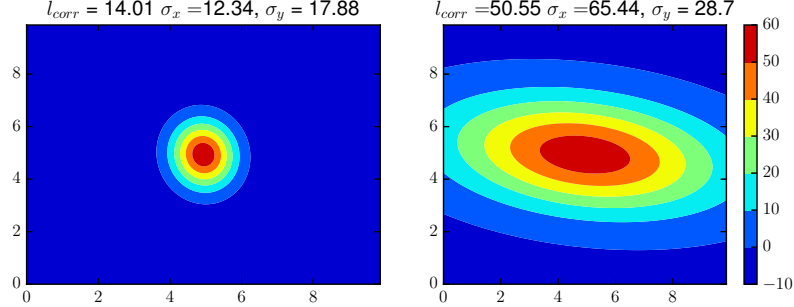


Figure 6.7: 2DACFs calculated from potentials generated for identical parameters ($\sigma = 2l_0$, $V_{max} = 0.1$ and $N_{scatt} = 4000$). The potentials with the smallest and largest correlation length (evaluated from 100 trials) were selected and the 2D ACF fitted to a two dimensional Gaussian. The correlation length and the parameters of the 2D Gaussian are given above each plot.

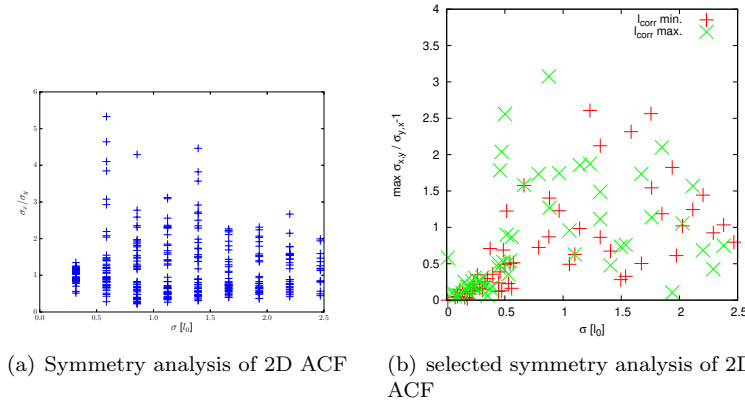


Figure 6.8: Left pane: Shown is $\frac{\sigma_x}{\sigma_y}$ as a measure for the symmetry of the 2DACFs (see Fig. 6.7). Shown are all results for 20 trials with identical parameters. (Right) $\max(\frac{\sigma_x}{\sigma_y}, \frac{1}{\sigma_y})$, calculated for the largest and smallest value of l_{corr} . Note that a value of 1 corresponds to perfectly symmetric Gaussian fit to the 2D ACF. The results shown in Fig. 6.7 correspond to values of 0 and 1.31 in the right pane here.

previous section show, that $V_{max}\sigma$ is the relevant parameter which controls the fluctuation and the correlation length of the potential. We shall develop a connection between the (local) properties of the individual Gaussian scatterer and the (global) stochastic properties of the random potential.

6.3.1 Fluctuation of gap and bandwidth due to the randomness of the potential

Before studying the electronic properties and the vortex distributions of the many-particle ground state it is necessary to establish what influence the randomness of the potential has on the spectrum and namely the correlation gap.

We calculated the spectra for different manifestations of the same potentials and evaluate both the gap and the bandwidth. This calculation was performed for 100, 1000 and 4000 impurities respectively with choices of the potential in such a way that a) small changes of the ground state and b) changes of the ground state with a remaining gap are covered. As we deal now with a stochastic potential, we expect the fluctuation of these characteristic properties to vanish when comparing various representations of a potential with the same values for $N_{scatt}, \sigma, V_{max}$. This requirement shall serve as another indicator for "enough" scatterers.

Summarizing those results it can be noted, that

- the fluctuation of the ground state energy and the bandwidth of the nearly degenerate ground state manifold are of the same order for all chosen numbers of impurities
- the impact of the particular choice of the potential is reduced with the number of impurities
- for potentials generated from (\geq) 4000 individual Gaussian scatterers this influence can be neglected.

Detailed results are shown in the Appendix (Table F.1, p. 180).

6.3.2 Ground state energy, spectra, correlation gap and bandwidth

We present now the changes of the ground state energy (E_0), the ensuing lifting of the degeneracy of the ground state, the bandwidth and the correlation gap when subjecting our system to a random potential generated from a wide range of parameters σ, V_{max} and some choices of N_{scatt} . We present the results dependent on $V_{max}\sigma$ only, details about the influence of the independent parameters V_{max}, N_{scatt} and σ are given in the appendix (??, p. ?? ff)⁶.

Let us first study the evolution of the spectrum with $V_{max}\sigma$ as shown in Figs.6.9. The *ground state energy* (E_0) depends quadratically on $V_{max}\sigma$ as depicted in Figs. 6.9(a,b). This finding has to be contrasted with the findings for systems with a single impurity, where we found two regimes for the $E_0(V_0)$ characteristic, a linear regime for weak impurities and a quadratic regime for stronger impurities (cf sec. 5.2, p. 82 and Fig. 5.4). The ground state energy

⁶We show results for systems with 4000 impurities for $N_e = 5$ and 4800 impurities for $N_e = 6$ in what follows.

of a system with a random potential however, does not show these two regimes, only a quadratic dependence is observed instead (Fig.6.9 (a,b)). To understand this difference we get back to the perturbation calculus performed above (sec. 5.2.1.5, p. 89 and sec. B, p. 166). We made use of a special symmetry of the system with a single impurity and traced the origin of the quadratic regime to the higher order of perturbation theory and a coupling over the correlation gap. This particular symmetry is not present when a random potential is introduced.

Further analysis of the spectra reveals, that for weak impurities (i.e. $V_0\sigma < 10^{-5}$) the spectrum shows different features from the single impurity case. Namely the ground state degeneracy is completely lifted even for small values of V_{max} , in the case of a single impurity we found a partial lifting only. The reason behind this is again the absence of the symmetry mentioned above.

With an increase of $V_{max}\sigma$, the spectrum changes its characteristic form. In Fig. 6.9 (c,d) we show the evolution of the spectrum with increasing $V_{max}\sigma$. The three lowest states form a band of near degenerate states for $V_{max}\sigma < 2 \cdot 10^{-5}$. The fourth state however is already lifted in energy, hence closing the correlation gap. The picture of the three lowest states forming a band and a well separated state is still true for $V_{max}\sigma < 4 \cdot 10^{-5}$ (SRI) and $V_{max}\sigma < 2 \cdot 10^{-5}$ (Coulomb interaction). For larger values of $V_{max}\sigma < 4 \cdot 10^{-5}$ the states are nearly equidistant in energy, rendering our definition of the correlation gap meaningless, since the energy differences ΔE_{0-2} and ΔE_{2-3} are roughly of the same size. Those states will be discarded in the latter calculations of r_{ev} , on the ground that they lack one major ingredient for the FQH⁷. Figs. 6.9 (c,d) show also, that no state from the continuum crosses into the gap.

Analyzing the results displayed in Fig. 6.10(c,d)⁸ we find, that the *correlation gap* closes according to $E_{gap} \propto \frac{1}{V_{max}\sigma}$ over a wide range of correlation lengths σ for both interaction types. When turning $V_{max}\sigma$ to values $> 3 \cdot 10^{-5}$ (Coulomb interaction) or $> 7 \cdot 10^{-5}$ (SRI), the splitting of the ground state is responsible for an apparent increase of the gap (see Fig. 6.9(c,d)).

The bandwidth increases with $V_{max}\sigma$ (Figs. 6.10(a, b)). For both interaction types the magnitudes of the bandwidth are nearly identical as is the case for the single impurity system.

An interpretation of the parameter $V_{max}\sigma$ is obtained when recalling, that mathematically it is the space integral of the potential of a single impurity and hence a measure of the energy of a single impurity with (V_{max}, σ) .

$$\int V(x)dx = \int V_{max} \exp -\frac{x^2}{\sigma^2} dx \quad (6.5)$$

The discussion of the stochastic properties of the potential showed, that the variance of the potential is determined by those two parameters. Hence we conclude, that it is the variance of the potential which determines the correlation gap. One may imagine this entity as a measure for the fluctuation of the potential, “seen” by the electrons.

Only states with $V_{max}\sigma < 10 \cdot 10^{-5}$ (for a system containing 4000 impurities) seem to have “potential” to preserve FQH-like correlations and will be analyzed

⁷This measure is obviously somewhat crude and the value of the ratio might even be higher. Since the ratio serves as benchmark with regard to the FQH-likeness we shall be conservative here and do not exclude more states than necessary. The evaluation of the electron-vortex correlation shall give us a final picture.

⁸See also supplementary data provided in the appendix, e.g. Fig ??

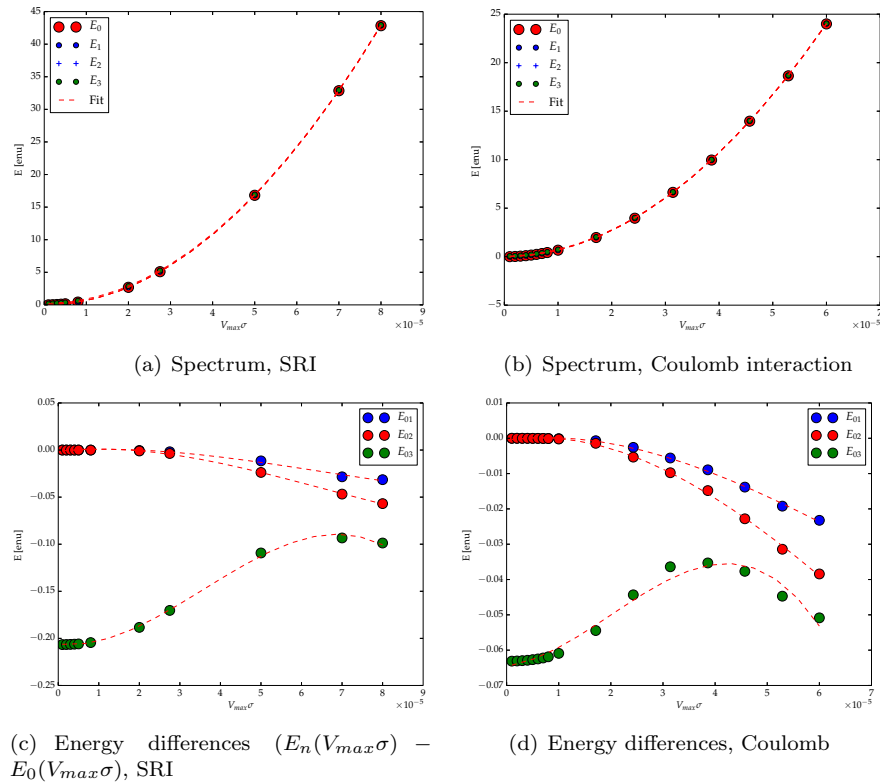


Figure 6.9: Top row: Energy spectrum of a 5-15 state, subject to 4000 impurities for SRI and Coulomb interaction respectively. Note that the splitting of the ground state manifold is not visible on this energy scale. Bottom: Energy differences of the excited states, relative to the respective ground state energy, SRI and Coulomb interaction. Quadratic fits are provided as guide to the eye. The data were generated for 10 values of σ and 30 trials for each parameter set (V_{max}, σ) .

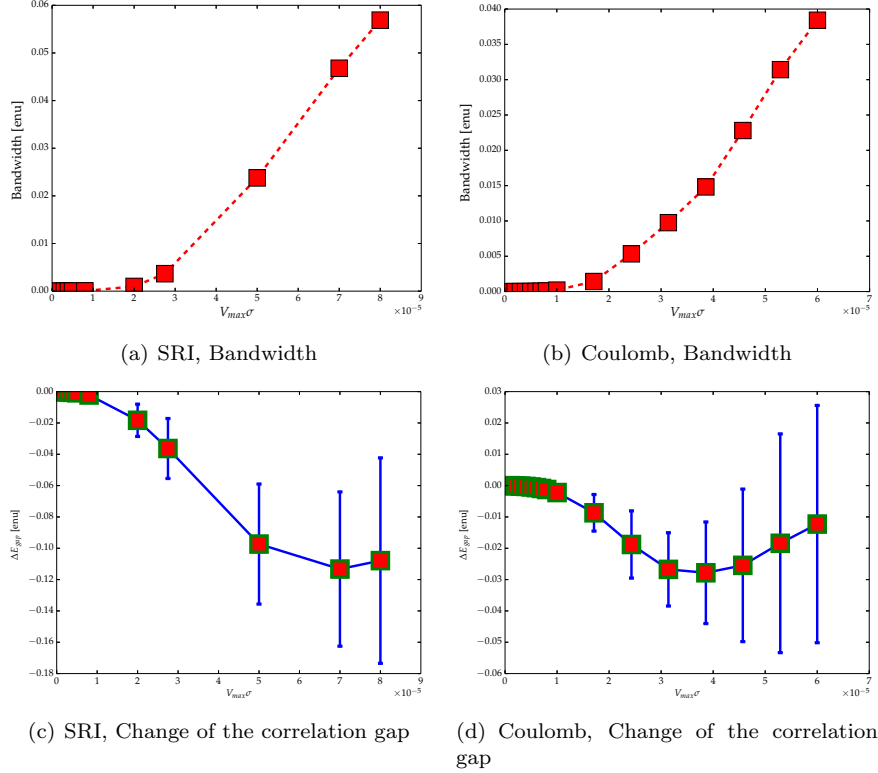


Figure 6.10: Top row: These figures show the bandwidth -along with a quadratic fit to guide the eye for both interaction types. The bottom row shows the change of the correlation gap (ΔE_{corr}) over a range of $V_{max}\sigma$. Each datapoint was generated from 30 identical sets of parameters and 10 values of σ respectively. Shown are the mean values with the variance as errorbars (not visible in all panes). Left column **SRI**, right column **Coulomb interaction**

in the subsequent sections.

6.3.3 Summary - which kind of background potentials are suitable for calculating the electron-vortex distributions?

In this section we have shown, that the superposition of (artificial) Gaussian shaped impurities creates a background potential which is suitable for the simulation of systems encountered in experiments.

To conclude the investigations put forward in this section, we are finally able to answer the following question: What values for the impurity number (N_{scatt}), width of the individual impurity (σ) and maximal value of the individual scatterer (V_{max}) are suitable to

1. produce ground states which show the hallmark of FQH systems, namely the correlation gap
2. show a near degeneracy of the 3 lowest lying states (a small bandwidth)

3. allow us to tune the correlation length of the overall potential over a wide enough range (up to half a unit cell length)?

To fulfill the condition 3, we need more than 500 impurities, taking into considerations the results from the literature discussed in subsection 6.2.2 we shall proceed with systems built up from 4000 individual scatterers ($N_{\text{scatt}} \geq 4000$)⁹.

To fulfill the first two conditions, we note that the analysis of the previous section shows, that the product (σV_{\max}) serves as an unifying parameter. The investigations on the correlation gap and the bandwidth leads us to apply **a limit to the parameter $\sigma V_{\max} < 10^{-4}$** .

6.4 About Electron - Vortex correlations and the persistence of the FQH state in systems subject to a random potentials

We have reached the point, where we investigate the electron-vortex correlations for systems with random potentials. We will employ the same methodology as for systems with a single impurity (see 5.6 at p. 117).

Let us briefly recapitulate the findings of section 5.6 where homogeneous systems and systems with a single impurity have been investigated. The binding between electrons and vortices was strongest for the homogeneous system, this is reflected in the δ -peak shape of the electron-vortex and vortex-vortex correlations g_{ev}, g_{vv} and a subsequent maximum of these distributions at $r_{ev} = 0$ (SRI) and at $r_{ev} \approx 0.7l_0$ (Coulomb interaction). The weaker correlations for inhomogenous systems showed themselves in distributions with finite values for $r_{ev} > 0$ and $r_{vv} = 2r_{ev} > 0$. We used the maximum position of $g_{ev,vv}(r)$ ($r_{ev,vv}$) as an indicator for the persistence of FQH-like correlations in an inhomogenous system. We identify $r_{ev} = 0$ with perfect FQH-type correlations and $r_{ev} > 1l_0$ with their absence. We observed a gradual expansion of the electron-vortex complex with stronger and narrower impurities. For the Coulomb interaction, the latter statements are also valid, provided that the electron-vortex composite in the homogeneous state has a finite size already. Comparison of the influence of the width and strength of the impurity showed r_{ev} to be most sensitive to changes in the width (σ) of the impurity. Infact we found systems with identical gaps (defined chiefly by the impurity strength), which either showed or lacked the FQH-type correlations.

In this section we will establish a connection between the (global) stochastic properties (correlation lengths and variance) of the external potential and the electron-vortex correlations as a measure for the persistence of the FQG type correlations.

In order to generalize our findings and to make general statements some care must be given to ensure, that the randomly generated potentials exerts no undue influence on our interpretations. Remember that the calculations are done with a fix set of parameters V_{\max} and σ with randomly distributed impurity

⁹Some checks will be performed however with systems built from 6000 impurities. Calculations for larger systems (6 electrons) were performed with 4800 impurities, keeping the impurity concentration constant.

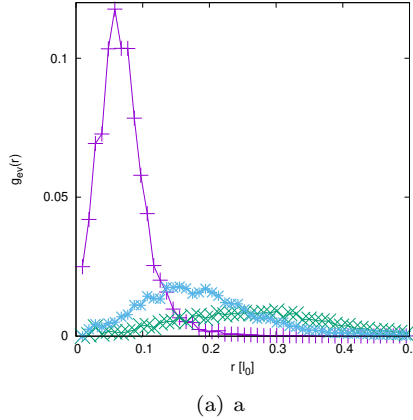


Figure 6.11: (a) Shows g_{ev} (not normalized) for three representations of a potential generated from 4000 impurities with $\sigma = 1l_0$ and $V_{max} = 0.0001$, **SRI**. The correlation lengths of the random potentials are 0.7, 0.8 and $2 l_0$ respectively.

positions. These parameters result in different representations of the potential with varying values for the correlation lengths and fluctuation, subsequently changing the electron-vortex distributions. To further this notion we show in Fig. 6.11 selected results for such a constant set of parameters $V_{max}, \sigma, N_{scatt}$. We find the influence on the maximum position of $g_{ev}(r)$ to be substantial. Further analysis for 50 representations of the potential for this particular set of parameters unveils an average position of the maximum of appr. $0.2 \pm 0.02l_0$. In what follows we give the average value of r_{ev} (for identical parameter sets $(\sigma, V_{max}, N_{scatt})$) and the standard deviation as the error margin when noted.

6.4.1 How does the size of an electron-vortex composite change? - Results for random potentials-

We present the results in two different ways. First the dependence of the electron-vortex distance (r_{ev}) with respect to the fluctuation of the potential and to the correlation gap is presented and discussed. In the second part of this subsection we will address the interdependence of r_{ev} and the correlation length of the underlying potential field and the influence of l_{corr} onto the electron-vortex correlations.

6.4.1.1 The size of the electron-vortex complex vs. the variance and the correlation gap

Results describing the impact of a changing variance on the size of the electron-vortex complex are shown in Fig. 6.12. We find the electron-vortex correlations to vary within the margin of error over a wide range of parameters and hence to be independent of the fluctuation of the potential.

Since we found the fluctuation of the background potential to determine the correlation gap, we analyze the change to the electron-vortex correlations also with respect to the correlation gap. In Fig. 6.13 (a) we show r_{ev} vs E_{gap} calculated over a wide range of the parameter space (with $V^{max}\sigma \leq 10^{-4}$).

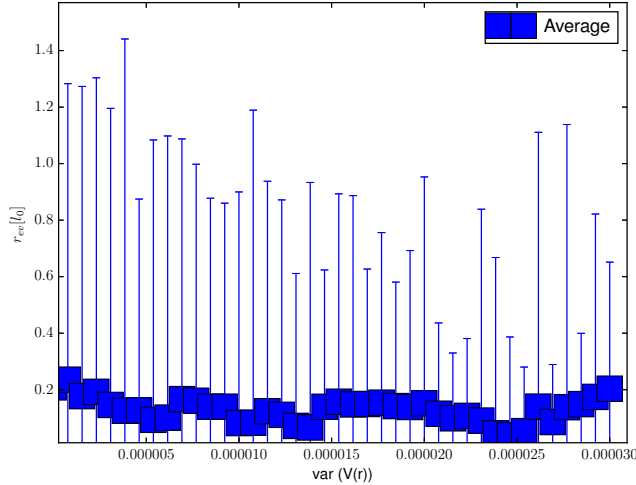


Figure 6.12: This image shows the dependency of the size of the electron-vortex complex on the fluctuation of the generating potential. The values were generated from 6000 calculations and averaged over 30 equally large intervals, indicated by its mean values, of the variance. System with 6 electrons and Short Range interaction. The full data are provided in the appendix (Fig. ??, p. ??).

, Fig. 6.13 (b) shows the same data in a double logarithmic plot . Since the results fluctuate in particular for larger values of $V^{max}\sigma$, only results where the bandwidth is smaller than the correlation gap have been plotted (see page ?? for supplementary data and discussions)¹⁰.

Inspection of the plots suggests, that the size of the electron vortex complex increases with decreasing correlation gap and no FQH-like correlations persist in systems with correlation gaps smaller than 80 % of the homogeneous value. For small deviations of the correlation gap from its homogeneous value, the electron-vortex correlations remain on average at the homogeneous form (2 vortices on top of each electron), thus signaling unperturbed FQH-correlations in the ground state, with a large variance of r_{ev} however. The double logarithmic plot shown in Fig. 6.13(b) suggest $r_{ev}(E_{gap}) = \sqrt{aE_{gap}} + b$ as an analytical description.¹¹

The increasing size of the electron-vortex composite with the shrinking correlation gap (or the lifting of the degeneracy of the ground state) as a hallmark of the weakening and possible dissolution of the FQH regime is in agreement both with literature and the results presented in the previous chapter (cf Section 5.7, p. 130).

In Figs. 6.14¹² we show the electron-vortex correlations only for systems with a gap essentially unchanged from the homogeneous system. For both interaction

¹⁰This restriction results in fewer admissible datasets with smaller values for r_{ev} .

¹¹with $a = 9.95 \pm 0.055$ and $b = 0.031 \pm 0.012$ for this particular dataset

¹²The negative values of Δr_{ev} for the Coulomb interaction are attributed to the finite size of the electron-vortex complex in the homogeneous system and the related margin of error for the fitting process.

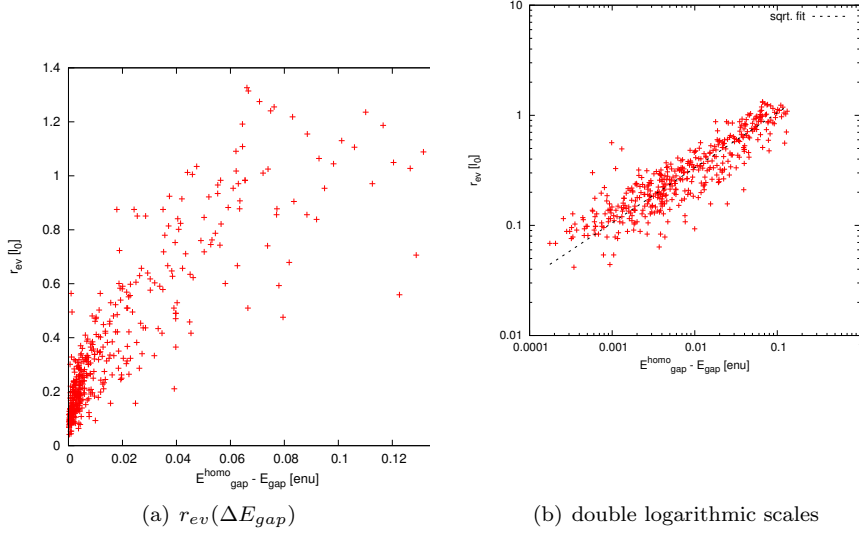


Figure 6.13: r_{ev} vs E_{gap} calculated for a system generated from 4000 impurities (SRI, $N_e = 5$). The right pane shows the same data as the left pane but in a double logarithmic plot along with a fitted square root function

types, we find the size of the electron vortex complex to be somewhat increasing with a closing gap. However, the size of the electron-vortex complex fluctuates within a large range - we find systems with and without FQH-type correlations for an essentially constant gap. We hence conclude, that neither the variance nor the correlation gap are the dominating factors which destroy or preserve the FQH-type electron-vortex correlations.

6.4.1.2 The degeneracy of the ground state and the size of the electron-vortex complex

The three-fold degenerate ground state, which is a topological property of the FQH-systems was analyzed by a great many authors¹³ and its topological nature is one of the main arguments for the stability of the FQH-state. It is therefore appropriate to establish, whether the bandwidth (as a measure for the degeneracy in our finite size system) can also be used as an indicator of the transition from FQH-states of Laughlin type¹⁴ to insulating states or whether the size of the electron-vortex complex is an appropriate and in fact the best indicator for the existence of Laughlin-type correlations in the sample.

In Fig. 6.15 we show the size of the electron-vortex composite over the degeneracy of the ground state (bandwidth). The plots show two different slopes of $r_{ev}(\Delta E)$, hence two different regimes. For small values of the bandwidth

¹³See chapter 3.2.5, 2.4.2 for discussion of the literature and chapter 5.2.1.5 for a treatment of the bandwidth by perturbation theory).

¹⁴FQH correlations for a better readability from hereon

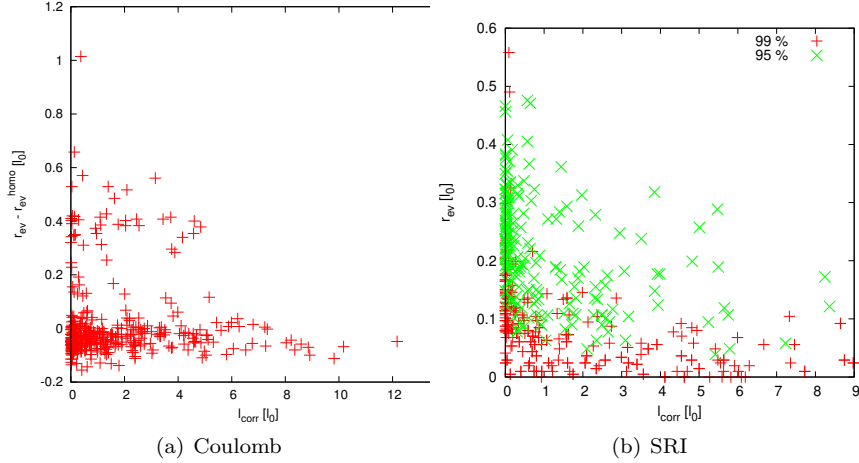


Figure 6.14: Size of the Electron- Vortex complex vs. correlation length for systems with constant correlation gaps, **coulomb interaction** (left) and **short range interaction** (right). Note that the The correlation gap is within a range of 1% or 5% of the homogeneous value respectively.

$(\Delta E < 10^{-3})$ - hence nearly degenerate ground states - the size of the composite increases weakly and linearly, while for larger values of ΔE the averaged electron-vortex distance grows faster. The appearance of these two regimes are in accordance with the finding (see sec. 5.2.1.5, p. 89), that a strong increase of bandwidth is caused by coupling over the correlation gap changes only weakly over the parameter range tested. In particular (apart from a linear dependence for small values of the band width) the size of the electron-vortex complex is not strongly influenced by the bandwidth within the smaller bandwidth regime.

To underpin the last statement we provide another analysis in Fig. 6.16, which makes it even more clear, that even for a nearly perfect degenerate ground state, the size of the electron vortex varies strongly for both interaction types.

6.4.2 The size of the electron-vortex complex and the correlation length of the impurity potential

In the previous chapter we have compared the size of the correlation gap and the quality of the electron-vortex correlations (e.g. Fig. 5.46) for single impurities. We found, that for a wider impurity (which we relate to a larger correlation length of the potential), a system with an essentially constant gap is rendered incompressible, while for a narrow impurity (a shorter correlation length), the defining electron-vortex correlations are not of the FQH type. In the next part, we study whether such a behavior can also be observed for systems with a random background potential. Therefore we analyze the connection between the correlation length of the potential and the quality of the FQH-type electron-vortex correlations and hence the existence of an incompressible FQH state. We analyze this relation from different angles. First we use aggregated values for the correlation length and the size of the electron-vortex complex. We follow this analysis by an analysis of the raw data.

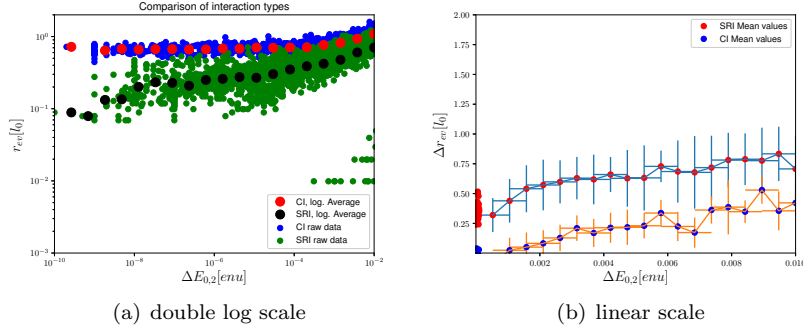


Figure 6.15: These images show the size of the electron-vortex complex versus the bandwidth (degeneracy of the ground state) for Coulomb and Short range interaction. Note the double logarithmic scale in the left pane. The averaged value were generated in such a way, that for the left pane the values for ΔE were chosen to be logarithmic equidistant, while in the right pane linearly equidistant values were chosen. The error bars in the right pane denote the standard deviation. In the right pane, the difference of r_{ev} from the values of the respective homogeneous system are shown. Lines are guides to the eye.

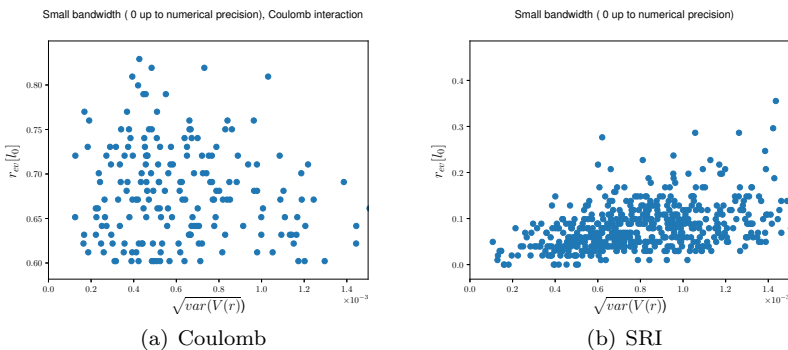


Figure 6.16: Size of the electron-vortex composite for systems with perfect degenerate groundstates over fluctuation of the background potential. (a) Coulomb (b) Short Range interaction. Note that absolute values for r_{ev} are given and the average electron-vortex distance is 0.7 magnetic lengths for coulombic systems.

Let us first examine the results shown in Figs. 6.17(a-b). All plots show the same characteristic: for small correlation length - hence uncorrelated potentials- the size of the electron-vortex complex is significantly larger than for strongly correlated potentials. This indicates a weakening of the correlations between electrons and vortices for uncorrelated potentials. For weak potentials ($V_{max}\sigma < 5 \cdot 10^{-5}$), the average size of the electron-vortex composite remains smaller than $1 l_0$ for all correlation lengths. For stronger potentials, the FQH correlations vanish for small correlation lengths, while for stronger correlated potentials ($l_{corr} > 1.5l_0$) the size of the electron-vortex complex is smaller than $1 l_0$ and hence the state is incompressible. This leads us to the conclusion, that a (phase) transition from the Fractional Quantum Hall state to an insulating state - driven by random disorder - takes place at a correlation length of approximately $1 l_0$ in our model system.

When comparing the impact of the two types of electron-electron interactions (Fig. 6.19), we find the same characteristic for both interaction types. However the change in r_{ev} is slightly more pronounced for systems subject to the short-range interaction. One may speculate, that the higher order components of the pseudopotentials of the long range electron-electron interaction reduce the effect of the background potential.

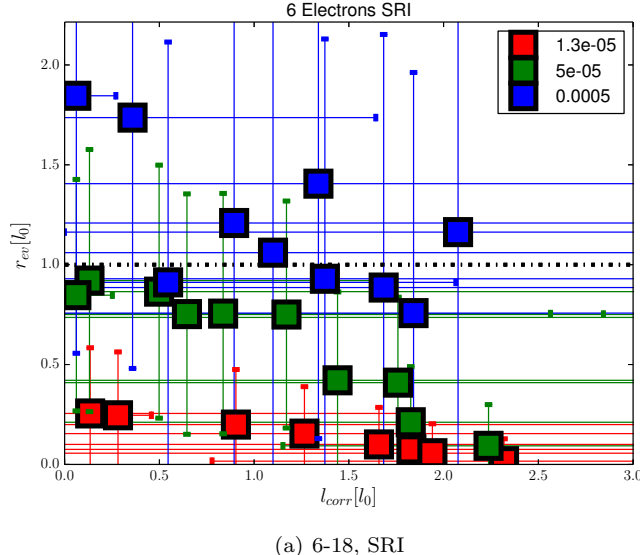
Let us now study the results without performing any prior averaging. In Figs.6.20 (a) we show the strength of the electron-vortex correlations (color coded) over the fluctuation and the correlation length of the potential for all many-body states. We find clear evidence for the existence of two regimes with regard to the electron-vortex correlations, those of Laughlin type (with small values of r_{ev}) and those without those correlations. The measure and the threshold values used in this argument are the same as for the single impurity system (see 5.6.3.1, p. 129). With some averaging we obtain a slightly clearer picture (Fig.6.20 (b)). Although the data are not fully conclusive, we find the regime of FQH-type correlations for potentials with correlation length larger than one magnetic length.

Following the idea of Arovas [11] et. al, which interpreted the transition from localized to delocalized states in the single electron picture as an activated process, we fit all calculated data to an exponential of the form $r_{ev}(l_{corr}) = a \exp(-l_c \cdot l_{corr}) + c$ (Figs. 6.22) We obtain for both interaction types $l_c \approx 1l_0$ ¹⁵. In Fig. 6.18 we apply an exponential fit to two sets of data generated from potentials with constant parameters V_{max} and σ . For these particular data we find the critical correlation l_{crit} to be reduced for stronger fluctuations of the potentials.

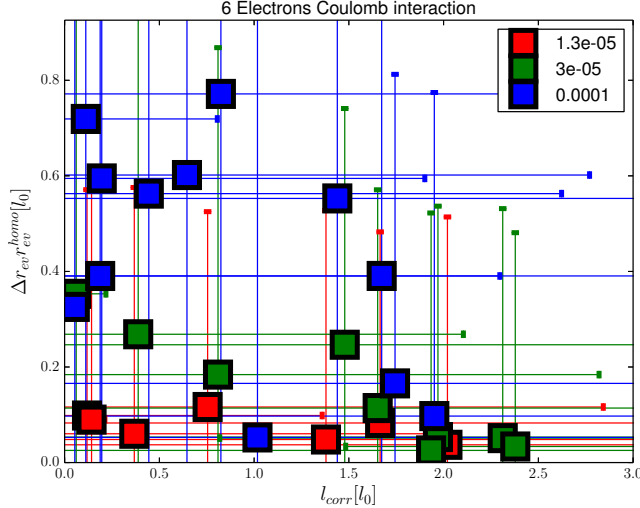
6.5 Summary, Conclusions and Discussions

In this section we extended our study by analyzing random electrostatic potentials and their influence on the spectra and the electron-vortex correlations. The potentials are constructed by superposition of single gaussian impurities (which we studied in sec. 5) in such a way, that the global stochastic properties fluctuation and correlation length are the determining parameters. The potentials were chosen in such a way, that no additional charge is introduced into the

¹⁵with a slightly larger value for the Coulomb interaction. In Fig. 6.18 we provide data and fits for selected values of $V_{max}\sigma$.



(a) 6-18, SRI



(b) 6-18, Coulomb

Figure 6.17: This figure summarizes the dependency $r_{ev}(l_{corr})$ for systems with six electrons interacting via SRI and Coulomb interaction respectively, subject to a background potential generated from 4800 impurities. The data were generated from 50 systems with fixed sets of values $V_{max}\sigma$ (as shown in the legends). Shown are the mean values of r_{ev} and l_{corr} , the errorbars denote the respective standard deviation for each set of the systems representations. For the Coulomb interaction plot, the change of r_{ev} with respect to the value for the homogeneous system ($0.7 l_0$) is given. See also Fig. ?? for a complete set of results for the individual systems.

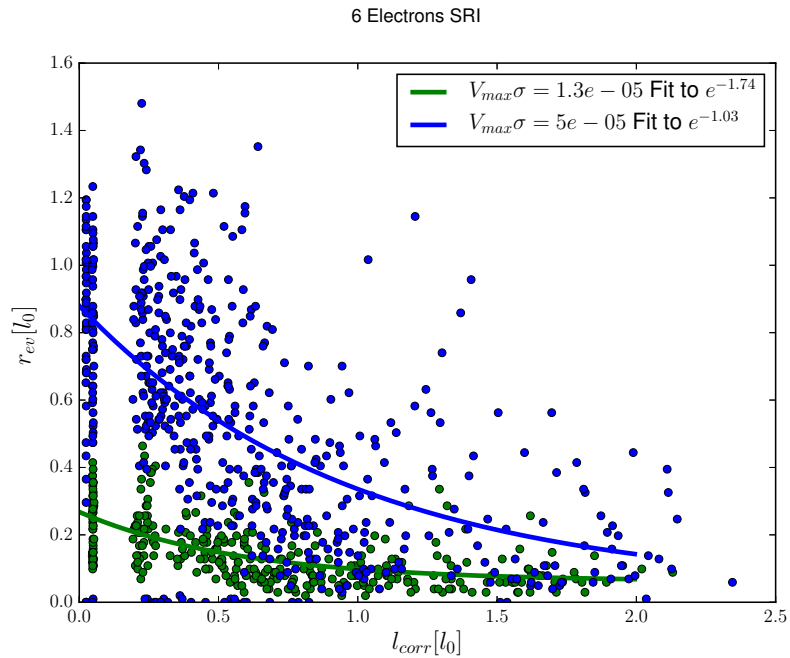


Figure 6.18: Size of the electron vortex complex - $r_{ev}(l_{corr})$ - for a 6/18 system for some choices of $V_0\sigma$, **Short range interaction**, For each value of $V_0\sigma$ a fit to $ae^{-bl_{corr}} + c$ is provided as a guide to the eye.

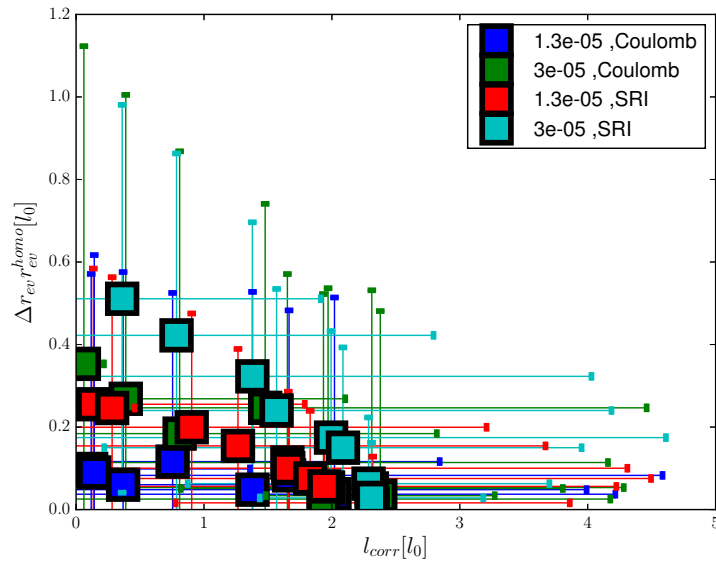


Figure 6.19: This image shows $r_{ev}(l_{corr})$ to compare the effect of the two electron-electron interaction types for some selected values of $V_{max}\sigma$, calculated for systems with 6 electrons.

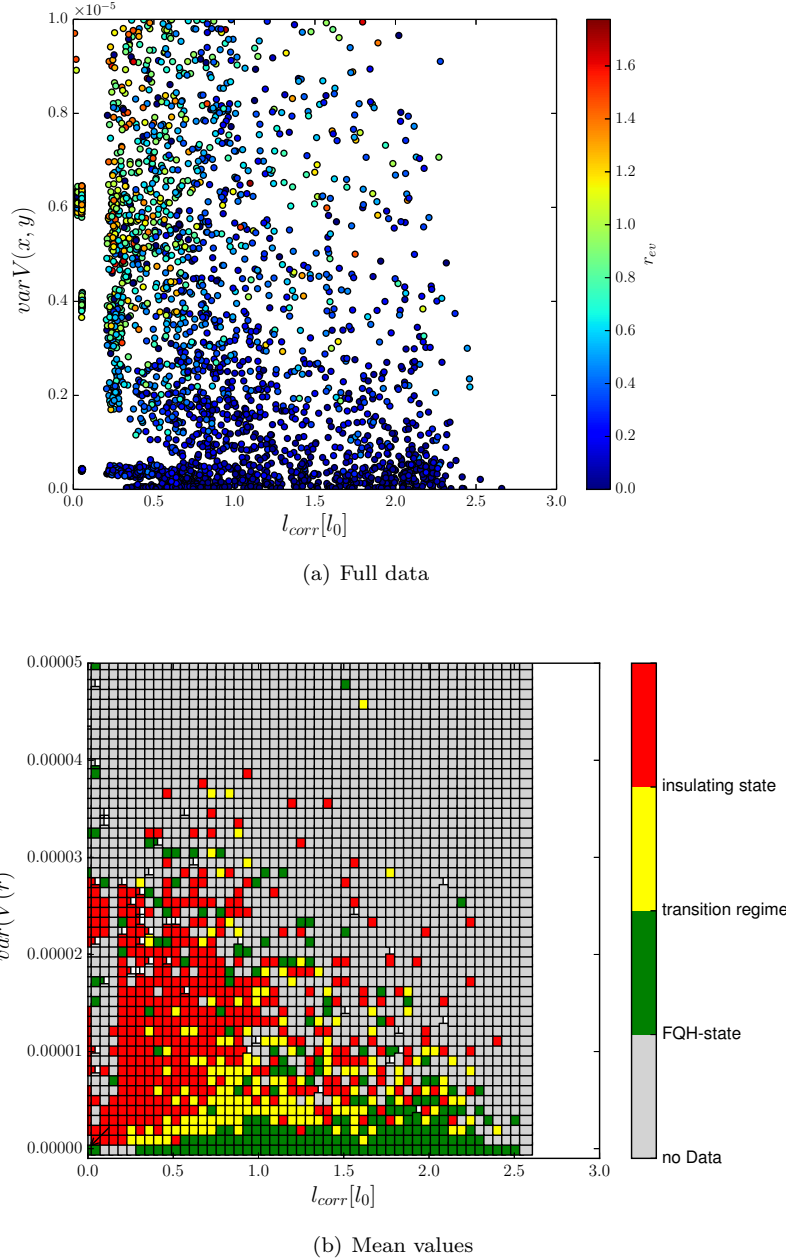


Figure 6.20: This image shows the size of the electron-vortex complex (color-coded) vs. the variance and correlation length of the random potential. (Top) Dark blue color of the data points indicate Laughlin type correlations, light green to red color indicates $r_{ev} > 1l_0$. (Bottom) shows the mean value of r_{ev} for the states within an interval of l_{corr} and $var(V(x, y))$. We apply the following limits to the coloring: $\langle r_{ev} \rangle < 0.3l_0$, $\langle r_{ev} \rangle < 0.8l_0$ and $\langle r_{ev} \rangle > 0.8l_0$. Each point represents 7 different values on average. Data for systems with six electrons, 4800 impurities and **Short Range Interaction** over a wide range of the parameters σ, V_{max} .

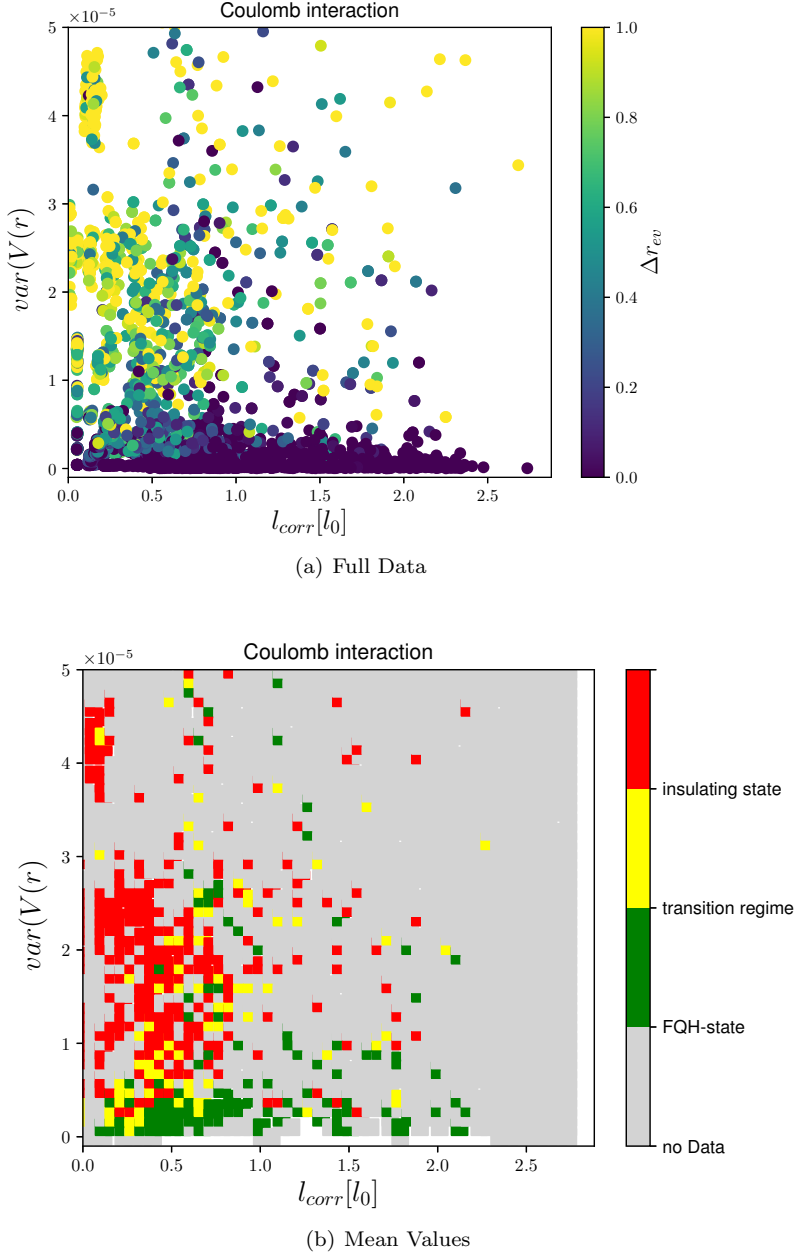
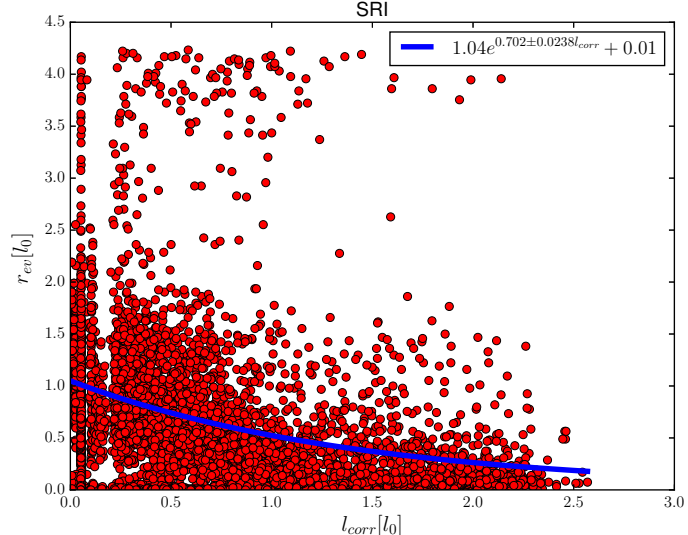
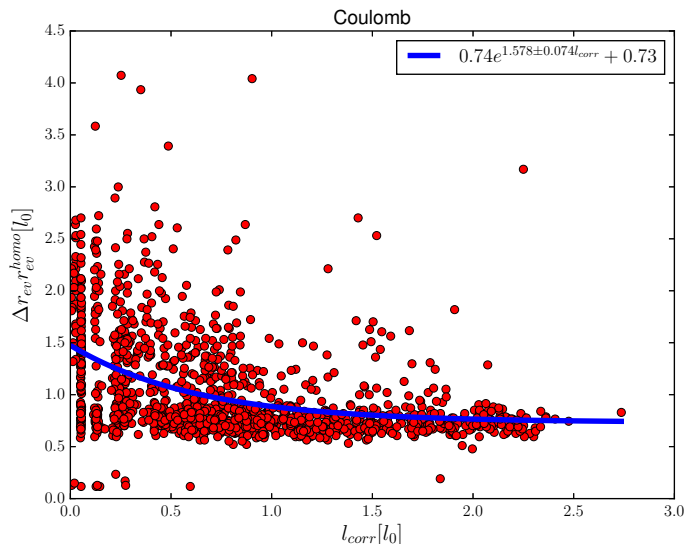


Figure 6.21: This image shows the change in size of the electron-vortex complex (color-coded) vs. the variance and correlation length of the random potential calculated for appr. 3500 different systems. (Top) Dark blue color of the data points indicate correlations which are identical to homogeneous system , light green to yellow color indicates $r_{ev} > 1l_0$. (Bottom) shows the mean value of $\Delta\langle r_{ev} \rangle$ for the states within an interval of l_{corr} and $\text{var}(V(x, y))$. We apply the same limits as in Fig. 6.20 to the coloring: $\Delta\langle r_{ev} \rangle < 0.3l_0$, $\Delta\langle r_{ev} \rangle < 0.8l_0$ and $\Delta\langle r_{ev} \rangle > 0.8l_0$. Each point represents 7 different values on average. Data for systems with six electrons, 4800 impurities and **Coulomb Interaction** over a wide range of the parameters σ, V_{max} . Note that the data shown here are not subject to the condition, that the correlation gap shall be larger than the bandwidth. In the appendix, we show (Fig. ?? (p. ??)) the same plots for systems with $\Delta E_b < \Delta E_{\text{corr}}$



(a) 6-18, SRI



(b) 6-18, Coulomb

Figure 6.22: These images show the size of the electron-vortex complex ($r_{ev}(l_{corr})$) generated from all data calculated over the whole parameter space. To guide the eye, the data were fitted to an exponential function ($\propto e^{-l_c l_{corr}}$) as described in the legend. For the case of SRI (left pane), the exponential was fitted to the mean values of $r_{ev}(l_{corr}^i)$, where the intervals were chosen for minimum fitting error. The value of l_c however changes within a range of $0.1l_0$ among different choices of the intervals.

system. The many-particle spectra showed essentially the same behavior as in the case of a single impurity - the size of the correlation gap and the bandwidth are determined by the fluctuation of the potential¹⁶. The bandwidth increases and the correlation gap closes with stronger fluctuating potentials. The ground state degeneracy is lifted completely, even for weakly fluctuating fields. These effects are independent of the correlation length.

The electron-vortex correlations on the other hand are determined by the correlation length of the potential. For constant correlation gaps, the size of the electron-vortex composite is larger for weakly correlated potentials ($r_{ev} \propto \frac{1}{l_{corr}}$). A weak exponential interrelation between the correlation length and the quality of the FQH-type correlations (measured by r_{ev}) is observed. We found transitions between insulating states and FQH-states for correlation length $l_{corr} > 1l_0$. In this sense, we may rephrase the somewhat weak precondition of a 'weakly modulated background' for the existence of the FQH by the following statement - : *We expect a two dimensional electron gas under the influence of a magnetic field corresponding to a filling factor of $\nu = \frac{1}{3}$ to exhibit properties of the Fractional Quantum Hall state when the background potential is weakly fluctuating and has a correlation length larger than one magnetic length.*

When interpreting our results in the Composite Fermion picture we find that a CF dissolves more easily under the influence of an uncorrelated random background potential.

6.5.1 Generalization of the results to systems with Coulomb Interaction

The conclusion drawn so far are essentially applicable to the two electron-electron interaction types studied here. For both interaction types the essential changes of the studied properties are qualitatively identical (systems with Coulomb interaction showing smaller gaps, stronger susceptibility of the electronic density and a finite size of the electron-vortex complex) while some differences were observed for the rate of change of the entities studied under the influence of disorder.

However some caution must be used, when generalizing our findings from a model system (with a finite size and a model interaction) to systems with infinite size and Coulomb interaction. In particular the fact, that a system with Coulomb interaction does not show the perfect, delta-shaped Laughlin correlations among electrons and vortices raises the question, what limit should be applied to the average electron vortex distance in those systems.

The fact, that the FQH was observed experimentally in systems with some disorder forbids the application of the $r_{ev} < 0.7l_0$ limit to those systems. Comparing the results for systems with the two interaction types (in particular shown in Figs. 6.20 vs. 6.21) it becomes apparent, that the change r_{ev} with the correlation length and variance exhibits a similar characteristic within the limits of our method and system size..

With this analysis presented here and for single impurity systems in section 5.6.2, we advocate the use of the change (Δr_{ev}) of the average electron-vortex distance as the appropriate criterion for the persistence of FQH-type correlation

¹⁶Which corresponds to the amplitude V_0 in the single impurity case.

and the transition of the system into an insulating state. With this choice, the statement made above can be transferred to a system with Coulomb interactions.

Chapter 7

Summary of results

In this thesis we studied FQH-systems (electrons under the influence of a very strong magnetic field) disturbed by external potentials. Since the early experiments on the FQH-effect were carried out in very clean samples it is the aim of this study to influence of those impurities quantitatively. We carried out an extensive investigation of the effect of those long-range impurities onto the peculiar state of matter, in particular onto the electron-vortex correlations within this state. As a measure for the persistence of the typical FQH-type correlations in such a finite system, we study the electron-vortex correlations of the many-particle ground state

We use model systems with five and six electrons - interacting via the Short Range Interaction and the Coulomb interaction respectively - and a filling factor $\nu = \frac{1}{3}$ and investigate its many-particle ground states. These ground states were calculated numerically by methods of exact diagonalization.

For test purposes we investigated homogeneous systems, in particular the spectra, the correlation gaps and the electronic densities. All results are comparable with results from the literature. The evaluation of the electron-vortex-correlations showed the (three) vortices on top of each electron for SRI system, while the Coulombic systems exhibit an finite electron-vortex distance. We interpret this average distance to be the size of an Composite Fermion.

A thorough investigation of a model systems with one gaussian shaped impurity potentials shows the following results. The degeneracy of the ground state is lifted for weak potentials. Perturbation calculation showed, that this lifting is due to coupling of the ground state with states over the correlation gap only. The correlation gap closes with stronger impurities and the electronic density response for weak impurities shows traces of incompressibility. The characteristic width of the density distribution is of the order of one magnetic length, also for very narrow impurities. Investigating the electron-vortex correlations we found the Vortices to be displaced from the electrons. This displacement is much more sensitive to the impurities than the correlation gap. The data show, that the dominating influence is the width of the impurity, while the amplitude dominates the correlation gap size. We found that narrow impurities ($< 0.5l_0$) destroy the FQH state, while wide impurities ($> 1l_0$) preserve the typical FQH-correlations. These findings are qualitatively reproduced for systems with Coulomb interactions.

To study more realistic model systems, the electrons were subject to po-

tentials generated from stochastic impurity distributions. We find that the correlation length of the potential is responsible for the existence of the FQH-correlations, while the fluctuation (variance) of the potential dominates the correlation gap.

We found no FQH-type correlations for potentials with small correlation length ($l_{corr} < 0.5l_0$), regardless of change in the correlation gap while a potential with correlation lenght ($l_{corr} > 1l_0$) preserves the integrity of the Composite Fermions and hence the Fractional Hall state.

Chapter 8

Outlook and future plans

Appendix A

List of abbreviations, units etc.

Magnetic length	l_0	$\sqrt{\frac{\hbar}{eB}}$	$\approx 8 \text{ nm}$
energy scale	enu	$\frac{e^2}{el_0}$	
cyclotron energy	$\hbar\omega_c$	$\hbar\omega_c = \hbar \frac{eB}{m_b c}$	

Table A.1: Typical scales used in FQH calculations. The typical order of magnitudes have been given for $B = 15 \text{ T}$

Glossary

2DEG Two Dimensional Electron Gas. 8, 10

ACF Auto Correlation Function. 135

CF Composite Fermions. 36

EOM Equation of Motion. 6

IQH The Integer Quantum Hall Effect. 8

LGS Laughlin Ground State. 27

MBZ Magnetic Brillouin Zone. 20

PBC Periodic Boundary Conditions. 22

QD Quantum Dot. 110

QHE IQH + QHE. 9

QW Quantum Well. 110

SRI Short Range Interaction. 28

Appendix B

Details of perturbational calculus

Although perturbation theory is not usable to calculate the ground state of a FQH system (due to the lack of a “small” perturbation), we can derive some conclusions with regard to the gap(s) and bandwidth of inhomogenous systems.

The basic idea here is, that we obtained the many-particle groundstate(s) of a homogenous system numerically. Once we switch on an impurity ($V(\mathbf{r})$), we have a small perturbation, the effect of which we can estimate with the aid of perturbation theory and compare to the numerical results.

Let us start with the observation, that the ground state of a FQH system subject to PBC with SRI is m-fold degenerate. In this part we shall assume $m = 3$.

The perturbed Hamiltonian reads

$$\hat{H} = \hat{H}_{FQH} + \hat{V} = \hat{H}_{FQH} + V_0 \exp - \frac{(z - z_0)}{\sigma^2}, \quad (\text{B.1})$$

B.0.1 The effect of a single impurity on the bandwidth

B.0.1.1 The energy corrections

In order to treat a degenerate ground state, we apply the standard textbook approach of determining the secular equation ([84] p. 153 ff). We shall show, that the degeneracy of the ground state is not lifted in first order of perturbation theory, since the effect of the impurity potential on the degenerate states results merely in an (imaginary) phase factor. Since we observe an increasing bandwidth, we conclude (in agreement with the literature [92]), that the lifted degeneracy is due to coupling among the ground states and higher excited states (across the gap).

The perturbation matrix in our case of a threefold degenerate state reads:

$$\begin{bmatrix} H_{0,0} & H_{0,1} & H_{0,2} \\ H_{1,0} & H_{1,1} & H_{1,2} \\ H_{2,0} & H_{2,1} & H_{2,2} \end{bmatrix}$$

where

$$H_{i,j} = \langle \Psi_{0,i} | V | \Psi_{0,j} \rangle. \quad (\text{B.2})$$

We make use of the fact, that the ground state wavefunction decomposes into a center-of-mass and a relative part. The potential $V(r)$ acts only on the center of mass part, thus the matrix elements from B.2 simplify into

$$H_{i,j} = \langle \Psi_{0,i}^{CM} | V | \Psi_{0,j}^{CM} \rangle \quad (\text{B.3})$$

The impurity operator reads $\hat{V} \approx \sum_{i=1}^{N_e} e^{-r^2}$. We show now, that the particular form of the operator gives $\langle \Psi_{i,j}^{cm} | \hat{T}_{cm} \hat{V} \hat{T}^\dagger | \Psi_{i,j}^{cm} \rangle = \langle \hat{T}_{cm} \Psi_{i,j}^{cm} | \hat{V} | \hat{T}_{cm} \Psi_{i,j}^{cm} \rangle$. We switch from the r_i coordinates to the relative coordinates (\tilde{r}_i) and the center of mass coordinate R , with $r_i = \tilde{r}_i + R$. Rewriting the perturbation part of Eq.B.1 gives

$$\sum_i e^{-r_i^2} = \sum_i e^{-(\tilde{r}_i+R)^2} = \sum_i e^{-(\tilde{r}_i^2 + 2\tilde{r}_i R + R^2)}. \quad (\text{B.4})$$

The effect of the center of mass translation operator¹ onto the perturbation operator the other hand gives

$$\hat{T}_{\frac{L}{3}} V = \sum_i e^{-\tilde{r}_i^2} \cdot e^{-2\tilde{r}_i(R+a)-(R-a)^2} \quad (\text{B.5})$$

after some algebra (B.5) can be rewritten as

$$\hat{T}_{\frac{L}{3}} \hat{V} = \sum_i e^{-(Z_i+R)^2} = \hat{V}(r_i + a) \quad (\text{B.6})$$

with the substitution $Z_i = \tilde{r}_i + a$. The matrix elements (B.3) can now be rewritten as

$$\langle \Psi_{0,i}^{CM} | \hat{V} | \Psi_{0,j}^{CM} \rangle = \langle \Psi_{0,i}^{CM} | \hat{T}^{-1} V \hat{T}^{-1} | \Psi_{0,j}^{CM} \rangle = \langle \hat{T} \Psi_{0,i}^{CM} | \hat{V} | \hat{T} \Psi_{0,j}^{CM} \rangle \quad (\text{B.7})$$

The effect of the center of mass translation onto the cm wavefunction however (see [96]) is a phase factor $(-1)^{N_e(m-1)} e^{i\phi}$. The matrix elements evaluate therefore to

$$H_{i,j} = V(e^{i\phi})^{|i-j|} = V_0 \begin{pmatrix} 1 & e^{(i\phi)} & e^{(2i\phi)} \\ e^{(-i\bar{\phi})} & 1 & e^{(i\phi)} \\ e^{(-2i\bar{\phi})} & e^{(-i\bar{\phi})} & 1 \end{pmatrix} \quad (\text{B.8})$$

The secular equation reads

$$\lambda^3 - 3V_0\lambda^2 = 0 \quad (\text{B.9})$$

with the solutions $\lambda_{1,2} = 0$, $\lambda_3 = 3V_0$. This implies a twofold degeneracy of the ground state for small V_0 . This shows, that the degeneracy of the ground state is not lifted completely by the interaction of the three lowest states, but that (by virtue of higher order perturbation theory) the coupling with energetically higher states is responsible for the numerically found lifting.

The next order of perturbation theory introduces a $\frac{V_0^2}{\Delta E_{1,4}}$ term into the energy correction.

B.0.1.2 The corrections to the eigenstates

With the energy corrections from above, we are now able to write down the corrections to the eigenstates.

¹Here we restrict ourselves to a $\frac{1}{3}$ system

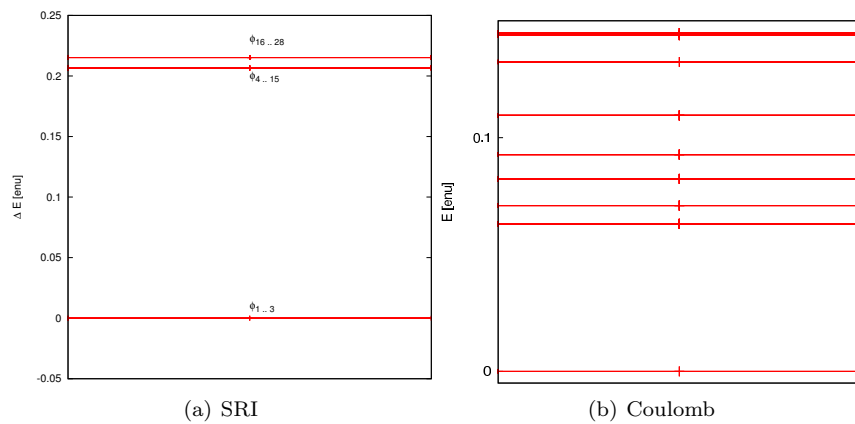


Figure B.1: The spectrum of a homogenous 5-15 system. In (a) the lowest 30 states of an SRI system are shown, while in (b) the Coulomb interaction is used. Shown are the 100 lowest eigenenergies. The degeneracy of the many particle states is 3, 24, 12, 12, 12, 15 and 3 respectively and is not visible on this scale.

Appendix C

Numerical precision of the employed algorithms and libraries

As mentioned above (see 2.5.2, p.40), different methods and libraries were used in this thesis. In particular the need for the storage of large matrices enforced the usage of sparse matrix storage formats and other diagonalization routines ([55]). A well known effect of the sparse diagonalization routines is the “mix in” of energetically higher states into the ground states. This leads to imprecisions on small energy scales, in particular when evaluating the nearly degenerate ground states (the bandwidth).

In Fig. C.1 we show the degeneracy lifting as calculated with the sparse matrix approach. The energy difference exhibits a jump, not the same smooth transition as seen in the case of a full matrix diagonalization performed with LAPACK (see Fig. 5.11)

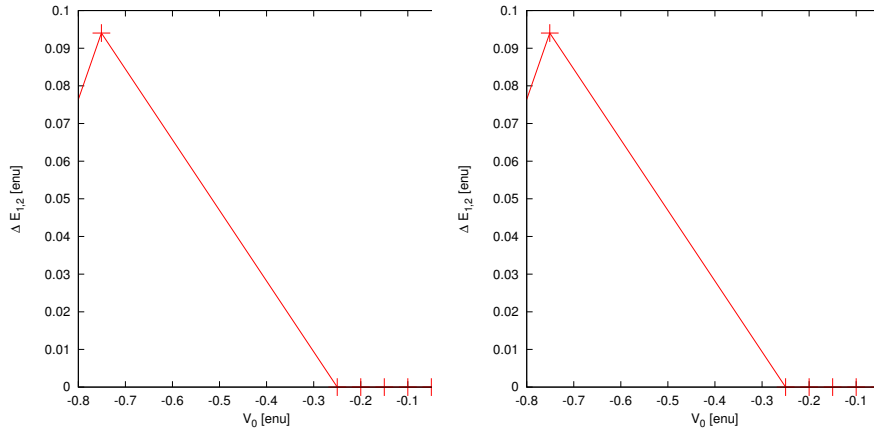


Figure C.1: (left)The energy difference between the two lowest states, calculated with the MKL implemented FEAST algorithm, 5/15 SRI. To be compared with Fig. 5.11

Appendix D

Dependency of the vortex distribution on the symmetry of the sampling electrons

The analysis of the simple displacement of vortices from "their" respective electron where we find a strong dependence of the displacement on the strength leaves us with the hope, that we can use the displacement as a measure for the "quality" of the FQH state. No displacement: Perfect FQH state, no clear attachment of vortices = no FQH state. Moreover, when choosing a particular geometry of the sampling electrons we might try to sample the FQH quality locally in the unit cell. To prove or rather disprove this idea we performed extensive numerical studies.

D.1 The sample electrons geometry

In a homogenous system the positions of the sampling electrons should have no impact on the displacement of their respective vortices. The same should hold in a disturbed system if we do not vary the distance among the electrons and the impurity.

An example calculation has been performed where the sample electrons were placed in a square structure around the impurity (which is always in the center of the unit cell). The angle α in Fig. D.1 (a) has been varied and the displacement of the vortices calculated for a system with $V_0 =$ and $\sigma = l_0$. The result is shown in Fig. D.1. We observe a variation in the vortex displacement of approximately 40 % between different sample configurations. This variation has nothing to do with a possible stronger perturbation of the many particle state but has only to do with the artificial symmetry introduced by the method we use.

From Fig. D.2 (a) we see a strong dependence of the displacement on the "artificial" rotation angle α . The order of magnitude is comparable with the size of the effect seen in Fig. Fig. D.2 (b) . This behavior is unphysical!

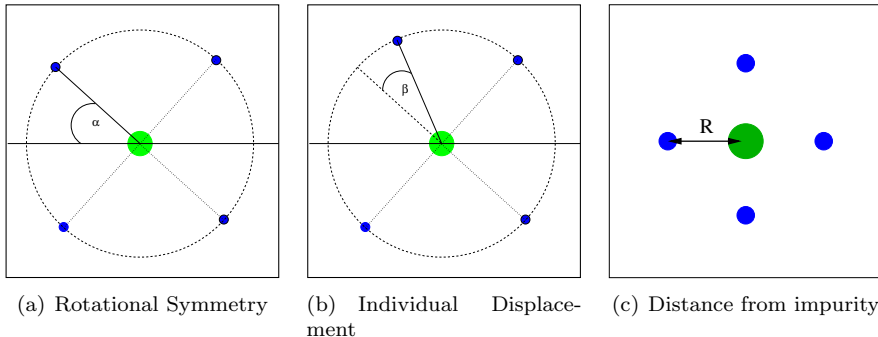


Figure D.1: Scheme of the geometrical changes of the sample electrons. The impurity is denoted by a green circle (in the center of the unit cell, the electrons are marked with blue circles. (a) shows a ratio of the whole structure, (b) the rotation of one sample electron and (c) the change of all inter-electron distances.

D.1.1 The symmetry of the electron configuration

The second test concerns the dependence of the displacement if one electron is displaced from its symmetric position on the square (Fig. D.1(b)). In D.1 (b) a value of $\beta = 0$ corresponds to a full symmetric arrangement of the electrons, while other values of β break the symmetry of the impurity sample electron ensemble. Here an unphysical dependence was found too.

interpreted as a quality measure) should occur when all electrons are on

D.1.2 Size of the sample electron configuration

The third check we perform here is on the dependence of ξ on the distance of the sampling electrons to the impurity position (cf. Fig. D.1 (c)). Here it is not a-priori clear what the expectation might be. Intuitively one could expect the state to be "more Laughlin-like" at greater distances (R) from the impurity. This would imply an inverse relationship $\xi \sim \frac{1}{R}$. An example is given in Fig. D.3. The displacement is small for $R < 3l_0$, for greater distances the displacement increases by a factor of 3.

It should be noted here, that the search algorithm refuses to accept zeroes for all electron configuration with a distance $z < 2l_0$ around the impurities maximum. All the vortices - apart from the Pauli vortices- are apparently found at the center of the unit cell (which is to say that all vortices go to the place of the attractive impurity).

Again, this is not a property due to the impurity but induced by the sample geometry. We must keep in mind the geometry of the periodic boundary conditions in which the unit cell (and the electrons) are repeated. For large values of R the sample electrons of the neighboring cell are closer to each other than to their respective impurity. Of course this is not what we are after.

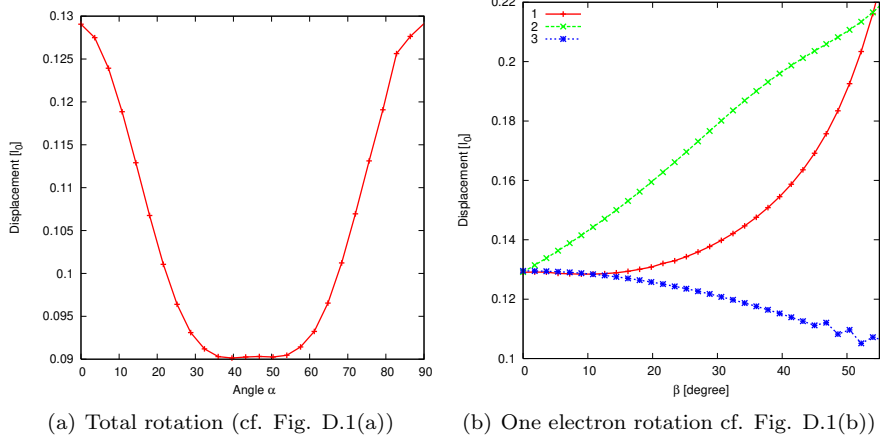


Figure D.2: Vortex displacement for a SRI state $V_0 = -0.1l_0$, $\sigma = 1l_0$, (a) rotation of the overall square (b) rotation of a single electron. Shown are the displacements for the 3 fixed electrons.

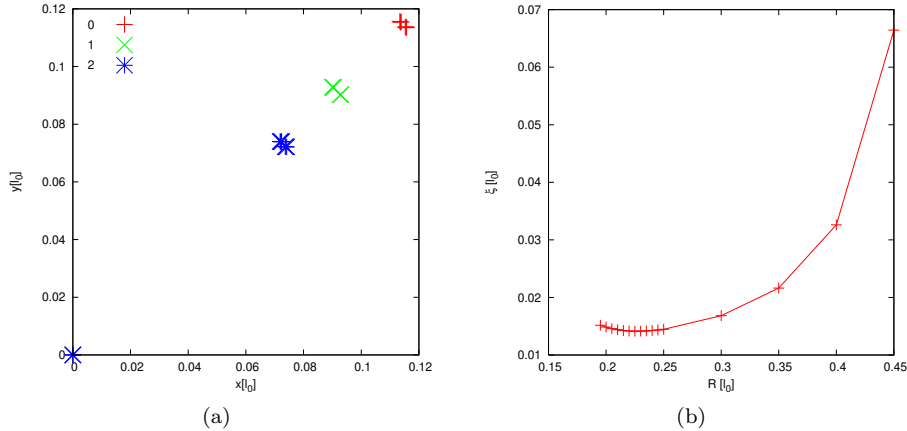


Figure D.3: (a) $\xi = r_{vortex} - r_{electron}$ for 3 choices of sample electron configuration. SRI system with $V_0 = -0.1enu$ $\sigma = 1l_0$ (b) the ξ , same system as (a).

Appendix E

Some details about the evaluation of the electron-electron correlation

In this appendix we provide a few details about the calculations performed to find the $\sim r^2$ characteristic of $g(r, r)$ as discussed in sec. 3.4. Remember that the electron-electron correlation ($g(r, r')$ or its 1D counterpart $g(r, r)$) showed a quadratic signature at small distances r . Our aim is, to find the distance r_{square} beyond which this characteristic ends and the $\sim r^6$ behavior dominates.

To do this we proceed in the following way (shown in Fig. E.1). We extract $g(r, r)$ by sampling $g(\mathbf{r}, \mathbf{r}')$ along the diagonal of the unit cell. The resulting distribution is transformed into a function, using a spline interpolation. The resulting function was differentiated twice ($g''(r, r)$, green line in the figure). We extracted the position r at which the second derivative is 5% larger than $g(0, 0)$ ¹, depicted in the figure by the arrow.

¹Obviously the choice of the threshold is somewhat arbitrary, the characteristic however is essentially the same when using other (eg 10 %) values for this threshold.

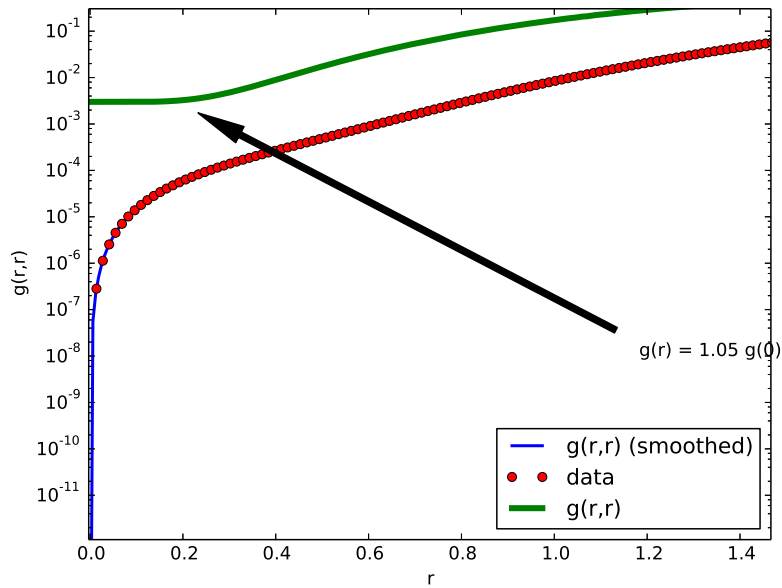


Figure E.1: Shown is the principal algorithm to estimate the extent of the r^2 dependency in the $g(r',r')$ correlation. The data (red dots) were smoothed using a 6 order spline (blue line). The green line shows the second derivative $g''(r',r')$. The point of interest is the value r_{square} were the second derivative deviates by 5 % from the $g(0,0)$ value.

Appendix F

The autocorrelation function

F.1 Outline

In Sec. 6.2 the model potential constructed from many randomly distributed gaussian scatterer has been introduced and its influence upon the vortex detachment was studied. In this appendix some background shall be given on how to characterize such a random potential. The aim of this section is not to give a full introduction on the theory of signal processing but rather to convince the reader, that the ACF is a meaningfull measure of the overall stochastic property of the potential.

In signal analysis one tries to find some periodicity in a class of random signals say $\{U(t)\}$ which answers the question: In case the signal has a value U_0 at $t = 0$ what is the probability to get the same value at some later time t . For a complete random signal (i.e. white noise) this probability distribution is a delta distribution, for a periodic signal a family of delta peaks will be found with their maxima at the time intervall, and so forth. The mathematical representation is the Autokorrelation distribution

$$A(t') = \int U(t)U(t')dt \quad , \quad (\text{F.1})$$

which we adapt to the potential distribution as

$$\Xi(\mathbf{r}') = \int_{\text{unitcell}} V(\mathbf{r})V(\mathbf{r} + \mathbf{r}')d\mathbf{r}^2 \quad . \quad (\text{F.2})$$

This is a convolution of the 2D potential function with itself. Although no general closed form of the autocorrelation function can be given, a few special cases are worth mentioning here.

In the sections below some example functions along with the autocorrelation functions are given.

F.1.1 The case of constant potential

Fehlt, correlation length = ∞

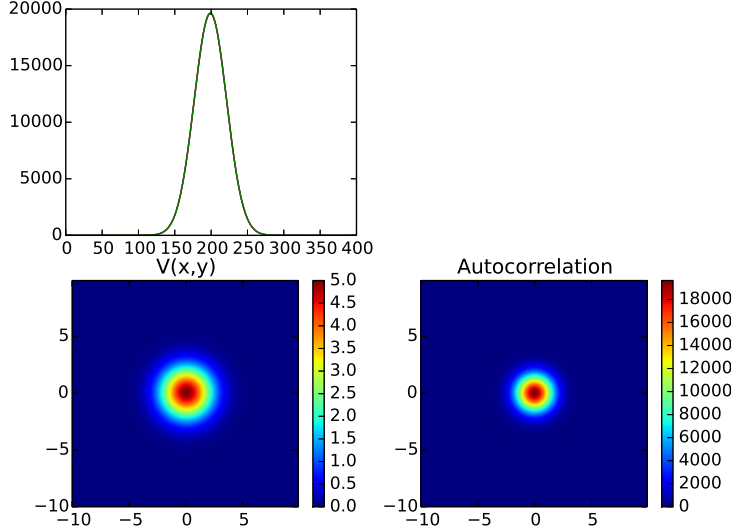


Figure F.1: The picture shows: (bottom left) the electrostatic potential $V(x, y) \propto \exp -\frac{r^2}{\sigma^2}$. Bottom right: The autocorrelation function $ACF(k)$ of $V(x, y)$. The 2D plot in the top row shows cut $ACF(x, y = \text{const.})$ $ACF(x = \text{const.}, y)$ respectively.

F.1.2 The case of a single gaussian potential

Lets start with the case of a single gaussian scatterer, where the autocorrelation can be calculated as

$$\Xi(\mathbf{r}') = \int V_0 e^{-\frac{r^2}{\sigma^2}} V_0 e^{-\frac{(r+r')^2}{\sigma^2}} \propto e^{-\frac{(r+r')^2}{\sigma^2}}. \quad (\text{F.3})$$

The ACF reads

$$ACF(\xi, \nu) = \int_{-\infty}^{+\infty} \int_{-\infty}^{+\infty} V \quad (\text{F.4})$$

along with the autocorrelation function is shown in Fig. F.1.

the autocorrelation function is again a gaussian function with σ - hence the correlation length is the same as that of their potential generating gaussian.

F.1.3 The case of a periodic potential

Another interesting example is the case, where the potential has a clear periodicity. In Fig. F.2 we show a potential $V(x, y) = \sin(x) + \cos(y)$ along with the autocorrelation function. It is obvious, that the ACF shows the periodicity clearly, with maxima distributed according to ...

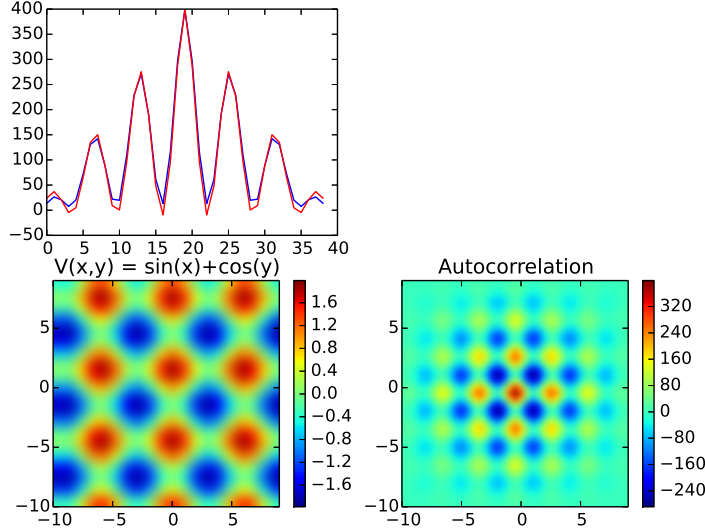


Figure F.2: The picture shows: (bottom left) the electrostatic potential $V(x, y) = \sin(x) + \cos(y)$. Bottom right: The autocorrelation function $ACF(k)$ of $V(x, y)$. The 2D plot in the top row shows cut $ACF(x, y = \text{const.})$ $ACF(x = \text{const.}, y)$ respectively.

F.1.4 The case of white noise

The last example is the case, where the potential is completely random with no correlation at all. This is modelled mathematically as a white noise distribution. Fig. F.3 shows such an example, along with the ACF. It is clear, that the CF in such a case is a delta function.

A typical shape of Ξ is shown in Fig. . The interpretation of the function shows (a)

- the maximum at the origin (V^2),
- the exponential decay with a typical length σ
- zero probability at longer distances

F.2 Metropolis Algorithm

Throughout the work extensive usage was made of “sampling the whole configuration space”. In order to do this in a meaningful way, we need to keep in mind, that the configuration space is not constantly populated, but some configurations of electrons are more likely to be found in reality than others. Physically this is due to the high energetic costs of having electrons close together as opposed to the equidistant - rather homogenous- distribution of the electrons. To capture this (and in order to avoid the overrepresentation of non-likely electron

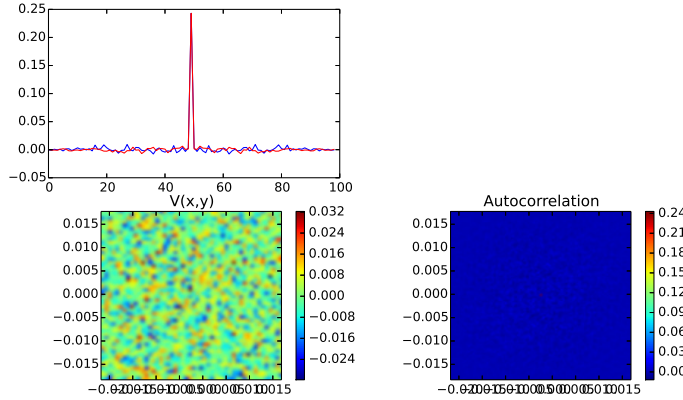


Figure F.3: The picture shows: (bottom left) the electrostatic potential $V(x, y)$ resembling white noise. Bottom right: The autocorrelation function $ACF(k)$ of $V(x, y)$. The 2D plot in the top row shows cut $ACF(x, y = \text{const.})$ $ACF(x = \text{const.}, y)$ respectively.

configuration) we need to include the physics in the generation of the electron positions.

A wide class of algorithms exists, which model those “tainted” monte carlo algorithms. They are tainted in the sense, that a pure stochastic sampling of configuration space is supplemented by an additional restriction to the selection process. Describe the algorithm here. Refer to simulated annealing and traveling salesman/Metropolis algorithm.

F.2.1 The algorithm

1. Use a standard random number generator to generate $N - 1$ electron positions.
2. calculate the “modulus” of the wave-function with those electrons
3. compare this modulus with the modulus from the previous step - accept this set of electron positions if either the modulus is smaller (i.e. the configuration is more likely in a physical sense). The step is rejected with a tunable probability if the modulus increases.
4. search the zeros and start over with 1.

F.3 Statistical properties of the many impurity states

In order to ensure that the choice of the randomly generated potential is not influencing the desired validity of our finding some checks have been performed. They are summarized in Table F.1.

The results have been obtained in the following manner:

Imp. count	average gap	σ_{gap}	bandwidth	$\sigma_{\text{bandwidth}}$
1000	0.201	0.02	0.00017	7e-05
1000	0.205	0.001	1.3e-05	1.45e-05
4000	0.19	0.01	0.008	1e-05
4000	0.205	0.001	1.5e-05	1.9 e-05
6000	0.206	2 e-05	1.72 e-06	1.1e-06
7500	0.201	0.006	0.00013	0.0001
7500	0.205			
10000	0.196	0.0082	0.0003	0.00043
10000	0.204	0.0024	9.2 e-05	7e-05

Table F.1: Statistical evaluation of the energies. Average value of the band gap and the band width and the standard deviation are shown. SRI , averaged over 100 runs with weak impurities.

1. 100 different potential with the same overall parameters were created and the ground state was calculated
2. the gap size and the bandwidth were obtained from the spectra and the mean value and the standard deviation have been calculated.
3. this procedure was performed for 3 different types of potentials (created from 100, 1000 and 4000 gaussian impurities respectively) and for 2 sets of parameters. Those parameters were chose in such a way, that for “weak” and “smooth“ potentials the gap size is essentilaly conserved and for ”strong“ and corrugated” potential the gap size is diminished.

The results of Table F.1 show, that for all cases the results do not vary greatly. This allows us to safely assume, that whatever conclusions we draw, they are independent of the particular distribution of the scatterer.

Glossary

2DEG Two Dimensional Electron Gas. 8, 10

ACF Auto Correlation Function. 135

CF Composite Fermions. 36

EOM Equation of Motion. 6

IQH The Integer Quantum Hall Effect. 8

LGS Laughlin Ground State. 27

MBZ Magnetic Brillouin Zone. 20

PBC Periodic Boundary Conditions. 22

QD Quantum Dot. 110

QHE IQH + QHE. 9

QW Quantum Well. 110

SRI Short Range Interaction. 28

Bibliography

- [1] Nobel Media AB 2014. The 2016 nobel prize in physics - press release. Web, Oct 2016. http://www.nobelprize.org/nobel_prizes/physics/laureates/2016/press.html.
- [2] Fuchs B. A., Berry J., Reed J.W., and Shabat B.V. *Functions of a complex variable : and some of their applications. Original translation by J. Berry. Revised and expanded by J. W. Reed*, volume 51 of *International series of monographs in pure and applied mathematics*. Pergamon Press, Oxford, 3 edition, 1964.
- [3] Abrikosov A.A., Gorkov L.P., and Dzyaloshinski I. E. *Methods of quantum field theory in statistical physics*. Dover Publications Inc., New York, 1975.
- [4] MacDonald A.H. Compressible strips, chiral luttinger liquids and all that jazz. [cond-mat/9512043](https://arxiv.org/abs/cond-mat/9512043), 1995.
- [5] Y. Aharonov and D. Bohm. Significance of electromagnetic potentials in the quantum theory. *Physical Review*, 115(3):485–491, August 1959.
- [6] A. Akhmerov, J. Sau, A. van Heck, S. Rubbert, R. R Skolasinski, B. Nijsjolt, I. Muhammad, and T. Rosdahl. Topology in condensed matter: tying quantum knots, 2021. <https://topocondmat.org>.
- [7] T. Ando and H. Aoki. Finite-size scaling study of localization in landau levels. *Journal of the Physical Society of Japan*, 54(6):2238, June 1985.
- [8] Tsuneya Ando, Alan B. Fowler, and Frank Stern. Electronic properties of two-dimensional systems. *Rev. Mod. Phys.*, 54(2):437–672, Apr 1982.
- [9] Tsuneya Ando and Yasutada Uemura. Theory of quantum transport in a two-dimensional electron system under magnetic fields. i. characteristics of level broadening and transport under strong fields. *Journal of the Physical Society of Japan*, 36(4):959–967, 1974.
- [10] H. Aoki and T. Ando. Effect of localization on the hall conductivity in the two-dimensional system in strong magnetic fields. *Solid State Communications*, 38:1079–1082, 1981.
- [11] Daniel P. Arovas, R. N. Bhatt, F. D. M. Haldane, P. B. Littlewood, and R. Rammal. Localization, wave-function topology, and the integer quantized hall effect. *Phys. Rev. Lett.*, 60(7):619–622, Feb 1988.

- [12] N. W. Ashcroft and D. W. Mermin. *Solid State Physics*. Saunders College Publishing, 1975.
- [13] G Boebinger, A. M. Chang, H. L. Stoermer, D. C. Tsui, J. C. M. Hwang, A. Cho, C. Tu, and G. Weimann. Activation energies and localization in the fractional quantum hall effect. *Physical Review B*, 36(15):7919 – 7928, 1987.
- [14] G. S. Boebinger, A. M. Chang, H. L. Stormer, and D. C. Tsui. Magnetic field dependence of activation energies in the fractional quantum hall effect. *Phys. Rev. Lett.*, 55(15):1606–1609, Oct 1985.
- [15] N. E. Bonesteel. Composite fermions and the energy gap in the fractional quantum hall effect. *Phys. Rev. B*, 51(15):9917–9921, Apr 1995.
- [16] Cambridge, editor. *Numerical Recipes in C*. Cambridge University, 1998.
- [17] T. Chakraborty and P. Pietiläinen. *The Quantum Hall Effects*, volume 85. Springer, Berlin and Heidelberg, 2 edition, 1995.
- [18] Tapash Chakraborty. Spin-reversed quasiparticles in the fractional quantum hall effect: Many-body approach. *Phys. Rev. B*, 34(4):2926–2928, Aug 1986.
- [19] Andrey Chaves, F. M. Peeters, G. A. Farias, and M. V. Milošević. Vortex-vortex interaction in bulk superconductors: Ginzburg-landau theory. *Phys. Rev. B*, 83:054516, Feb 2011.
- [20] Y. J. Chen. The equivalence of quasiparticles to one particle in the Laughlin state. *Journal of Physics A, Mathematical and General*, 23(4):597–600, 2 1990.
- [21] Mahan G. D. *Many-particle physics*. Physics of solids and liquids. Plenum Press, New York, 2 edition, 1990.
- [22] Mattuck Richard D. *A guide to Feynman diagrams in the many-body problem*. Dover Publications, New York, 2 edition, 1976.
- [23] A. F. Dethlefsen, E. Mariani, H.-P. Tranitz, W. Wegscheider, and R. J. Haug. Signatures of spin in the $\nu = 1/3$ fractional quantum hall effect. *Physical Review B (Condensed Matter and Materials Physics)*, 74(16):165325, 2006.
- [24] A. L. Efros. Homogeneous and inhomogeneous states of a two-dimensional electron liquid in a strong magnetic field. *Phys. Rev. B*, 45:11354–11357, May 1992.
- [25] A.L. Efros. Density of states of 2d electron gas and width of the plateau of iqhe. *Solid State Communications*, 65(11):1281 – 1284, 1988.
- [26] J. P. Eisenstein, K. B. Cooper, L. N. Pfeiffer, and K. W. West. Insulating and fractional quantum hall states in the first excited landau level. *Phys. Rev. Lett.*, 88(7):076801, Jan 2002.

- [27] J. P. Eisenstein, L. N. Pfeiffer, and K. W. West. Compressibility of the two-dimensional electron gas: Measurements of the zero-field exchange energy and fractional quantum hall gap. *Phys. Rev. B*, 50(3):1760–1778, Jul 1994.
- [28] Zyun F. Ezawa and Kenichi Sasaki. Skyrmions and quantum hall ferromagnets in improved composite-boson theory. *Journal of the Physical Society of Japan*, 68(2):576–585, 1999.
- [29] Reif F. *Statistische Physik und Theorie der Waerme*. de Gruyter Verlag, Berlin, New York, 3 edition, 1987.
- [30] G. Fano, F. Ortolani, and E. Colombo. Configuration-interaction calculations on the fractional quantum hall effect. *Phys. Rev. B*, 34(4):2670–2680, Aug 1986.
- [31] G. Fano, F. Ortolani, and E. Colombo. Configuration-interaction calculations on the fractional quantum hall effect. *Phys. Rev. B*, 34(4):2670–2680, Aug 1986.
- [32] E. Feenberg. *Theory of quantum fluids*, volume 31 of *Pure and Applied Physics*. Academic Press, London, 1969.
- [33] A. E. Feiguin, E. Rezayi, C. Nayak, and S. Das Sarma. Density matrix renormalization group study of incompressible fractional quantum hall states. *Phys. Rev. Lett.*, 100:166803, Apr 2008.
- [34] R. P. Feynman. Atomic theory of the two-fluid model of liquid helium. *Phys. Rev.*, 94(2):262–277, Apr 1954.
- [35] R. P. Feynman and Michael Cohen. Energy spectrum of the excitations in liquid helium. *Phys. Rev.*, 102(5):1189–1204, Jun 1956.
- [36] Wolfgang Fischer and Ingo Lieb. *Funktionentheorie*. Vieweg, Braunschweig [u.a.], 7 edition, 1994.
- [37] Eberhard Freitag and Rolf Busam. *Funktionentheorie*. Springer-Lehrbuch. Springer, Berlin, 2000.
- [38] Giuliani G. and Vignale G. *Quantum Theory of the Electron Liquid*. Cambridge University Press, Cambridge, New York, Melbourne, Madrid, Cape Town, Singapore, Sao Paulo, 2005.
- [39] Stephen Gasiorowicz. *Quantenphysik*. Oldenbourg, MÃ¼nchen and Wien, 5 edition, 1989.
- [40] S. M. Girvin. Introduction to the fractional quantum hall effect. *Seminaire Poincare*, 2:53–74, 2004.
- [41] S. M. Girvin and Terrence Jach. Formalism for the quantum hall effect: Hilbert space of analytic functions. *Phys. Rev. B*, 29(10):5617–5625, May 1984.
- [42] S.M. Girvin, A. H. MacDonald, and P.M. Platzman. Magneto-roton theory of collective excitations in the fractional quantum hall effect. *Physical Review B*, 33(4):2481 – 2493, 1986.

- [43] S.M. Girvin, A.H. MacDonald, and P.M. Platzman. Collective-excitation gap in the fractional quantum hall effect. *Physical Review Letters*, 54(6):581 – 583, 1985.
- [44] The GNU GSL Team, <http://www.gnu.org/software/gsl/>. *Manual of the Gnu scientific library, version 1.12*.
- [45] A. Gold. Excitation gap in the fractionally quantized hall effect. *Physical Review B*, 36(6):3268 – 3279, 1987.
- [46] Kenneth L. Graham, Sudhansu S. Mandal, and Jainendra K. Jain. Nodal correlations in the incompressible composite fermion liquid. *Phys. Rev. B*, 67(23):235302, Jun 2003.
- [47] F. D. M. Haldane. Many-particle translational symmetries of two-dimensional electrons at rational landau-level filling. *Phys. Rev. Lett.*, 55(20):2095–2098, Nov 1985.
- [48] F. D. M. Haldane and E. H. Rezayi. Finite-size studies of the incompressible state of the fractionally quantized hall effect and its excitations. *Phys. Rev. Lett.*, 54(3):237–240, Jan 1985.
- [49] F. D. M. Haldane and E. H. Rezayi. Periodic Laughlin-Jastrow wave functions for the fractional quantized hall effect. *Phys. Rev. B*, 31(4):2529–2531, Feb 1985.
- [50] Edwin Hall. Action of magnetism on a permanent electric current. *American Journal of Science*, XX:161, 1880.
- [51] B. I. Halperin. Theory of the quantized hall conductance. *Helvetica Physica Acta*, 56(1-3):75 – 102, 1983.
- [52] B. I. Halperin, Patrick A. Lee, and Nicholas Read. Theory of the half-filled landau level. *Phys. Rev. B*, 47:7312–7343, Mar 1993.
- [53] Moritz Helias. Moritz titel. Master's thesis, University of Hamburg, 2004.
- [54] Bodo Huckestein. Scaling theory of the integer quantum hall effect. *Rev. Mod. Phys.*, 67(2):357–396, Apr 1995.
- [55] Intel Corporation. *Intel Math Kernel Library - Documentation*. Revision: 008 MKL 2017.
- [56] Callaway J. *Quantum Theory of the Solid State*, chapter 5.4.2, pages 428–431. Academic Press, San Diego, London, 1991.
- [57] Jackson. *Electro dynamics*. Wiley and Sons, New York, 3 edition, 1999.
- [58] J. A. Jain. *Composite Fermions*. Cambridge University Press, Cambridge, New York, Melbourne, Cape Town, Sao Paolo, 2007.
- [59] J. K. Jain. The role of analogy in unraveling the fractional quantum hall effect mystery. *Physica E: Low-dimensional Systems and Nanostructures*, 20(1-2):79–88, 12 2003. Proceedings of the International Symposium @'Quantum Hall Effect: Past, Present and Future.

- [60] J. K. Jain and R. K. Kamilla. *Composite Fermions*, chapter 10. Singapore, 1997.
- [61] J. K. Jain and R. K. Kamilla. Quantitative study of large composite-fermion systems. *Phys. Rev. B*, 55(8):R4895–R4898, Feb 1997.
- [62] Miller Johanna. Semiconductor metamaterial fools the hall effect. *Physics Today*, 70(2):21, February 2017.
- [63] Robert Joynt and R. E. Prange. Conditions for the quantum hall effect. *Phys. Rev. B*, 29(6):3303–3317, Mar 1984.
- [64] V. S. Khrapai, A. A. Shashkin, M. G. Trokina, V. T. Dolgopolov, V. Pellegrini, F. Beltram, G. Biasiol, and L. Sorba. Direct measurements of fractional quantum hall effect gaps. *Physical Review Letters*, 99(8):086802, 2007.
- [65] Charles Kittel and Herbert Krömer. *Thermodynamik*. Oldenbourg, München and Wien, 5 edition, 2001.
- [66] U. Klass, W. Dietsche, K. von Klitzing, and K. Ploog. Image of the dissipation in gated quantum hall effect samples. *Surface Science*, 263(1):97 – 99, 1992.
- [67] K. v. Klitzing, G. Dorda, and M. Pepper. New method for high-accuracy determination of the fine-structure constant based on quantized hall resistance. *Phys. Rev. Lett.*, 45(6):494–497, Aug 1980.
- [68] M. Kohmto. Topological invariant and the quantization of the hall conductance. *Annals of Physics*, 160(2):342–354, 1985.
- [69] L. Landau. Theory of the superfluidity of helium ii. *Phys. Rev.*, 60(4):356–358, Aug 1941.
- [70] L. D. Landau and E. M. Lifshitz. *Quantenmechanik*. Akademie Verlag, 1979.
- [71] R. B. Laughlin. Quantized hall conductivity in two dimensions. *Phys. Rev. B*, 23(10):5632–5633, May 1981.
- [72] R. B. Laughlin. Anomalous quantum hall effect: An incompressible quantum fluid with fractionally charged excitations. *Phys. Rev. Lett.*, 50(18):1395–1398, May 1983.
- [73] R. B. Laughlin. Primitive and composite ground states in the fractional quantum hall effect. *Surface Science*, 142:163–172, Sep 1984.
- [74] Landau L.D. and Lifshitz E.M. *Statistische Physik Teil 2*, volume 9,2. Akademie Verlag, Berlin, 1992.
- [75] Guilarte J. M., J. M. M. Porras, and M. T. de la Torre Mayado. Elliptic theta functions and the fractional quantum hall effect. *Journal of Geometry and Physics*, 27:297–332, 1998.
- [76] A. H. MacDonald. Introduction to the physics of the quantum hall regime. *arXiv:cond-mat/9410047*, 1994.

- [77] A.H. MacDonald, K. L. Liu, S. M. Girvin, and P.M. Platzman. Disorder and the fractional quantum hall effect: Activation energies and the collapse of the gap. *Physical Review B*, 33(6):4014 – 4020, 1986.
- [78] R. Morf and B. I. Halperin. Monte carlo evaluation of trial wave functions for the fractional quantized hall effect: Disk geometry. *Phys. Rev. B*, 33(4):2221–2246, Feb 1986.
- [79] R. H. Morf, N. d'Ambrumenil, and S. Das Sarma. Excitation gaps in fractional quantum hall states: An exact diagonalization study. *Phys. Rev. B*, 66(7):075408, Aug 2002.
- [80] Ganpathy Murthy and R. Shankar. Hamiltonian theories of the fractional quantum hall effect. *Rev. Mod. Phys.*, 75(4):1101–1158, Oct 2003.
- [81] G. MÄ¶llenstedt and W. Bayh. Messung der kontinuierlichen phasenschiebung von elektronenwellen im kraftfeldfreien raum durch das magnetische vektorpotential einer luftspule. *Die Naturwissenschaften*, 49(4):81–82, 196.
- [82] Nash. *Topology and geometry for physicists*. Academic Press, London, 1983.
- [83] Qian Niu, D. J. Thouless, and Yong-Shi Wu. Quantized hall conductance as a topological invariant. *Phys. Rev. B*, 31:3372–3377, Mar 1985.
- [84] Wolfgang Nolting. *Grundkurs Theoretische Physik*, volume 5. Vieweg, Braunschweig and Wiesbaden, 2000.
- [85] The Numerical algorithm group, <http://www.nag.co.uk>. *Manual of the NAG library Mark 9*.
- [86] Travis E. Oliphant. Python for scientific computing. *Computing in Science and Engineering*, 9(3):10–20, 2007.
- [87] Streda P. Theory of quantised hall conductivity in two dimensions. *J. Phys. C: Solid State Phys.*, 15:L717–L721, 1982.
- [88] W. Pan, G. A. Csathy, D. C. Tsui, L. N. Pfeiffer, and K. W. West. Transition from a fractional quantum hall liquid to an electron solid at landau level filling $\nu = \frac{1}{3}$ in tilted magnetic fields. *Phys. Rev. B*, 88(7):076801, Jan 2002.
- [89] W. Pan, H. L. Stormer, D. C. Tsui, L. N. Pfeiffer, K. W. Baldwin, and K. W. West. Transition from an electron solid to the sequence of fractional quantum hall states at very low landau level filling factor. *Phys. Rev. Lett.*, 88(17):176802, Apr 2002.
- [90] Nicola Paradiso, Stefan Heun, Stefano Roddaro, Lucia Sorba, Fabio Beltram, Giorgio Biasiol, L. N. Pfeiffer, and K. W. West. Imaging fractional incompressible stripes in integer quantum hall systems. *Phys. Rev. Lett.*, 108:246801, Jun 2012.
- [91] D. Pfannkuche and A. H. MacDonald. The quantum hall effect of interacting electrons in a periodic potential. *Physical Review B*, 1996.

- [92] Daniela Pfannkuche. *Aspects of Coulomb interaction in semiconductor nanostructures*. PhD thesis, Universitt zu Kln, 1998.
- [93] Daniela Pfannkuche and A. H. MacDonald. Quantum hall effect of interacting electrons in a periodic potential. *Phys. Rev. B*, 56(12):R7100–R7103, Sep 1997.
- [94] A. Pinczuk, B. S. Dennis, L. N. Pfeiffer, and K. West. Observation of collective excitations in the fractional quantum hall effect. *Phys. Rev. Lett.*, 70:3983–3986, Jun 1993.
- [95] P. M. Platzman and Song He. Resonant raman scattering from mobile electrons in the fractional quantum hall regime. *Phys. Rev. B*, 49:13674–13679, May 1994.
- [96] E. H. Rezayi and F. D. M. Haldane. Incompressible states of the fractionally quantized hall effect in the presence of impurities: A finite size study. *Physical Review B*, 32(10):6924, 1985.
- [97] E. H. Rezayi and F.D.M. Haldane. state on stretched and squeezed cylinders and edge excitations in the quantum hall effect. *Physical Review B*, 50(23):17199 – 17207, 1994.
- [98] Ilani S., Martin J., Teitelbaum E., J. H. Smet, D. Mahalu, Umansky V., and A. Yacoby. The microscopic nature of localization in the quantum hall effect. *Nature*, pages 328–332, 01 2004.
- [99] H. Saarikoski, A. Harju, M. J. Puska, and R. M. Nieminen. Vortex clusters in quantum dots. *Phys. Rev. Lett.*, 93:116802, Sep 2004.
- [100] H. Saarikoski, S. M. Reimann, A. Harju, and M. Manninen. Vortices in quantum droplets: Analogies between boson and fermion systems. *Rev. Mod. Phys.*, 82:2785–2834, Sep 2010.
- [101] H. Saarikoski, S. M. Reimann, E. Rsnen, A. Harju, and M. J. Puska. Stability of vortex structures in quantum dots. *Phys. Rev. B*, 71:035421, Jan 2005.
- [102] Henri Saarikoski and Ari Harju. Ground state of two-dimensional finite electron systems in the quantum hall regime. *Phys. Rev. Lett.*, 94:246803, Jun 2005.
- [103] S. Das Sarma. Self-consistent theory of screening in a two dimensional electron gas under strong magnetic field. *Solid State Communications*, 36(4):357 – 360, 1980.
- [104] Sankar Das Sarma and Aron Pinczuk, editors. *Perspectives in Quantum Hall Effects*. John Wiley, New York and Chichester and Brisbae and Toronto and Singapore, 1997.
- [105] K. Sasaki and Z. F. Ezawa. Thermal and tunneling pair creation of quasi-particles in quantum hall systems. *Phys. Rev. B*, 60(12):8811–8816, Sep 1999.

- [106] C. Schüller, K.-B. Broocks, P. Schröter, Ch. Heyn, D. Heitmann, M. Bichler, W. Wegscheider, Tapash Chakraborty, and V. M. Apalkov. Optical probing of a fractionally charged quasi-hole in an incompressible liquid. *Phys. Rev. Lett.*, 91(11):116403, Sep 2003.
- [107] C. Schüller, K. Keller, G. Biese, E. Ulrichs, L. Rolf, C. Steinebach, D. Heitmann, and K. Eberl. Quasiatomic fine structure and selection rules in quantum dots. *Phys. Rev. Lett.*, 80:2673–2676, Mar 1998.
- [108] *SciPy Manual*.
- [109] D. N. Sheng, Xin Wan, E. H. Rezayi, Kun Yang, R. N. Bhatt, and F. D. M. Haldane. Disorder-driven collapse of the mobility gap and transition to an insulator in the fractional quantum hall effect. *Phys. Rev. Lett.*, 90(25):256802, Jun 2003.
- [110] J. Shumway and D. M. Ceperley. *Handbook of Theoretical and Computational Nanotechnology*, volume 3, chapter Quantum Monte Carlo Methods in the Study of Nanostructures, pages 605–641. American Scientific Publishers, 2006.
- [111] B Smit and D Frenkel. An explicit expression for finite-size corrections to the chemical potential. *Journal of Physics: Condensed Matter*, 1(44):8659, 1989.
- [112] Ady Stern. Anyons and the quantum hall effect a pedagogical review. *Annals of Physics*, 323(1):204 – 249, 2008. January Special Issue 2008.
- [113] Frank Stern. Polarizability of a two-dimensional electron gas. *Physical Review Letters*, 18(14):546, 1967.
- [114] Frank Stern and W. E. Howard. Properties of semiconductor surface inversion layers in the electric quantum limit. *Physical Review B*, 163(1):816–835, 1967.
- [115] Horst L. Stormer, Daniel C. Tsui, and Arthur C. Gossard. The fractional quantum hall effect. *Rev. Mod. Phys.*, 71:S298–S305, Mar 1999.
- [116] P Streda. Quantised hall effect in a two-dimensional periodic potential. *J. Phys. C: Solid State Phys.*, 15:L1299–L1303, 1982.
- [117] M. B. Tavernier, E. Anisimovas, and F. M. Peeters. Ground state and vortex structure of the $n = 5$ and $n = 6$ electron quantum dot. *Phys. Rev. B*, 74:125305, Sep 2006.
- [118] Jos Thijssen. *Computational Physics*. Cambridge, 1 edition, 2007.
- [119] D. J. Thouless, M. Kohmoto, M. P. Nightingale, and M. den Nijs. Quantized hall conductance in a two-dimensional periodic potential. *Phys. Rev. Lett.*, 49:405–408, Aug 1982.
- [120] David J Thouless. *Topological Quantum Numbers in nonrelativistic physics*. World Scientific, Singapore, London, River Edge, 1998.

- [121] S. A. Trugman and S. Kivelson. Exact results for the fractional quantum hall effect with general interactions. *Phys. Rev. B*, 31(8):5280–5284, Apr 1985.
- [122] D. C. Tsui, H. L. Störmer, and A. C. Gossard. Zero-resistance state of two-dimensional electrons in a quantizing magnetic field. *Phys. Rev. B*, 25(2):1405–1407, Jan 1982.
- [123] Vandermonde.
- [124] K. Vyborny, Müller C., and Pfannkuche D. Response of incompressible fractional quantum hall states to magnetic and non-magnetic impurities. *to be published*, 2006.
- [125] K. Vyborny, Müller C., Dethleffsen A. F., Haug R.J., and A. Woisz. Effect of disorder on spin and charge excitations in the fractional quantum hall effect. *Physica Polonica Acta A*, 112(2):249–257, 08 2007.
- [126] Karel Vyborny. private communication.
- [127] Karel Vyborny. *Spin in fractional quantum Hall systems*. PhD thesis, University of Hamburg, 2005.
- [128] J. Wakabayashi, S. Kawaji, J. Yoshino, and S. Hiroyuki. Activation energies of the fractional quantum hall effect in gaas/algaaas heterostructures. *Journal of the Physical Society of Japan*, 55(4):1319–1326, Apr 1986.
- [129] Xin Wan, D. N. Sheng, E. H. Rezayi, Kun Yang, R. N. Bhatt, and F. D. M. Haldane. Mobility gap in fractional quantum hall liquids: Effects of disorder and layer thickness. *Physical Review B (Condensed Matter and Materials Physics)*, 72(7):075325, 2005.
- [130] R. L. Willett, H. L. Stormer, D. C. Tsui, A. C. Gossard, and J. H. English. Quantitative experimental test for the theoretical gap energies in the fractional quantum hall effect. *Phys. Rev. B*, 37(14):8476–8479, May 1988.
- [131] Fengcheng Wu and A. H. MacDonald. Moiré assisted fractional quantum hall state spectroscopy. *Phys. Rev. B*, 94:241108, Dec 2016.
- [132] D. Yoshioka, B. I. Halperin, and P. A. Lee. Ground state of two-dimensional electrons in strong magnetic fields and $\frac{1}{3}$ quantized hall effect. *Phys. Rev. Lett.*, 50:1219–1222, Apr 1983.
- [133] Daijiro Yoshioka. Ground state of the two-dimensional charged particles in a strong magnetic field and the fractional quantum hall effect. *Phys. Rev. B*, 29(12):6833–6839, Jun 1984.
- [134] Daijiro Yoshioka. Theory of the fractional quantum hall effect. *Progress of Theoretical Physics Supplement*, 84:97–119, 1985.
- [135] Daijiro Yoshioka. *The Quantum Hall Effect*, volume 133 of *Springer series in Solid-State Science*. Springer, Berlin and Heidelberg, 2002.

- [136] Anthony Zee. *Quantum Field Theory in a nutshell*. Princeton University Press, Princeton, 2003.
- [137] F. C. Zhang, V. Z. Vulovic, Y. Guo, and S. Das Sarma. Effect of a charged impurity on the fractional quantum hall effect: Exact numerical treatment of finite systems. *Phys. Rev. B*, 32(10):6920–6923, Nov 1985.
- [138] Jize Zhao, D. N. Sheng, and F. D. M. Haldane. Fractional quantum hall states at $\frac{1}{3}$ and $\frac{5}{2}$ filling: Density-matrix renormalization group calculations. *Phys. Rev. B*, 83:195135, May 2011.